UNIVERSITÄT BONN
Physikalisches Institut

Measurement of neutral current deep inelastic e^+p scattering cross sections with longitudinally polarized positrons with ZEUS at HERA

by

Michał Własenko

Measurements of neutral current deep inelastic scattering of protons colliding with longitudinally polarized positrons, performed with data recorded in years 2006 and 2007 with the ZEUS detector, corresponding to an integrated luminosity of $\mathcal{L} = 113.3\,\mathrm{pb}^{-1}$, are presented. The single-differenatial cross sections $d\sigma/dQ^2$, $d\sigma/dx$, $d\sigma/dy$ and the double-differential reduced cross section $\tilde{\sigma}$ were measured in the kinematic region of $185 < Q^2 < 50\,000\,\mathrm{GeV}^2$ and $y < 0.95$ at the center-of-mass energy of 319 GeV. The parity violating polarization asymmetry A^+ and the generalized structure function $x\tilde{F}_3$ were extracted. All measurements agree well with the predictions of the Standard Model.

Postal address:
Nussallee 12
D-53115 Bonn
Germany

BONN-IR-2009-05
Bonn University
May 2009
ISSN-0172-8741

UNIVERSITÄT BONN
Physikalisches Institut

Measurement of neutral current deep inelastic e^+p scattering cross sections with longitudinally polarized positrons with ZEUS at HERA

by

Michał Własenko

Referent:	Prof. Dr. Erwin Hilger
Korreferent:	Prof. Dr. Klaus Desch

Angenommen am:	12.03.2009
Tag der Promotion:	04.05.2009

Contents

Chapter 1

Introduction

This work is an offspring of an adventure that I have had a chance to participate in, during the last few years. Even though the machines, named HERA and ZEUS, which were central parts of the scientific research described here, were huge, their goal was to study amazingly tiny scales. In fact, quantum mechanics has taught us, that in order to be able to ”see” into the realm of elementary building blocks of matter and interactions between them, we need to accelerate them to velocities just a little bit smaller than the speed of light. That exactly was happening at HERA, a machine which we could call a special kind of a super-microscope, where we used the simple point-like leptons (electrons and positrons) to test our notion of the proton, its building blocks - quarks and gluons, and the forces between them.

A deeper story of how physics has arrived at today's stage of understanding the basic interactions between leptons and quarks (bound in hadrons) will be given in the next chapter, but here let me mention the questions which have been addressed in the course of the analysis described in this thesis.

The current, thoroughly tested, confirmed and accepted paradigm of elementary particle physics, the Standard Model, embracing the three quantized forces (electromagnetic, weak and strong) gives us the picture of the proton as a “sea” of point-like quarks and gluons formalized within the theory of the strong force, Quantum Chromodynamics (QCD). While the interactions between these hadron constituents are to a large extent calculable, the theory cannot predict the specific fractions between e.g. different quark kinds (flavors) from first principles. Therefore, we make use of simpler objects - electrons and positrons - to break the proton up in collisions (a process called deep inelastic scattering, DIS), and by studying the products of these collisions, to deduce the composition of the proton. This endeavor has been very successful for four decades now, and the work presented here is aimed to make use of the last e^+p data recorded by the ZEUS collaboration at the HERA collider, to provide input in form of double-differential e^+p

neutral current deep inelastic scattering cross sections, which will allow further constraints on the already very precise picture of the proton (through QCD fits of the parton density functions). Moreover, even though the electroweak part of the Standard Model has already been successfully tested, it has never (before HERA) been studied in the $e^{\pm}p$ environment at electroweak energy scales. Thanks to the fact that the magnitude of $e^{-}p$ and $e^{+}p$ interactions differs, we are able to test the electroweak theory down to spatial distances of $10^{-18}\,\mathrm{m}$, available thanks to the high HERA center-of-mass collision energy of 319 GeV. The electroweak interactions also depend on the orientation of the lepton spin w.r.t. its vector of momentum, and at the electroweak scale one can study this phenomenon by observing how different will the strength of the interaction be when using bunches of e.g. positrons oriented parallel or anti-parallel to its momentum vector. These two tests, through the measurement of the proton structure function $x\tilde{F}_3$ and the polarization asymmetry A^{+}, have been performed for the first time with such a high accuracy, and will be reported later in the body of this thesis.

The work presented in this thesis has been focused on understanding the $e^{+}p$ neutral current (NC) DIS data recorded by the ZEUS collaboration in years 2006/07 and measuring the single- and double-differential cross sections. NC DIS ep interactions have been studied at ZEUS from the beginning of its existence, therefore techniques aimed at selecting the signal of high quality and unfolding the cross sections have been developed and refined over a few generations of analyses. However, a certain behavior of the data recorded in years 2006/07, w.r.t. to the simulation used to describe it, required careful studies, which rose to become the biggest task of the analysis presented here.

Apart from contributing to the analysis presented in this thesis, I had a chance to take part in the life of the ZEUS collaboration in several ways. My commitments included serving as a member of the shift crew, the task of which was to take care of efficient data taking by the detector. I also maintained the ZEUS-Bonn group computer cluster at DESY, Hamburg and joined the team which selected the most interesting physics events, as they were being recorded and reconstructed. In course of the preparation to the NC DIS analysis, I wrote a ZEUS internal note on unfolding and sensitivity to $F_2^0, F_2^P, xF_3^0, xF_3^P$ neutral current structure functions at HERA II. I was awarded the pleasure to present the results of several ZEUS and H1 analyses (including mine), on the structure of the proton and electroweak physics at HERA, at the International Conference on Particles And Nuclei (PANIC08) in Eilat, Israel. The partial (single-differential) results of the analysis presented in this thesis were declared preliminary by the ZEUS collaboration on the Summer of 2008 and presented at several conferences. Currently, they are being prepared to be published in form of an article, which is expected in Summer of 2009. I am also listed as a co-author of more than 40 papers published by the ZEUS collaboration. Finally, I had an opportunity of tutoring courses on introduction to elementary particle physics and computing, at the Physikalisches Institut of the Bonn University.

This thesis is organized as follows. Chapter 2 presents history and physics of the deep inelastic scattering and defines quantities to be measured in the analysis presented here. The experimental setup, including the description of the HERA collider and the ZEUS detector, is given in Chapter 3. The basic toolbox employed to reconstruct neutral current deep inelastic scattering events is given in Chapter 4, and is followed by the description of techniques of selecting interesting physics events among the ones of the background, in Chapter 5, which also presents the data and Monte Carlo simulated samples employed in this analysis. The curious features of the data mentioned before are treated in detail in Chapter 6, which focuses on the systematic studies dedicated to the best possible understanding of the recorded samples. The method of extracting the cross sections, the $x\tilde{F}_3$ structure function and A^+ polarization asymmetry is then described in Chapter 7, including all the obtained results. The thesis is completed by the Summary and a set of tables in Appendix A containing a detailed list of the obtained results.

Chapter 2

Deep Inelastic Scattering

2.1 Historical perspective

Discovery of the quarks

The discovery[1] of Deep Inelastic Scattering (DIS) was achieved by walking the path carved by many scattering experiments conducted throughout the XXth century. The idea was proven successful already by Rutherford and his collaborators [10, 11] in 1911. They managed to understand that an atom consists of a nucleus and a cloud of electrons surrounding it, by bombarding a thin gold foil with a beam of simpler objects than the one under study (α-particles), and analyzing the scattering angle distribution. It was noticed that while usually the probes would be deflected only slightly, in rare events they were deflected at large angles or even bounced backwards, supporting the concept of a positively charged nucleus containing almost full mass of an atom within a compact space in its center.

Postulating the uncertainty principle named after him, Heisenberg set a limit on the best spatial resolution with which a particle beam of momentum p can probe the substructure of a composite object. This limit is the associated wavelength of the beam particles, given by $\lambda = h/p$, which in modern notation leads to the relation: $\delta = \frac{0.2 \cdot 10^{-15}\,\mathrm{m}}{Q[\,\mathrm{GeV}]}$, where Q is the four-momentum exchanged in the interaction. This means that for a momentum transfer of $\mathcal{O}[\,\mathrm{GeV}]$ the probed distances are comparable to the size of the proton, while at the highest Q^2 achieved by the HERA experiments, the proton is probed down to $\mathcal{O}[10^{-18}\,\mathrm{m}]$.

In the 1950s at the linear accelerator at Stanford University, California, the same idea of scattering a simple probe off an object under study in order to resolve its structure was employed in experiments colliding electron beams of energies up

---

[1] The sketch presented here must be, for obvious reasons, grossly oversimplified and fails in fully presenting the fascinating and complicated way to understanding of the electron-proton scattering, as we see it today. The reader can find a more complete picture elsewhere, e.g. [1–9].

to 0.25 GeV with nuclear targets, demonstrating that the proton was not a point particle, but a complex object with finite dimensions of $\mathcal{O}[1\,\mathrm{fm}]$ [12].

On the theory side, exploring the symmetry between the lightest strongly interacting baryons: the proton and the neutron, Zweig [13] and independently Gell-Mann [14] found that all of the observed hadrons could hypothetically be built from point-like objects with spin-1/2 and fractional charges-*quarks*. In order to comply with the Pauli exclusion principle, claiming that e.g. the spin-3/2 Δ^{++} resonance cannot be built of three exactly like quarks, a new quantum number-*color*, taking three possible values (e.g. red, green, blue), was proposed [15]. Additionally, all hadrons were postulated to be *colorless* (or *white*) and constructed from the color triplet of quarks (q_R, q_G, q_B). The hadronic color-bound states are then baryons (qqq) or mesons $(q\bar{q})$, but existence of single free quarks which carry color is forbidden by the model (*color confinement*).

Further insight into the structure of the proton was gained in the first series of DIS experiments, in the late 1960s and early 1970s at the (at that time) 20 GeV Stanford electron linear accelerator (SLAC) [16, 17]. At that time the nucleons were believed to be extended objects with a diffuse internal structure. In such a case the *ep* scattering cross section should depend on two kinematic variables. The interaction (in the kinematic range then accessible) is mediated by a virtual photon of energy $\nu = E_e - E_e' = Q^2/(2M_N)$, where E_e denotes the electron beam energy, E_e' - energy of the scattered electron and $-Q^2 = q^2\nu^2 - \boldsymbol{q}^2$ is the squared four-momentum transferred between the electron and the nucleus of mass M_N (from the stationary target). Additionally defining a variable $x = Q^2/(2M\nu)$ (M being the mass of the proton), physicists at SLAC observed *scaling*, i.e. the phenomenon of the scattering cross section being dependent only on x, and not anymore on the resolving power (Q^2) of the photon exchanged in the interaction (see Fig. 2.1). It was Bjorken who first understood [18] that scaling is the experimental evidence of the proton to be composed of (three) point-like constituents. It was later shown that the scaling variable x can be interpreted as the fraction of the proton momentum carried by the struck quark.

Introducing structure functions of the proton and the quark parton model

Even though DIS revealed the existence of quarks, it was not clear how the proton breaks up as a result of the interaction with a hard virtual photon. This ignorance was first parametrized in form of the structure functions (in contemporary notation) F_1 and F_2, of variables Q^2 and x, while the differential cross section took the

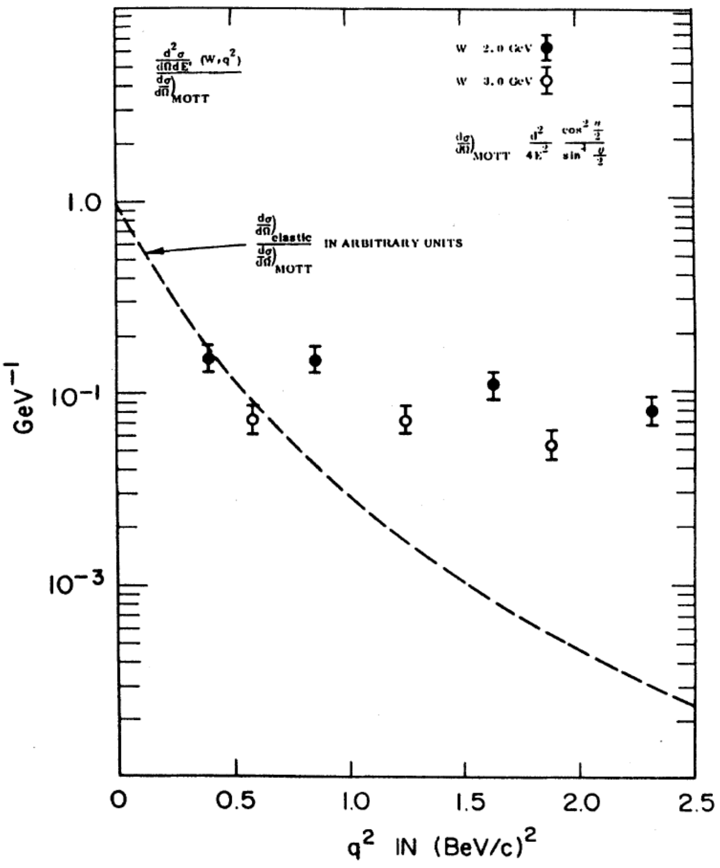

Figure 2.1: First DIS measurements from SLAC at $W = 2$ and $W = 3\,\mathrm{GeV}$, where W is the invariant mass of the hadronic final state given by $W^2 = 2M\nu + M^2 - q^2$ [1]. The data plotted against the curve characterizing elastic *ep* scattering displays weak dependence on q^2 at constant W (leading to scaling of the structure function F_2).

form of:

$$\frac{d^2\sigma}{dxdQ^2} = \frac{4\pi\alpha^2}{xQ^4}\left[y^2 xF_1(x,Q^2) + (1-y)F_2(x,Q^2)\right], \tag{2.1}$$

where α is the fine-structure constant and $y = Q^2/(xs) = (\nu/E_e)_{lab}$ with $\sqrt{s}$ being the total collision energy in the center-of-mass frame. Two structure functions were required as the low-Q^2 *ep* DIS is mediated either by transversely or longitudinally polarized virtual photons.

Understanding the relationship between the proton structure functions and theoretically motivated quarks cannot be attributed to a single person, as it took years of experimental and theoretical developments [19]. However Feynman [20] created what we now call the *naive parton model*, which later evolved into the *quark-parton model* (QPM). Working in the infinite momentum frame, in which the relativistic time dilation freezes the motion of the proton constituents, he concluded that the proton consisted of charged point-like partons which do not interact with each other during the exchange of the virtual photon, being *free* in that short moment of time (about $1/Q$). This phenomenon was later shown to be a consequence of *perturbative* QCD (pQCD) and is now known as *asymptotic freedom* [2].

Before long, Callan and Gross [21] considering spin states of the constituent partons showed, that for spin-1/2 of the partons, $R = \sigma_L/\sigma_T$, where σ_L is the part of the cross section carried by longitudinally and σ_T by transversely polarized photons, should be small[2], and for the QPM $R = q^2/\nu^2$, leading to $F_2 = 2xF_1$. Measurements which followed, confirmed the Callan-Gross relation in the kinematic range then accessible, (see Fig. 2.2), establishing the spin of the charged partons to be 1/2. Already in the early 1970s, Feynman predicted [22] that, at higher order, deviations from the Callan-Gross relation were expected at low x and low Q^2, and it took decades of DIS experiments to measure and understand the character of scaling violations (the evolution of precision measurements of the structure of the proton can be appreciated by studying e.g. the following list of results spanning almost 40 years of experiments: [16, 17, 23–29]).

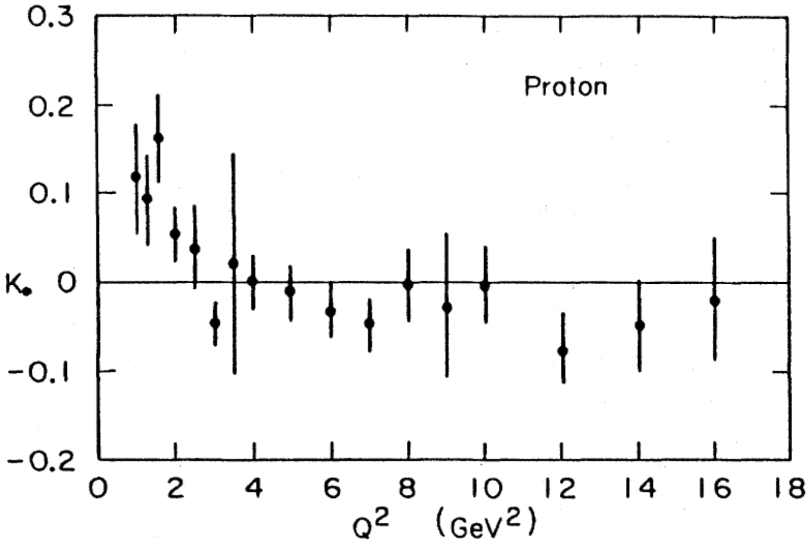

Figure 2.2: First measurements [1] of the Callan-Gross relation, where $K_0 = F_2/(2xF_1) - 1$.

In the framework of the QPM, the DIS cross section can be written as the

---

[2] In case of spin-0 or spin-1 partons, $R \neq 0$, and the proton could contain elementary bosons.

incoherent sum of probabilities of electron scattering off a single free quark:

$$\frac{d^2\sigma}{dxdQ^2} = \sum_i \int_0^1 dx q_i(x) \left(\frac{d^2\sigma}{dxdQ^2}\right)_{eq}, \tag{2.2}$$

where $q_i(x)$ is the probability of finding the quark q_i in the proton carrying a fraction x of the proton momentum and i runs over all considered quark flavors (assuming $Q^2 \gg m_{q_i}^2$). Generally, the functions $q(x, Q^2)$ are known as *parton density functions* (PDFs) and their shapes will be shown later. Because of color confinement, the struck quark recombines (with unit probability) with the spectator quarks to form colorless hadrons which form the hadronic final state. In the language of quark probabilities, the previously introduced structure functions take the form:

$$F_2 = 2xF_1 = \sum_i e_{q_i}^2 x q_i(x), \tag{2.3}$$

where e_{q_i} is the fractional charge of the struck quark. An example of the F_2 structure function measurement of DIS of muons on the hydrogen target, by the BCDMS collaboration in 1989 [24] is presented in Fig. 2.3.

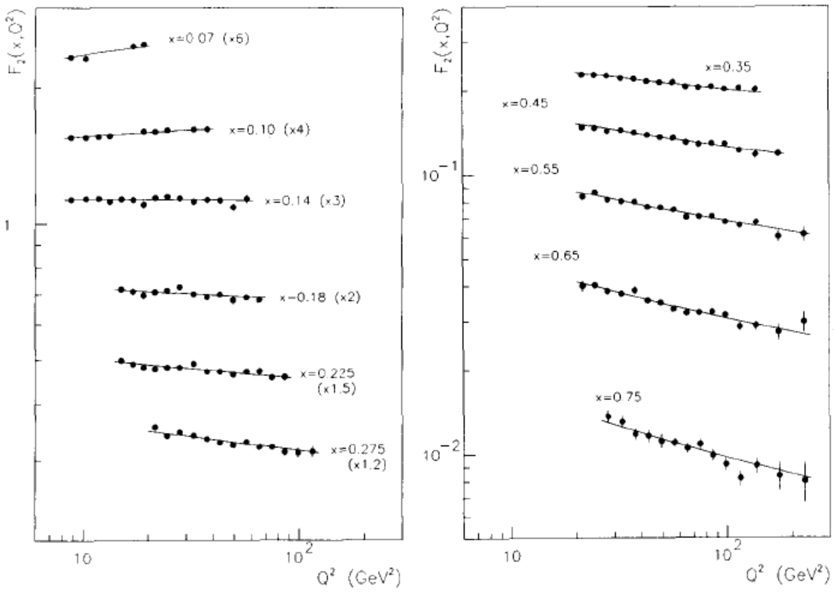

Figure 2.3: The proton structure function F_2 dependence on Q^2 in different bins of x, measured by the BCDMS collaboration in DIS of muons on a hydrogen target [24].

QCD, gluons and α_s

The existence of both, scattering off free quarks (at distances of $1/Q \ll R$, with R being the size of the proton) and color confinement (at distances of the order of R), posed a serious theoretical paradox in the 1970s, and resulted in formulating a new paradigm - Quantum Chromodynamics (QCD) - a quantum field theory of the strong interaction [2, 30–34], now one of the building blocks of the Standard Model (SM) of elementary interactions. Even though the discovery of QCD was achieved by the joint efforts of many researchers, Gell-Mann and 't Hooft were the two masterminds to whom its invention is attributed by a wide consensus[3].

QCD can be summarized as a quantum field theory, which describes the strong force to be mediated by the exchange of colored spin-1 massless gauge bosons, the *gluons*, and the strength of which depends on the conserved color charges. The eight gluons of QCD, being generators of the non-Abelian $SU(3)_C$, symmetry group, carry color themselves and therefore, unlike the photons (the gauge bosons of Quantum Electrodynamics, QED), couple to all color-carriers, so not only to quarks, but to each other as well.

While in QED, the running coupling constant α increases with Q^2 (being responsible for screening of the bare charge), because of the gluon-gluon coupling, the QCD running coupling constant α_s decreases with Q^2 (see Fig. 2.4). In QCD the color charge is then anti-screened:

$$\alpha_s(Q^2) = \frac{\alpha_s(\mu^2)}{1 + [\alpha_s(\mu^2)/6\pi](33/2 - n_f)\log(Q^2/\mu^2)}, \tag{2.4}$$

where n_f is the number of different flavors of virtual $q\bar{q}$ pairs (see next paragraphs) and μ is an arbitrary normalization scale at which the coupling α_s has been measured.

The high-Q^2 behavior of α_s forces QCD to be asymptotically free, for distances between color charges $r \to 0$, i.e. $Q^2 \to \infty$, we have $\alpha_s \to 0$. In the kinematic range of DIS, QCD is a perturbative theory as α_s is small. The running of α_s also induces the phenomenon of color confinement. As the force binding e.g. two quarks rises with the distance between them, the energy density of the field of gluons exchanged by them also rises, and at some point creation of a new virtual $q\bar{q}$ pair becomes energetically more favorable than further separation of quarks. The process of further recombination of colored charges into color-neutral hadrons, called *fragmentation* or *hadronization* is not yet entirely understood, and so far is

---

[3] From Wilczek's Nobel prize acceptance speech: "[...] I'd like to thank Murray Gell-Mann and Gerard 't Hooft for not quite inventing everything, and so leaving us something to do [...]" [2].

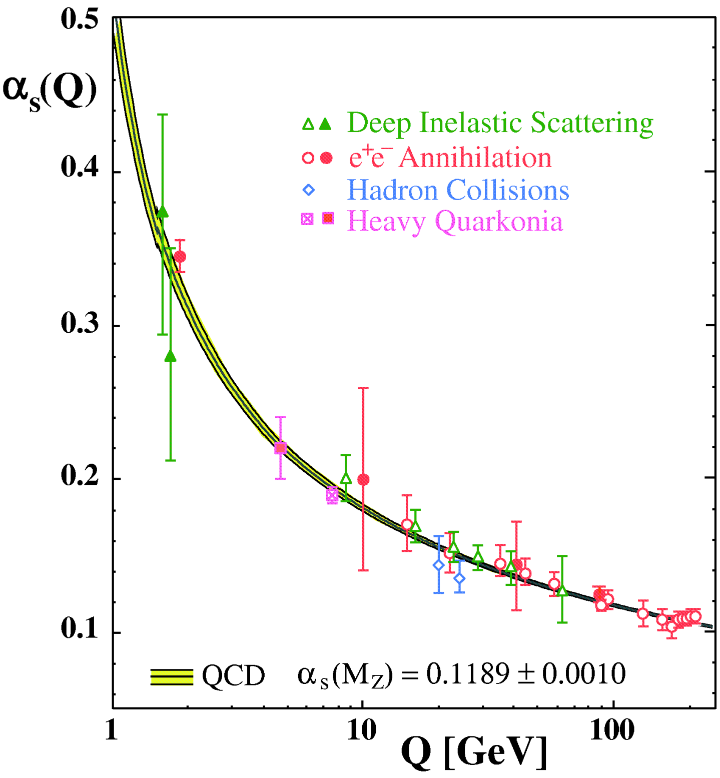

Figure 2.4: Summary of measurements α_s as a function of the energy scale Q [35].

based on phenomenological models [37].

As Q^2 decreases, the perturbative expansion in α_s breaks down and the theory enters its non-perturbative region, which is dealt with using different methods. While it is not possible to solve problems like calculating masses of observed baryons and mesons analytically, in e.g. *lattice* QCD [38] modern powerful computing techniques succeed in e.g. calculating the mass of the proton or the neutron with precision of 2% [39] from first principles.

One of the first direct experimental manifestations of the predictions of QCD was the observation of three-jet events at the e^+e^- PETRA storage ring at DESY in 1979 [36, 40], depicted in Fig. 2.5. Two of the hadronic jets emerging from the interaction vertex were associated with a $q\bar{q}$ pair, while the third one stems from a radiated gluon. Since then QCD has been tested in various conditions, and its predictions have been confirmed with great precision, e.g. [41, 42].

QCD-improved parton model

After introducing QCD, we now have to review the parton model discussed earlier. The QPM picture (scattering of the virtual photon γ^* off a free valence quark of proton momentum fraction x, Fig. 2.6(a)) completely ignored the dynamical role

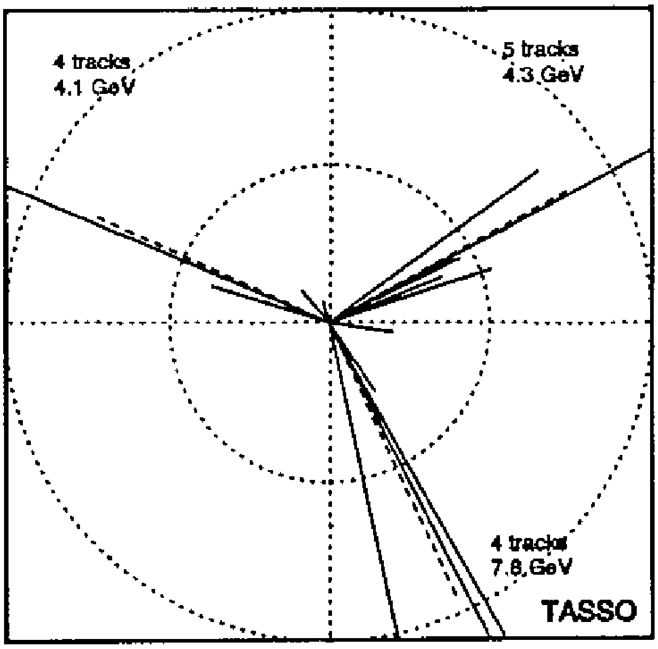

Figure 2.5: The three-jet event, being the first direct experimental observation of a gluon, from e^+e^- scattering at PETRA collider observed by the TASSO collaboration in 1979 [36]. Gluons were also found to carry about half of the proton momentum.

of gluons as carriers of the color field between the quarks in the proton. But QCD has shown, that if we e.g. just consider the lowest order (LO) processes in the QCD perturbative expansion of the DIS cross section, the quark, before or after being struck by the virtual photon, can radiate a gluon (Fig. 2.6(c)). The gluon can also produce a quark-antiquark pair, and contribute to the DIS cross section via the so called boson-gluon fusion: $\gamma^* g \to q\bar{q}$ (Fig. 2.6(b)).

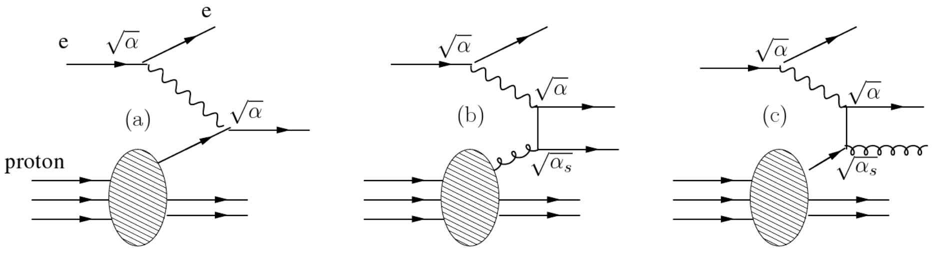

Figure 2.6: $\mathcal{O}(\alpha)$ (a) and $\mathcal{O}(\alpha\alpha_s)$ (b, c) contributions to the parton model picture of DIS [43].

Experimentally, the now *QCD-improved* parton model differs from the QPM by the violation of scaling of cross sections, structure functions and parton density functions, which now rise towards low x (see Fig. 2.7) and therefore depend also on

Q^2. In the QPM, the quarks probed by the photon do not interact with each other, and exact scaling is predicted. In the improved model, however, as we increase the resolving power Q^2, valence quarks appear to be surrounded by a "sea" of soft partons which increase in number as x lowers. The evolution in Q^2 of the *universal* (i.e. characterizing the proton, with no dependence on the nature of the probe) parton density functions for both quarks and gluons is given by the DGLAP equations [44, 45]:

$$\frac{\partial q_i(x,Q^2)}{\partial \log Q^2} = \frac{\alpha_s}{2\pi}\sum_j \int_x^1 \frac{d\xi}{\xi} P_{q_i q_j}(\frac{x}{\xi}, \alpha_s(Q^2)) q_j(\xi, Q^2) + P_{q_i g}(\frac{x}{\xi}, \alpha_s(Q^2)) g(\xi, Q^2), \tag{2.5}$$

$$\frac{\partial g(x,Q^2)}{\partial \log Q^2} = \frac{\alpha_s}{2\pi}\sum_j \int_x^1 \frac{d\xi}{\xi} P_{g q_j}(\frac{x}{\xi}, \alpha_s(Q^2)) q_j(\xi, Q^2) + P_{gg}(\frac{x}{\xi}, \alpha_s(Q^2)) g(\xi, Q^2), \tag{2.6}$$

where for each quark flavor i the *splitting function* $P_{ij}(z)$ is the probability distribution of a parton j (quark or a gluon) emitting a parton i with momentum fraction z of that of the parent parton. These evolution equations provide a formalism for calculating how parton densities change with Q^2, however the model does not allow for calculation of the distributions at any Q^2 without measuring $q(x, Q_0^2)$ and $g(x, Q_0^2)$ at some starting scale Q_0^2.

Moreover, in QPM all final-state jets would be collinear with the virtual photon, while after including the QCD gluon emission cross section we find the transverse momentum p_T of the jets or of the bremsstrahlung hadrons of these jets to be non-zero.

DIS as an electroweak process

Parallel to developments in understanding of the proton structure, the modern theory of the (electro)weak interaction which also enters the DIS realm studied in this thesis, was born. In order to explain the β-decay Fermi proposed the first form of the theory of the weak force in 1932 [46]. In 1956 Lee and Yang, in a survey of all the weak interaction data then available discovered the violation of parity conservation [47], which was very soon confirmed experimentally [48] and the $V - A$ theory of the weak force [49] was published in the 1950s. In the 1960s came the Glashow-Salam-Weinberg (GSW) model [8, 50–52] of spontaneously broken electroweak local gauge symmetry, unifying electromagnetic and weak interactions. The GSW model received experimental confirmation of its prediction of the weak

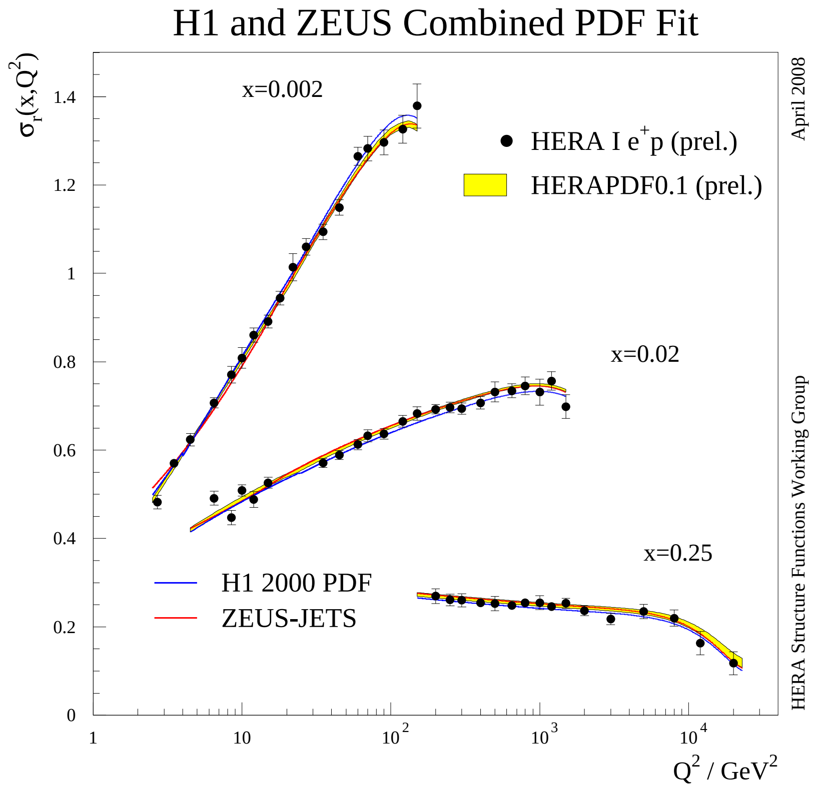

Figure 2.7: The NC DIS reduced cross section in function of Q^2 in three bins of x [28, 29]. Approximate scaling visible for the high-x case, scaling violations rising dramatically towards low x.

neutral currents, discovered by the Gargamelle Collaboration in 1973 [53]. The GSW model enjoyed further successes, when the weak gauge bosons $W^{\pm}$ and Z^0 were discovered in $p\bar{p}$ collisions at CERN [54, 55] and also when the electroweak coupling constants and the weak mixing angle were found (in several experiments) to be precisely as predicted by the model.

Further studies of DIS in the 1970s and 1980s by numerous stationary target collaborations like e.g. EMC and E665 with muons and CHARM and CCFR with neutrinos allowed better understanding of the nucleon structure functions and universal parton densities. However, by far the most precise results on DIS, both on low-x (QCD and scaling violations) as well as high-Q^2 (electroweak sector) physics, came with the advent of the HERA collider operated from 1992 until 2007.

Let us end here this brief historical overview of the developments leading to the contemporary understanding of DIS, and focus on the description of the cross sections, structure functions and parton density functions, which this work is intended to improve.

2.2 DIS processes and observables

Let us summarize the leading order (LO) picture of DIS and the observables describing it. The two major modes of DIS, depicted in Fig. 2.8, are the Neutral Current (NC, mediated by either a photon or a Z^0 boson) and the Charged Current (CC, mediated by the $W^\pm$ boson) processes. The final state consists of the scattered lepton, which emerges undetected in the case of CC, and the hadronic final state emerging from the QCD radiation and hadronization of the struck quark (current jet) and the proton remnant.

The DIS reaction is characterized by the following four-momenta: k - of the incoming lepton, P - of the incoming proton, k' - of the scattered lepton and $q = (k - k')$ - of the exchanged gauge boson. The Lorentz-invariant variables spanning the phase space of the interaction are defined by:

$$s = (k + P)^2, \tag{2.7}$$

$$Q^2 = -q^2 = -(k - k')^2, \tag{2.8}$$

$$x = \frac{Q^2}{2q \cdot P}, \tag{2.9}$$

$$y = \frac{q \cdot P}{k \cdot P}, \tag{2.10}$$

$$W = \sqrt{(q + P)^2}, \tag{2.11}$$

where s, the squared center-of-mass energy of the process, is constant for unchanged beam energies (and not considering initial-state photon radiation), while the other invariants characterize individual events. In the regime of the QPM, the Bjorken scaling variable x is associated with the fraction of the proton momentum carried by the struck quark and in the center-of-mass of the electron-quark system y is related to the polar scattering angle of the electron θ^* through $y = \frac{1}{2}(1 - \cos\theta^*)$, with $\theta^* = 0$ for no deflection [56]. Additionally, in the proton rest frame, the *inelasticity* y represents the fractional energy loss of the incoming lepton $y = \frac{E_e - E'_e}{E_e}$.

Finally, it can be shown that the following relations hold:

$$Q^2 = xys, \tag{2.12}$$

$$W^2 = (1 - x)ys, \tag{2.13}$$

which means that with s constant, just two of the given Lorentz invariants fully describe the interaction kinematically.

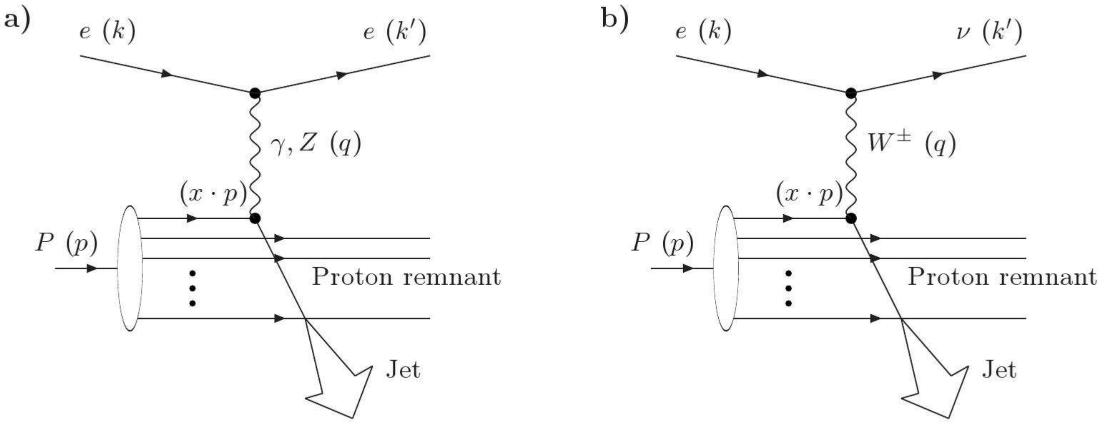

Figure 2.8: Leading-order Feynman graphs for the (a) Neutral Current and (b) Charged Current process in DIS [57].

2.3 Neutral Current cross section and Structure Functions

The electroweak Born-level double-differential cross section for the $e^{\pm}p$ NC interaction (see Fig. 2.9) can be written as [45, 58, 59]:

$$\frac{d^2\sigma^{\pm}_{NC}}{dxdQ^2} = \frac{2\pi\alpha^2}{xQ^4}\Big(Y_+\tilde{F}_2(x,Q^2) \mp Y_- x\tilde{F}_3(x,Q^2) - y^2\tilde{F}_L(x,Q^2)\Big) \tag{2.14}$$

where α is the fine-structure constant, $Y_{\pm} = 1 \pm (1-y)^2$, and $\tilde{F}_2(x,Q^2)$, $x\tilde{F}_3(x,Q^2)$ and $\tilde{F}_L(x,Q^2)$ are generalized structure functions. Because the double-differential cross section changes greatly due to the $1/(xQ^4)$ term, it is convenient to introduce the *reduced* cross section (see Fig. 2.7) defined as:

$$\tilde{\sigma}^{e^{\pm}p} = \frac{xQ^4}{2\pi\alpha^2}\frac{1}{Y_+}\frac{d^2\sigma^{\pm}_{NC}}{dxdQ^2} = \tilde{F}_2(x,Q^2) \mp \frac{Y_-}{Y_+}x\tilde{F}_3(x,Q^2) - \frac{y^2}{Y_+}\tilde{F}_L(x,Q^2). \tag{2.15}$$

The $\tilde{F}_2(x,Q^2)$ and $\tilde{F}_3(x,Q^2)$ structure functions can further be written as:

$$\tilde{F}_2 = F_2^{\gamma} - (v_e - P_e a_e)\chi_Z F_2^{\gamma Z} + (v_e^2 + a_e^2 - 2P_e v_e a_e)\chi_Z^2 F_2^Z, \tag{2.16}$$

$$x\tilde{F}_3 = -(a_e - P_e v_e)\chi_Z xF_3^{\gamma Z} + (2v_e a_e - P_e(v_e^2 + a_e^2))\chi_Z^2 xF_3^Z \tag{2.17}$$

where, the vector and axial-vector couplings of the electron to the Z boson in the SM are respectively given by $v_e = -1/2 + 2\sin^2\theta_W$ and $a_e = -1/2$, and θ_W is the Weinberg angle. F_2^{γ}, F_2^Z, $F_2^{\gamma Z}$ represent the contributions to the cross section coming from pure photon exchange, pure Z exchange and their interference, respectively. The contributions of γ and Z exchange are scaled by the powers of the propagator term:

$$\chi_Z = \frac{1}{\sin^2 2\theta_W} \frac{Q^2}{M_Z^2 + Q^2}, \tag{2.18}$$

which varies between 0.2 and 1.1 over the range $1500 < Q^2 < 50\,000\,\mathrm{GeV}^2$ accessible at HERA [59]. The cross section also depends on the helicity of the incoming lepton, which is accounted for by the lepton polarization term which scales $F_2^{\gamma Z}$, F_2^Z, $xF_3^{\gamma Z}$ and xF_3^Z:

$$P_e = \frac{N_R - N_L}{N_R + N_L}, \tag{2.19}$$

where N_R and N_L are the numbers of right- and left-handed leptons in the beam[4].

In the language of parton densities in LO QCD, the structure functions can be written as:

$$[F_2^\gamma, F_2^{\gamma Z}, F_2^Z] = \sum_q [e_q^2, 2e_q v_q, v_q^2 + a_q^2] x(q + \bar{q}), \tag{2.20}$$

$$[xF_3^{\gamma Z}, xF_3^Z] = \sum_q [e_q a_q, v_q a_q] 2x(q - \bar{q}), \tag{2.21}$$

where v_q and a_q are the vector and axial-vector couplings of the quark flavor q, e_q is the quark's electric charge and $q(x, Q^2)$ are quark densities. Due to Eq. 2.2 the sums run over all quark flavors except the t quark.

The $\tilde{F}_2$ structure function is proportional to the sum of q and $\bar{q}$ parton densities, and therefore receives contributions from both the valence and the sea quarks. Also, because it includes the pure γ exchange term, $\tilde{F}_2$ dominates the cross section at lower-Q^2 (over most of the HERA kinematic space). At the next to leading order of perturbative QCD (NLO QCD), the gluonic contribution drives the scaling violation of $\tilde{F}_2$ at lower x, through a relation $\partial \tilde{F}_2 / \partial \ln(Q^2) \approx (10\alpha_s(Q^2)/(27\pi)) x g(x, Q^2)$ [60], where $g(x, Q^2)$ is the gluon density.

The $x\tilde{F}_3$ structure function on the other hand (see Fig. 2.10) is proportional to the difference of q and $\bar{q}$ contributions to the proton structure. Assuming (in LO QCD) equal contributions of the sea-q and sea-$\bar{q}$, $x\tilde{F}_3$ is then proportional to the valence quark PDFs only. We further notice, that the difference of the e^-p and

---

[4] At beam energies available at HERA, the mass of the incoming lepton may be neglected, and therefore the difference between handedness and helicity may also be neglected.

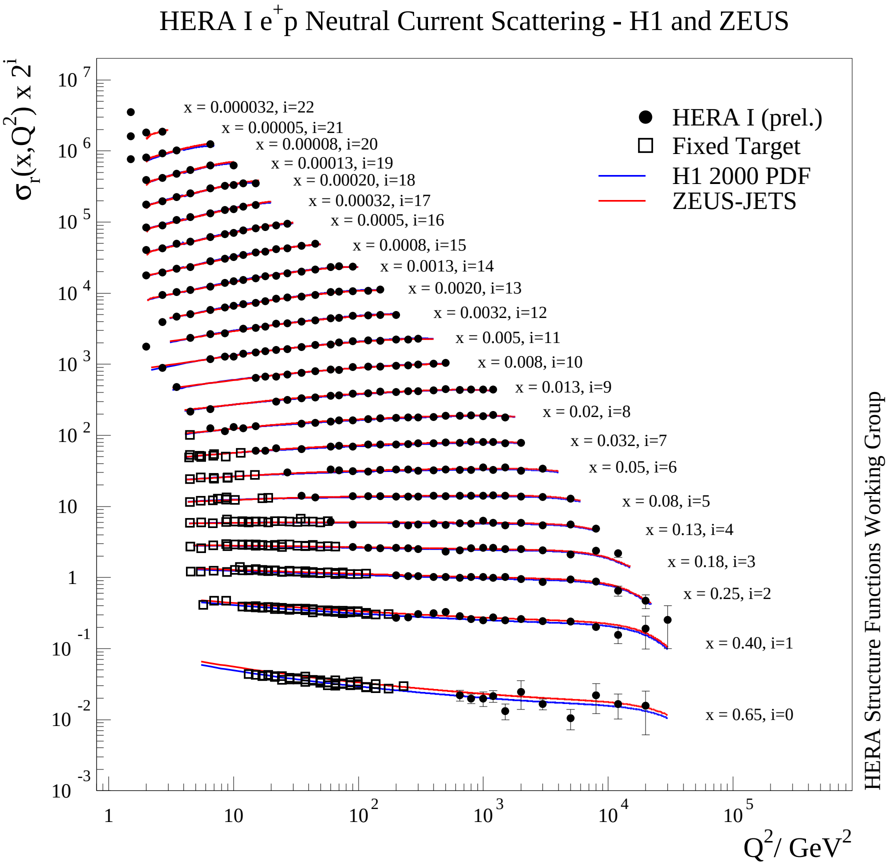

Figure 2.9: Reduced NC DIS cross section of the e^+p scattering from the HERA I data taking period obtained by combining the published H1 and ZEUS measurements [28, 29].

e^+p unpolarized reduced cross sections is fully contained within $x\tilde{F}_3$ and yields:

$$x\tilde{F}_3 = \frac{Y_+}{2Y_-}(\tilde{\sigma}^{e^-p} - \tilde{\sigma}^{e^+p}), \tag{2.22}$$

so $x\tilde{F}_3$ describes the parity violating part of the cross section due to lepton charge asymmetry [61].

As it has already been mentioned, in the framework of the QPM the longitudinal structure function $\tilde{F}_L$ parameterizing the part of the ep cross section mediated by the longitudinally polarized photon vanishes. At NLO QCD however, it can be shown that $\tilde{F}_L$ is directly related to the gluon density in the proton [63]:

$$xg(x) = \frac{2.7\pi}{\alpha_s}(\tilde{F}_L(0.4x) - \tilde{F}_2(0.8x) \simeq \frac{8.3}{\alpha_s})\tilde{F}_L. \tag{2.23}$$

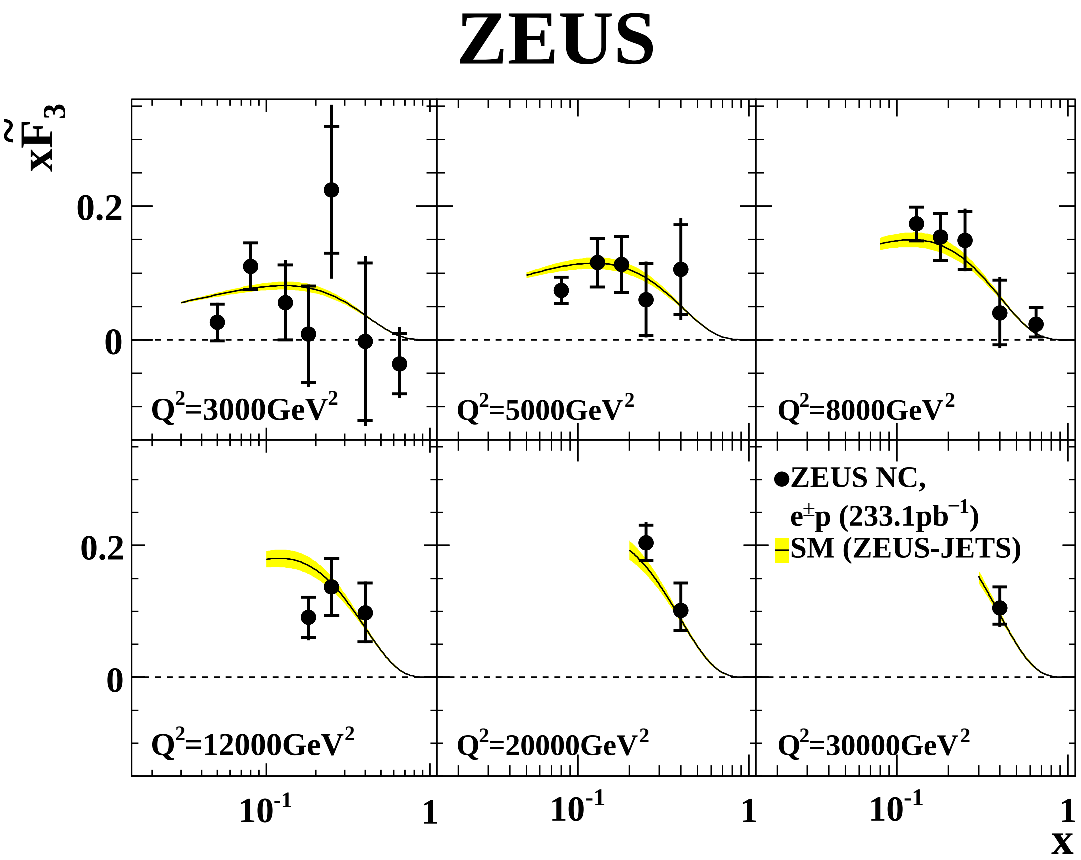

Figure 2.10: The structure function $x\tilde{F}_3$ plotted as a function of x at fixed Q^2 measured using HERA I e^+p and HERA II e^-p data [59].

Through NLO QCD calculations it has been shown [59] that the contribution of $\tilde{F}_L$ to $d^2\sigma/dxdQ^2$ is approximately 1.5%, averaged over the kinematic range considered in this thesis. The first direct measurements of $\tilde{F}_L$ were published in 2008 (see Fig. 2.11) [62, 64].

2.4 Global and HERA parton analyses

The PDFs introduced in Sec. 2.1 cannot yet be derived from theory, and therefore must be obtained through experiment. The method of extracting a complete set of quark $q(x, Q^2)$ and gluon $xg(x, Q^2)$ density functions requires a parameterization of their dependence on x at some initial low (but still "perturbative") value of $Q^2 = Q_0^2$, of a few GeV^2. Typically, the parameterization is of the form [4]:

$$xf(x, Q_0^2) = A(1-x)^{\beta}x^{\alpha}(1 + \epsilon\sqrt{x} + \gamma x), \tag{2.24}$$

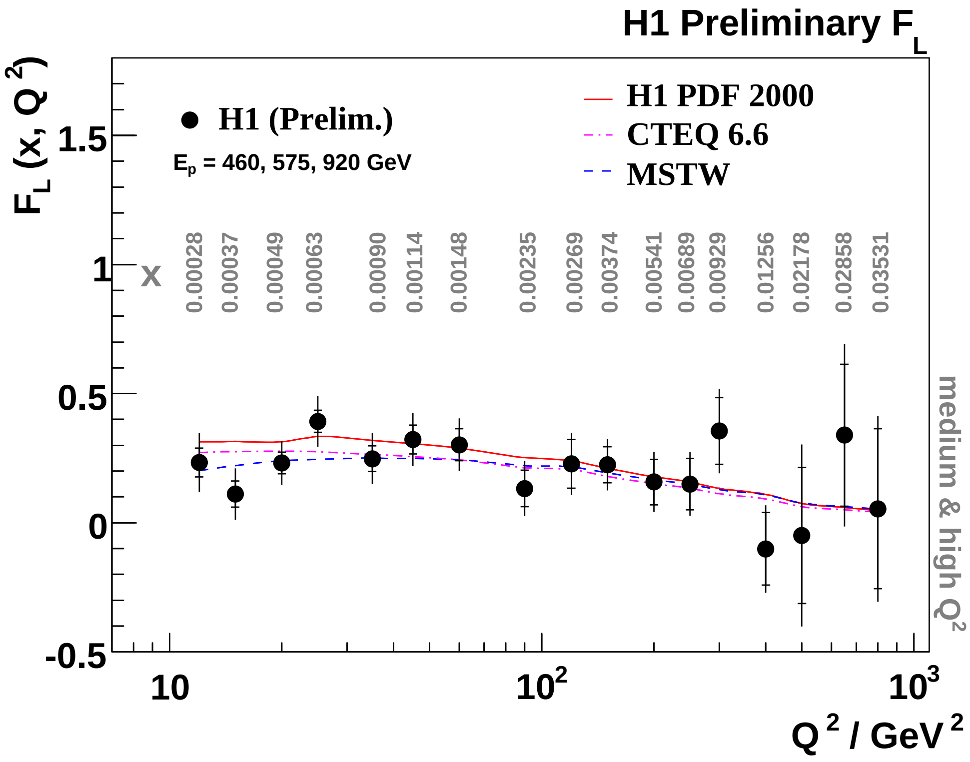

Figure 2.11: First direct measurement of the $\tilde{F}_L$ structure function, averaged in x at given value of Q^2 [62].

with up to five parameters for each parton. Additionally, the two valence quark sum rules must be satisfied:

$$\int_0^1 dx(u-\bar{u}) = 2, \qquad \int_0^1 dx(d-\bar{d}) = 1, \tag{2.25}$$

as well as the momentum sum rule (for all Q^2):

$$\int_0^1 dzz\big(\sum_q (q(z,Q^2)+\bar{q}(z,Q^2))+g(z,Q^2)\big) = 1. \tag{2.26}$$

The cross sections are then fitted, using a χ^2 minimization procedure to the data under study at Q_0^2, and the DGLAP evolution equations are used to evolve these functions in Q^2, and to fit all available cross section points. By increasing the number of free parameters in the fit, it is also possible to measure additional quantities, e.g. the strong coupling constant α_s or couplings of quarks to the Z boson: v_q, a_q (see Fig. 2.13).

Usually the fits have been obtained in the global analyses by such groups as CTEQ [65] or MRST/MSTW [66], employing data from several sources (e.g. DIS reduced cross sections, Drell-Yan production, Tevatron jet and W production). Both HERA collider collaborations have also performed these analyses using their high statistics sets of DIS and photoproduction[5] data [67, 68]. As the uncertainties of these separately obtained PDFs, based on the HERA I running phase, were limited by systematic effects, both collaborations decided to merge their sets of measured cross sections using a procedure with which the experimental uncertainties of both measurements were cross-calibrated [28, 29]. Example results of this procedure, also compared to the CTEQ PDFs, are shown in Fig. 2.12.

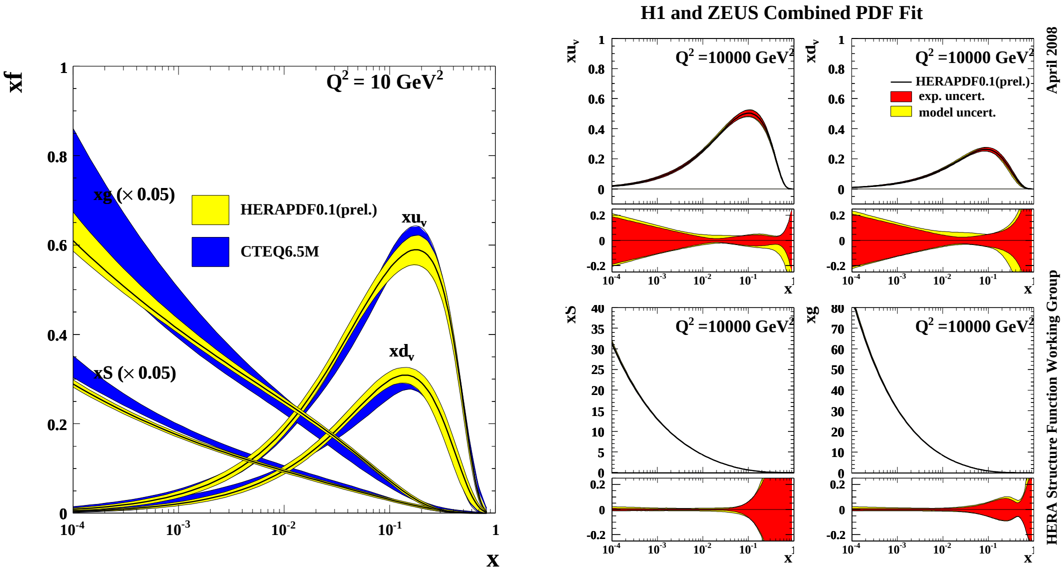

Figure 2.12: Quark and gluon distributions determined by the NLO QCD fit to the combined ZEUS and H1 data from the HERA I running phase at $Q^2 = 10\,\mathrm{GeV}^2$ (left) and $Q^2 = 10\,000\,\mathrm{GeV}^2$ (right) [28, 29].

2.5 Parity violation and polarization asymmetry in DIS

As we have already seen $x\tilde{F}_3$ describes the parity violating part of the cross section due to lepton charge asymmetry. Parity violation in NC can be also studied directly by employing longitudinally polarized lepton beams in ep collisions. The charge

---

[5] See e.g. Section 5.2.3.

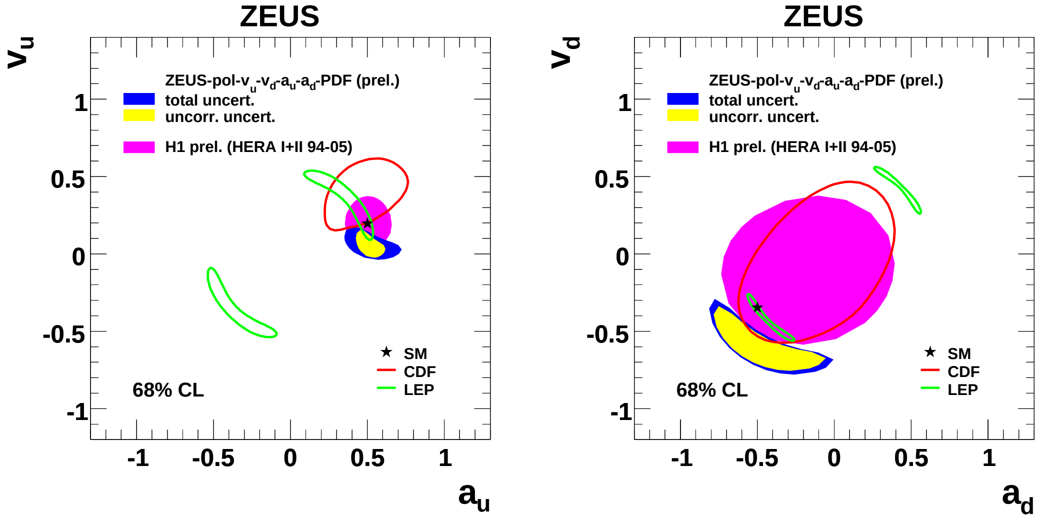

Figure 2.13: The values of the axial-vector and vector couplings of the Z^0 boson to the u (left) and the d (right) quarks, extracted in the common QCD and electroweak fit [69]. The contours represent 68% confidence limits.

dependent polarization asymmetry is defined as [5]:

$$A^{\pm} = \frac{2}{P_+ - P_-} \frac{\sigma^{\pm}(P_+) - \sigma^{\pm}(P_-)}{\sigma^{\pm}(P_+) + \sigma^{\pm}(P_-)}, \tag{2.27}$$

where P_+ and P_- give the positive and negative lepton beam polarizations, and $\sigma^{\pm}(P)$ are the cross section, measured at a particular polarization. Such polarization asymmetry can give direct evidence of parity violation (with minimal sensitivity to the proton PDFs [59]), as to a good approximation it is equal to the ratio of the $F_2^{\gamma Z}$ and F_2^{γ} structure functions, and is proportional to the product $a_e v_q$:

$$A^{\pm} \simeq \chi_Z a_e \frac{F_2^{\gamma Z}}{F_2^{\gamma}} \propto a_e v_q. \tag{2.28}$$

As the asymmetry scales with χ_Z, it is expected to grow with rising Q^2, and therefore parity violation can be tested at HERA down to distances of about 10^{-18}m.

The first results on $A^{\pm}$ asymmetry, obtained by combining measurements of H1 and ZEUS collaborations (performed with $e^{\pm}p$ data recorded in years 2003 - 2005) are shown in Fig. 2.14. The work presented here will allow to further increase the precision of A^+, as well as of the PDFs at high momentum transfers, fitted either to HERA data alone, or within the global analyses. Finally, it also presents

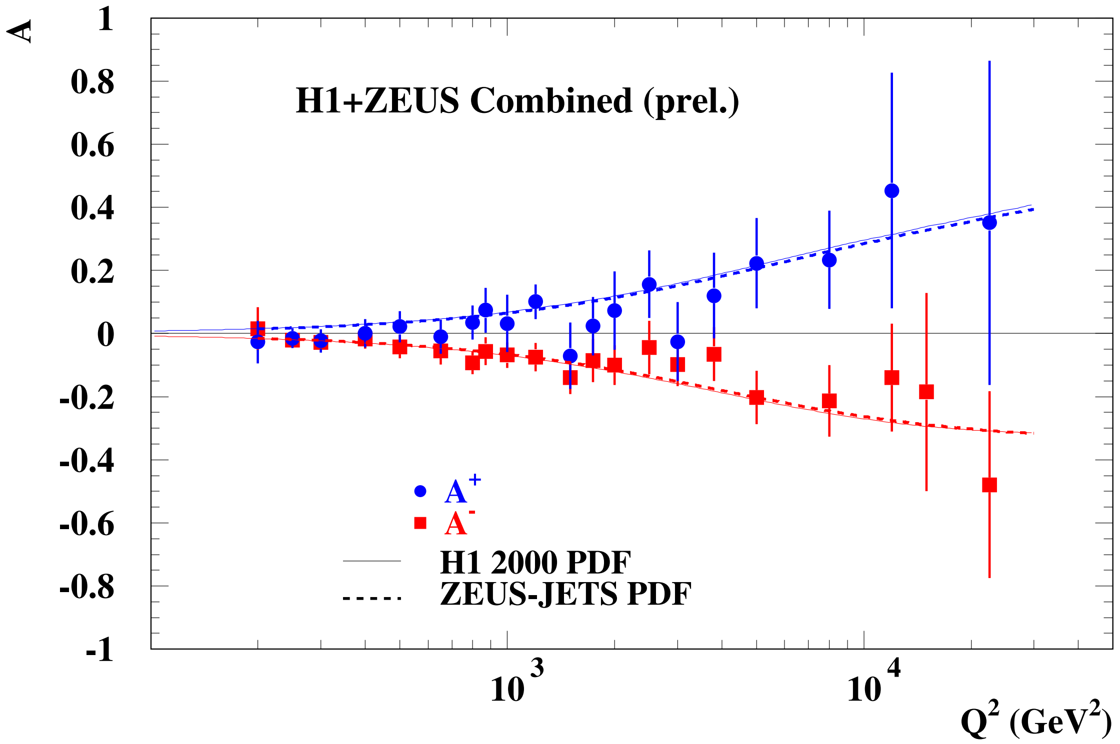

Figure 2.14: First measurement of the polarization asymmetries $A^{\pm}$ obtained by combining results from H1 and ZEUS collaborations [70]. Data collected corresponds to the integrated luminosity of $\sim 219.7\,\mathrm{pb}^{-1}$ $(P_+ \sim 0.35, P_- \sim -0.27)$ for A^- and to of $\sim 71.4\,\mathrm{pb}^{-1}$ $(P_+ \sim 0.33, P_- \sim -0.40)$ for A^+.

the first measurement of the double-differential reduced e^+p cross sections $\tilde{\sigma}$, with longitudinally polarized positron beams.

Chapter 3

Experimental setup

3.1 HERA collider

HERA (Hadron Elektron Ring Anlage) [71], which ran from 1992 until 2007 at the DESY (Deutsches Elektronen Synchrotron) laboratory in Hamburg, Germany, was the only electron-proton collider in the world (Fig. 3.1). Situated $10 - 25$ meters underground, with a circumference of 6.3 km, it accelerated beams of protons and electrons (or positrons)[1]. The beams were pre-accelerated in a system of 6 smaller machines to the energies of 40 GeV (protons) and 14 GeV (electrons) and then injected into HERA, where final energies of 920 GeV and 27.5 GeV (limited by the available magnet and RF power, and costs) were reached[2], respectively. The center-of-mass energy of the *ep* collisions was $\sqrt{s} = 319\,\text{GeV}$ (equivalent [71] to scattering of 51 TeV electrons off a stationary proton target[3]).

The HERA tunnel contained two independent accelerating rings, installed one above the other. The electron ring, constructed using the warm technology (operating in ambient temperature), consisted of 416 magnets, bending and collimating the beam, as well as 82 accelerating cavities. The superconducting proton ring, operating at the liquid helium temperature of 4.2 K, consisted of 104 magnets with 2 radio frequency accelerating cavities. Such very different accelerator designs were necessary, because of the large mass difference between electrons and protons [4]. At two opposite points on the circumference, where the detectors ZEUS and H1

---

[1] From now on, unless it is stressed otherwise, words *electron* and *positron* are used interchangeably.

[2] Until 1997 the proton beam energy was 820 GeV. In the final 3 months of the HERA running, the proton beam energy was lowered to 460 GeV and 575 GeV, to measure the longitudinal proton structure function F_L [64].

[3] In the collider, the squared center-of-mass energy $s = 4E_pE_e$, is approximately $2E_p$ times greater than the fixed target energy, for a given lepton beam energy.

[4] The synchrotron radiation energy loss ΔE of a particle of mass m_0 and energy E during one circulation around a ring with radius R can be expressed as: $\Delta E \propto \frac{1}{m_0^4}\frac{E^4}{R}$ [72, 73].

were located, the pipes of the two beams merged into one and beams were brought to head-on collisions (at 180° angle).

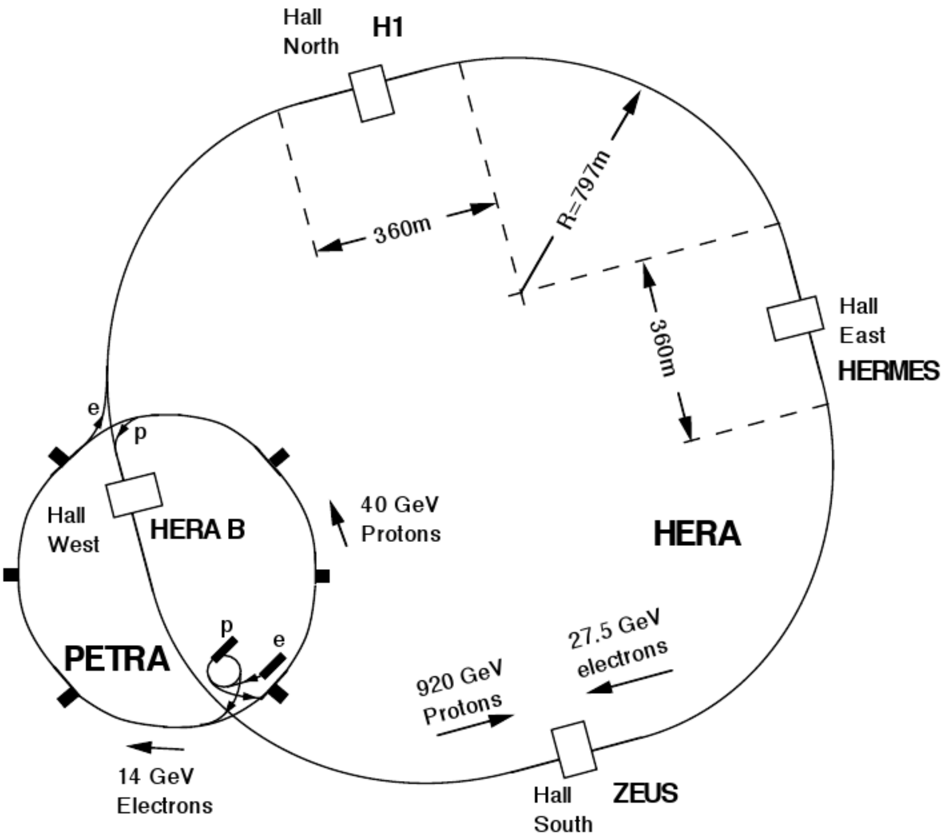

Figure 3.1: Scheme of the HERA collider ring.

A key parameter of colliding beams is the collision rate in the interaction region. The rate of reaction is given by:

$$R = \sigma L, \tag{3.1}$$

where σ is the interaction cross section and L is the instantaneous luminosity, defined as:

$$L = fn\frac{N_1 N_2}{A}, \tag{3.2}$$

where n is the number of bunches in either beam around the ring, f is the revolutionary frequency, N_1 and N_2 are the numbers of particles in each bunch, and A is the effective cross-sectional area of the beam overlap. Figure 3.3 shows an example of instantaneous luminosity fall vs. time during a HERA fill. Years 1992 until 2000 are known as the HERA I period, while 2003 until 2007 as HERA II.

Both periods were separated by upgrades of the collider and the detectors on the ring, which resulted in higher delivered instantaneous luminosities and improved performance of the data taking (e.g. the instantaneous luminosity rose by a factor of 4) [74, 75]. The growth with time of the integrated luminosity, $\mathcal{L} = \int L dt$, delivered by the collider in both periods is summarized in Fig. 3.2 [76].

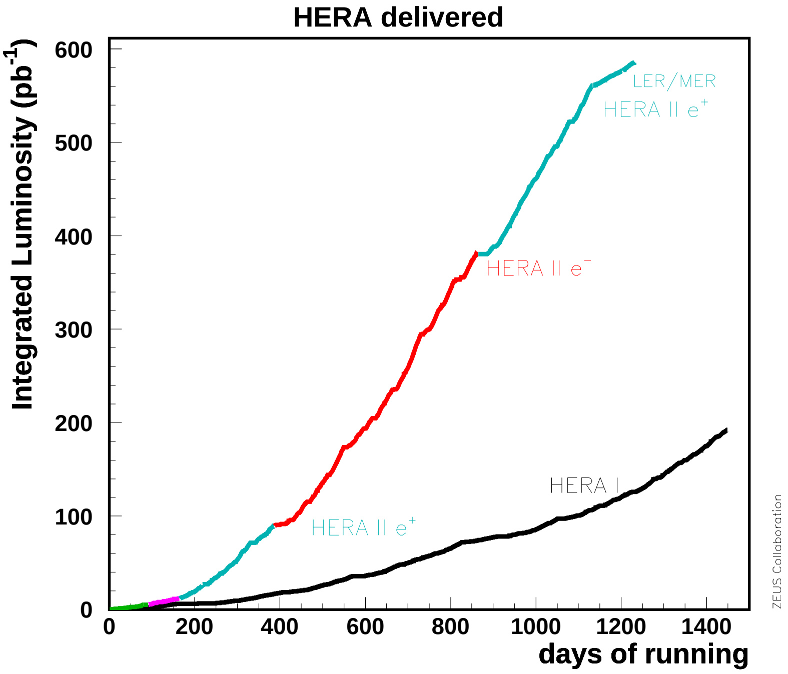

Figure 3.2: Integrated luminosity delivered by HERA as a function of the number of days of operation. Various running periods are indicated using different colors.

At HERA, some physics processes are sensitive to the polarization of the lepton beam [77]. A mechanism known as the Sokolov-Ternov effect [78, 79] is responsible for lepton beams in storage rings becoming transversely polarized. After being injected into the ring, with their spins randomly oriented, the electrons are being accelerated and emit photons of synchrotron radiation. This causes the projection of the spin onto the vertical axis to change direction, so that the natural transverse polarization:

$$P_T = \frac{N_{up} - N_{down}}{N_{up} + N_{down}}, \tag{3.3}$$

builds up over time, through the relation:

$$P_T(t) = P_{ST}(1 - e^{-t/\tau_{ST}}), \tag{3.4}$$

where N_{up} and N_{down} are the numbers of particles with their spins pointing upwards

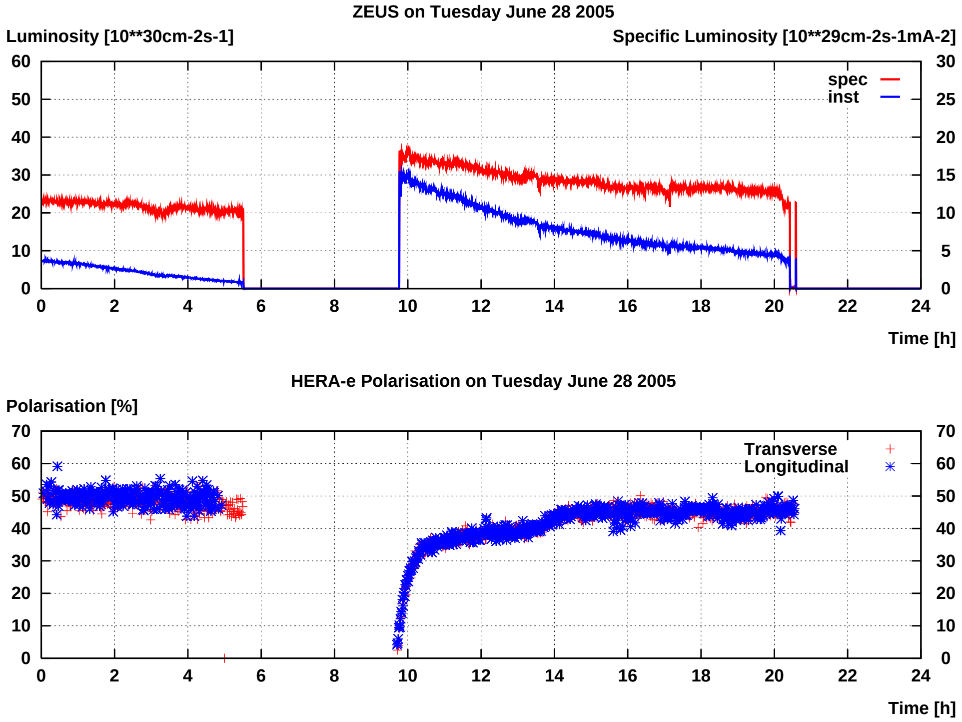

Figure 3.3: The instantaneous and specific luminosity (top) and polarization (bottom) at ZEUS vs. time, during a 24h period.

or downwards, t is time, P_{ST} is the asymptotic polarization[5] (0.924) and τ_{ST} is the polarization rise time constant (37 minutes at HERA) [80].

In order to provide longitudinally polarized leptons, systems of interleaved horizontal and vertical bending magnets, called spin rotators [71, 80] were mounted around the ring (Fig. 3.4). The longitudinal lepton beam polarization achieved by HERA was typically about ±30%, with maximum values of up to $\pm(40 - 50)\%$. Figure 3.3 shows an example of the longitudinal polarization rise vs. time during a HERA fill.

The polarization of the lepton beam was measured by two independent instruments, the *transverse polarimeter* (TPOL) [80] and the *longitudinal polarimeter* (LPOL) [81, 82]. Figure 3.4 shows their positions on the HERA ring. Both polarimeters used Compton scattering of circularly polarized laser beams off the lepton beam to measure polarization of the latter. In the TPOL system, the Compton photons were converted into e^+e^- pairs, after which a small sampling calorimeter measured energy asymmetries of the converted pairs. Hence, asymmetries of the energies and positions of the scattered photons were known, which allowed for the

---

[5] The maximum asymptotic polarization was never achieved at HERA due to de-focusing beam effects. The achieved maximum values were about 70%.

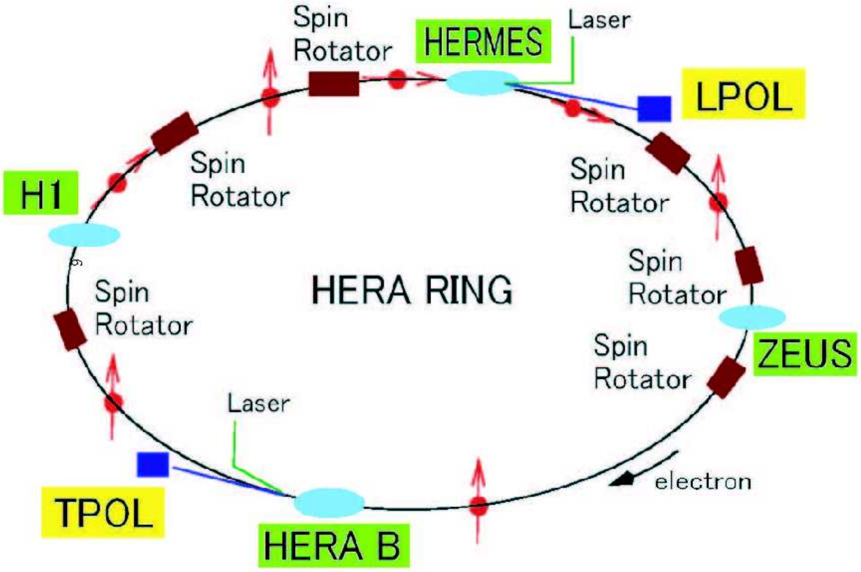

Figure 3.4: The locations of spin rotators and polarimeters around the HERA ring. The arrows represent the directions of leptons' spins at different points around the ring.

calculation of the lepton beam polarization. In the LPOL case, the Compton photons were measured directly by a crystal calorimeter. The individual systematic uncertainties of both TPOL and LPOL were estimated to be 3% [83].

At HERA, due to the principle of phase stability (common to all radio frequency accelerators [84]), both beams had the structure of bunches, where a bunch consisted of approximately $2 \cdot 10^{10}$ particles. The position of the bunch in the beam orbit is called a bucket. Electron-proton interactions took place when filled electron and proton buckets met. There were 220 possible buckets in each beam, but only about 180 were filled in optimal conditions. The unpaired buckets were kept for background studies. The time interval between 2 bunch crossings was 96 ns, which defined the 10.4 MHz clock for the data acquisition (DAQ) electronics systems of the detector.

Four main collaborations were using the HERA accelerator. The ZEUS and H1 collaborations made use of the *ep* collisions. They were designed to study proton structure functions in DIS, to deepen the understanding of QCD, the photon structure as well as to search for signals of physics beyond the Standard Model. The HERMES detector made use of the transversely polarized lepton beam by colliding it with a polarized proton gas target to study the proton spin structure [85]. The HERA-B detector used wire targets inserted into the proton beam halo to study CP violation [86].

The HERA collider, which physicists were thinking of already during the 1970s [87], was designed and built in the 1980s, and first collisions between electrons and protons were produced on October 19, 1991 [88]. During its existence, it delivered $0.5\,\text{fb}^{-1}$ of data to both ZEUS and H1, thanks to which the collaborations could produce a wealth of breakthrough results [89–91] on various topics. After 15 years of fruitful operation[6], the collider and the detectors were switched off on June 30, 2007. Current plans to analyze the collected and still unpublished data extend until 2012.

3.2 ZEUS detector

ZEUS [92] was a nearly 4π-hermetic, general purpose detector designed to study every possible aspect of high energy *ep* collisions, from perturbative QCD, through photoproduction, high Q^2 interactions to exotic phenomena. It was located in the southern hall of HERA, 30 m underground, centered around an interaction region, where electron and proton beams collided. It weighed 3600 tons and was roughly the size of a three storey house. The ZEUS detector started operations in 1992 and was collecting data, undergoing severe upgrades, until 2000. During the HERA shutdown, in the years 2000 - 2003, new powerful tracking devices (MVD, STT) were added [75], and the detector continued running smoothly until June 30, 2007 (end of HERA running). While this thesis is being written, in the Fall of 2008, the detector is being gradually dismantled.

The onion-like layout of ZEUS included tracking detectors (MVD, CTD, STT) located closest to the beam-pipe. This system measured momenta and angles of charged particles originating from the interaction region (IP). A coil producing a magnetic field of 1.43 T which bent the charged particles was installed between the CTD and the uranium calorimeter (CAL), in which most of the final state particles showered and were absorbed. The outermost layer consisted of muon chambers and the backing calorimeter (BAC), also known as the instrumented iron yoke, which closed the magnetic field. Longitudinally, ZEUS was designed to cope with the asymmetry of the beam energies, which in consequence led to a boost of the center-of-mass system in the direction of the proton beam in the lab frame. The so-called forward (proton direction) region was therefore much richer in tracking layers as well as, deeper than elsewhere, CAL modules.

---

[6] A quote from the introduction to [89]: "The observations at HERA led to an enormous development in the understanding of the underlying field theory of the strong interactions, Quantum Chromodynamics (QCD). New fields of study emerged and existing fields entered a new precision phase; among these are the physics of high parton densities, the physics of high scale photoproduction and photon structure, the chromodynamic theory of heavy quark production and of hard

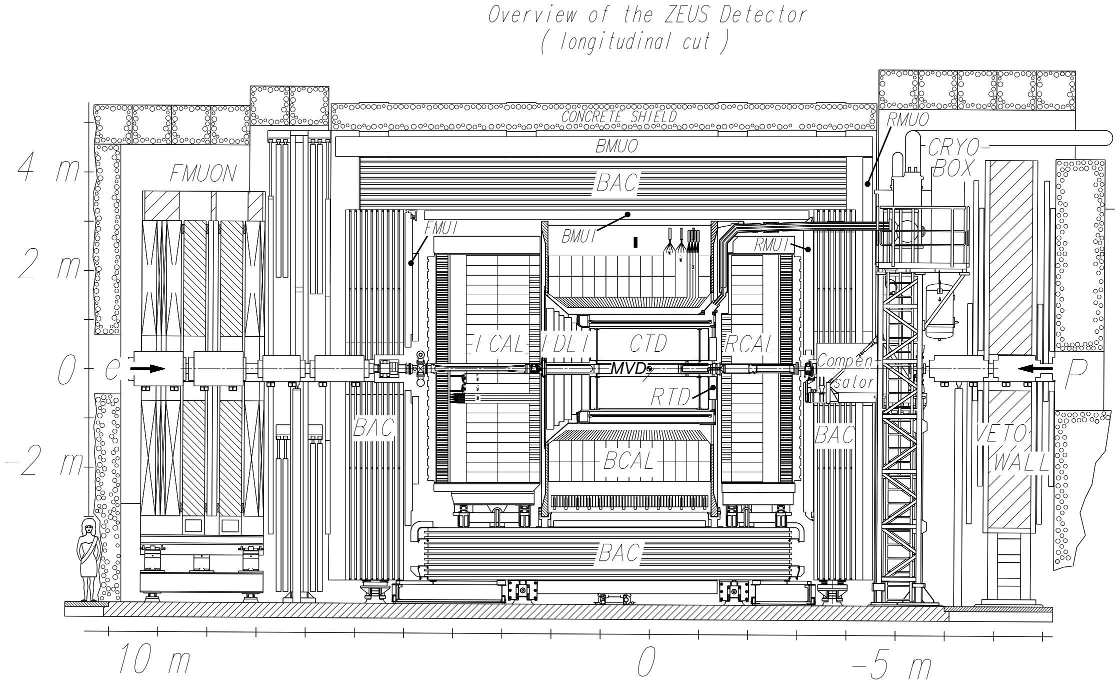

Figure 3.5: Side-view of the ZEUS detector.

The ZEUS coordinate system is a right-handed Cartesian system, with the Z axis pointing in the proton beam direction, referred to as the “forward direction”, and the X axis pointing left towards the center of HERA. The coordinate origin is at the nominal interaction point. The angles ϕ and θ represent the azimuthal and polar angles. The polar angle can be transformed into a Lorentz additive variable called the pseudo-rapidity $\eta = -\ln(\tan(\theta/2))$. The ZEUS coordinate system is shown in Figure 3.6.

The detector and its DAQ had more than 30 different components (sub-detectors and data-flow elements). Only the ones vital for the analysis under study are briefly described in the following sections. A detailed report on design and construction of the ZEUS detector is to be found in [92].

3.2.1 The high-resolution calorimeter

The ZEUS sampling calorimeter (CAL) [93–96], the main part of the ZEUS detector, was used to measure energies of particles by their total absorption and positions of the energy deposits. It was a sandwich of absorber (depleted uranium) and detector (plastic scintillator) layers (up to 185 layers in a module) of thickness 3.3 mm and 2.6 mm, respectively. The principle of operation is that particles enter

---

diffraction.”

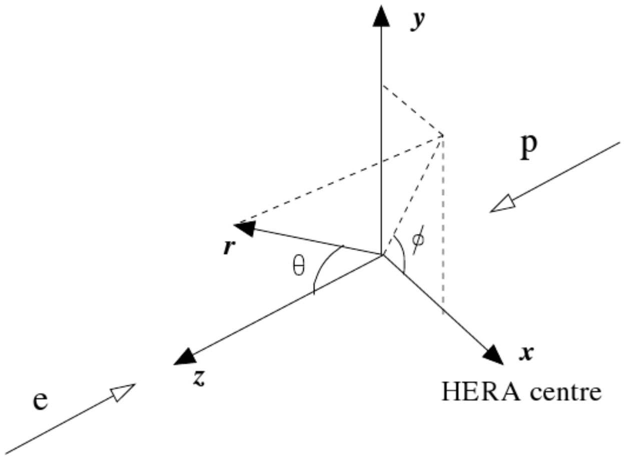

Figure 3.6: The ZEUS coordinate system.

the absorber and interact with the dense uranium layer producing secondary particles and hence generating showers. This method ensures that not only charged, but also neutral particles can be detected. The light generated in the scintillator is collected by wavelength shifters, light guides, and photomultiplier tubes (PMTs), on both sides of each tower. The position of energy deposits is then measured using the imbalance between these two signals. The typical showers of electrons, photons and decaying π^0's are shallow, while the ones of all other particles are deeper and broader. Muons as minimum ionizing particles usually do not shower in the CAL. Figure 3.7 shows examples of these three scenarios.

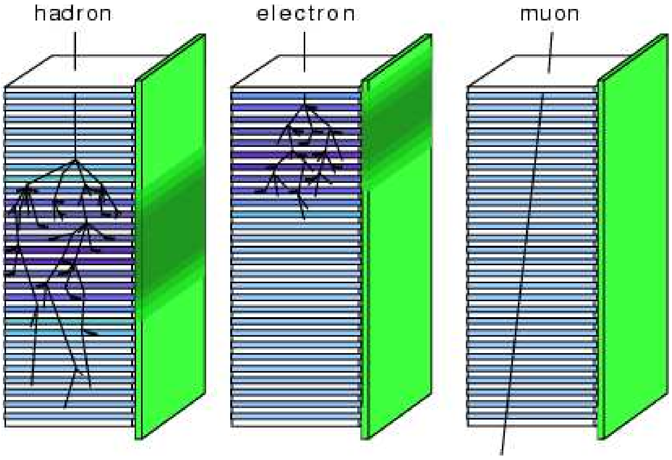

Figure 3.7: The showering of different types of particles in the CAL.

To ensure the best possible hadronic energy resolution, the CAL's responses to electromagnetic and hadronic energy deposits, E and H, respectively were balanced (i.e. $E/H \approx 1$), so the CAL was a compensating calorimeter [97]. Such a ratio was achieved by tuning the thickness of the layers of depleted uranium and plastic scintillator [96].

The CAL covered 99.7% of the solid angle around the interaction point (with holes in the FCAL and RCAL for the beam pipe). It consisted of three parts: the forward (FCAL), the barrel (BCAL) and the rear (RCAL) calorimeters (see Fig. 3.8). Each part was subdivided transversely into towers and longitudinally into one electromagnetic section (EMC) and either one (in RCAL) or two (in BCAL and FCAL) hadronic sections (HAC). The smallest subdivision of the calorimeter was called a cell. The CAL energy resolutions, as measured under test-beam conditions, were $\sigma(E)/E = 0.18/\sqrt{E}$ for electrons and $\sigma(E)/E = 0.35/\sqrt{E}$ for hadrons (E in GeV). The angular resolution (for jets) was better than 10 mrad and the time resolution, thanks to the scintillators, was 1 ns for energy deposits larger than 4.5 GeV.

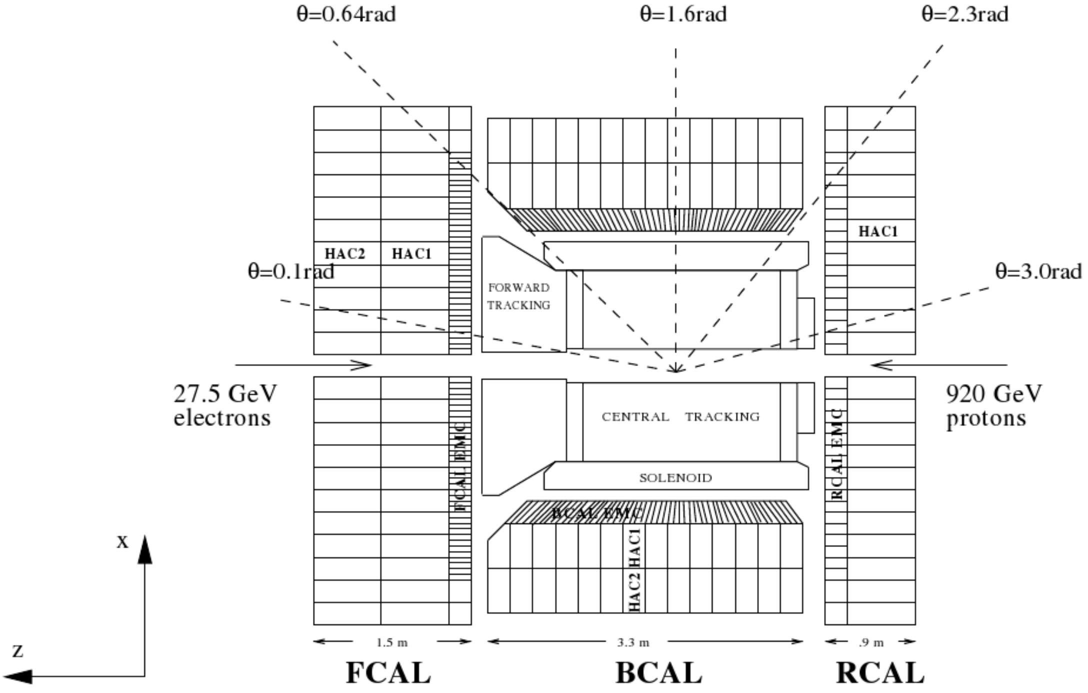

Figure 3.8: Side-view of the ZEUS calorimeter.

On their way from the interaction point, particles must traverse detector material such as detector walls, magnets or cables (known as dead material). With the use of pre-samplers [98], measuring the multiplicity of particles entering the RCAL and FCAL, it is possible to estimate the energy loss due to such interactions. The pre-samplers consisted of $20 \times 20\,\mathrm{cm}^2$ scintillator tiles read out by PMTs.

3.2.2 Tracking

During the HERA I period, the ZEUS tracking was mainly based on just one component, the CTD. During the 2000 – 2003 HERA shutdown, ZEUS gained a precise vertex reconstruction detector (MVD) and a forward region tracker (STT).

Central Tracking Detector

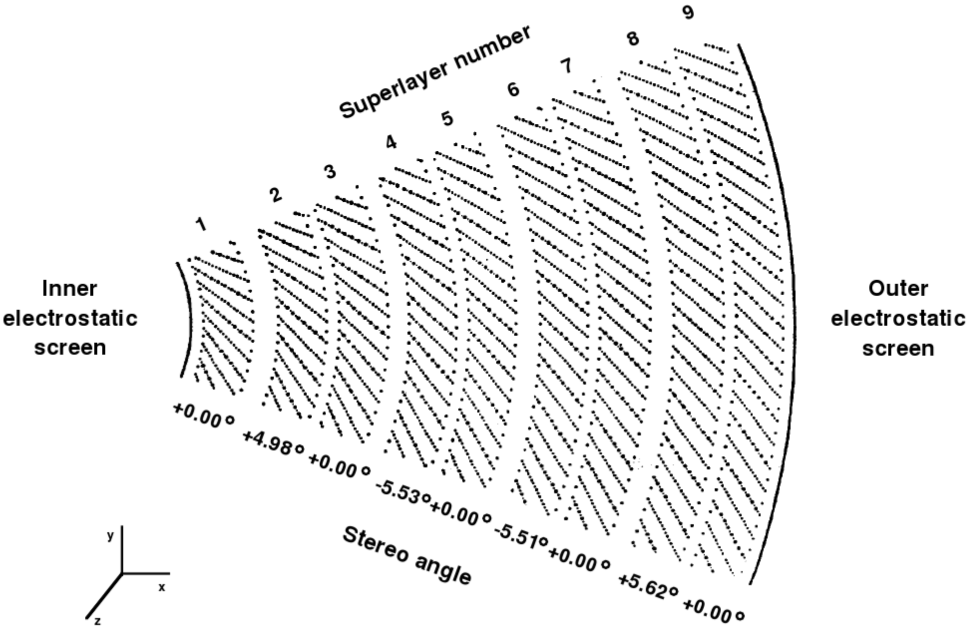

Figure 3.9: A CTD octant divided into nine superlayers. The stereo angle in each of the superlayers is indicated.

The main ZEUS tracker was the Central Tracking Detector (CTD) [99, 100] which operated in a magnetic field of 1.43 T provided by a thin superconducting coil. The CTD consisted of 72 cylindrical drift chamber layers, organized in 9 superlayers covering the polar-angle region $15^\circ < \theta < 164^\circ$. There were 4608 sense wires in total. In the 5 axial superlayers, the sense wires were strung parallel to the Z-axis, while in the 4 stereo superlayers, the wires were at a small stereo angle of $\pm 5^\circ$. The nine superlayers in one octant of the CTD are shown in Figure 3.9. The chamber's inner and outer radii were 18.2 cm and 79.4 cm, respectively, and it was 2.05 m long, with $Z_{CTD} \in (105, -100)$ cm with respect to the nominal interaction point. The filling mixture contained argon, ethane and carbon dioxide gases.

The reconstruction of tracks was performed with use of the information on hits in the $r - \phi$ plane, for which the positions of the wires were known and the drift time was measured. The $Z-$by-timing system (which measured the time difference between pulses arriving at each end of a wire) as well as information from the stereo and axial wires were used to determine the Z positions of tracks.

The hit position resolution of the chamber was 230 µm in the $r - \phi$ plane, while the transverse-momentum resolution for full-length tracks was $\sigma(p_T)/p_T = 0.0058p_T \oplus 0.0065 \oplus 0.0014/p_T$, with p_T in GeV.

Silicon Microvertex Detector

The Microvertex Detector (MVD) [101, 102], located between the beam pipe and the inner CTD radius, was a semiconductor silicon tracking detector with polar a angle coverage from 7.6° to 160°. It consisted of two sections: the barrel, in which 600 silicon sensors were organized into 30 ladders (see Fig. 3.10) and the forward section, made of four wheels containing 14 strip sensors each. The MVD offered an intrinsic hit resolution of 20 µm for normal incident tracks and the two-track separation better than 200 µm [103].

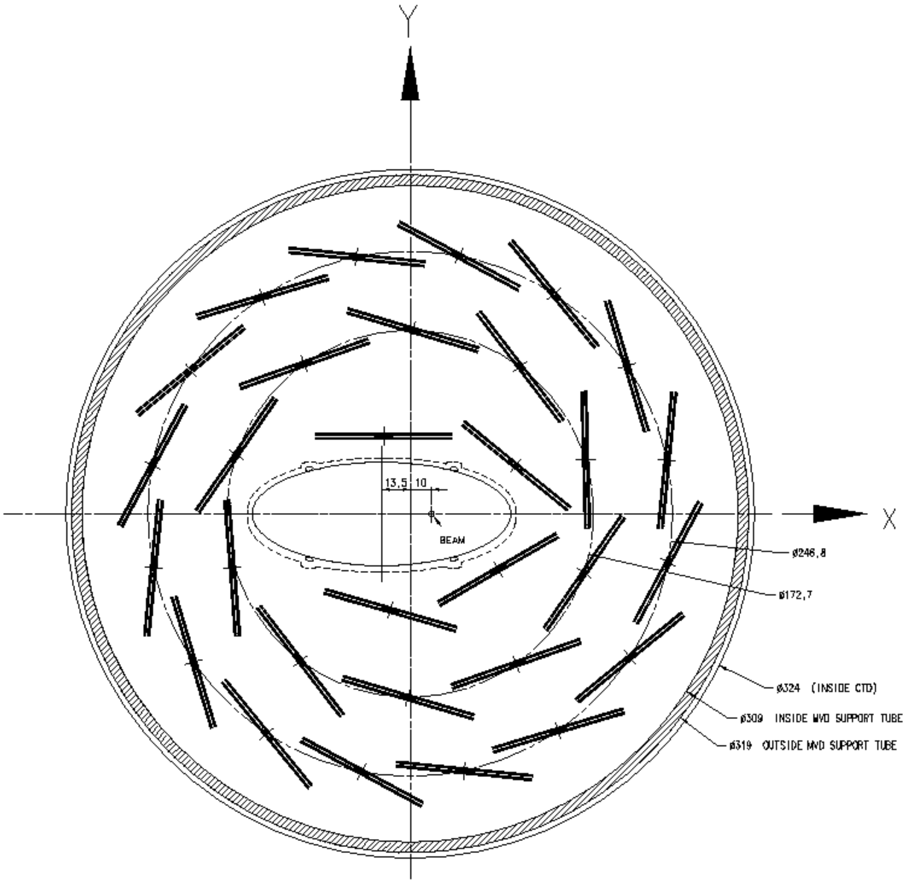

Figure 3.10: Cross section of the layout of the silicon sensors in the barrel MVD.

Other trackers

The Forward Tracking Detector (FTD) [104], Rear Tracking Detector (RTD) and Straw Tube Tracker (STT) [105, 106] were designed to supplement track measurement in directions almost parallel to the beam. The FTD and RTD drift chambers covered polar angels in the ranges of $7.5^\circ - 28^\circ$ and $159^\circ - 170^\circ$, respectively. The STT, which was based on the more modern technology of drift tubes, covered polar angels between 5° and 25°. Together with the CTD and MVD it offered a more powerful Z vertex reconstruction and improved tracking resolution in the much occupied forward region [107].

3.2.3 Luminosity detectors

Two independent monitors were used to measure the luminosity at the ZEUS detector, the *photon calorimeter* (PCAL) [108] and the *spectrometer* (SPEC) [109]. Both systems made use of the $ep \to e'p\gamma$ bremsstrahlung process, the cross section of which is known with the precision of 0.5%. In this process the incoming electron radiates a high energy photon in the electromagnetic field of the proton charge, under a very small angle with respect to the collision axis ($\leq 1\,\mathrm{mrad}$). The photon and electron spectra are well described by the Bethe-Heitler formula [110] derived in the Born approximation. The instantaneous luminosity was calculated from the measured rate, R, of these photons via a formula:

$$L = R/\sigma^{obs}_{B-H}, \tag{3.5}$$

where σ^{obs}_{B-H} is the theoretical cross section corrected for detector acceptance (and for the fraction of the bremsstrahlung photons which converted into electron pairs). The schematic layout of both PCAL and SPEC systems is shown in Fig. 3.11 [111].

The bremsstrahlung photons first travelled inside the beam pipes, and could only be separated from the HERA beams after they passed the bend of the proton beam located at about 80 m from the IP. The heart of the PCAL system consisted of a lead-scintillator sampling calorimeter with a detector measuring shower position. The detector measured efficiently photons with energies larger than a fraction of a GeV emerging from the IP at small angles with respect to the Z axis. The bremsstrahlung electrons were also detected by scintillator sampling calorimeters at $Z = -8\,\mathrm{m}$, $Z = -35\,\mathrm{m}$ and $Z = -44\,\mathrm{m}$, which was helpful in view of studies on the systematic effects in the system. The fractional uncertainty on the integrated luminosity measurement was 2.6% [112]. The PCAL system was also used to detect photons radiated by an electron prior to (initial state radiation) or after (final state radiation) the interaction with a proton.

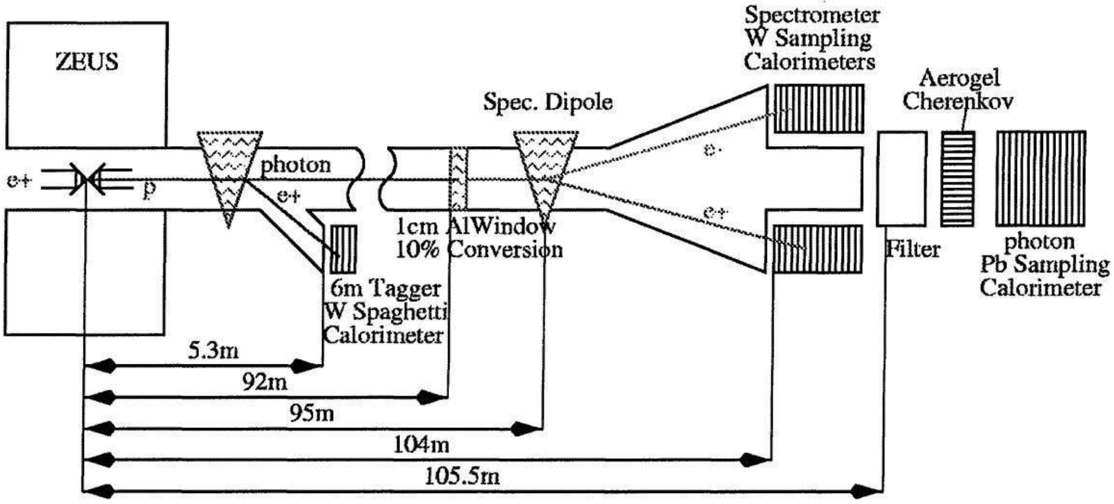

Figure 3.11: General layout of the ZEUS luminosity system.

In case of the SPEC system, about 10% of the bremsstrahlung photons converted into electron pairs in material of the exit window of the long vacuum pipe, 95 m downstream of the interaction region. Electron pairs were separated from the circulating beams, and then spatially split by the magnetic field of a dipole magnet. Two small electromagnetic sampling calorimeters, placed at transverse distances from the direct synchrotron radiation and un-converted bremsstrahlung beams, were used to detect the converted electrons. Finally, the observed rate of converted photons was proportional to the luminosity. Additionally, via the measurement of the converted electron energies and positions, the photon energy was calculated. The systematic uncertainty on the SPEC luminosity measurement was estimated to be 3.5%.

During the time period of interest to the analysis described here, the SPEC system was running in a less stable manner than the PCAL, so the latter was used for the run-by-run luminosity measurement. The SPEC was still used though, for systematic checks and normalization of the measurement.

3.2.4 Trigger and data acquisition

The aim of the trigger system [113, 114] was to select interesting physics events, and to reject on-line background of unwanted events. The most interesting process measured in ZEUS - DIS at higher Q^2 - has a small cross section, while the background rates were significant. The ZEUS storage capacity could hold $\mathcal{O}(10^8)$ events per year (restriction coming from both technical and economical reasons).

Thus the task of the ZEUS trigger system was to reduce the event rate to about 10 events per second (≈ 500 kB/s). Each event had to fulfill predefined criteria of three sophisticated trigger levels, before being recorded on tape. This ambitious goal was achieved and the typical efficiency of the ZEUS DAQ was about 80%. In the following, sources of background at HERA and all levels of the trigger system are described. The schematic view of the trigger system is given in Figure 3.12.

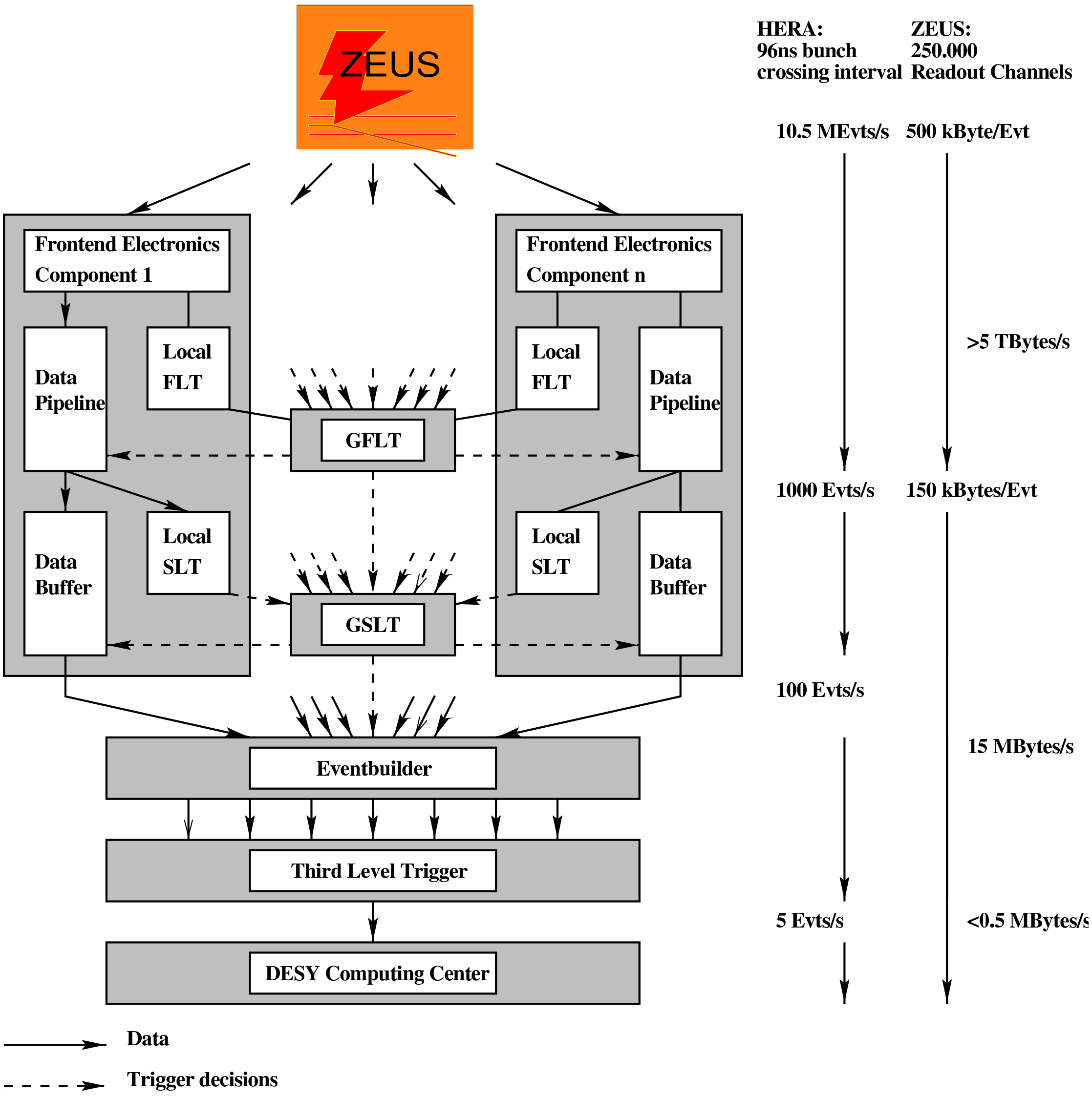

Figure 3.12: A scheme of the ZEUS trigger system [115].

Sources of backgrounds at HERA

The three most important sources of background that the trigger had to reject included [116]:

- Background associated with the proton beam. Firstly, *off-momentum protons* kept causing showers of secondary particles when hitting parts of the beam pipe close to the beam, and produced so-called *beam-halo*[7]. Secondly, particles produced by proton collisions with the *rest-gas* (H_2, O_2, N_2, CO, CO_2, etc.) in the beam pipe induced the so-called *beam-gas* events. These two classes constitute the main source of background at HERA, with a typical rate of these events, observed by the ZEUS detector, of $\mathcal{O}(50)$ kHz. The rate of electron beam-gas events was much lower.

- *Cosmic rays*, were not so troublesome. The rate of these events was of $\mathcal{O}(1)$ kHz, but they usually deposited low energies in the detector, and could be rejected by triggering with threshold requirements and additional vertex positioning.

- Finally, when selecting the DIS events, *photoproduction* (PHP) events had to be suppressed due to the high cross section for this process. Photoproduction is associated with the exchange of an almost real photon (hence low Q^2), and its topology is special, due to the escape of the scattered electron down the beam pipe. This kind of events resulted in a background of $\mathcal{O}(180)$ Hz and, due to limited data storage, could not all be written to tape. But because photoproduction events are of interest as well, some dedicated trigger channels were set to accept their fraction.

The First Level Trigger (FLT)

The data coming from about 0.5 million channels of the detector components flew through the front-end electronics of the ZEUS components with the HERA bunch-crossing frequency, 10.4 MHz. This data-flow went through analog (like in the CAL case) or digital pipelines (like in the tracking detectors) and in parallel a subset of it was used to compute the local FLT decisions. Then each component sent its decision to the Global First Level Trigger (GFLT) [117]. The GFLT computed a word containing 64 bits and if at least one of them was positive, an overall positive GFLT decision was taken. Total time for all these operations was 5 μs per event,

---

[7] A ZEUS trigger-system component dedicated to reject events induced by the proton-beam halo was a VETO Wall. It was a large iron wall (approx. 8 m high, 8 m wide and 90 cm thick), covered with scintillators on both sides, and placed in the rear area of the detector.

hence local component triggers used quite simple accept/reject algorithms. The FLT output rate was designed to be of less than 1 kHz. The First Level Trigger was implemented on the hardware level using dedicated circuits [118].

The Second Level Trigger (SLT)

After receiving the 'accept' signal from the GFLT, components computed their second level trigger local decisions and sent them to the Global Second Level Trigger (GSLT) system [116]. At this level, implemented using parallel microprocessors (IMMOS T800 transputers), as the data volume was smaller than in FLT, there was more time (10 ms) for more complex accept/reject algorithms, both on the component and the GSLT side. Typical analyzed quantities included: angular distribution of energy deposits, number of tracks, muon hit patterns or vertex position and timings. The output rate of GSLT was less than 200 Hz.

The Third Level Trigger (TLT)

After the Event Builder (EB) [119] system broadcasted the 'accept' signal from the GSLT to all components, it received full sets of data from them. Then the EB packed the event data into the ADAMO database tables (the standard ZEUS database system), and delivered it to the Third Level Trigger [120]. The TLT worked on a farm of Silicon Graphics and PC Linux machines. It used more sophisticated algorithms than the FLT and SLT, to produce a final decision whether the event should be recorded on Data Summary Tapes (DST). The TLT system employed simplified physics filters - similar to those used in data analysis, so the final rate got reduced to typically 5 Hz, which was equivalent to $0.5 - 1.0$ MB/s data transfer.

Reconstruction and Data Summary Tapes

All events accepted by the Third Level Trigger were written to the mass storage tapes. They formed the so-called 'raw data' sample, which was used for further off-line analysis. The reconstruction program ZEPHYR [121], reproduced physics observables out of raw data, using algorithms specific for each readout component to compute global quantities and wrote the files onto Mini Data Storage Tapes (MDST), using the Adamo [122] database system. The user has access to both: raw and reconstructed data (available via the dCache system).

Chapter 4

Event reconstruction

This chapter serves as an overview of the main elements of the reconstruction algorithms for neutral current physics events. As the development of these tools has not been the main scope of the analysis presented here, the descriptions are brief and the reader is directed to the original and more exhaustive documents.

4.1 ZEUS analysis environment

Over more than two decades of the existence of the ZEUS collaboration, its members have developed a multi-level analysis environment, which enables to reconstruct physics events.

After the events have been processed by the trigger system, reconstructed by the ZEPHYR program, and written to tape (see Section 3.2.4), users are in a position to run their own (standardized or not) off-line analysis jobs on data (and Monte Carlo) sub-samples. The standard tool designed to handle this task is the orange/phantom library [121, 123] (implemented in FORTRAN language) which is a collection of mid-level reconstruction functions for data analysis. This library is a platform for ZEUS physicists to share code with each other and avoid unnecessary duplication, offering a core of the code for all ZEUS analyses. Analysis batch jobs are executed on a PC cluster [124, 125] based on the Linux operating system, producing ntuples [126] or ROOT files [127], containing the final data requested by the user.

Procedures described in this chapter are elements of either ZEPHYR or orange/phantom libraries. The final procedures applied in this analysis, implemented in the form of a ROOT/C++ program, are described in Chapter 5.

4.2 Calorimeter pre-corrections

The common technique for studying physics at ZEUS is based on comparison of data events to those simulated with the FUNNEL [128] Monte Carlo (MC) program, that is based on several event generators and the GEANT package [129]. Since November 2004, the ZEUS MC production was produced primarily on the Grid [130]. Several steps of corrections are necessary to improve both the signal-to-background ratio of the recorded data, as well as the agreement of the simulated events with the ones in the data. Here, the orange/phantom steps vital to this analysis are briefly presented.

The calorimeter pre-corrections include [57, 131]:

- *Noise suppression.* Relying on the pure uranium noise being well described by the MC, an additional cut was applied in order to ensure a good description of the CAL cell-energies turn-on curves. Only cells with energies greater than 100 MeV (EMC) or 150 MeV (HAC) were taken into account in further procedures.

- *Dead or noisy photomultipliers.* The electronics channels of some PMTs broke occasionally, and since their physical maintenance was only possible during regular monthly shutdowns, the reconstruction software included methods to handle these problems. The dead channels were removed, in a time-wise manner, from the cell lists by the dedicated CAL DQM team. Noisy cells were identified on the basis of their fire rate compared to the average rate of other cells. In the time period of this analysis, the average number of dead cells was 30/130/90 in the R/F/BCAL, respectively [132] (while the calorimeter consists of the total number of $\sim 12\,000$ channels).

- *Energy scales of the R/B/FCAL.* Studies of the calorimeter energy scale [133–136] revealed a systematic difference between its response to data and Monte Carlo events. Such discrepancies come from local imperfections in simulation of e.g. the dead material or of response of cell gaps, as well as effects of detector aging. Due to large statistics in the RCAL, a time-dependent cell-by-cell correction could be developed for the EMC section, contrary to the RCAL HAC section, the BCAL and the FCAL, where overall correction parameters were determined for each section separately. On the orange/phantom level, the energy scale was shifted by +5% in the FEMC, −3.5% in the FHAC, +6.3% in the BEMC, +10% in the BHAC and by +2.2% in both the REMC and RHAC. Further corrections applied on top of these mentioned here were applied on the ROOT/C++ level and are discussed in Chapter 5.

4.3 Calorimeter alignment

By convention, the CTD provides a reference system for all other components of the ZEUS detector. Their precise alignment, especially of the calorimeter, with respect to the tracker is crucial, as it affects the quality of the reconstruction of the kinematic variables. Alignment constants were measured by survey while the detector was open during the shutdown, and later checked by employing standard NC events. For that purpose, the position of the electron track hitting the CAL, after being extrapolated from the CTD, was compared to the one measured by the CAL alone [57, 137, 138]. After the results of these studies had been applied, the calorimeter positions were proven to be known (for RCAL and BCAL) to a precision better than 1 mm, and 1 mrad, [1] while the FCAL was aligned with a precision of 2 mm. This exceeds the overall position resolution for electrons in the CAL.

4.4 Event vertex reconstruction and tracking

Trajectories of charged particles and event vertices are reconstructed from the hits they left traversing the ZEUS tracking devices (Sec. 3.2.2). This complicated procedure [139–141] begins with a hit coordinate reconstruction. All the hits are then used to find track seeds formed from at least three hits in the outermost CTD superlayer. The pattern recognition program [142] extends seeds to tracks by extrapolating inwards in the xy plane towards the interaction point. After the combined (MVD+CTD+STT) track pattern recognition has been performed, the hits are used within the Kalman filter track fitting program, which determines the track helix parameters. This method takes into account effects like multiple scattering and ionization energy loss [143, 144].

After the tracks have been found, the primary event vertex is determined, using the global vertex fit [139, 145]. Finally, tracks which originate from the primary vertex are refitted using the primary vertex as an additional point. The accurate vertex position description is vital for the calculation of some quantities like polar angles of the scattered positron or the hadronic final state. Therefore, the distribution of vertex Z-coordinates for the sample used for this analysis has been precisely measured, and the Monte Carlo events have been re-weighted to this distribution (see Sec. 5.5).

---

[1] Two degrees of freedom were studied in the BCAL: a shift of the BCAL along z and a rotation around the z axis. In the RCAL, three degrees of freedom were used: position in x, z, and the azimuthal angle ϕ.

4.5 Scattered $e^{\pm}$ reconstruction

Positron finding and reconstruction is a crucial step in identification of a neutral current event. The presence of the scattered e^+ distinguishes NC from other event classes like photoproduction (where the positron escapes through the beam-hole) or charged current (where the e^+ turns into an invisible neutrino). At ZEUS, several so called *electron finder* programs have been developed in order to perform this task, each tuned to a different class of events. The one used primarily in this analysis, called EM [57, 146], has been designed particularly for the middle and high Q^2 events with scattered positrons hitting the BCAL or the FCAL.

The EM algorithm, looking for a CAL energy cluster created by the scattered e^+, is based on 7 variables calculated from calorimeter and tracking information. The CAL input includes the spread of energy in the cluster and its isolation, while e.g. angles of a track assigned to a CAL cluster serve as a comparison to the ones calculated from the cluster polar angle and event vertex. For candidates which lie outside the tracking acceptance, only the calorimeter information is used.

The electron finding algorithm [146] begins by grouping calorimeter cells into clusters using either the cell islands or the cone islands approach [131, 147, 148]. At this level, the purely calorimetric variables of the candidate cluster and the calorimeter probability P_{Cal} are calculated, and first cuts examined (particularly, $P_{Cal} > 10^{-5}$). If the polar angle of the candidate cluster lies within $0.3 < \theta_e < 2.85\,\mathrm{rad}$, the matching track is sought, with i.e. transverse momentum exceeding 0.1 GeV, the distance of closest approach to the beamline less than 2 cm, $|\theta_{Trk} - \theta_{Cal}| < 45^\circ$ and $|\phi_{Trk} - \phi_{Cal}| < 45^\circ$ (θ_{Trk}, ϕ_{Trk} - polar and azimuthal angles reconstructed from a track associated to an electron candidate, θ_{Cal}, ϕ_{Cal} - angles reconstructed from a CAL cluster position). A sub-probability, parametrized by comparing the signal and background response of the detector, is assigned to each of the 7 EM variables (see Fig. 4.1[2]), and the Grand Probability is calculated as a product of the sub-probabilities (see Fig. 5.22). If a candidate passes all the requirements, it is considered an electron. Candidates are sorted by probability, with the candidate representing the scattered lepton having the highest probability on the list.

Another electron finder - SINISTRA [149], implemented as a neural network working purely on the CAL information, was used for cross checks. A dedicated comparison study [150] has proven that even though SINISTRA is very efficient in the RCAL alone, EM suits the purposes of the high Q^2 analysis better, in particular providing a more satisfactory PHP background rejection than SINISTRA.

---

[2] Throughout this thesis, whenever the vertical axis of the plot is not labelled, it contains the number of events (unless stated otherwise in the caption).

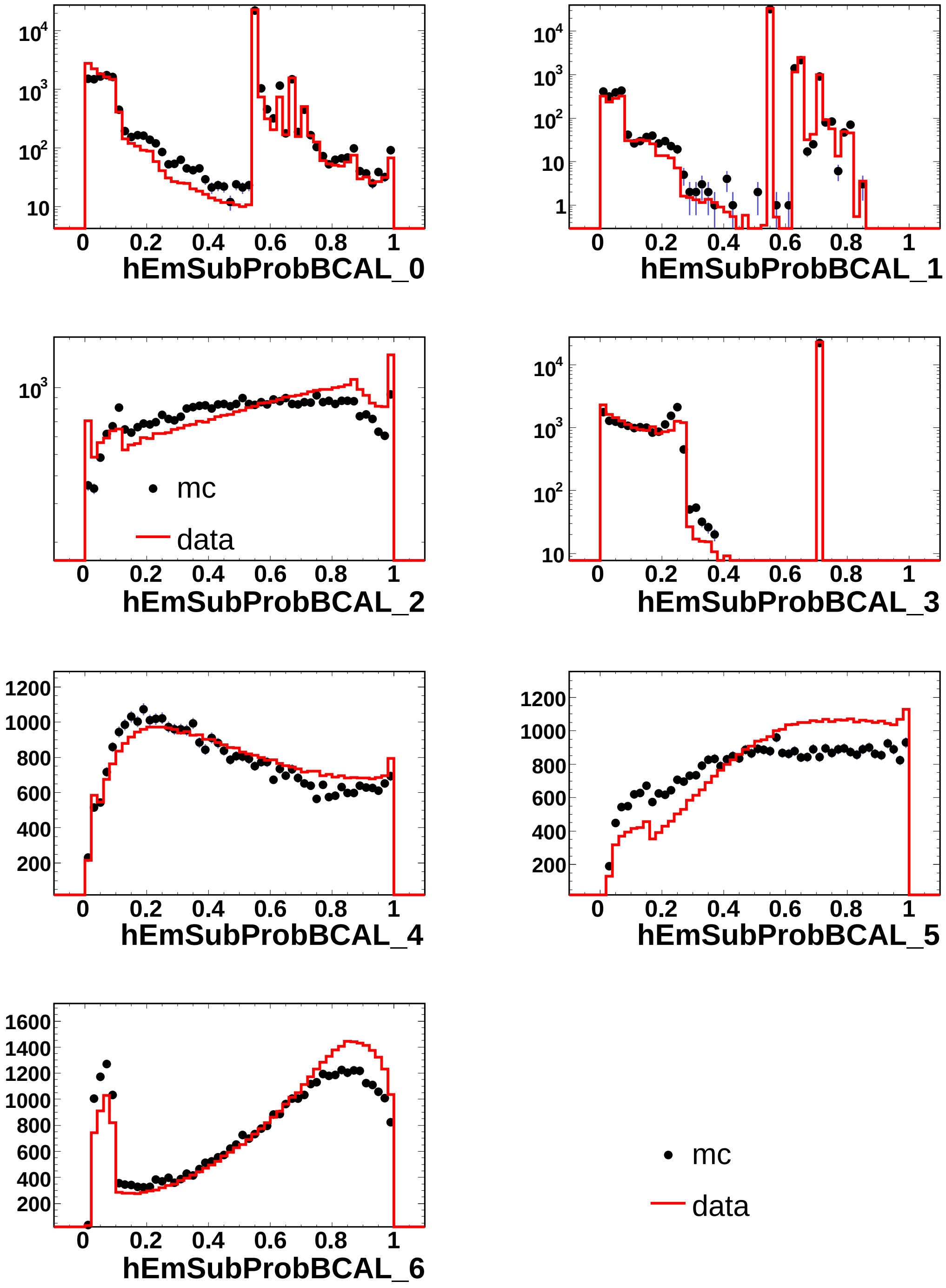

Figure 4.1: EM electron finder sub-probabilities calculated for all 7 input variables shown for the final data and MC NC e^+p samples. Sub-probabilities 0 to 3 represent energy spread of the candidate cluster, Sub-probability 4 and 5 represent $|\theta_{Trk} - \theta_{Cal}|$ and $|\phi_{Trk} - \phi_{Cal}|$, respectively and Sub-probability 6 represents $|1/E - 1/P_{Trk}|$ The vertical axis contains the number of events in a given bin.

4.6 Reconstruction of the hadronic final state

After the scattered lepton has been identified and reconstructed, it is time to reconstruct the *hadronic final state* (HFS), defined by all energy deposits and tracks except the ones assigned to the scattered lepton.

A few effects account for sources of errors on the final energy and polar angle of the HFS, which include:

- finite energy and spatial resolutions;
- energy leakage in the super-cracks (gaps between the CAL parts);
- backsplash - energy deposits scattered back from the CTD inner wall, beampipe, FCAL surface and other objects (see Fig. 5.5);
- energy loss of the HFS particles passing through the dead material.

Again, several algorithms are available in the ZEUS software for HFS reconstruction and correction, but only one of them, called *CorAndCut* [151] was mainly used for this analysis, another one called *ZUFOS* [152] reserved for cross-checks.

The CorAndCut algorithm, using exclusively the CAL and vertex information, first clusters the energy deposited in the calorimeter. The total energy of the cluster is calculated as the sum of the energies of all its cells, and the angle is the energy weighted mean of the individual cell angles. The program includes a correction for energy loss by dead material in front of the CAL, parametrized in bins of X_0 and measured energy. The low-energy deposits found far away from the center of the HFS (backsplash) are then removed, in order to prevent their long lever-arms to bias the measured hadronic angle (considerably). Finally, the hadronic energy E_{had} and the polar angle γ_{had} (Eq. 4.2) are calculated and the energy gets corrected for losses in the super-cracks.

In this work, the original parameterization of the backsplash correction has been used. Also, the hadronic energy scale has been studied [43, 138] by comparing the hadronic transverse momentum ($P_{T,had}$) to the value calculated with the double-angle method ($P_{T,DA}$) (see Sec. 4.7.3). It has been found, that overall the Monte Carlo agrees with the data on a percent level.

4.7 Measurement of Kinematic Variables

Finally, after reconstruction of the scattered lepton and the hadronic final state, the kinematic variables for a DIS event (depicted on Fig. 4.2) can be calculated. The incoming and scattered lepton have momenta k and k', respectively, while

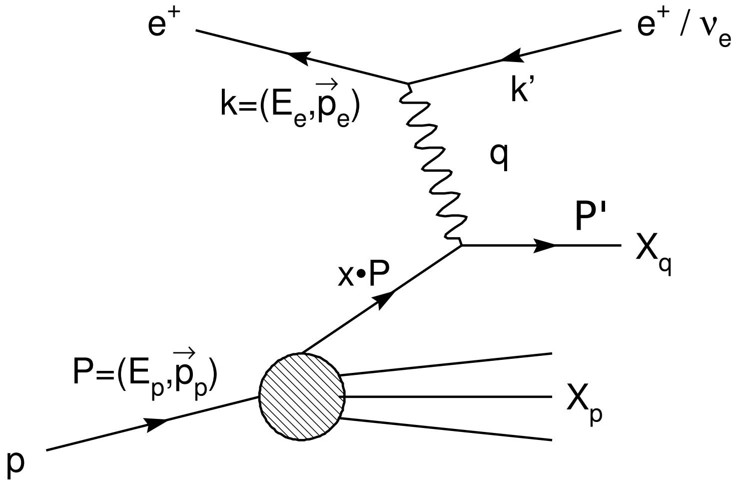

Figure 4.2: Feynman diagram of DIS at Born level. The incoming and scattered leptons have momenta k and k', respectively, the incoming proton and the struck quark have momenta P and P'. Figure modified after [153].

the incoming proton and the struck quark, have momenta P and P'. Neglecting particle masses, these four momenta can be written in the ZEUS reference frame as :

$$k = \begin{pmatrix} E_e \\ 0 \\ 0 \\ -E_e \end{pmatrix}, k' = \begin{pmatrix} E'_e \\ E'_e \sin\theta\cos\phi \\ E'_e \sin\theta\sin\phi \\ E'_e \cos\theta \end{pmatrix}, P = \begin{pmatrix} E_P \\ 0 \\ 0 \\ E_P \end{pmatrix}, P' = \begin{pmatrix} E_{had} \\ P_{x,had} \\ P_{y,had} \\ P_{z,had} \end{pmatrix}, \tag{4.1}$$

where E_e is the electron beam energy, E'_e is the energy of the scattered positron, E_P is the energy of the proton beam and θ and ϕ are polar and azimuthal angles of the scattered lepton, respectively. The initial momentum of the struck quark is xP. In the framework of the Quark-Parton Model, without the color flow between the current (X_q) and the remnant jet (X_p), the four momentum of the struck quark P' can be reconstructed as the sum of the momenta of particles of the hadronic final state. The scattering polar angle of a struck quark, necessary for the measurement of the double-angle kinematic variables (see 4.7.3), can be reconstructed from the HFS particles via the formula [56]:

$$\cos\gamma_{had} = \frac{P_{T,had}^2 - (E - P_Z)_{had}^2}{P_{T,had}^2 + (E - P_Z)_{had}^2} \quad . \tag{4.2}$$

γ_{had} allows to determine the kinematic variables regardless of the topology of the final state (e.g. number of jets or their spacing in the detector) [56]. As we shall see in Sec. 4.7.2, other particularly useful quantities characterizing the hadronic final state include:

$$P_{T,had} = \sqrt{P_{x,had}^2 + P_{y,had}^2} \quad , \tag{4.3}$$

$$\delta_{had} = (E - P_Z)_{had} \quad , \tag{4.4}$$

where $P_{T,had}$ is the hadronic transverse momentum.

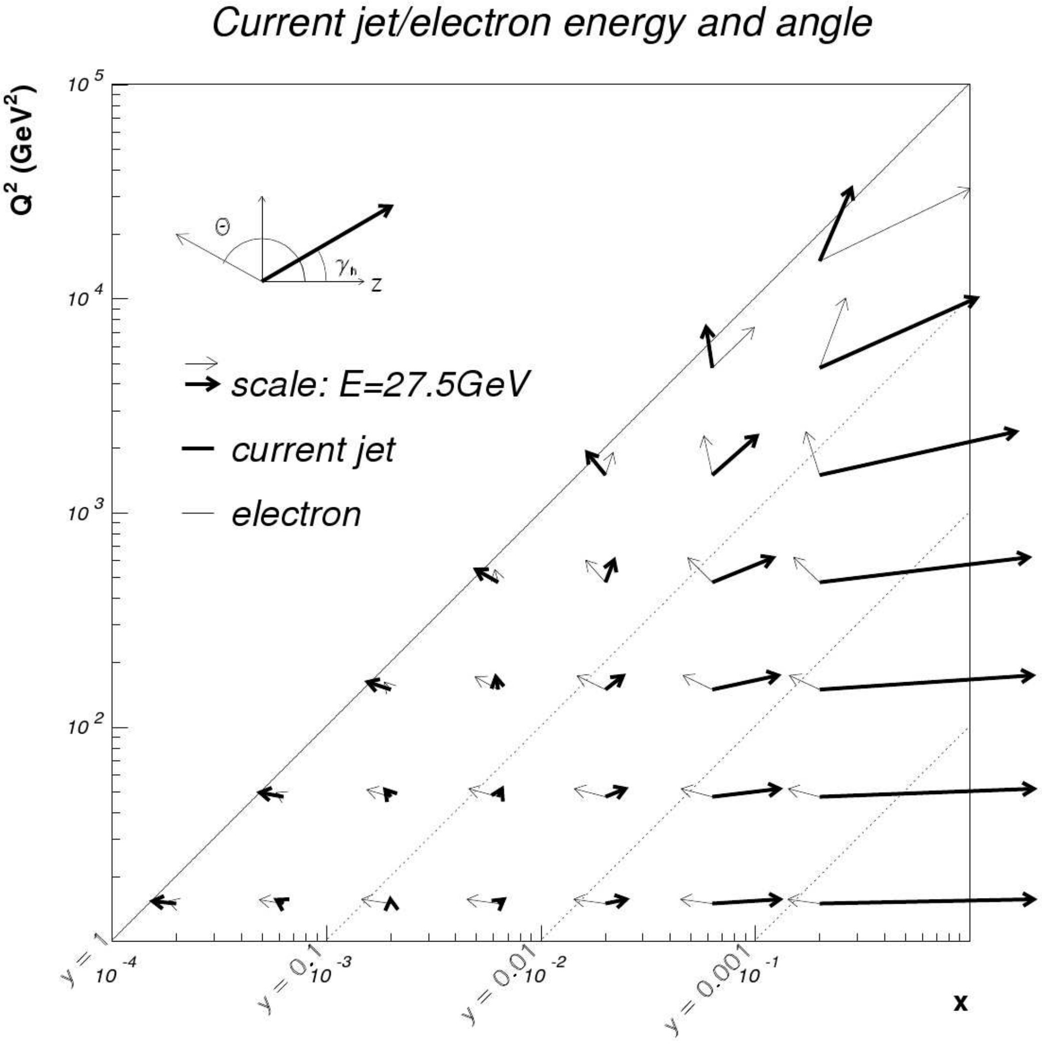

Figure 4.3: Schematic representation of the NC DIS event topology. Thick arrows represent polar angle and energy of the current jet, while thin arrows correspond to the scattered lepton [148].

Three more *global variables* will be needed, to construct an efficient set of selection cuts discussed in the following chapter, i.e.:

$$E_T = \sum_i E_i \sin\theta_i \quad , \tag{4.5}$$

$$P_T = \sqrt{(\sum_i E_i \sin\theta_i \cos\phi_i)^2 + (\sum_i E_i \sin\theta_i \sin\phi_i)^2} \quad , \tag{4.6}$$

$$\delta = (E - P_Z) = \sum_i E_i (1 - \cos\theta_i) \quad , \tag{4.7}$$

where now, the sums run over all reconstructed energy deposits in the calorimeter (both of the lepton and the hadronic final state) E_i .

The variables E'_e, θ, $P_{T,had}$ and δ_{had} can now be used to reconstruct the Q^2, x and y variables that characterize the event kinematically. At ZEUS, three different methods are in use [154], able to fulfill the needs of different physics analyses. Figure 4.3 depicts energies and polar angles of the scattered electron and the hadronic final state, on the kinematic $x - Q^2$ plane.

4.7.1 The electron reconstruction method (EL)

The electron method uses exclusively the input from the scattered lepton, i.e. its energy and polar angle:

$$Q^2_{EL} = 2E_e E'_e (1 + \cos\theta_e), \tag{4.8}$$

$$x_{EL} = \frac{E_e}{E_p} \cdot \frac{E'_e (1 + \cos\theta_e)}{2E_e - E'_e (1 - \cos\theta_e)}, \tag{4.9}$$

$$y_{EL} = 1 - \frac{E'_e}{2E_e} (1 - \cos\theta_e), \tag{4.10}$$

This method, sensitive to the positron energy scale, is used for example in the F_L measurement [155], in which the scattered positron hits only the RCAL, which allows for a better control over the energy measurement (compared to cases when the hadronic final system and the rest of the CAL is involved). It provides accurate Q^2 reconstruction, but for low values of y, the measurement of x is known to be of low precision.

4.7.2 The Jacquet-Blondel reconstruction method (JB)

The Jacquet-Blondel method relies exclusively on the variables of the hadronic final state, namely the transverse momentum $P_{T,had}$, and $(E - P_Z)_{had}$:

$$Q^2_{JB} = \frac{P^2_{T,had}}{1 - y_{JB}}, \tag{4.11}$$

$$x_{JB} = \frac{Q^2_{JB}}{s \cdot y_{JB}}, \tag{4.12}$$

$$y_{JB} = \frac{(E - P_Z)_{had}}{2E_e}. \tag{4.13}$$

This reconstruction method is used particularly in the charged current analysis, where direct information on the outgoing lepton is not available.

4.7.3 The Double-Angle reconstruction method (DA)

The Double-Angle method uses solely the polar angles of both the scattered positron (θ_e) and the hadronic final state (γ_{had}):

$$Q^2_{DA} = 4E^2_e \cdot \frac{\sin\gamma_{had}(1 + \cos\theta_e)}{\sin\gamma_{had} + \sin\theta_e - \sin(\gamma_{had} + \theta_e)}, \tag{4.14}$$

$$x_{DA} = \frac{E_e}{E_p} \cdot \frac{\sin\gamma_{had} + \sin\theta_e + \sin(\gamma_{had} + \theta_e)}{\sin\gamma_{had} + \sin\theta_e - \sin(\gamma_{had} + \theta_e)}, \tag{4.15}$$

$$y_{DA} = \frac{\sin\theta_e(1 - \cos\gamma_{had})}{\sin\gamma_{had} + \sin\theta_e - \sin(\gamma_{had} + \theta_e)}. \tag{4.16}$$

Figure 4.4 depicts lines of constant scattered electron angle (left) and the hadronic angle (right) on the $x - Q^2$ plane. This method is independent of the calorimeter energy scale and insensitive to final state radiation, but is highly sensitive to a precise determination of the angle γ_{had} of the current jet. It was found that the DA method is superior to other methods in the phase space region studied in this analysis [154].

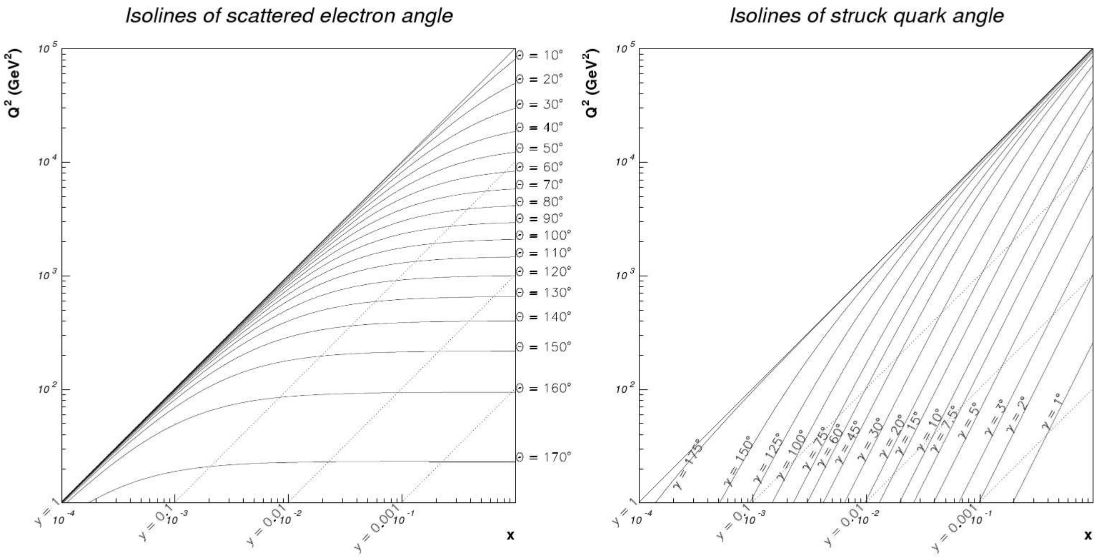

Figure 4.4: Isolines of scattered lepton polar angle θ_e, and of the hadronic angle γ_{had} [148].

Chapter 5

Data sets and event selection

This chapter characterizes the main features of NC events, and introduces classes of background events needed to be rejected from the final sample. Afterwards, all the selection cuts are explained and the data and Monte Carlo samples are presented and compared.

5.1 Characteristics of signal events

The most distinctive feature of a neutral current event, an example of which is depicted in Fig. 5.1, is the presence of a scattered lepton. Since the NC differential cross section (see Eq. 2.15) is proportional to $1/Q^4$, most of the scattered leptons emerge from the event vertex at (in the ZEUS reference frame) large polar angles and are reconstructed in the RCAL. Positrons from events of higher Q^2 ($\gtrsim 500\,\mathrm{GeV}^2$) are mostly found in the BCAL, while the FCAL contains very rare events of the highest Q^2.

Since both the scattered lepton and the hadronic final state are detected and reconstructed, the transverse momentum P_T (Eq. 4.6) of NC events should be close to zero, in contrast to the transverse energy E_T (Eq. 4.5). Particles of the spectator jet, which escapes through the forward beam-hole, carry negligible P_T, due to momentum conservation.

The total energy of the event is $E = E_P + E_e$ and the sum of the longitudinal momentum is $P_Z = E_P - E_e$, hence their difference (introduced by Eq. 4.7) yields

$$\delta = E - P_Z = 2E_e \quad , \tag{5.1}$$

twice the energy of the lepton beam. Now, in case of the undetected particles that escape through the forward beam-hole, their longitudinal momentum is equal to their energy $P_{z,i} \approxeq E_i$, which cancel in Eq. 5.1, not modifying the total $E - P_Z$.

On the contrary, for particles that escape through the rear beam-hole $P_{z,i} \approxeq -E_i$, reducing the total $E - P_Z$ by twice the particle energy. This is the case for events in which the incoming lepton emits a high-energy collinear photon before interacting with the proton (initial state radiation) and for events in which the lepton is scattered at $\theta \approxeq 180°$ (photoproduction).

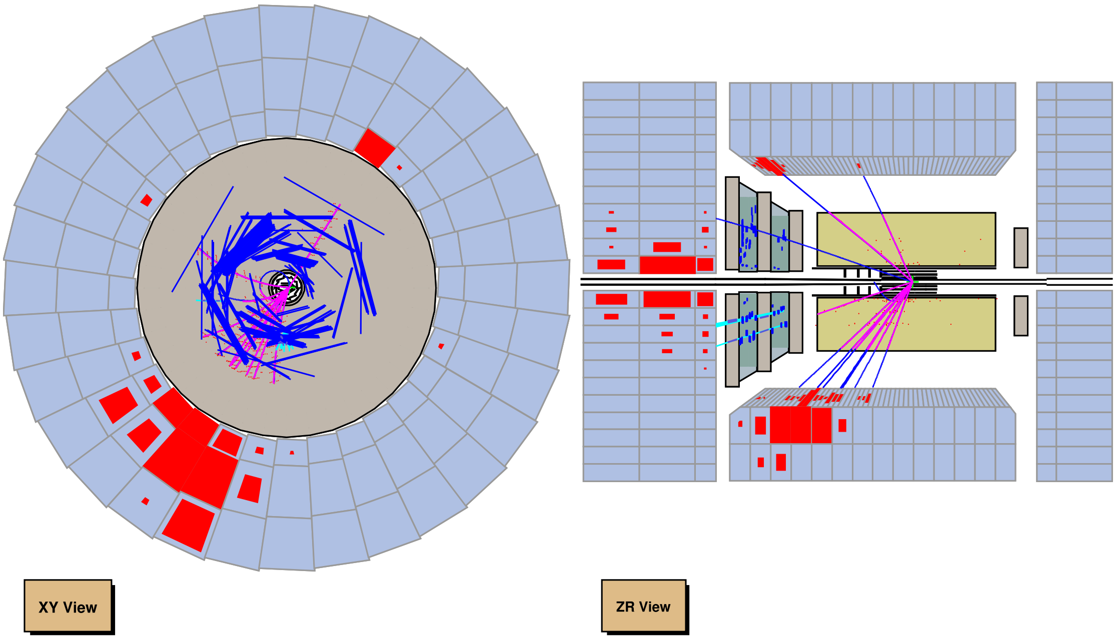

Figure 5.1: An NC event example, shown in the XY-view on the left and the ZR-view on the right. Lines emerging from the event vertex represent the tracks, while pads depict energy deposits in the CAL. The scattered e^+ and the current jet are observed in the BCAL. Event pictures were prepared using the ZEVIS program [156]. $Q^2 \simeq 10\,000\,\text{GeV}^2$, $E_{e^+} \simeq 86.5\,\text{GeV}$, $P_T \simeq 8\,\text{GeV}$, $E_T \simeq 86.5\,\text{GeV}$.

5.2 Characteristics of background events

Neutral current interactions which are under study here are just one class of events reconstructed using the ZEUS detector, while all the others need to be considered as background and removed from the final sample. Background events can be classified according to their source, as one of the other *ep* processes (photoproduction, Charged Current DIS, etc.), or have non-*ep* sources, e.g. cosmic rays. Overlays of the non-*ep* events with the NC ones have to be removed as well. The most important ones are described below.

5.2.1 Beam-gas interactions

The pressure in the beam-pipe was maintained on a level as low as approximately 10^{-8} Pa [157], but the residual gas could still be a source of background when either protons or positrons from the beams scattered off its molecules (or off an element of the beam-pipe). Several measures were available to remove such events.

- If a beam proton interacted with either residual gas or an element of the beam-pipe producing secondary particles upstream of the detector, such an event was likely to be rejected using information from the Veto Wall or timing cuts.
- If the same happened within the body of the detector, its secondary particles typically rendered the total transverse momentum P_T unbalanced. Additionally, the effect was reduced by cuts on the position of the primary vertex.
- On the other hand, beam-gas events caused by collisions with beam positrons may have topologies indistinguishable from the NC signal. It has been found however, using dedicated runs with the proton bunch being empty [148], that such events do not pass the full NC selection applied typically at ZEUS, and hence are negligible.
- Finally, NC events overlayed with beam-gas ones are characterized by high total $E - P_Z$, and hence are easily removed.

5.2.2 Halo and cosmic muons

Muons are created via the decay of charged pions, after interactions of particles from the proton-beam halo with residual gas or elements of the beam-pipe. Most of these muons are rejected by the Veto Wall, but some of them pass through, moving almost parallel to the beam axis (see Fig. 5.2) and produce fake electrons when interacting with the EMC section of the calorimeter. However, in such cases the total transverse momentum P_T is typically unbalanced and combined with an energy deposit having arrived early in the RCAL compared to the timing of an hypothetically overlayed NC event, enables rejection of this type of background.

From the abundance of particles created in high energy showers produced in the interaction of cosmic rays with gas in the upper atmosphere, only muons can reach the ZEUS detector (see Fig. 5.3), as it is placed $10-25$ m underground. The same precautions as for the halo muons, namely calorimeter timing cuts and the requirement on the event transverse momentum P_T to be low are used to reject them.

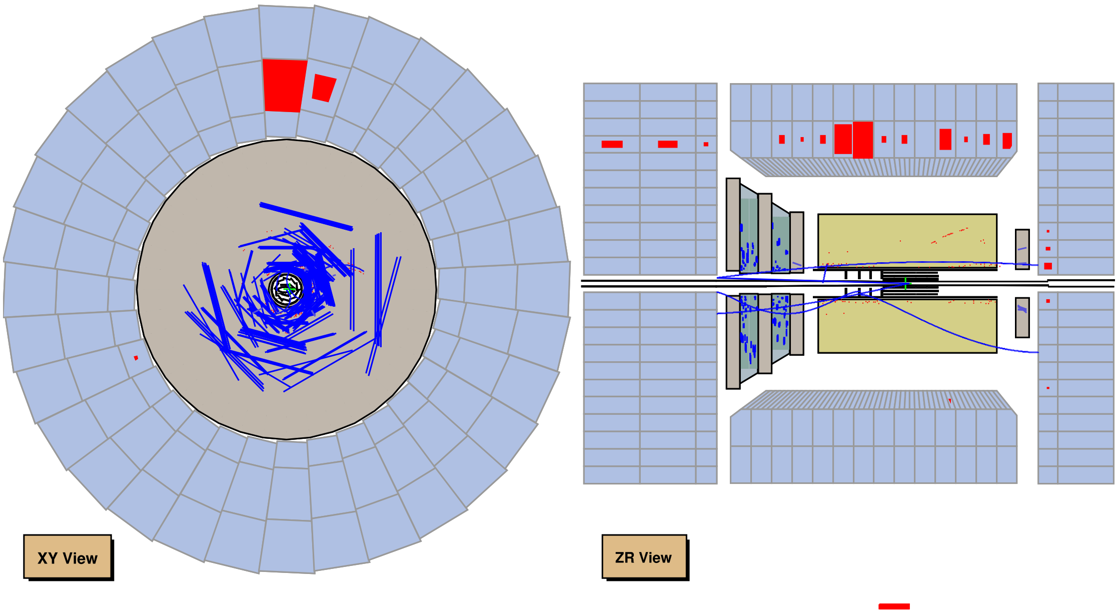

Figure 5.2: An example of a halo muon passing through the upper calorimeter half.

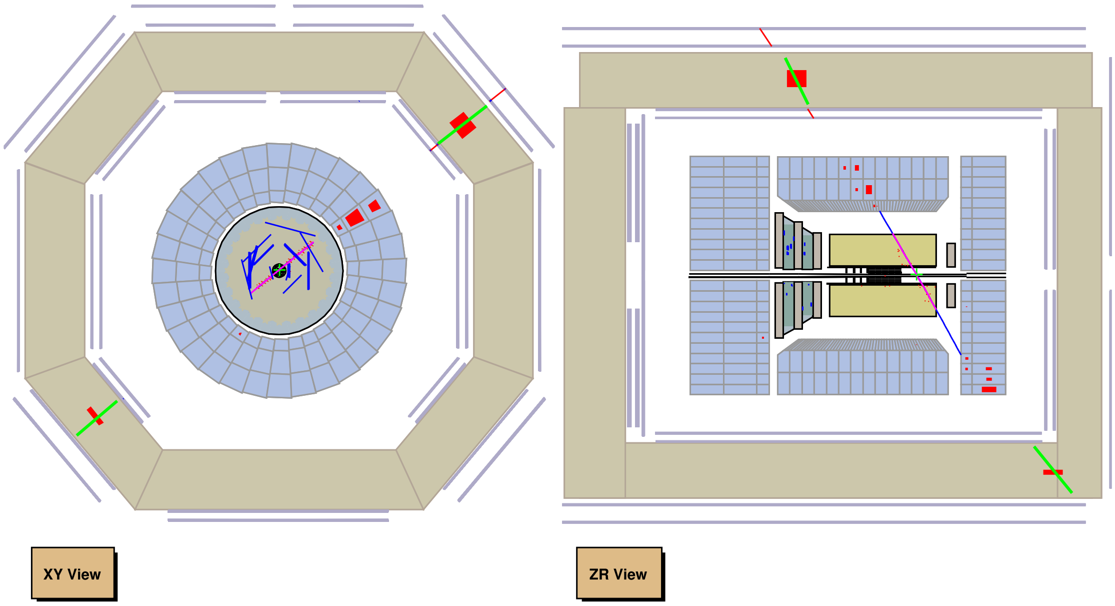

Figure 5.3: An example of a cosmic muon event.

5.2.3 Photoproduction

The most significant and problematic background processes in the measurement of NC cross sections is photoproduction of high-E_T jets [56]. In this process, mediated by a quasi-real photon ($Q^2 \approx 0$), the incoming lepton scatters off the proton at a very low angle ($\theta \approxeq 180°$ in the ZEUS reference frame) and escapes through the rear beam-pipe. If the exchanged photon participates in the hard scatter, we call the process *direct* photoproduction. If, on the other hand, the photon fluctuates into a hadronic system which then acts as a source of partons interacting with a proton, we call the process *resolved* photoproduction (in this case only a fraction of the photon momentum participates in the hard scattering). Feynman graphs of these two subprocesses are shown in Fig. 5.4.

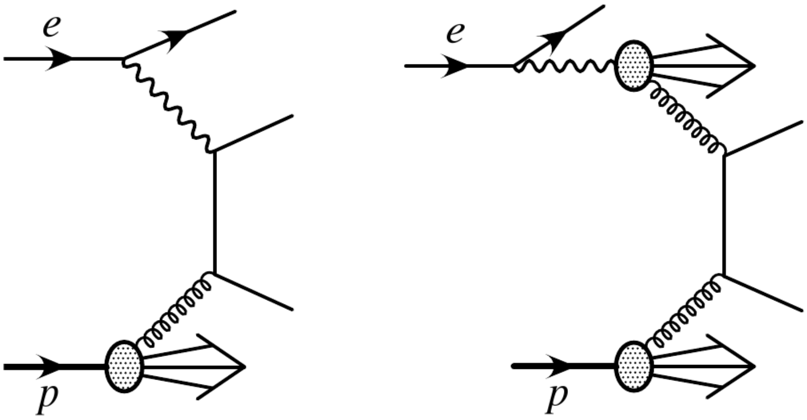

Figure 5.4: Feynman diagrams for the direct (left) and resolved (right) photoproduction process [158].

A PHP event may be misclassified as neutral current if either a high-energy photon or a high-energy jet are misidentified as the scattered electron, or else if the jet contains a high-P_T electron from e.g. a decay of either a beauty or a charm meson. Several measures, quantified in Sec. 5.7, may be used for discriminating PHP events. Firstly, since the scattered lepton is lost and E_P cancels in Eq. 5.1, the $E - P_Z$ distribution has a peak around 0 GeV. Secondly, only electrons of a high enough isolation in the calorimeter are accepted. And finally, the cut on the energy of the scattered lepton improves the suppression of the PHP background.

5.2.4 Charged Current

Another class of physics events (interesting in itself) that need to be rejected from the final NC sample are the charged current (CC) interactions [159]. In this process, the incoming lepton interacts with the proton exchanging a charged boson

W, yielding the presence of an undetected neutrino as the outgoing lepton. An example of a charged current event is shown in Fig. 5.5. Since only the hadronic final state is reconstructed, the total transverse momentum P_T is heavily unbalanced, which makes removal of CC events relatively easy.

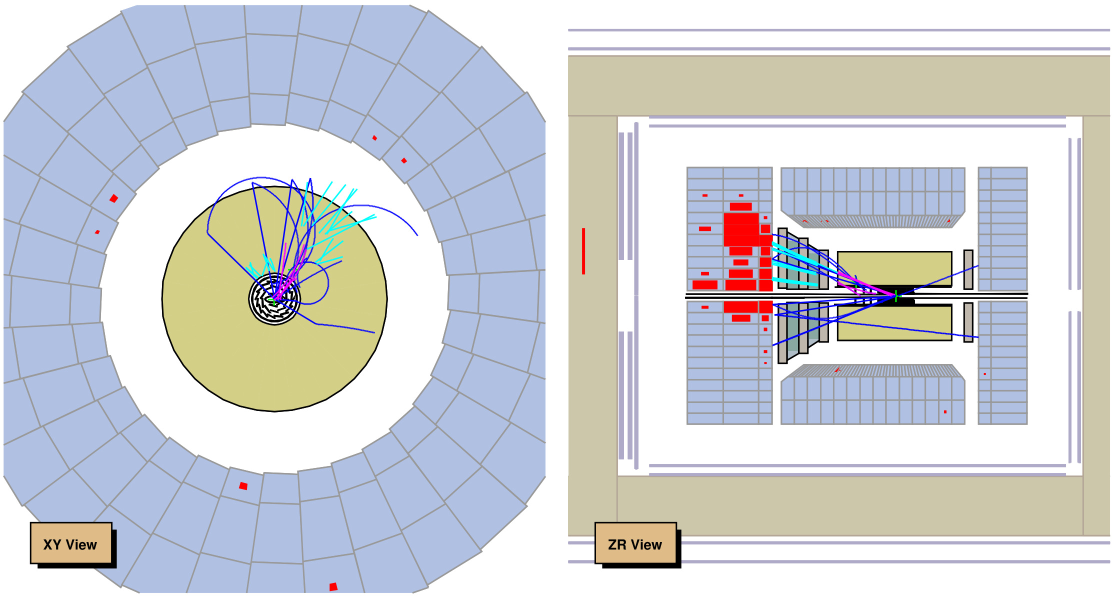

Figure 5.5: An example of a CC event. The unbalanced current jet is observed in the bottom part of the BCAL. Backsplash tracks going backwards w.r.t. the spectator jet are visible in the ZR view. $Q^2 \simeq 11\,000\,\mathrm{GeV}^2, P_T \simeq 85\,\mathrm{GeV}, E_T \simeq 92\,\mathrm{GeV}$.

5.2.5 Elastic QED Compton scattering

The QED Compton process (QEDC, see Fig. 5.6) is very similar to initial- and final-state radiation from a lepton taking part in the interaction (see Sec. 5.3.1). It involves (acollinear) emission of a hard photon from an incoming or outgoing lepton, leaving the lepton off-shell. The lepton reacts then with an exchanged boson (γ, Z^0). The QEDC process can be elastic (when the proton does not dissociate) or inelastic (when it does). The latter is known to be well simulated by the Monte Carlo [160], while the former is not and hence has to be removed from the final sample (or else, the hard photon reconstructed within the HFS would bias the reconstruction of kinematic variables considerably). Fortunately a typical QEDC event has a clean topology, with two isolated EMC clusters (created by the photon and the scattered lepton) containing almost the full energy of the whole event and being well balanced in ϕ and E_T.

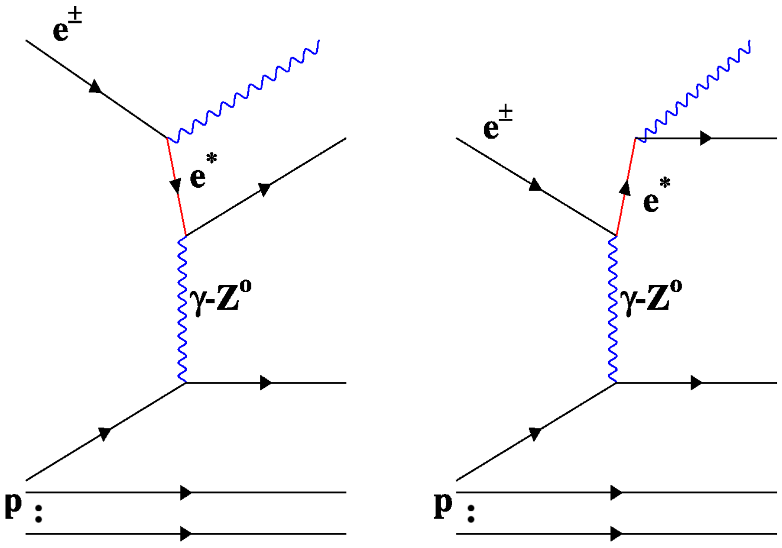

Figure 5.6: Feynman graphs for the QEDC process (fig. modified after [148]).

5.3 Monte Carlo samples

The modern high-energy-physics experiments have become so complicated, that in many cases it is impossible to fully analyze the recorded data without the use of the Monte Carlo (MC) techniques. MC is used to simulate physics processes practically on all levels of such a complex experiment like ZEUS: it allows to generate lists of four-momenta of particles emerging from the hard interaction, simulate their decays, describe the response of each detector component to passage of these particles. It is also irreplaceable in the process of describing detector local and time-wise inefficiencies. Finally, because of the wide use of MC at ZEUS, practically the whole process of the analysis of systematic effects also relies on observations how the recorded data and its simulated counterpart behave under particular variations of analysis requirements or parameters of the simulation. The wider description of the wealth and power of such techniques can be found elsewhere [161].

5.3.1 Signal Monte Carlo

As higher-order corrections to the Born-level NC DIS cross sections are almost indistinguishable in data from the lowest-order signal, it is necessary that they are included in the simulation. Only then the simulation can mimic the real signal well. Some corrections to the hadronic side of the reaction have already been mentioned in Sec. 2.1 (boson-gluon fusion, gluon emission from a struck quark). Let us now mention the correction to the electron-side of the reaction.

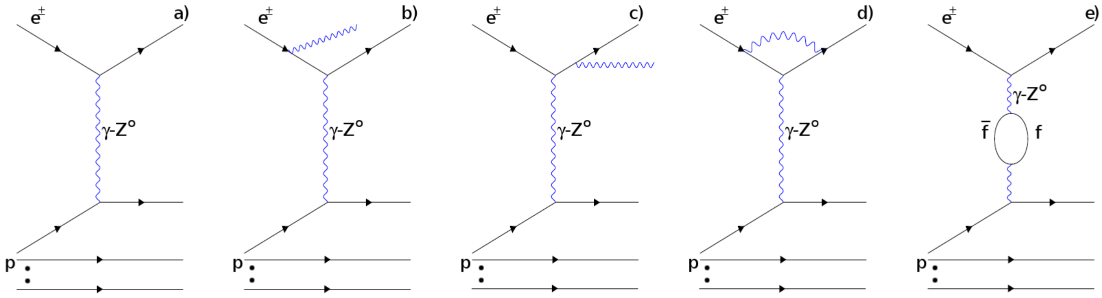

Figure 5.7: Feynman graphs for (a) the Born-level NC DIS process, (b) ISR, (c) FSR, (d) vertex correction, (e) self-energy correction (fig. modified after [148]).

The lowest-order of the NC DIS process is mediated through the exchange of a boson (γ, Z^0) with no particles being radiated from an incoming or outgoing lepton (or incoming proton and outgoing quark), and depicted in Fig. 5.7(a). The cross section, as well as the kinematics of NC DIS events, are modified when initial- and final-state radiation (ISR and FSR, respectively, Fig. 5.7(b,c)) is considered. As the ISR photon, emitted collinearily with the incoming electron takes a fraction of its momentum, the center-of-mass energy of the electron-proton reaction is decreased. The FSR photon, on the other hand, lowers the energy of the electron outgoing from the DIS reaction. The cross section is further modified when the NLO-loops are included in the picture, namely the vertex correction (Fig. 5.7(d)) and the self-energy correction (Fig. 5.7(e)).

In this analysis, NC DIS events were generated with DJANGOH 1.6 [162] MC program, using CTEQ5D PDFs [163]. DJANGOH is an event generator, which includes both QED and QCD radiative effects. It contains HERACLES (4.6.6) [164], which takes into account a complete set of one-loop EW radiative corrections and radiative scattering. DJANGOH is an interface for HERACLES as well as for the ARIADNE (4.12) program [165, 166], which, using the color dipole model (CDM), simulates QCD cascades. The output from ARIADNE consists of a set of colored quarks and gluons, which then are an input for the final stage of event generation - the hadronization. Within the MC chain used in this analysis, this last task was handled by the JETSET 7.4 program [161], which applies the Lund string fragmentation algorithm [167]. JETSET (distributed together with PYTHIA generator), produces color-neutral objects, hadrons, from quarks and gluons generated by the previously mentioned algorithms. Finally, the unstable hadrons are simulated to decay, and these that reach the components of the ZEUS detector (such as the CTD or CAL) included in the detector model, are simulated to react with detector material within the FUNNEL program (see Sec. 4.2).

The MC sample used in this analysis was created with the FUNNEL version num07t2.1, with various minimum-Q^2 cuts. The whole set of NC signal samples is listed in Tab. 5.1, where the minimum-Q^2 cut is applied on the Q^2 calculated at the incoming lepton vertex. The NC DIS cross section falls with $1/Q^4$, and therefore not to create huge samples with just one minimum-Q^2 cut, the full sample consists of many subsamples, assuring very high MC statistics in each point of the kinematic plane. The lowest-Q^2 element of this MC set has almost 9 times events more than the whole 06/07 data set, ensuring that statistical errors coming from the MC are negligible.

Q^2_{min} [GeV^2]	no. events	σ [pb]	$\mathcal{L}$ [pb^{-1}]
100	7999900	8111.06	986.3
400	1999990	1168.43	1711.7
1250	990808	198.12	5001.1
2500	490266	59.2	8280.9
5000	500000	14.94	33475.3
10000	237651	2.83	84081.3
20000	40000	0.32	126005.7
30000	60000	$5.66 \cdot 10^{-2}$	1060895.3
40000	20000	$1.15 \cdot 10^{-2}$	1739735.6
50000	18477	$2.29 \cdot 10^{-2}$	8080909.7

Table 5.1: Set of (FUNNEL version num07t2.1) DJANGOH NC MC samples with different minimum-Q^2 cuts.

To obtain the same normalization of data and MC for comparisons and cross section unfolding, each of the elements of the discussed simulated sample was weighted according to its luminosity, such that the weight w for MC events is defined as:

$$w = \frac{\mathcal{L}^{data}}{\mathcal{L}^{MC}}, \tag{5.2}$$

where $\mathcal{L}^{data}$ is the integrated luminosity of the data sample under consideration and $\mathcal{L}^{MC}$ corresponds to the MC generated luminosity for a particular sample, listed in Tab. 5.1. As each next MC sample (counting from the low-Q^2 to the high-Q^2 ones) fully overlaps with all the previous ones, one needs to calculate the final weight w for a MC event with $Q^2 = Q_0^2$, according to:

$$w = \frac{\mathcal{L}^{data}}{\sum_i \mathcal{L}_i^{MC}}, \tag{5.3}$$

where i runs over all samples with $Q_0^2 > Q_{min}^2$, with Q_{min}^2 being the lower-Q^2 limit on the range of a particular sample listed in Tab. 5.1.

5.3.2 Diffractive Monte Carlo

In the previous ZEUS MC versions, the standard NC signal simulation did not include *diffractive* events, which have no hadronic activity in the rapidity gap between the current jet and the proton remnant [168]. The current version, on the other hand, offers such an option, so one does not have to mix signal events generated by DJANGOH with the ones coming from e.g. RAPGAP (program for generating hard-diffractive scattering in *ep* collisions [169]) separately, but rather use a DJANGOH option to include diffraction in the generated DIS sample. In the detector frame, one can see the clear difference between diffractive and non-diffractive events in the distribution of the maximum pseudo-rapidity of DIS events, defined as:

$$\eta_{max} = -\ln\left(\tan\frac{\theta_c}{2}\right), \tag{5.4}$$

where θ_c is the polar angle corresponding to the most forward energy cluster found in the CAL (with a minimum energy of 400 MeV). The rapidity gap of the diffractive events reveals itself in the presence of the signal in the low-η_{max} region, w.r.t. the non-diffractive DIS. Figure 5.8(a) and Fig. 5.8(b) depict a comparison of DIS NC data in function of η_{max} variable without the diffractive contribution mixed-in, while Fig. 5.8(c) and Fig. 5.8(d) present the current status. The latter case was used in this analysis.

5.3.3 Background Monte Carlo

Photoproduction

The main background source in the measurement of NC DIS comes from misidentification of PHP events (described in Sec. 5.2.3) as those of the NC signal. The MC sample with which the contribution from PHP to the final sample was evaluated was generated with the HERWIG 5.9 program [170] with CTEQ4D PDF parameterization. As the PHP cross section is enormous, compared to that of DIS, kinematic cuts were applied at the generator level in order to avoid gener-

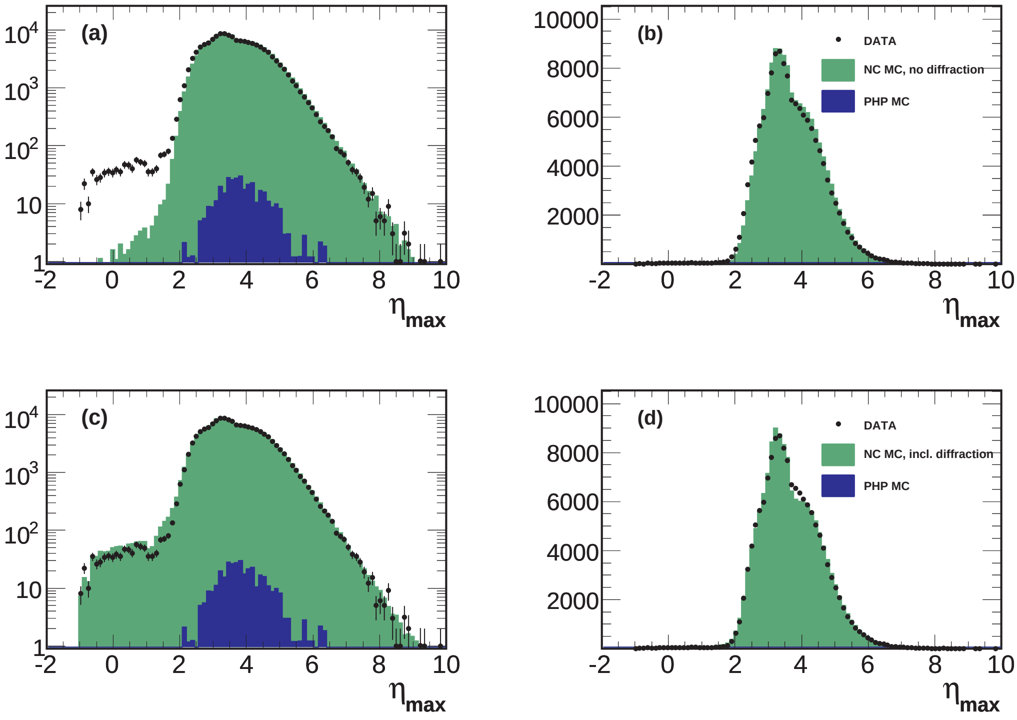

Figure 5.8: Comparison of data and MC samples in function of the η_{max} variable without (a,b) and with (c,d) diffractive contribution mixed in.

ating samples larger than necessary. Therefore first, the transverse momentum of the hard scatter was required to exceed 4 GeV. Moreover, either the transverse energy E_T was required to exceed 30 GeV, or the total transverse momentum had to be greater than 6 GeV. The summary of the PHP samples used in this analysis is given in Tab. 5.2.

	direct			resolved		
Q^2_{max} [GeV^2]	no. events	σ [pb]	$\mathcal{L}$ [pb^{-1}]	no. events	σ [pb]	$\mathcal{L}$ [pb^{-1}]
4	530000	2830	$1.873 \cdot 10^2$	630000	11900	$5.294 \cdot 10^1$

Table 5.2: Direct and resolved contributions to PHP MC, generated with HERWIG and used in this analysis.

Normalization of the photoproduction MC

The value of the total PHP cross section in a given kinematic range is not very well known compared to the ones of e.g. NC and CC DIS. Moreover, the generator-level cuts mentioned above introduce an additional ambiguity on σ_{PHP}. Therefore,

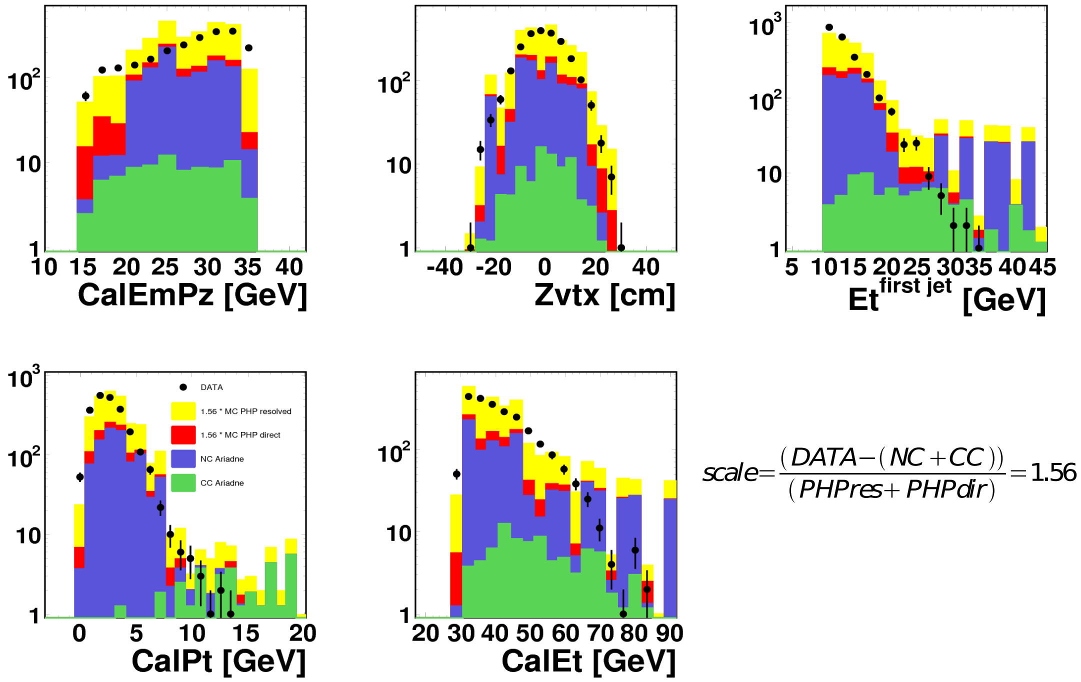

Figure 5.9: Control histograms used for the PHP normalization procedure, presenting: the total $E - P_Z$ (CalEmPz), Z_{VTX}, E_T of the highest-energy jet ($Et^{firstjet}$), the total transverse momentum P_T (CalPt) and the total transverse energy E_T (CalEt). The points represent the data of the enriched data sample, while the shaded area consists of DIS and PHP combined samples. Both, the direct and resolved PHP MC contributions were scaled by a factor of 1.56.

apart from attributing weights to the PHP MC events, according to the values listed in Tab. 5.2, a scaling factor multiplying this weight was determined in a normalization of the PHP MC procedure. The method was based on selecting a PHP enriched sample from the 06/07 e^+p ZEUS data, and scaling the discussed PHP MC, so that it agrees with the PHP enriched sample. It should be noticed, that in the course of this procedure, the PHP direct and resolved samples were treated as signal, while the NC ($Q^2 > 4\,\mathrm{GeV}^2$) and CC ($Q^2 > 10\,\mathrm{GeV}^2$) DIS samples were treated as background.

The following cuts were applied (to be fulfilled by both data and MC events), in order to select PHP enriched samples (for comparison of this list to the cut mixture applied to select a final NC DIS sample, and for a wider description of selection criteria, see Sec. 5.6 and Sec. 5.7):

- an event had to be accepted by the HFL05 trigger slot, which is designed to select di-jet PHP events, with at least two cone-jets of $E_T > 4.5\,\mathrm{GeV}$, for $\eta < 2.5$; moreover the slot logic requires that $E - P_Z < 100\,\mathrm{GeV}$;

- the longitudinal interaction point Z_{VTX} had to be well reconstructed and within the limit of $|Z_{VTX}| < 30\,\mathrm{cm}$;

- to remove NC DIS events, no e^+ candidate found by the SINISTRA electron finder, with SINISTRA probability value greater than 0.9 and $E'_e > 10\,\mathrm{GeV}$;

- in order to remove events with low transverse energy, the total transverse energy $E_T^{1st-jet}$ of the most energetic jet (among the required two, localized with a k_t jet-finder) had to exceed 10 GeV;

- the reconstructed $E - P_Z$ parameter, introduced in Eq. 5.1 must lie within a PHP enriched region of $15 < E - P_Z < 35\,\mathrm{GeV}$;

- the total energy E_{CAL} reconstructed in the whole calorimeter must exceed 30 GeV.

Finally, using the PHP enriched samples obtained with a procedure defined above, a PHP MC scaling parameter was calculated according to:

$$s = \frac{N_{DATA} - (N_{MC}^{NC} + N_{MC}^{CC})}{N_{MC}^{directPHP} + N_{MC}^{resolvedPHP}}, \tag{5.5}$$

where N_{DATA} is the number of data PHP events, N_{MC}^{NC} is the contribution estimated from the NC DIS MC, N_{MC}^{CC} is the contribution estimated from the CC DIS MC. $N_{MC}^{directPHP}$ and $N_{MC}^{resolvedPHP}$ represent the number of, respectively, direct and resolved PHP events reconstructed from MC, weighted to the integrated luminosity of the test data sample under study, according to the numbers given in Tab. 5.2. The final scaling factor obtained from this procedure read $s = 1.56$ and multiplied the cross sections of both direct and resolved PHP MC samples, in a procedure of the PHP background estimation in the e^+p NC DIS cross section measurement. As it will be discussed in Sec. 7.1.2, in order to estimate the uncertainty of the PHP cross section in the NC DIS measurement, the total normalization of the former was varied by ±50%, in the course of the analysis of systematic effects. Fig. 5.9 depicts the control plots employed in the PHP normalization procedure described here, after the scaling factor s of 1.56 had been applied on MC PHP.

5.4 Scattered lepton energy corrections

The level of agreement of the simulation of the scattered positron energy with the real measurement does have a significant impact on the final sample through the cuts on $E'_e, E - P_Z, E_T$ and P_T (see Sec. 5.7). Among several phenomena that affect the E'_e measurement, three have already been described in Sec. 4.2, while here let us mention the remaining ones.

A scattered lepton travelling from the interaction point towards the CAL surface traverses the so called *dead material* (e.g. magnets, cables, supporting structures), so that a fraction of its energy gets dissipated. Additionally, since the calorimeter surface is *not uniform*, the spacing of its towers and modules needs to be accounted for in the Monte Carlo. Separate analyses have been performed to describe the losses due to dead material and non-uniformity for the RCAL [134, 135, 171] and the BCAL [135, 172].

Calorimeter non-uniformity corrections

Two known effects may bias the description of the measured electron energy in default MC, due to non-uniformities of the calorimeter. First, in the case that the electromagnetic shower develops in plates of wavelength shifters running between calorimeter modules, the measured energy is overestimated due to emission of Cerenkov light in wavelength shifters. Secondly, if an electron enters the calorimeter very near to cell boundaries, the losses in the active material between cells cause the measured energy to be underestimated.

In order to describe the non-uniformity effects in MC for the RCAL, a high-statistics 06/07 NC DIS e^+p data test sample was selected. Events which entered the test sample were required to include a positron found with the SINISTRA (or EM in the alternative study) electron finder of, among other requirements, the reconstructed energy $E'_e > 4\,\mathrm{GeV}$, and the longitudinal event vertex position $Z_{VTX} < 50\,\mathrm{cm}$. Using this sample, a comparison (as a function of e.g. the RCAL radius) of the the double angle electron energy $E_{e,DA}$, where (with γ_{had} and θ_e being polar angles of the hadronic system, and the scattered lepton, respectively):

$$E_{e,DA} = 2E_e^{beam} \frac{\sin\gamma_{had}}{\sin\gamma_{had} + \sin\theta_e - \sin(\gamma_{had} + \theta_e)}, \tag{5.6}$$

and the measured electron energy were used to obtain the correction. Also in the BCAL the non-uniform detector response due to gaps between calorimeter modules and cells must be corrected at some step of the event reconstruction. Here, a sample of NC DIS e^+p events of $Q^2 > 185\,\mathrm{GeV}^2$, with a positron found by the EM program and $38 < E - P_Z < 65\,\mathrm{GeV}$, was used in the correction procedure. The same method as in the case of the RCAL, which used the ratio of $E_{e,DA}$ to the measured electron energy for calibrating the energy scale by correcting the ratio to unity, was used in the case of the BCAL.

Dead-material correction

As the amount of the dead material in front of the calorimeter surface was much better known for the BCAL than for the RCAL, corrections developed for these two detector parts were originally designed differently. In the case of the BCAL, test beam studies of the calorimeter were combined with the default response of the detector in the simulation, to derive the relevant correction. In case of the RCAL, the energy measured in the pre-sampler was used as a measure of the number of particles in the shower caused by elements of the dead material. The correction factor was determined using kinematic peak events, which are characterized by the energy of the scattered lepton being close to the beam energy. The measured energy was compared to the energy calculated from the DA method (Eq. 5.6), and different factors were obtained for the case of data and MC.

5.5 Longitudinal vertex re-weighting in MC

Precise knowledge of the distribution of the longitudinal vertex positions of the *ep* interactions is highly important, as this quantity plays a direct role in the measurement of kinematic variables. Hence, its imperfection could have a negative impact on the accuracy of the acceptance correction (see Sec. 7.1).

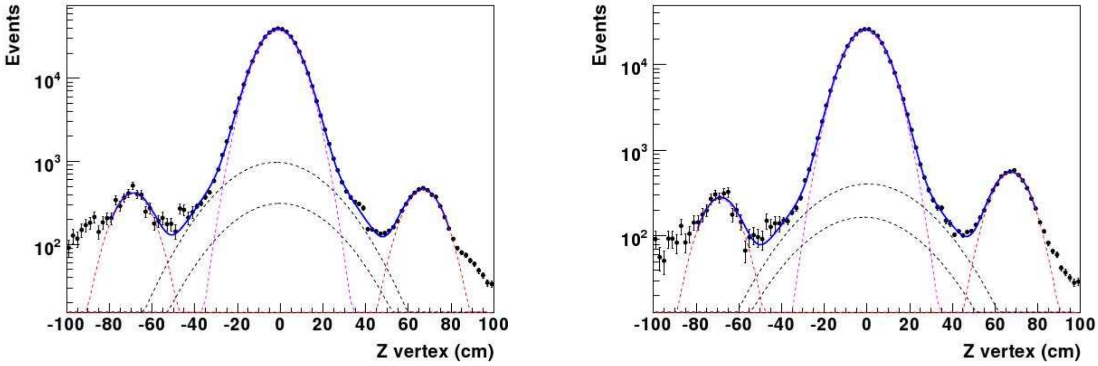

Figure 5.10: A composition of the Gaussian fits applied to the Z_{VTX} data distribution [173] for the P_+ e^+p sample (left) and the P_- one (right).

The true distribution of Z_{VTX} was different for each machine fill, as it is governed by the tuning of the beam-optics. The main vertex peak is Gaussian [1] (see Fig. 5.10), and its width depends on the length of the proton and positron bunches (8.5 and 0.83 cm respectively). Additionally, particles that accidently entered in

---

[1] Due to existence of additional small peaks (satellites), the final fit is a composition of five Gaussians.

the neighboring (to the desired ones) packets in the beam filling procedure of the storage ring, yield extra peaks visible on either side of the main peak (so called *satellite peaks*) [160]. Therefore, an unbiased measurement of this distribution has been performed and fitted [173] in order to determine the weights which could later be applied to the raw MC distribution (it has been done for each of the two P_+ and P_- samples, where P_+ and P_- denote samples with positively-polarized and negatively-polarized incoming e^+ beams, respectively).

Overall, the re-weighting allowed to increase the agreement of data and MC expressed in terms of sample normalizations, where the sample normalization is defined as:

$$Norm. = \frac{N_{DATA} - N_{MC}}{N_{MC}}, \tag{5.7}$$

by an absolute value of 1% (e.g. changing the normalization value from $Norm. = -0.035$ to -0.025). The comparison of data with MC before and after the re-weighting is presented in Fig. 5.11.

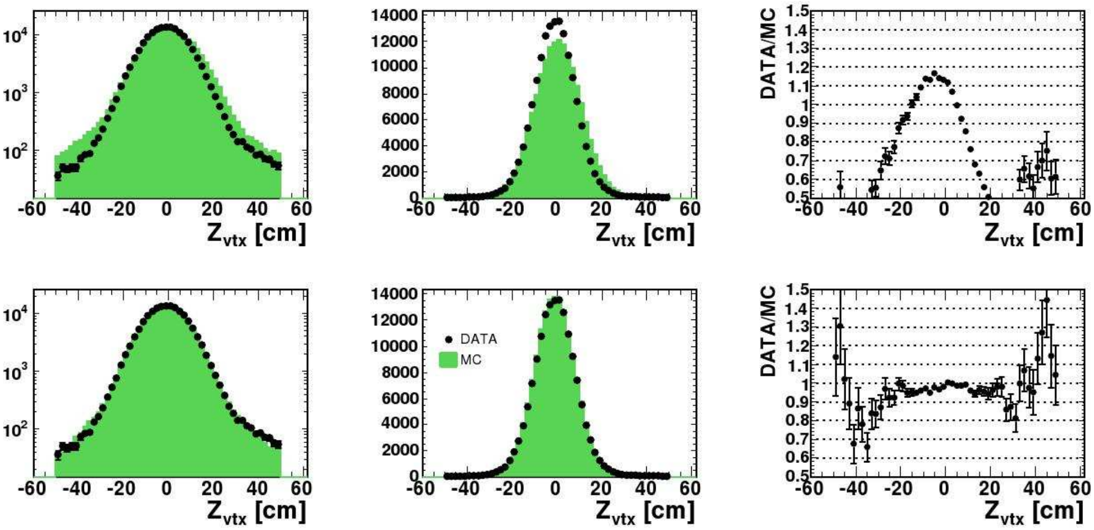

Figure 5.11: The effect of the re-weighting of the original MC Z_{VTX} distribution using the fits described in [173]. The upper row shows data versus bare MC, while the lower plot contains the re-weighted MC. The right column presents the single ratio of data to MC for both cases.

5.6 Data pre-selection

As many different analyses performed at ZEUS required a huge variety of events to be recorded on tape, it is not efficient to run specific final-analysis programs (called jobs) on the whole ZEUS data sample. Therefore a tool called *zesLite* [174] (a successor of the ZES system) has been created, to provide such *pre-selection* functionality to the end users. Moreover, a task to only pre-select events interesting in scope of the NC measurement is enabled with the *DST* trigger bits, which contain definitions of basic requirements for any typical analysis already at the trigger level (see Sec. 3.2.4), i.e. using uncorrected reconstruction variables. Nevertheless, to avoid a possible bias coming from using uncorrected quantities (such as Q^2, or electron energy measured at the trigger level), in this analysis only the DIS03 TLT (see Sec. 5.6.3) trigger bit was employed.

Each trigger level has been designed in form of several logical bits which can be combined as needed. In the following sections, specific requirements applied on all three trigger levels are discussed.

5.6.1 First Level Trigger

As mentioned in Sec. 3.2.4, only very basic quantities were available on the FLT level, as the system needed to accept or reject a given event in a very short period of time ($5\,\mu$s). The FLT was based on signals coming from the CTD and the CAL. All the decision bits were combined by a logical OR operation into one boolean variable. The bits have been designed not only to cover the full detector acceptance, but also to allow combinations of requirements providing satisfactory signal purity and efficient background rejection at the same time. Table 5.3 lists all ten FLT bits used for NC event selection.

In order to make it easy for the reader to understand Table 5.3, let us discuss two powerful bits in greater detail. FLT30 made use of a pattern of up to four trigger towers in the RCAL to be *isolated*, so that the sum of the energies of the EMC sections of these towers was above 2 GeV, and they were surrounded by the quiet towers. Additionally, it was required that the total energy of the RCAL EMC sections was greater than 4 GeV (for all the towers with EMC energy exceeding 600 MeV). A different approach was used in the definition of the FLT43 slot. The total transverse energy in the CAL was required to be greater than 15 GeV, and a track passing at least 3 CTD super-layers had to be reconstructed. For the sake of trigger speed, no attempt was made to match the track with any energy deposit in the CAL. Finally, the timing information from components such as the Veto Wall was expected to be consistent with expected events of the *ep* bunch crossing.

trigger bit	bit requirements
FLT28	(isolated energy in the FCAL or in the BCAL) AND (good track)
FLT30	(isolated energy in the RCAL) AND (>4 GeV in the EMC section of the RCAL)
FLT36	similar to FLT30
FLT39	(total energy in the EMC section of the BCAL > 3.5 GeV) AND (isolated energy in the BCAL) AND (good track)
FLT40	(total energy in the EMC section of the whole CAL > 20 GeV)
FLT41	(total $E_T > 30$ GeV)
FLT43	(total $E_T > 15$ GeV) AND (good track)
FLT44	similar to FLT39, using both BCAL and RCAL
FLT46	similar to FLT30, using 3 quadrants of the RCAL
FLT47	similar to FLT46

Table 5.3: Description of FLT bits used in this analysis.

5.6.2 Second Level Trigger

The full chain of GSLT requirements for the NC analysis is fully discussed in [148] and [43], while a thorough technical report on the GSLT implementation is available in [116]. Just as in case of the FLT, information on the SLT level has been organized into boolean bits, which renders testing various combinations easy to the end user[2]. Several key elements are worth mentioning here.

- First of all, this trigger level employed various combinations of the GFLT bits.
- An important element of the SLT chain was a calorimeter-based algorithm recording moments in time in which relativistic particles hit the detector (the so called SLT *timing system*). It assumed that these particles emerge from the nominal interaction point of $(x, y, z) = (0, 0, 0)$. After corrections on effects of delays, the resolution of this measurement was as fine as $1 - 2$ ns. Moments of arrival of particles in the CAL parts separated in space were then compared in order to check if particles come from the same *ep* event.

---

[2] Note for the ZEUS experts: a combination of the GSLT bits used in this analysis reads precisely: (DIS07 OR EXO01 OR EXO02 OR EXO03).

For example, cosmic muons were rejected by checking the relative arrival time of the particle in the top half of the BCAL, w.r.t. its time of arrival in the bottom BCAL half (reject if $t_{top} - t_{bottom} > 10\,\text{ns}$).

- The total $E - P_Z$ available on this level of fast event reconstruction (by the local GSLT algorithms only) should lie in the interval $(29, 100)\,\text{GeV}$.
- For the HERA II period a new SLT element, called the Global Tracking Trigger (GTT) has been prepared [175]. This system used event data from different tracking components for fast reconstruction of tracks and vertices from the information available at the SLT level. Beam-gas events were rejected by checking the relative number of tracks not coming from the primary event vertex, w.r.t the ones indeed coming from the vertex.

5.6.3 Third Level Trigger

The TLT DIS03 high-Q^2 NC bit was used on the highest trigger level of this analysis. Its definition contained the following cuts performed on global variables available on this trigger level, combined by a boolean AND operation.

- The total $E - P_Z$ was found in the interval of $(30, 100)\,\text{GeV}$ and a primary vertex was reconstructed.
- An electron candidate of energy exceeding $4\,\text{GeV}$ was reconstructed by a fast version of the electron finding algorithm. If the candidate is found in the RCAL, its CAL cluster center should lie outside a circle of $35\,\text{cm}$ radius around the beamline.

In this analysis, 5 million and 2.8 million events of P_+ and P_- samples, respectively, survived the DIS03 TLT pre-selection and were written into the final ROOT-files.

5.6.4 Data quality

The last step before imposing the final set of cuts was to verify whether all of the sub-detectors relevant to the NC measurement worked fine for a given run. This step was necessary *before* the run-wise quantities such as luminosity or polarization were calculated.

Firstly, a logical bit defined by the EVTAKE algorithm [76] has value TRUE for a given data run, only if:

- luminosity monitor was in a good condition;

- CTD was at its full operating voltage with no significantly large non-active region;
- CAL was fully operational and had a low number of dead channels;
- the magnetic field was switched on;
- number of events processed in the run was greater than 99.

Similar algorithms (MVDTAKE and STTTAKE) were required to produce TRUE decision bits assuring the fully operational status of MVD and STT, respectively. Additionally the luminosity and polarization recorded for the run and the bunch-crossing type recognized by the trigger system had to be *ep*-like. All runs belonging to the run-number interval of [62004, 62284] (of the LH sample, which will be defined in Sec. 5.8) had to be skipped as in this period the BCAL pre-sampler, used for correcting the electron energy, was malfunctioning [135].

As two detectors measuring the longitudinal polarization of the lepton beam were running, for each run it had to be decided which of them to make use of. Generally, the systematic uncertainties of the LPOL were better known and smaller than the ones of the TPOL, so the LPOL was always the first choice. The polarization values recorded by the TPOL were used for a given run only if the polarization value recorded by the LPOL was unavailable or flagged as suspicious [83]. Finally, the run would be rejected if its polarization measurement was found to be exactly equal to 0.0.

Finally, luminosities of the data runs for which all of the conditions mentioned above were fulfilled were added in order to calculate the luminosity of a given sample. This holds true for polarization as well, with a remark that the polarization sum was weighted by the luminosity.

5.7 Off-line event selection

The following sections contain the full description of the final NC selection. This collection of cuts and analysis techniques has been under constant development over many generations of ZEUS analyses [43, 57, 138, 148, 152, 160, 176–180]. It has been optimized with the goal of obtaining a final sample of high purity and significant statistics. Some of the cuts are presented as superimposed lines on histograms comparing data points to the simulation. Such figures were prepared using the full selection cocktail, except for the cut under study. Points in histograms represent data, while colored or shaded areas are filled with Monte Carlo samples. All the cuts are applied both to data and MC samples.

5.7.1 Scattered lepton identification

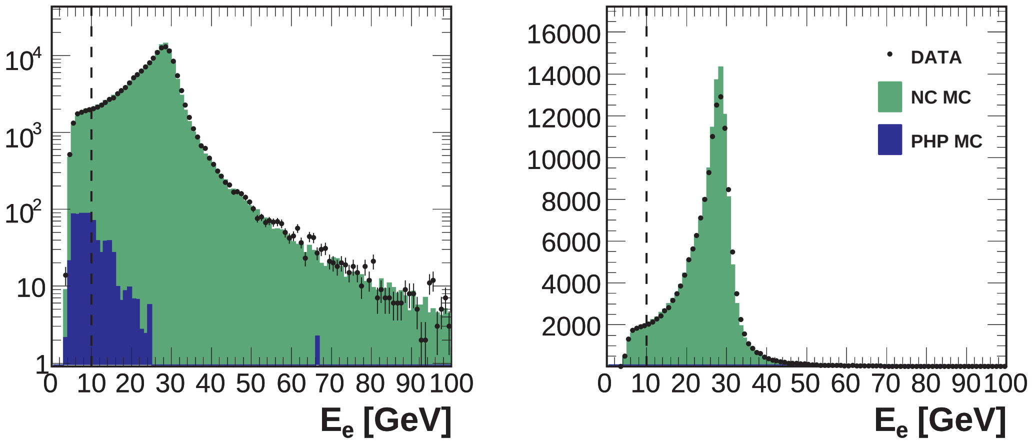

Figure 5.12: Reconstructed energy of the scattered positron after all cuts except for the one depicted. The dashed line represents a cut: $E_e > 10\,\mathrm{GeV}$.

The fundamental elements of the EM electron finding program have been discussed in Sec. 4.5. The EM provided several variables which are useful in extracting the NC signal.

- **EM Probability**. Among the typically few electron candidates reconstructed, only the one of highest EM Grand Probability was considered. It was required that this 'probability' was greater than 10^{-3}.

- **Positron energy**. The corrected energy of the outgoing lepton E'_e was required to be greater than $10\,\mathrm{GeV}$. This requirement allows to remove the photoproduction background coming from neutral pions decaying into two photons that are not spatially separated [57], and hence faking the electron signature. The reconstructed positron energy after all cuts except for $E'_e > 10\,\mathrm{GeV}$ is depicted in Fig. 5.12.

- **Matched track**. The fact that the EM uses not only the CAL input, but also the tracking information renders this algorithm superior for the electrons found in the BCAL (and hence the high-Q^2 events) over its competitor SINISTRA [150]. Therefore a track was required to be matched by the EM program to the electron candidate cluster, if the polar angle of that cluster was found within the acceptance of the CTD[3]. It was also required that the

---

[3] If the polar angle of the candidate satisfies $0.3 < \theta_e < 2.85$, the electron is considered to be found within the CTD acceptance [146].

momentum of this track P'_e was greater than 3 GeV (to enhance the purity), and that the distance of closest approach (DCA) between the track and the electron cluster center was smaller than 10 cm (to reject events where a photon shower is seen as the electron cluster [148]). As the energy measurements close to the calorimeter module-edges might not be reliable, also events with the extrapolated positron track within the distance of 1.5 cm to a module edge (DME) were rejected. It is worth mentioning, that the tracking reconstruction provides the most accurate measurement of the position of the scattered electron hitting the CAL (in θ, ϕ, x_e, y_e, see Fig. 5.13). Therefore, within the acceptance of the CTD, the scattered-positron track coordinates and angles were used, contrary to the situation when the lepton was found outside of the CTD acceptance and the CAL cluster based coordinates were assigned to the e^+ candidate.

- **Isolation**. Typically, the scattered leptons hitting the CAL should be well isolated from the hadronic jets. Therefore, the energy measured by the calorimeter in a cone around the electron-candidate position, but not assigned to the electron cluster was demanded to be smaller than 5 GeV. This cone was defined by $R_{cone} = \sqrt{(\Delta\phi)^2 + (\Delta\eta)^2} < 0.8$, where ϕ is the azimuthal angle around the trajectory of the scattered electron candidate and $\eta = -\ln(\tan(\theta/2))$ is the pseudo-rapidity, defined by the electron polar angle θ.

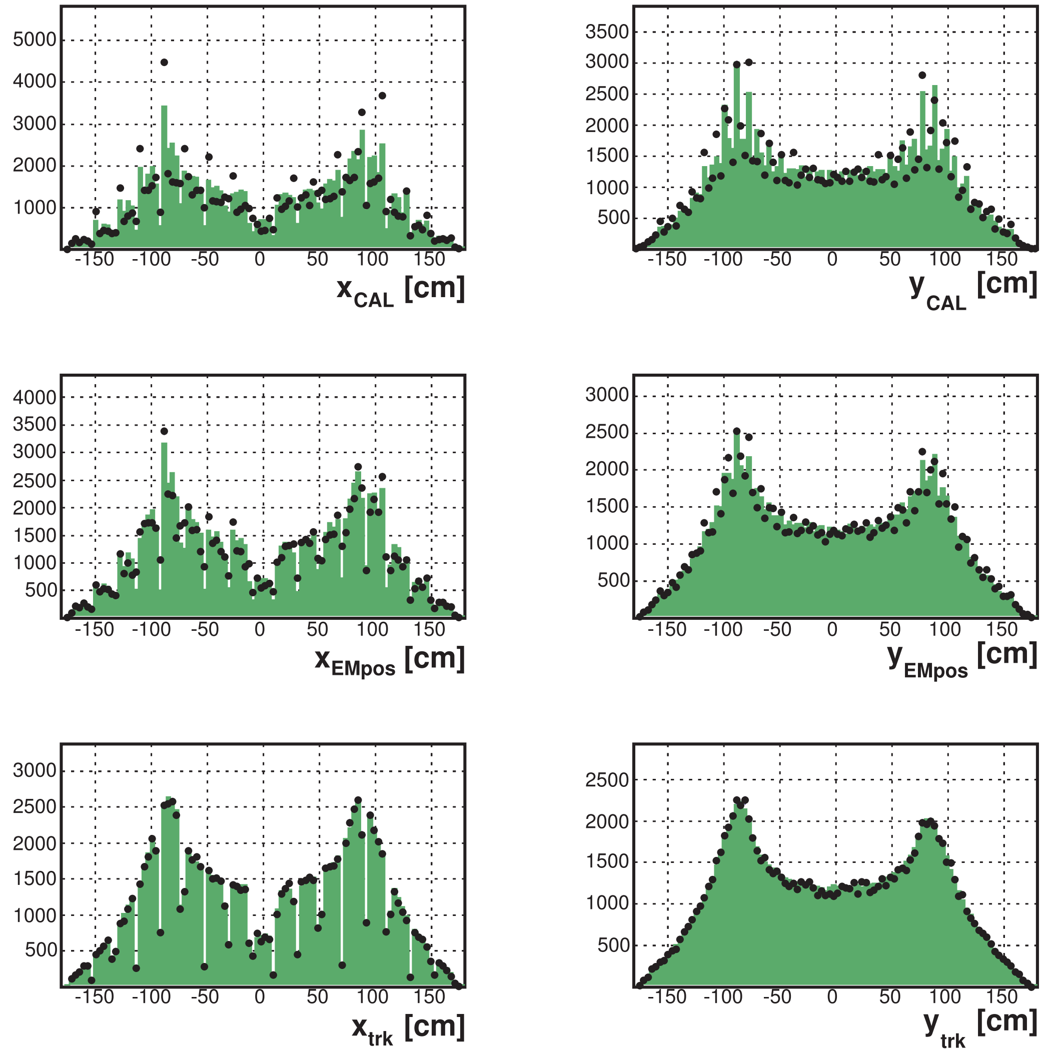

Figure 5.13: Comparison of the accuracy of the simulation for the three available methods of reconstructing the scattered positron position in the RCAL. x_e, y_e, reconstructed with the CAL algorithm only (top row), combining CAL, SRTD and HES algorithms (middle row) and using extrapolated track position whenever possible (bottom row). SRTD was a rear tracking detector placed in front of the RCAL, extending the tracking range of the tracking system towards large polar angles corresponding to small electron scattering angles. HES, a small-area silicon diode detector, located inside the F/RCAL, at the shower maximum for electrons, was mainly used to separate electrons from hadrons.

5.7.2 Background suppression

After discussing the scattered lepton-based cuts, let us focus on several further ones, which contribute to the satisfactory final level of purity of the selected NC sample.

- **Total $\boldsymbol{E - P_Z}$.** As already discussed in Sec. 5.1, the total $E - P_Z$ should peak around 55 GeV for a fully reconstructed NC event. Moreover, particles escaping through the rear beam-hole reduce this quantity by two times their energy, and those escaping through the forward beam-hole don't change the total $E - P_Z$. Finally, overlaid events are characterized by a high value of that quantity. Therefore in this analysis it was required that $38 < E - P_Z < 65$ GeV [160]. See Fig. 5.14 for a plot of the variable and the cuts.

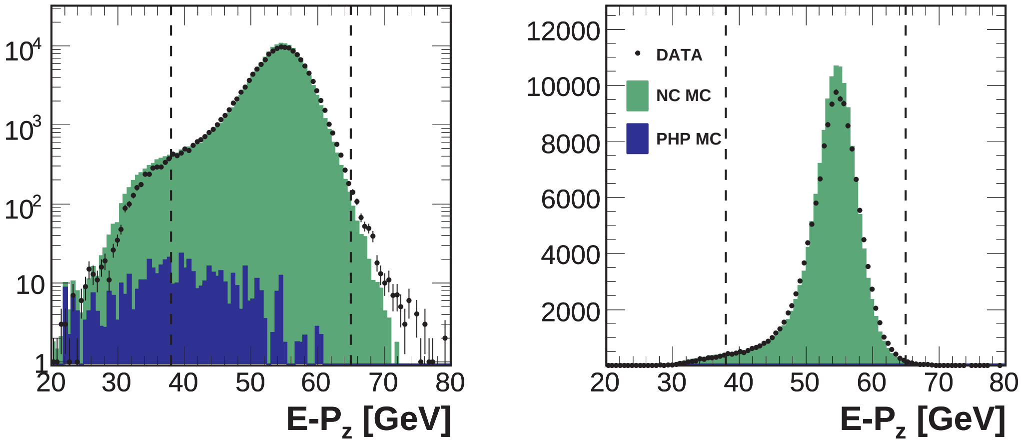

Figure 5.14: Reconstructed $E - P_Z$ with lower and upper cuts superimposed as dashed lines.

- $\boldsymbol{y_{EL}}$. In a situation of a photoproduction event with no scattered $e^{\pm}$ detected, di-photons coming from the decay of neutral pions could fake the electron signal in the CAL. This occurs mainly in the FCAL (so at low θ polar angle), where the tracking information cannot be used to complement the electron finder. Additionally, since the photons have typically low energy, a cut of $y_{EL} < 0.95$ (see Eq. 4.10) is useful in suppressing this type of background (see Fig. 5.15).

- **Elastic QEDC**. As explained in Sec. 5.2.5, while the non-elastic QED Compton scattering is well modelled in the MC, the elastic process is not, and

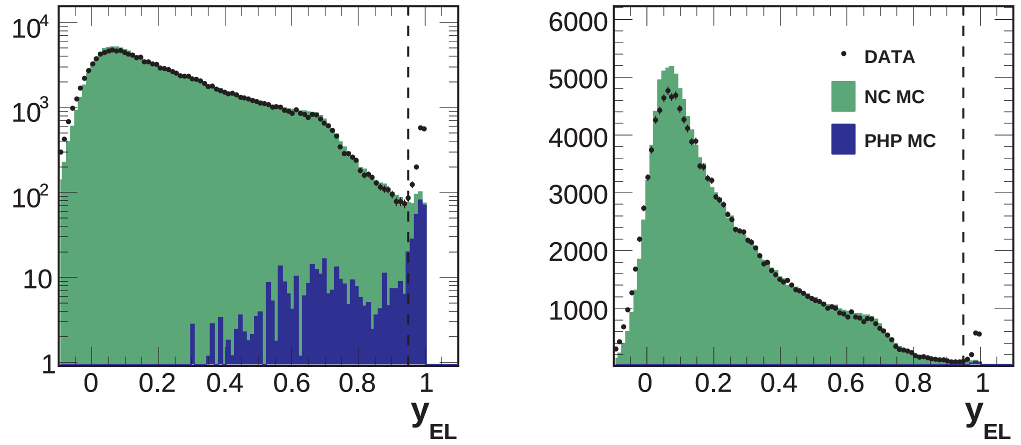

Figure 5.15: Plot of inelasticity, using the electron reconstruction method, with the upper cut superimposed.

therefore needs to be rejected from the final signal sample. It was performed using its clean topology, namely searching for two back-to-back positioned electron candidates, with ratio of their transverse momenta within $0.8 - 1.2$, and almost the full energy reconstructed in the calorimeter assigned to these candidates (one of them being a high-energy photon, while the other one the scattered positron) [138].

- $\boldsymbol{P_T}$ **and** $\boldsymbol{E_T}$. For a perfectly reconstructed NC event, the total transverse momentum (Eq. 4.6) should be equal to $0\,\mathrm{GeV}$. However, in the ZEUS calorimeter, the resolution of the measurement of P_T is proportional to $\sqrt{E_T}$, and therefore these two cuts were applied: $P_T/E_T < 0.7$ and $P_T/\sqrt{E_T} < 4\sqrt{\mathrm{GeV}}$. Previous studies have shown [148], that events from beyond these limits are not described by the MC (e.g. cosmic muons that survived the timing cuts on the trigger level or beam-originating background).

5.7.3 Geometrical cuts on positron position

In particular regions of the calorimeter, the identification of the positron and the simulation of its showers becomes difficult due to their geometrical complexity. These places were removed using the so called *fiducial* cuts, which were applied using both the position of the scattered positron reconstructed by the calorimeter algorithms, as well as position of a matched positron track extrapolated onto the CAL surface.

- **Super-cracks**. The two spaces between the three major parts of the calorimeter are called *super-cracks*. It is typical, that a scattered electron moving towards one of them pre-showered in the BCAL but did not get fully absorbed within it, and also penetrated the RCAL or FCAL. The detector simulation is known not to model such events accurately enough, and therefore they were removed by rejecting events with the following longitudinal positions (in the CAL) of the scattered lepton: $-104.0 < z_{e^+} < -98.5\,\mathrm{cm}$ and $164.0 < z_{e^+} < 174.0\,\mathrm{cm}$.

- **RCAL radius of e^+ position**. The outer ring of the RCAL was screened by the barrel calorimeter. The detector simulation of the trigger acceptance of that region has been known to be also quite unsatisfactory [160], and therefore events with scattered electrons flying into the RCAL ring of radius greater than 175 cm were rejected.

- **RCAL chimney**. To make room for the cryogenic pipes of the superconducting coil of the ZEUS detector, some EMC cells could not be mounted in the upper half of the RCAL central module [92]. Moreover the pipes partially covered this narrow area. In order to avoid problems with simulating this structure (see Fig. 5.16), events with the positron flying in the direction of the RCAL chimney were rejected if their position was found within: $|x_{e^+}| < 12\,\mathrm{cm}$ and $y_{e^+} > 80\,\mathrm{cm}$.

5.7.4 Other cuts

- **Monte Carlo validity**. The DJANGOH/ARIADNE Monte Carlo program fails to simulate the signal in a small kinematic space region of very low y and high x [181]. Hence, a cut on $y_{JB}(1 - x_{DA})^2 > 0.004$ was applied in order not to introduce artificial migrations between bins.

- **Longitudinal vertex position**. Though the *ep* interactions do happen along the full length of the tracking devices, their spatial distribution peaks

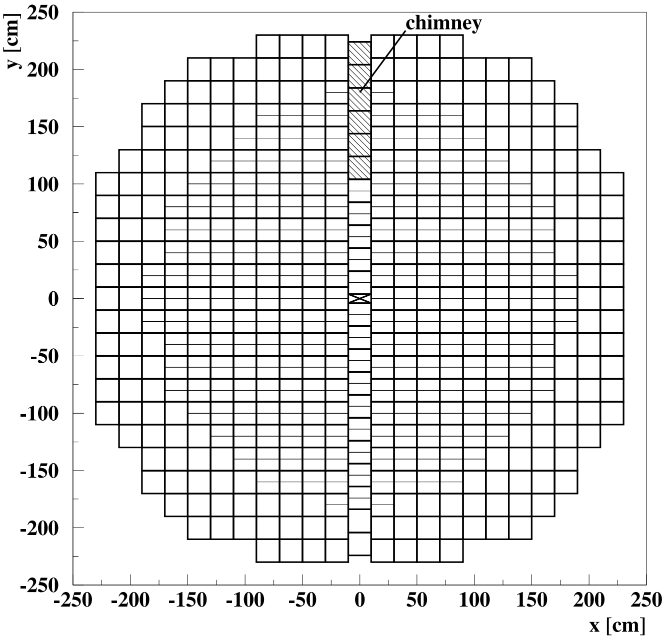

Figure 5.16: RCAL structure, with the area of the chimney marked. The thicker lines mark the towers, while the thinner lines display cell boundaries [57].

around $z = 0\,\text{cm}$ [160]. The longitudinal interaction point Z_{VTX}, being reconstructed by the fit of the reconstructed tracks is best understood in the neighborhood of the nominal interaction point [173]. Therefore a cut on the absolute value of this quantity is applied $|Z_{VTX}| < 30\,\text{cm}$, in order to only use the events well modelled by the MC (see Fig. 5.7.4).

- **Projection of γ_{had} onto FCAL**. Previous studies [57, 148] have proven the simulation of the hadronic activity around the forward beam-hole to be imperfect. While, for most events this effect is not significant (in terms of the reconstructed kinematic variables), it could bias the measurement of the hadronic polar angle γ_{had}, for events with very forward-aimed jets. Such events were therefore removed by applying a cut on the radius of the projection of the hadronic angle γ_{had}: $R^{FCAL}_{\gamma_{had}} < 18\,\text{cm}$.

- **Lower Q^2 limit**. Previous ZEUS NC analyses were divided into low- and high-Q^2 categories, both of which used slightly different analysis techniques. These findings delivered an input to the PDF fits [182] and in case of this analysis, the approximate kinematic boundaries and binning were taken over from [183] in order to obtain coherent results. Hence the lower limit (in Q^2) on the kinematic phase space was set to $Q^2_{DA} > 185\,\text{GeV}^2$, see Fig. 5.18.

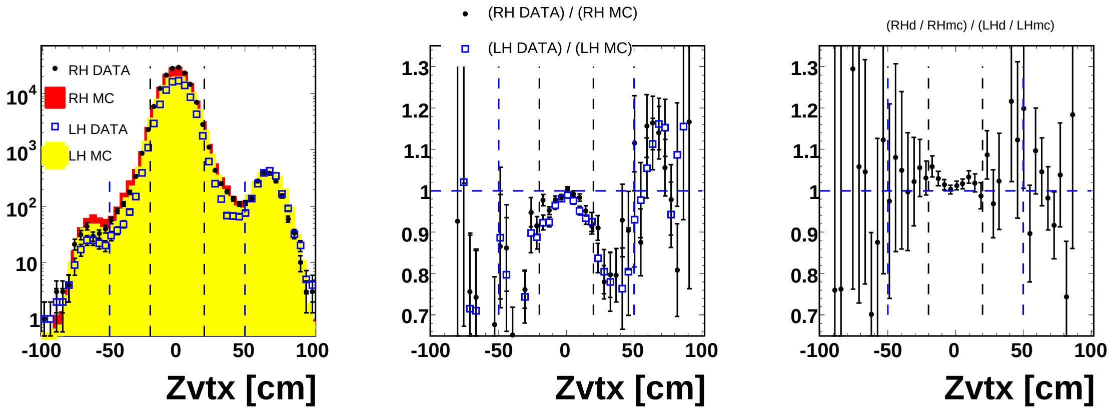

Figure 5.17: Comparison of data and MC samples for RH and LH samples, defined in Section 5.8, (normalized to the same luminosity) in function of the longitudinal vertex position, depicted as histograms on the logarithmic vertical scale (left), single-ratios $(DATA_{RH}/MC_{RH})$ and $(DATA_{LH}/MC_{LH})$ (center) and as a double-ratio $(DATA_{RH}/MC_{RH})/(DATA_{LH}/MC_{LH})$ (right).

- **Number of Good Tracks**. The topology of a typical NC event includes an isolated scattered lepton and at least two hadronic jets: the current and the remnant one. Such a final state should produce a few good tracks (at least), with a *good track* fulfilling both of the following criteria:

  - P_T of the track $> 0.2\,\mathrm{GeV}$;
  - the track should penetrate at least three CTD superlayers.

  Since the unusual case when one of these requirements is not satisfied is not well modelled by the simulation, a loose cut on the total number of good tracks was implemented: $N_{goodtracks} > 0$.

- **POLTAKE**. A ZEUS software common function, similar to EVTAKE (see Sec. 5.6.4) called POLTAKE [76] holds information on whether the LPOL or the TPOL polarimeter measurements could be used for a given event. However, while POLTAKE provides event-wise boolean bits, EVTAKE only provides run-wise ones. Therefore, for each event POLTAKE would be queried, and whenever not all events in the run would be accepted by it, the total luminosity of the run would be decreased by the fraction of events for which polarimeters were not available.

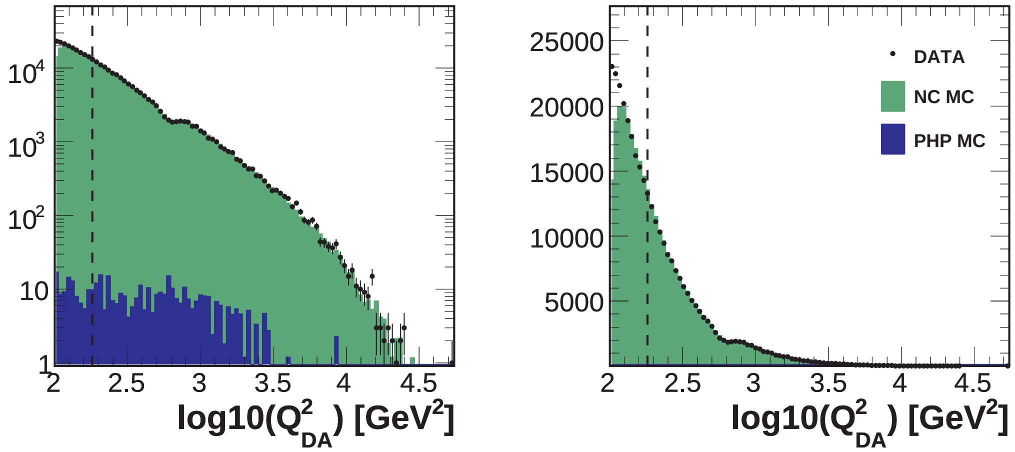

Figure 5.18: Plot of the Q^2_{DA}, with the lower cut of 185 GeV superimposed.

5.8 Final data and MC samples

The final samples of selected data and MC events are presented as functions of various variables in Figures 5.19-5.24. Let us define names with which we shall be referring to the two samples of different polarization of the lepton beam. The sample corresponding to the positive polarization of the positron beam (P_+), recorded between June and December of 2006, will be called *right-handed* (RH). The sample corresponding to the negative polarization of the positron beam (P_-), taken between December 2006 and March 2007, will be referred to as *left-handed* (LH). The process of MC simulation to describe the recorded events and unfold the cross sections is described has been Sec. 5.3.

A luminosity of 70.9 pb^{-1} corresponding to the RH data set, and 42.4 pb^{-1} corresponding to the LH data set was considered in this analysis. The weighted polarization of the RH sample read 0.32, while for the LH sample it read −0.36.

The final RH data sample consisted of 149177 events, the LH one of 85351 events. The MC sample describing the RH data sample consisted of 151619 events, while the one describing the LH data sample had 89522 events. These numbers then render the normalization (defined in Eq. 5.7) to be equal to −1.6% for RH, and −4.6%. The summary of the data and MC samples is given in Tab. 5.4.

Figure 5.19 presents the yield and data polarization as a function of run number. The yield is defined as the ratio of the number of events recorded and the integrated luminosity, for a given luminosity (each point represents ≈ 1 pb^{-1} of data). The flatness of the yield plot represents the quality of the data sample, under the assumption that it only depends on the total cross section of the recorded

	RH sample	LH sample	RH+LH sample
$\mathcal{L}$ [pb^{-1}]	70.9	42.4	113.3
P	0.32	-0.36	0.07
N_{DATA}	149177	85351	234528
N_{MC}	151619	89522	241141
$Norm.$ [%]	-1.6	-4.6	-2.7

Table 5.4: Summary of the final data and MC samples. The consecutive rows contain: the integrated luminosity ($\mathcal{L}$), polarization (P), number of data (N_{DATA}) and MC (N_{MC}) events, and data/MC normalization ($Norm.$) of each sample.

data sample. Within the statistical uncertainties, the recorded data was stable and well under control. The polarization on the other hand, is plotted for each accepted run separately. The yield plot and its comparison to the expectation from theory is further discussed in Chapter 6.

Figure 5.20 shows scatter plots of the reconstructed data events that passed all selection requirements in the $x - Q^2$ and $x - y$ plane, with several lines of constant y, θ_e, Q^2 and the MC validity cut superimposed.

The quality of the MC description of the recorded data sample is also presented in Fig. 5.21-5.22 in function of all the variables used for analysis cuts. The points represent the data of both the RH and LH samples, while shaded histograms depict the signal and background MC samples. The left-column histograms are plotted using logarithmic vertical axes, while the right-column ones have linear vertical axes. The detailed description, against which variables these histograms are plotted, is given in captions of the plots. The quality of the MC description of the recorded data sample is satisfactory and allows to proceed to the cross section unfolding procedure (Ch. 7).

Figure 5.23 presents the comparison of the full RH+LH data sample with the MCs in functions of Q^2_{DA}, x_{DA} and y_{DA} (these variables were later used for the cross section unfolding procedure). The left-column presents the comparison of the histograms using the logarithmic vertical axis, the middle-column using the linear vertical axis, while the right-column presents a data/MC ratio. We conclude, that within the statistical uncertainties (the systematic uncertainties will be presented in Ch. 7) the data is well described by the MC.

Finally, Figure 5.24 presents the kinematics of the recorded data samples and the MC, separately for the RH and the LH sets. The comparison of data and MC histograms, using the linear vertical axis is presented in the left column. The middle column shows single-ratio of data/MC, separately for RH and LH samples. The

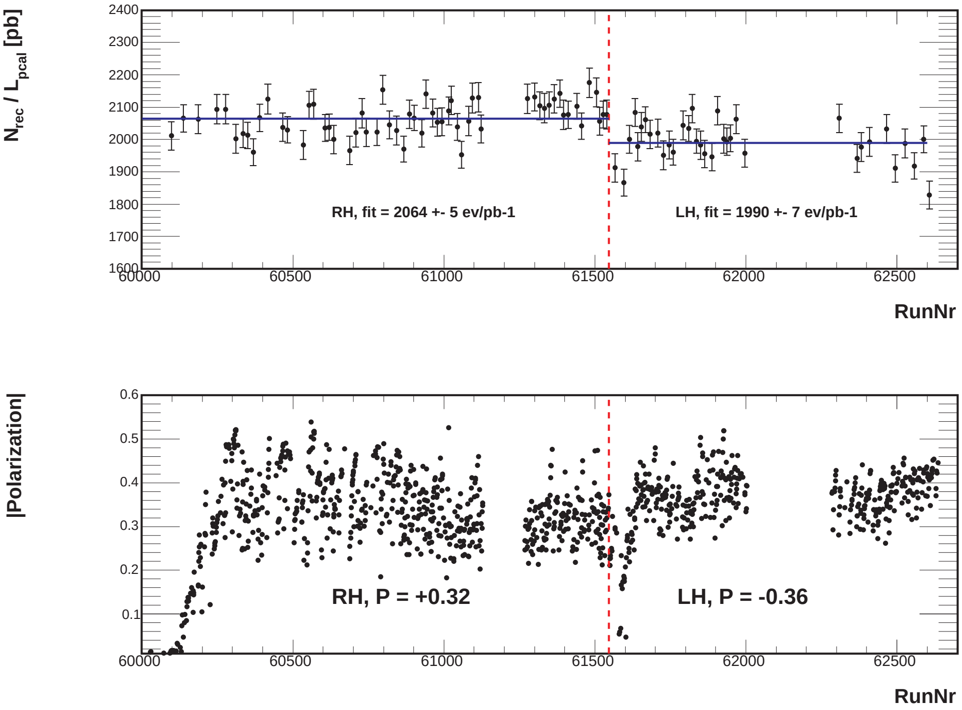

Figure 5.19: The yield of data (upper) and polarization of the lepton beam corresponding to a given run (lower), as functions of the run number. Each point in the yield plot corresponds to $\approx 1\,\mathrm{pb}^{-1}$, the error bars represent statistic uncertainties.

right-column, on the other hand, depicts a comparison of the MC description for RH and LH samples, as a double-ratio: $(DATA_{RH}/MC_{RH})/(DATA_{LH}/MC_{LH})$. While the quality of the MC description of the RH sample is very good, one may notice that the double-ratio in function of Q^2 (Fig. 5.24(c)) deviates from 1.0 by up to 10%. Many detailed and lengthy studies have been performed in order to understand this behavior of the LH data (Chapter 6 is devoted entirely to this topic) and the best observed description of this data set is presented in Figure 5.24. Despite of these small local imperfections of the description of the LH data sample, the quality of the data understanding is concluded to be satisfactory, and the cross section unfolding procedure and results are presented in Chapter 7.

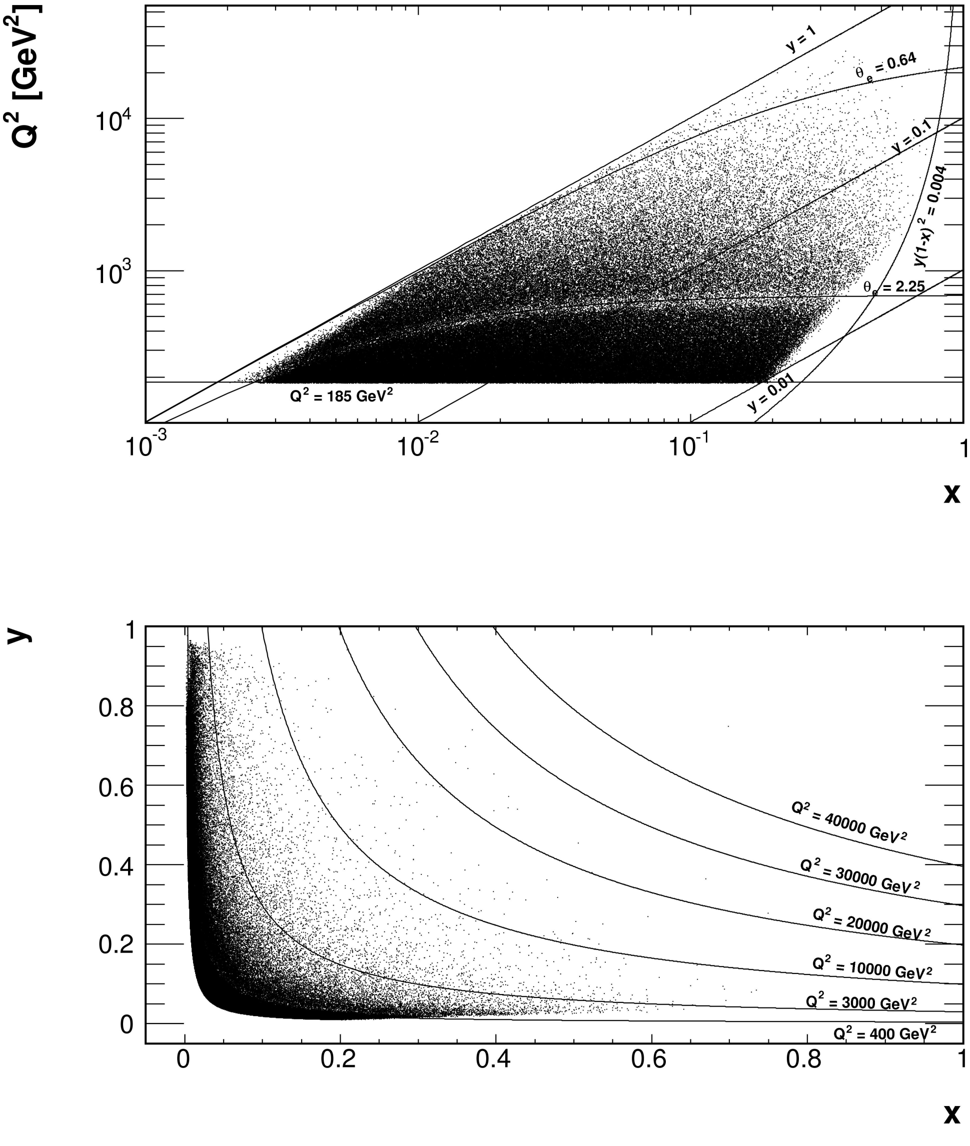

Figure 5.20: Scatter plot of reconstructed data events after all selection cuts in the $x - Q^2$ (top) and $x - y$ (bottom) plane. Also shown are example lines of constant y, θ_e, Q^2 and the MC validity cut.

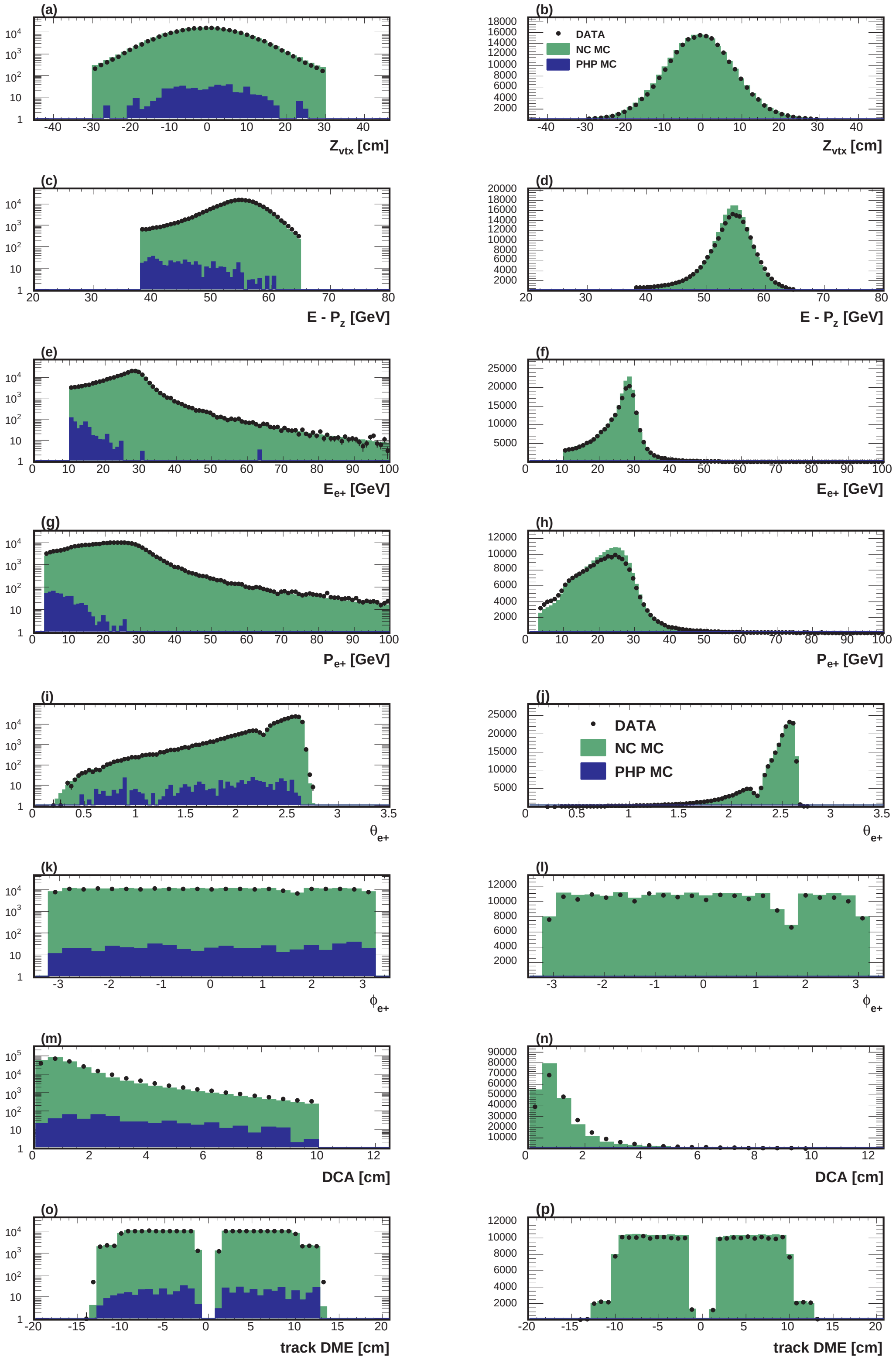

Figure 5.21: Control histograms of the final data and MC samples plotted against variables used in the selection procedure: longitudinal vertex position Z_{VTX} (a,b), total $E - P_Z$ (c,d), scattered lepton energy E'_e (e,f), momentum of the scattered e^+ track P_e (g,h), e^+ polar angle θ_e (i,j), e^+ azimuthal angle ϕ_e (k,l), DCA between the track and the e^+ cluster (m,n), and the e^+ track DME (o,p).

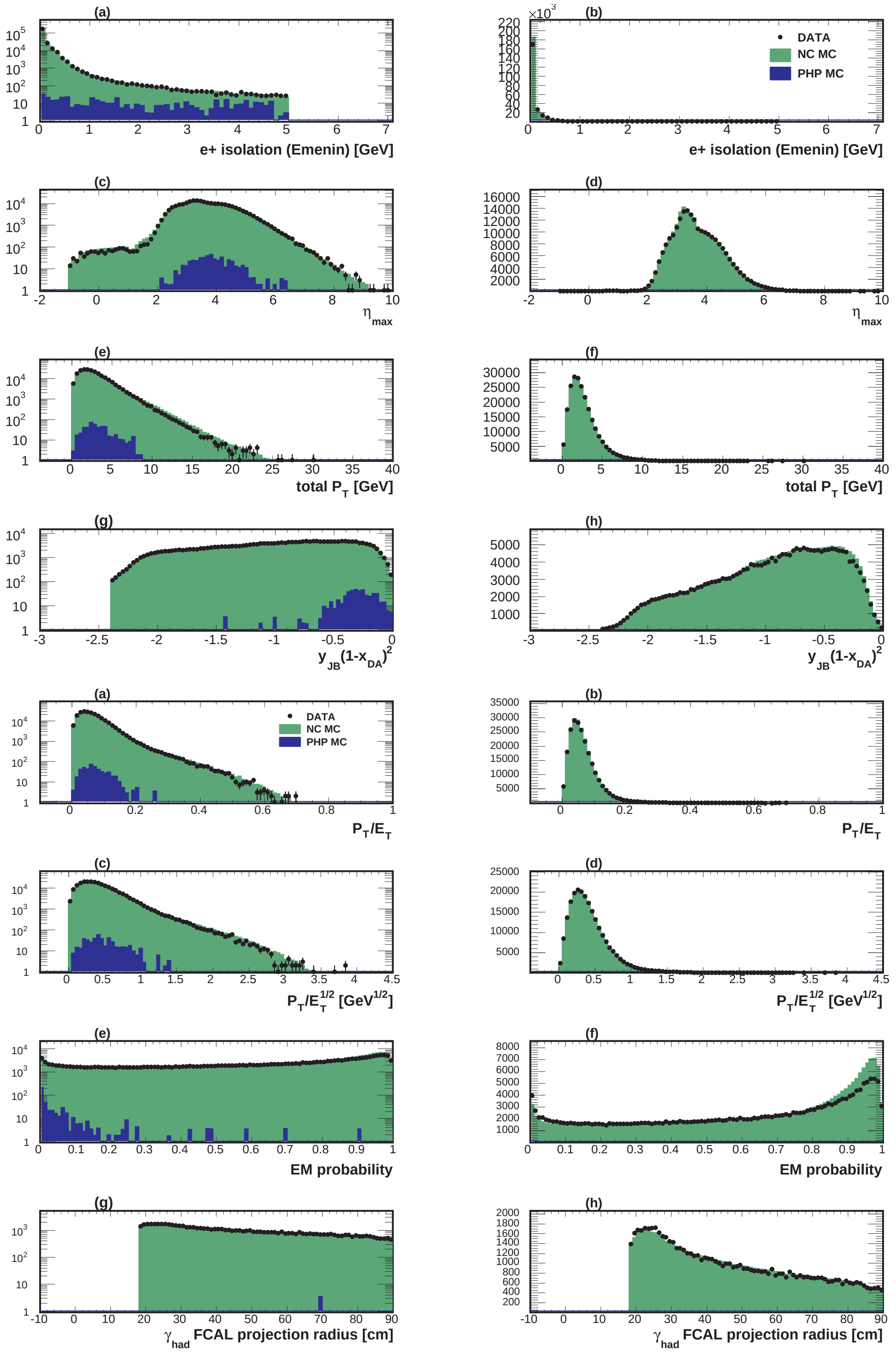

Figure 5.22: Control histograms of the final data samples plotted against variables used in the selection procedure: the e^+ cluster isolation (upper a,b), η_{max} (upper c,d), total P_T (upper e,f), MC validity variable (upper g,h), total P_T/E_T (lower a,b), total $P_T/\sqrt{E_T}$ (lower c,d), EM probability (lower e,f), FCAL projection of γ_{had} (lower g,h).

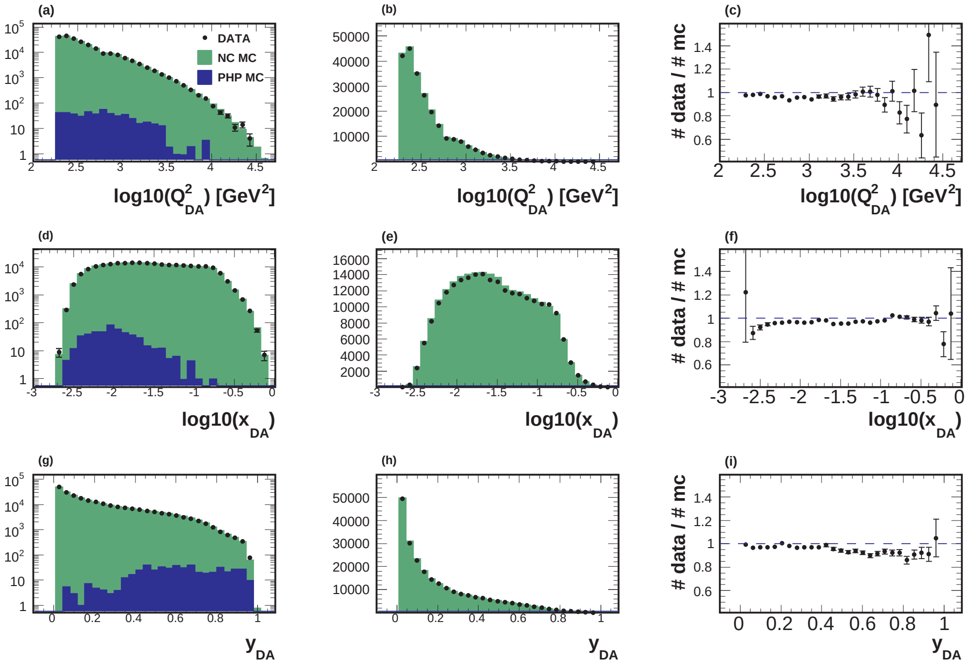

Figure 5.23: Control histograms of the final data samples plotted against kinematic DA variables, for the combined RH+LH samples and MC. The left-column presents the comparison of the histograms using the logarithmic vertical axis, the middle-column using the linear vertical axis, while the right-column presents a data/MC ratio

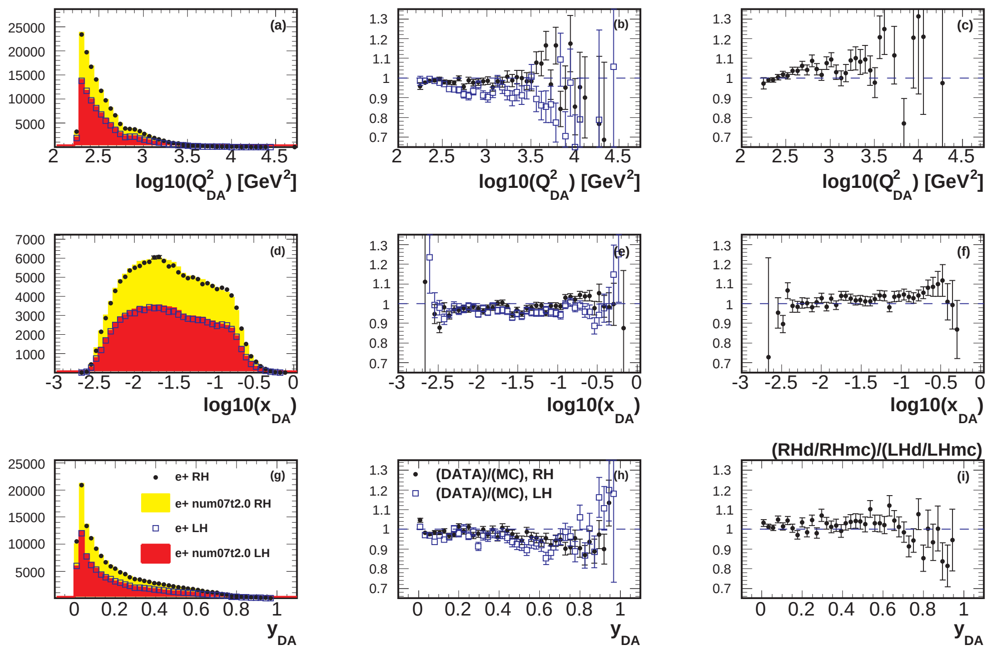

Figure 5.24: Control plots of the final data samples plotted against kinematic DA variables, for RH and LH samples separately and MC. Histograms with the linear vertical axis are presented in the left column. The middle column shows single-ratio of data/MC. The right-column shows the double-ratio: $(DATA_{RH}/MC_{RH})/(DATA_{LH}/MC_{LH})$.

Chapter 6

Systematic studies

While several of the important elements of the NC measurement presented in this thesis, have been adopted from previous works (e.g. [43, 138, 146, 148, 151]), one of the key points of the work presented here was a set of tedious studies concentrated on understanding subtle differences between data and MC distributions, particularly pronounced in the shape of the Q^2_{DA} distribution. These differences were first observed in July 2007 [184][1], and delayed making the result public [69] by more than a year. However, after applying the most recent versions of MC and reconstruction software the level of MC description of the data now has achieved the satisfactory level, observed e.g. in previous high-statistics e^-p NC DIS measurement [59], and allowed to proceed to the cross sections measurements (see Ch. 7). Some of the technical studies investigating these issues are discussed in the following sections.

6.1 Introduction

Let us first define the problem at hand. Having two data samples (RH and LH, defined in Sec. 5.8), it was observed that while the kinematic variables of the RH sample were well described by the MC, the description of the LH sample was inferior. The case was particularly pronounced in the plot of Q^2_{DA}, depicted in Fig. 6.1, in which the region of roughly $250 < Q^2_{DA} < 1200\,\mathrm{GeV}^2$ of the LH sample contained too little data w.r.t. to the MC. Since the same set of MC files had been used to describe both the RH and the LH sample (being suitably re-weighted to both samples' special conditions like polarization, luminosity or Z_{VTX}), it became obvious that the issue was rather on the side of the data than the simulation. Additionally, studying the behavior of the yield plot (see Fig. 6.1,), it was noticed

---

[1] Most of references in this chapter lead to unpublished talks available only to ZEUS members and are listed here in case more information is required by an insider reader.

that a drop of the event rate accompanying the polarization switch (from positive to negative polarization) happened to be larger than expected. Given the measured polarizations, the theory predicts a decrease of the total cross section (for $Q^2 > 185\,\mathrm{GeV}^2$) of 2.25% [185], while the (RH/LH) ratio of the straight-line fits to the data amounted to 4.5% [186].

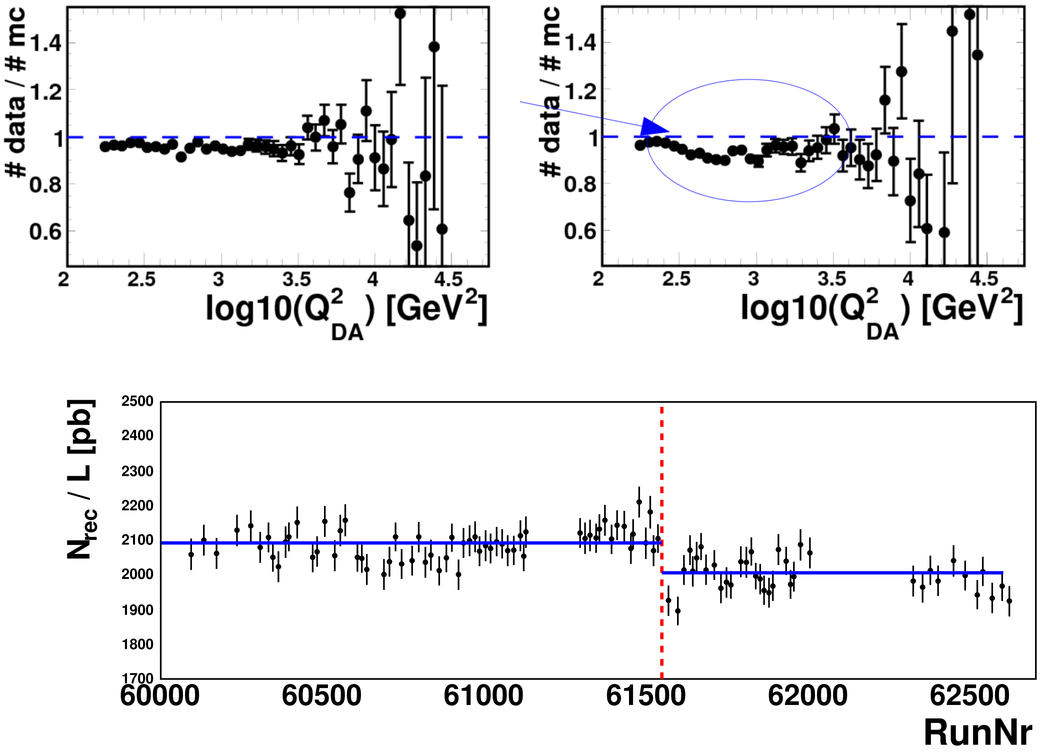

Figure 6.1: Distributions of Q^2_{DA} for RH and LH samples (on the top left and right, respectively). The problematic region of the LH distribution is highlighted with an arrow. Lower plot presents the data yield in bins of $1\,\mathrm{pb}^{-1}$. Runs [60005,61546] contain the RH sample, while runs [61547,62000] contain the LH sample.

6.1.1 Geometrical and kinematic dependencies

Among several possible sources of such a discrepancy which were considered, let us focus on the geometrical dependencies first. According to Eq. 4.16, Q^2_{DA} is defined by polar angles of the scattered lepton and of the hadronic final state. Since the LH discrepancy was limited to roughly $250 < Q^2_{DA} < 1200\,\mathrm{GeV}^2$, a natural assumption was to look for similar effects in the parent distributions which could shed light on e.g. local detector inefficiencies. Such a search, based on comparing the (data/MC) distributions for RH and LH samples separately was performed for the full samples, as well as for subsets of the kinematic space, in particular focusing on the region of $500 < Q^2_{DA} < 700\,\mathrm{GeV}^2$. In order to decouple hypothetic effects coming from different sub-detectors, the search was conducted on the one hand using the positron polar angle reconstructed from the position of the CAL cluster, and on the other hand using the angle based on the positron track. No particular region displaying partial lack of data data was found in any of the inspected regions, and distributions of e.g. θ_e and γ_{had}, depicted in Fig. 6.2 suggest that the problem at hand was rather of a global character (distributed over almost the whole detector geometrical acceptance) than localized.

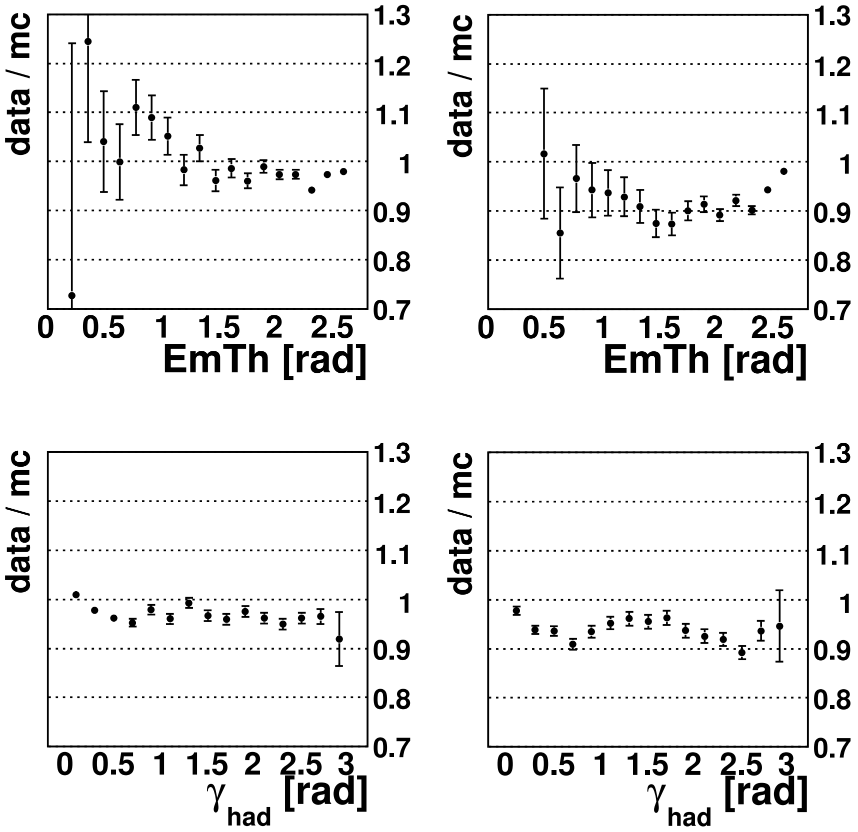

Figure 6.2: (Data/MC) plots of the positron and hadronic final state polar angles for the RH sample (left column) and the LH one (right column). θ_e plotted in the top row, γ_{had} in the lower one.

Additional studies were performed, searching for kinematic and spatial inefficiencies separately in the RCAL and the BCAL. Following the symmetries of the sub-detectors, plots of (x, y) coordinates in the RCAL and (z, ϕ) in the BCAL were of interest. Fig. 6.3 is one example among many which were investigated, displaying the (data/MC)-ratio of positron positions reaching the RCAL for the LH sample. None of such plots could confirm the hypothesis of one of the sub-detectors to be locally inefficient during a part of the LH running period.

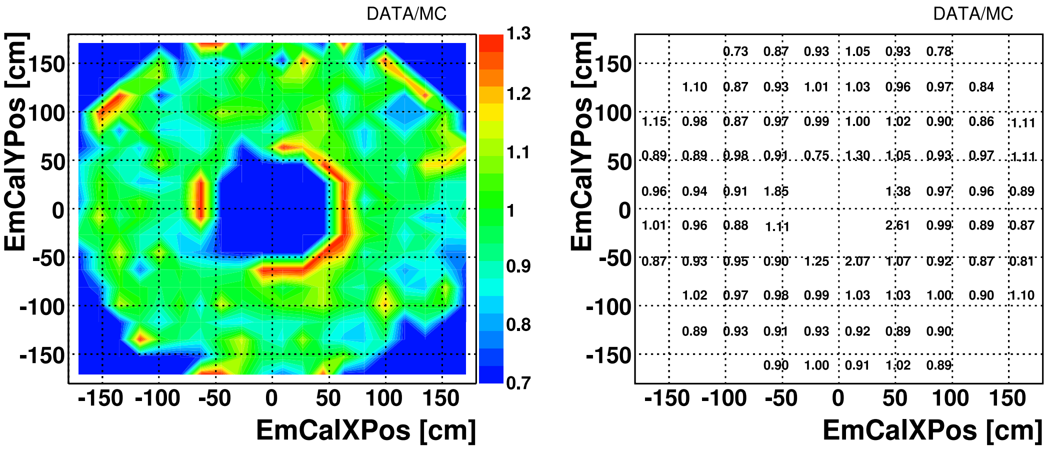

Figure 6.3: (Data/MC) ratio plot of the positions of the scattered positrons in the RCAL for the LH sample, in the color/shade scale on the left and numerical scale on the right (x and y coordinates of the ZEUS reference frame depicted on the horizontal and vertical axis, respectively) .

6.1.2 Other tests

Apart from the checks described above, several others were undertaken to understand the data as well as possible.

- **2004/05/06 electron sample test**. In order to verify the quality of the code implemented to perform selection and plotting in this analysis, the same program was run on the e^-p data set, recorded in years 2004-2006 by ZEUS and on the appropriate MC. No visible deficit was found in this sample, and deviations observed in it were at a level of 2%, while the local deficit in the e^+p sample rose maximally up to 10% [2]. Moreover, the analysis code proved to be able to reproduce the results of the e^-p analysis [137], therefore it was concluded to be free of major bugs.

- **Cut sequence test**. Had it been found, that the application of one particular cut was correlated with the emergence of the LH data discrepancy, it could point towards a detector element or an algorithm responsible. Therefore starting from the pre-selected TLT DIS03 files level, cuts were added in a sequence and the (RH/LH) ratio of the total number of events in each sample was evaluated after each step. The RH and the LH data sample

---

[2] It needs to be stressed however, that at the time when this check was performed, both the e^-p data and MC were in the final re-processed state. Contrary to that, the e^+p data set, being recorded later in time was in the preliminary state, and its final simulation files were not yet available. As is shown in Sec 6.2.3, once the final e^+p MC was generated and the data re-processed, the discrepancy decreased to an acceptable level.

were each normalized to $1\,\mathrm{pb}^{-1}$, and the expectation value provided by theory was 1.025 (see Sec. 6.1). Let us present the mentioned sequence (which will also allow to evaluate the the power of discrimination of signal from background of the cuts discussed), grouping some of the cuts.

Table 6.1 summarizes the results in five steps, starting from TLT DIS03 level.[3] The left column lists the cuts applied at each step, the middle one shows the ratio of the normalized total number of events in the RH and the LH samples. The right column shows an approximate size of the RH sample. $Prob_{EM}$ denotes the cut on the Grand Probability of the EM electron finder. For the description of other cuts see Sec. 5.7.

cuts applied	(RH/LH)	approx. size of the RH sample
TLT DIS03	1.0	4.7 M
$+(E'_e > 10\,\mathrm{GeV})$	0.98	2.7 M
$+(E - P_Z, P_T/E_T, Z_{VTX}, P'_e)$	1.02	600 K
$+(Prob._{EM}, y_{EL}, E'_e$ isolation$)$	1.03	400 K
all cuts applied	1.05	150 K

Table 6.1: Table of sequence of the NC selection cuts. Size of samples indicated in the left column are given in millions of events (M) and thousands of events(K).

The cut sequence test has shown, that no single cut was responsible for the emergence of the LH data vs. MC discrepancy, and that the effect grew step-by-step as the sample got purer.

- **Cut separation test, switch to SINISTRA**. The existence of several reconstruction methods in the ZEUS software environment allowed to use alternatives to the default ones applied in the high-Q^2 NC measurement. In one switch, reconstruction of the hadronic final state was performed with the ZUFO algorithm [152], which not only works on the calorimeter information, but incorporates tracking as well. In another attempt, the EM electron finder was substituted by the SINISTRA program [149] which is based purely on the CAL input. None of these switches altered the Q^2_{DA} distributions significantly. Additionally, investigating the hypothesis that the problem might lie in the tracking part of the selection, all cuts rooted in the tracking variables were switched off, with the same result obtained.

---

[3] The sequence test was also performed on the not yet re-processed data set.

- **Independent pre-selection**. As shown in the previous sections, the code prepared to perform this analysis has come under careful scrutiny. In order to discard the improbable hypothesis of the common zesLite pre-selection tool (see Sec.5.6) being faulty, an independent pre-selection task was run [187] directly on the MDST files (see Sec. 3.2.4) using the EAZE environment (a predecessor of the orange library discussed in Sec. 4.1). The data sample obtained by by this alternative way was found no different to the one selected using zesLite.

Apart from the ones described above, several other scenarios were investigated e.g. checks of history of the ZEUS trigger quality [186] in both e^+p and e^-p data, switching between particular trigger bit combinations in the pre-selection [188], history of the impact of the updates of the reconstruction code on the final NC sample [189] or looking for culprits through studies of the inner EM electron finder variables [186]. None of the tests described or mentioned above pointed at a probable direct reason for the observed difficulty of the available MC to simulate both the RH and LH samples with equal precision. Nevertheless, as it will be shown in Sec. 6.2.3 and in Ch. 7, the level of data understanding achieved allowed for a competitive and precise measurement of the high-Q^2 NC e^+p cross sections.

6.1.3 Cell-by-cell check

Using the re-processed data and corresponding MC samples it was possible to conclude, that the discussed discrepancy between the shape of the Q^2_{DA} distribution and its shape in the MC for the LH sample is limited to the range of approximately $(380, 1200)\,\mathrm{GeV}^2$ (see Fig. 6.4).

Furthermore, having a sample with the discrepancy enhanced, of $Q^2_{DA} > 380\,\mathrm{GeV}^2$, maps of calorimeter cells were studied to investigate the frequency with which they were firing and the energies which they measured [190]. The purpose of this check was to verify the stability of performance of all the CAL cells contributing to the total energy sums, and to evaluate their description in the detector simulation. Therefore, plots displaying single-ratios $(DATA_{RH}/MC_{RH})$ and $(DATA_{LH}/MC_{LH})$, as well as $(DATA_{RH}/MC_{RH})/(DATA_{LH}/MC_{LH})$ double-ratios were investigated for each CAL module. An example of a typical plot of single- and double-ratios is given in Fig. 6.5.

In a situation when the double-ratio plot exhibited a bump, a particular group of cells or a tower would be suspected of malfunctioning (and not being simulated well enough). Scanning plots of both firing frequency and sums of energies for each cell (weighted by the sample luminosity), for all modules in the calorimeter,

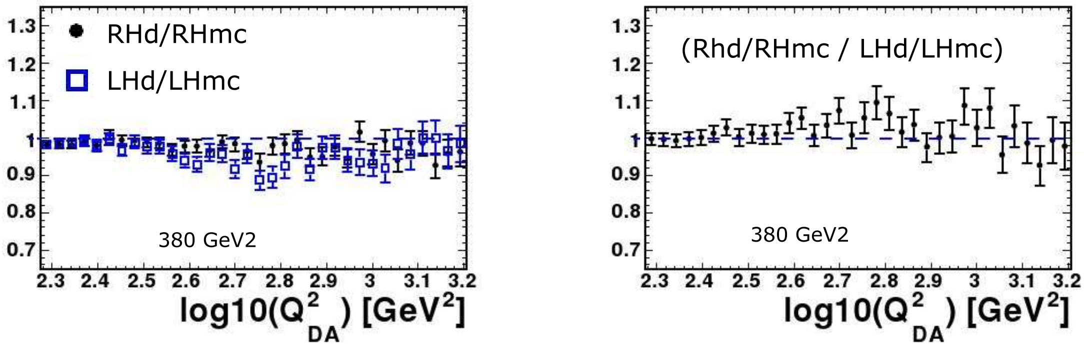

Figure 6.4: Comparison of the Q^2_{DA} distribution of the final RH and LH samples in the middle Q^2_{DA} region. Single-ratios $(DATA_{RH}/MC_{RH})$ and $(DATA_{LH}/MC_{LH})$ on depicted on the left and double-ratio $(DATA_{RH}/MC_{RH})/(DATA_{LH}/MC_{LH})$ on the right.

did not disclose such behavior, with only very few points being more than three standard deviations away from the 1.0 line.

Furthermore, in order to statistically confirm the good cell-by-cell description of the calorimeter, histograms of all the double-ratio values were plotted separately for each section of each CAL part (see Fig. 6.6) and fitted with Gaussian curves. This time an asymmetry of such plots w.r.t. the 1.0 line should point at the region of the calorimeter hypothetically responsible for the discrepancy. It was observed, that for almost all fits, the central values were equal to ~ 1.03, which pointed to a shifted normalization of one of the samples rather than anything else. Moreover, the HAC0 and HAC2 sections of the FCAL contained minor bumps for the double-ratio values $\gtrsim 1.4$. Therefore, to test whether these hadronic cells could bias one of the samples, all HAC0 and HAC2 cells falling outside $\pm 3\sigma$ of the fit central values were removed from data and MC samples, and the full reconstruction and selection chain was repeated. Nevertheless it was found that the Q^2_{DA} distributions of both the RH and LH sample did not change significantly, and therefore concluded that these removed cells could not harm the description of the calorimeter performance in the detector simulation.

6.1.4 Normalization issue

As mentioned in Sec. 6.1, the drop of the event rate accompanying the polarization switch of the e^+ bunch was more than 2% larger than predicted. However, this observation was valid for the not yet re-processed data files. After the re-processing had taken place, in winter of 2007/08, four independent analyses have confirmed

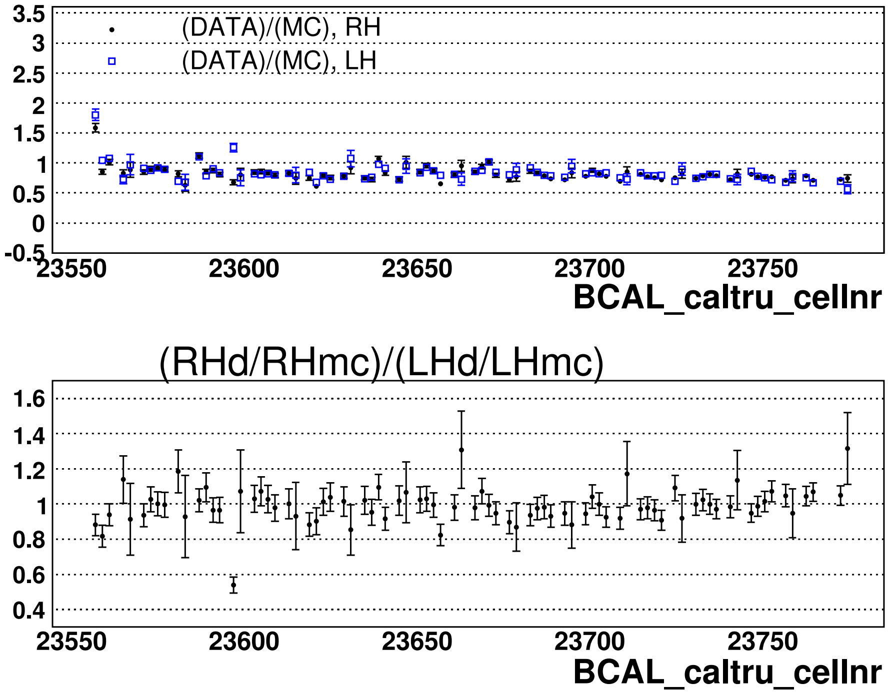

Figure 6.5: Example of a single-ratio [$(DATA_{RH}/MC_{RH})$, $(DATA_{LH}/MC_{LH})$, upper plot] and a double-ratio [$(DATA_{RH}/MC_{RH})/(DATA_{LH}/MC_{LH})$, lower plot] for BCAL module 15 as a function of cell number. The upper plot compares the quality of MC description of each cell firing separately for RH and LH samples. A flat distribution in the lower plot confirms the existence of no major changes in this module performance in one sample w.r.t. to the other.

this finding: the high-Q^2 NC analysis found the event rate drop to be 2.9% too deep w.r.t. the theory prediction and the NC DIS analysis studying the dijet cross section in NC DIS[4] found a similar result of 3.1%. The observation has also been confirmed by a similar analysis of high-E_T dijet production in PHP and by a low statistics analysis of production of D^* mesons in DIS. All these findings [187, 194, 195] suggested a probable normalization problem which could be generated by e.g. an offset in the measurement of the luminosity. At the time when this thesis is being written (Fall 2008), studies of such effects are still in progress [196–198] and the final conclusion has not been reached. Nevertheless we can conclude, that only a fraction of the observed LH sample data vs. MC discrepancy is caused by a real (and not yet understood) inefficiency of the detector, while a possible normalization flaw is responsible for the other part.

---

[4] Analyses mentioned in this section, but the high-Q^2 NC DIS, are successors of previous ones covered in [191–193].

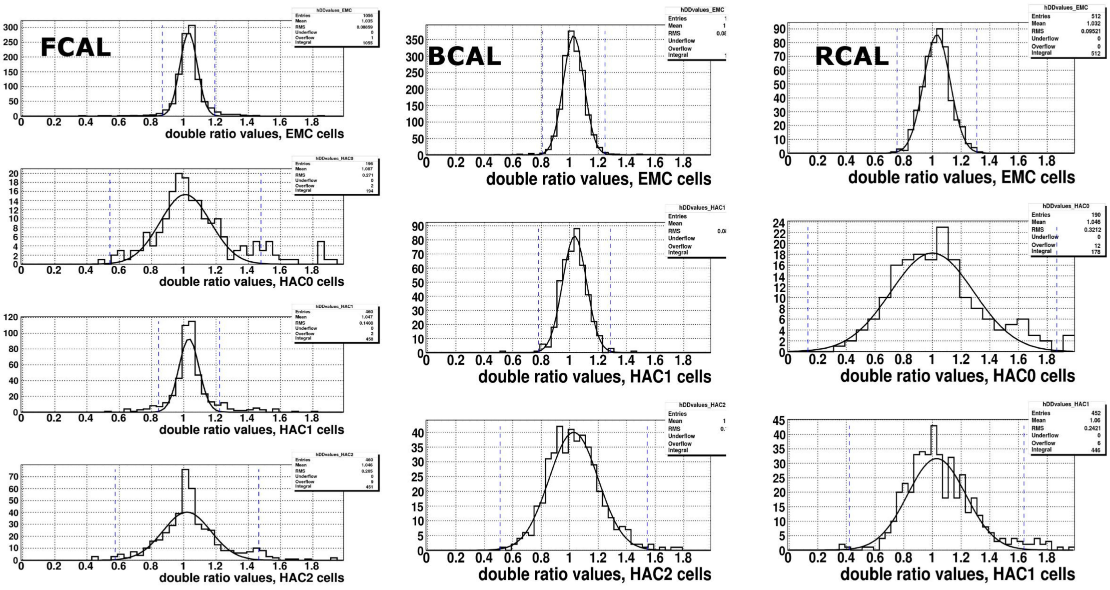

Figure 6.6: Histograms of $(DATA_{RH}/MC_{RH})/(DATA_{LH}/MC_{LH})$ double-ratios plotted separately for the three CAL parts (in three columns) and for each electromagnetic or hadronic section CAL. Curves depict the Gaussian fits, while the blue vertical dashed lines depict the $\pm 3\sigma$ ranges of the fits.

6.2 Trigger studies

Precise understanding of the performance of the trigger system (see Sec. 3.2.4) is one of the most crucial elements of any particle physics measurement based on the method of comparing data events and MC. Let us assume that a different (than the trigger itself) detector component was malfunctioning during the data taking, or was not well understood in the simulation. Still, successful data taking would be possible and offline corrections (performed when the data is already on tape) could cure such a (hypothetical) failure. On the other hand, if a given event does not pass one of the trigger levels it is irreversibly lost. Moreover, all the events of the final sample are passed through the same combination of cuts, which includes the trigger cocktails applied during the data taking (see Sec. 5.6). It is hence important to assure the high quality of the trigger simulation.

The following sections describe studies on the trigger efficiency performed on the e^+p sample under consideration.

6.2.1 FLT efficiencies

To gain a view on the relative power of the particular FLT channels w.r.t. the DIS sample, Fig. 6.7 depicts their total efficiencies for the RH and LH samples e^+p

separately. Each bin (denoting a particular FLT bit) contains a fraction of events w.r.t. the DIS03 TLT pre-selected sample, for which a particular FLT bit fired. Bins of all FLT bits which are included in the trigger chain defined by the DIS03 TLT bit are shaded. For a description of how each of the FLT bits is designed, see Sec. 5.6.1.

As different FLT bits were implemented to focus on DIS events of different topologies and properties, the total efficiencies vary considerably, and bits FLT30, FLT36, FLT41, FLT43 and FLT44 are the most inclusive ones. Moreover, looking for differences between the RH and LH samples, we observe that the total efficiency of the bit FLT30 was lower by more than 7% for the RH sample w.r.t. the LH one. This observation led to investigation of the yields and efficiencies of all the FLT bits involved.

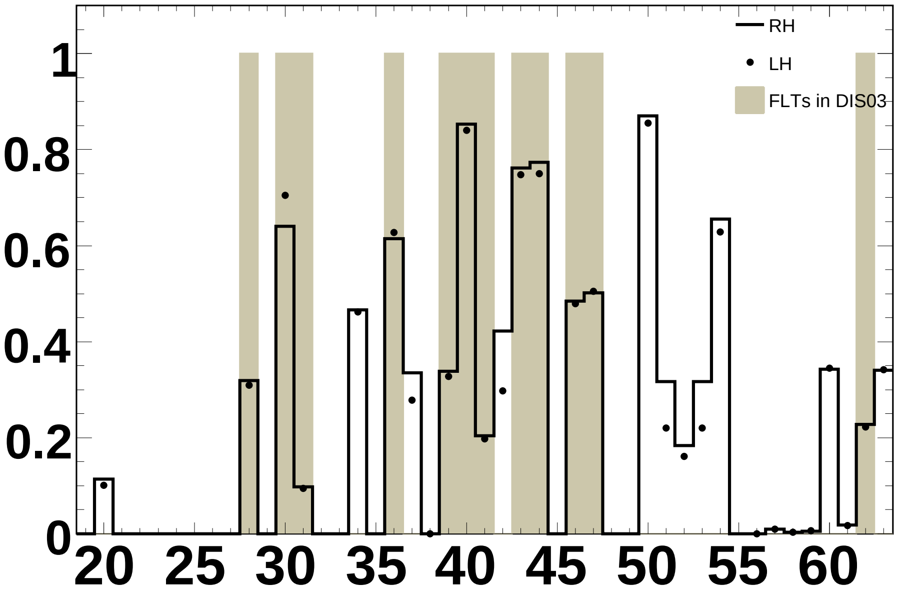

Figure 6.7: Total trigger efficiencies of the RH and LH data samples shown in function of the FLT trigger bit number. The shaded bars indicate which of the FLT bits took part in the DIS03 TLT selection.

FLT30 correction

In order to check the time development of the behavior of the bit FLT30 and others, rates of events accepted by a given trigger bit were studied as a function of run number. Fig. 6.8 depicts the number of events of the final sample accepted by the FLT30 bit. It is clear, that its performance was unstable during a significant

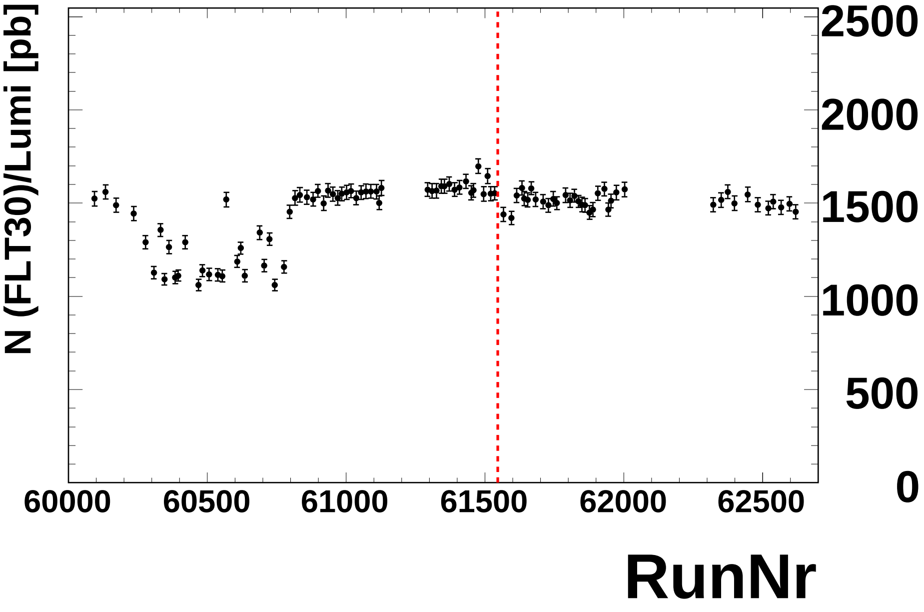

Figure 6.8: Rate of events of the final sample, accepted by the FLT30 bit, shown in function of run number. Each point corresponds to ≈ $1\,\mathrm{pb}^{-1}$ of integrated luminosity.

part of the RH running[5], and it also explains why the FLT30 total efficiency is lower for the RH sample w.r.t. LH one (Fig. 6.7). However, it also means, that the temporary loss of FLT30 efficiency could not explain the LH data vs. MC discrepancy, as it happened in time of the RH running. Yield plots of all other FLT slots have also been inspected and performance of these bits with time was found to be stable.

The ZEUS trigger group has identified the problem of FLT30 already during the RH running and later prepared a correction compensating for the loss of the bit efficiency [199, 200]. The problem was present in the run range of [60226, 60778] and corresponding to the following trigger configurations: STD_060801_HIGH, STD_060801_LOW and STD_060823_HIGH. All FLT bits which included a variable FLT_REMC[6] in their requirements were affected, as in this period it was required that FLT_REMC was greater than infinity (a typical correct implementation yielded FLT_REMC to be greater than 4 GeV.) The correction function was prepared on the basis of rates of other complementary FLT slots, and designed to

---

[5] Let us remind that the RH running period corresponds to runs (60005,61546), while the LH one to (61547,62000).

[6] FLT_REMC variable measured the total energy in the RCAL EMC section, excluding the first ring of towers around the beam-pipe.

be applied on data events which fulfill the following conditions:

- run number from range of [60226,60778];
- FLT30 bit fired;
- DST9 bit fired;
- an EM positron of $E'_e > 8\,\mathrm{GeV}$ found in the RCAL, outside the box cut of $x \in [-31, 29]\,\mathrm{cm}$ and $y \in [-32, 21]\,\mathrm{cm}$;
- total $E - P_Z > 38\,\mathrm{GeV}$.

The function returns the correction factor $[1/(1 - \textit{inefficiency})]$, where the inefficiency is depicted in Fig. 6.9a as a function of $\ln(Q^2)$ and Bjorken y. Fig. 6.9b shows the effect of the correction in function of y. The correction factor is significant for $y >\sim 0.15$ and reaches maximally 6%, which after integration in y amounts to 2% for the considered run range, and 0.5% for the full RH luminosity. It is worth mentioning, that the reason for the correction effect being so small and fully contained within statistical uncertainties of the measurement is the fact that trigger bits had been designed in a compensating manner.

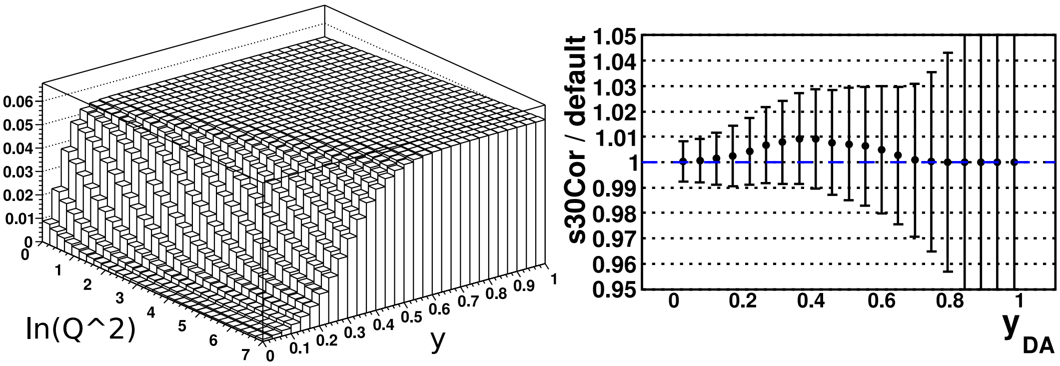

(a) (b)

Figure 6.9: Lego plot (a) of the inefficiency of the FLT30 trigger bit for the run period [60226,60778]. Axis on the left is $\ln(Q^2)$, and on the right Bjorken y [199]. Effect (b) of application of the correction function in function of y. Vertical bars represent statistical uncertainty on the $d\sigma/dy$ cross section measurement.

Closer look at FLT efficiencies

Among the three ZEUS trigger levels, a precise description of the FLT is crucial, as its basic variables are being used throughout the whole system. We have already looked at the stability in time of FLT performance, let us now focus on the quality of the FLT simulation.

The basic concept behind the bit-by-bit trigger efficiency study is to select a so called *unbiased sample*, using FLT variables independent from the bit under study (as much as it is possible). Then, a fraction of such a sample for which also a given bit fired defines its efficiency and is plotted against relevant quantities, both for data and MC [138]. Therefore, a definition of $BIT(x)$ efficiency could be written as:

$$\mathcal{E} = \frac{\textit{No. of events in unbiased sample which fired BIT(x)}}{\textit{No. of events in unbiased sample}}. \tag{6.1}$$

A typical unbiased sample is created using all selection cuts, but only selected FLT bits.

Among several unbiased samples defined for the purpose of this study, two have proven to be suitable best, with trigger combination of the first being $US1 = FLT40+FLT43+FLT44$, and of the other $US2 = FLT28+FLT36+FLT46$ (see Sec. 5.6.1 for bits definitions). Sample US1, being based on inclusive calorimeter energy sums helped to check efficiencies of bits based on identification of isolated electromagnetic cluster (FLT28, FLT30, FLT36, FLT39, FLT46, FLT47). On the other hand, the inclusive bits (FLT40, FLT41, FLT43, FLT44) have been checked against sample US2 [201].

RCAL CFLT inefficiency

When studying the trigger efficiencies, two questions were addressed. Is the RH sample efficiency different from the LH one? And is the efficiency well modelled by the detector simulation?

Plots for bits FLT30 and FLT36 disclosed that for a region of the RCAL defined by a box: $x > 20\,\mathrm{cm}$ and $y < -117\,\mathrm{cm}$, efficiencies of both the RH and the LH data samples were lower than in MC. This situation is depicted in Fig. 6.10, in which we also observe, that for $x > 0\,\mathrm{cm}$ of the RCAL, $\mathcal{E}_{RH}$ was locally lower than $\mathcal{E}_{LH}$. However, the latter problem has been attributed to the incorrect cut on the FLT_REMC variable, and solved as described in Sec 6.2.1.

The former (local RCAL triggering inefficiency for data) was identified by the CFLT group [202] to be caused by a malfunctioning Trigger Encoder Card (TEC) of the Calorimeter First Level Trigger (CFLT) electronics system[7]. Among all signals transmitted through the CFLT hardware, only the ones coming from the

---

[7] CFLT TEC0 card of crate 7 was found to be broken since 2004 until the end of HERA running.

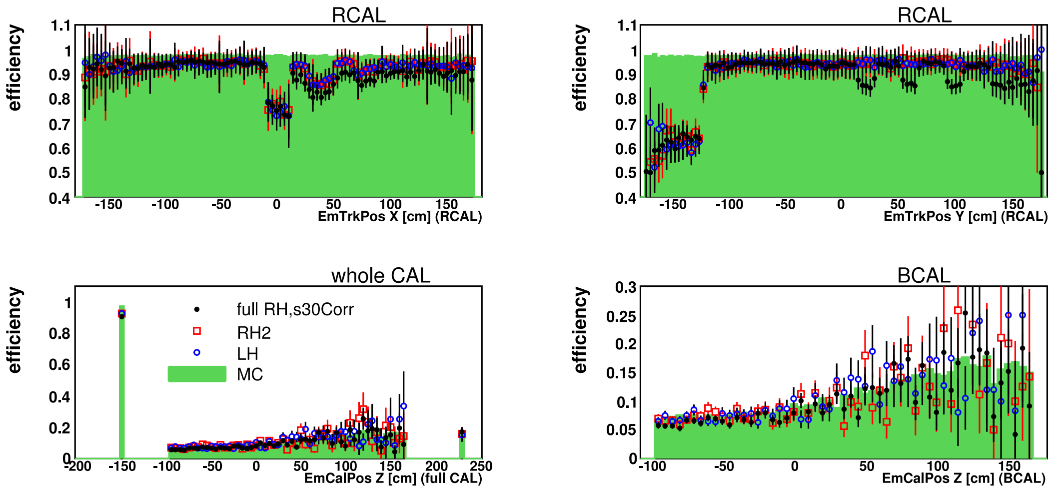

Figure 6.10: Efficiency of bit FLT36 before corrections in function of x_e and y_e (position of the scattered positron) in the RCAL (upper left and right plot), z_e in the full CAL (lower left), z_e only in the BCAL.

EMC section of the RCAL were lost in a region corresponding to the broken card (hence the problem was visible in the lower right region of the RCAL, only when inspecting FLT30 and FLT36 efficiencies). The CFLT group has provided a routine modelling this hardware behavior dedicated for the trigger simulation package (ZGANA) of the ZEUS detector MC. Thanks to that, the CFLT inefficiency will be modelled in the upcoming global release of ZEUS MC (expected to be produced in Spring 2009).

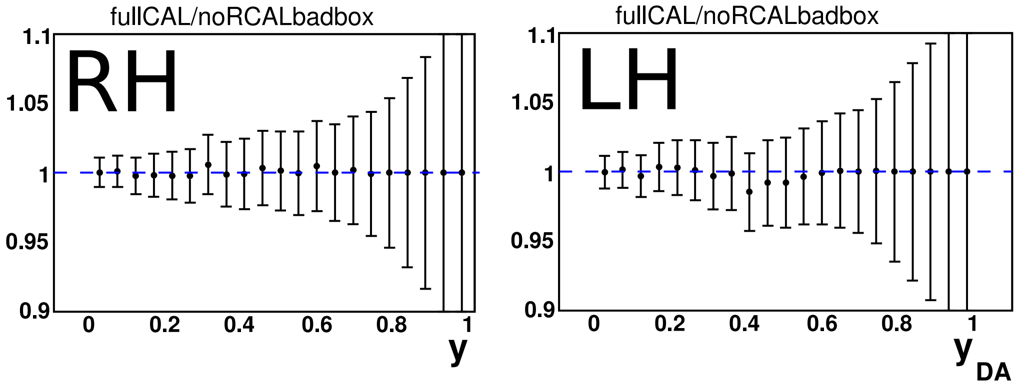

Figure 6.11: Double-ratios $[DATA/MC]_{fullCAL}/[DATA/MC]_{noBADbox}$ plotted for the RH (left) and LH (right) case.

Since at the time of writing of this thesis, the local trigger inefficiency in the RCAL was not known to the available MC release, it was required to verify whether this effect influenced the shape of the final NC data sample and its simulation. In order to do so, two samples were prepared, one - with the whole faulty geometrical

RCAL region excluded, and a second one - with a full standard selection. A double-ratio $[DATA/MC]_{fullCAL}/[DATA/MC]_{noBADbox}$ of both samples is plotted in Fig. 6.11 both for RH and LH case. The influence of the faulty CFLT card was found to be negligible, as other trigger slots (primarily inclusive ones: FLT40, FLT41, FLT43) have accepted events potentially lost by FLT30 and FLT36.

Other FLT bits

Efficiencies of inclusive-energy bits FLT40, FLT41, FLT43 and FLT44 are displayed in Fig. 6.12, for two halves of the RH data sample separately, LH data and MC. They are very well modelled by the detector simulation, with the exception of FLT44 which has lower efficiency in data than in MC. However, both RH and LH data points agree, and FLT44 has lower efficiency in data due to the fact that it also used information from the RCAL-EMC section, which included the inefficiency described in the previous section. Therefore just as in the case of FLT30 and FLT36, the loss of FLT44 efficiency has been compensated by other inclusive slots.

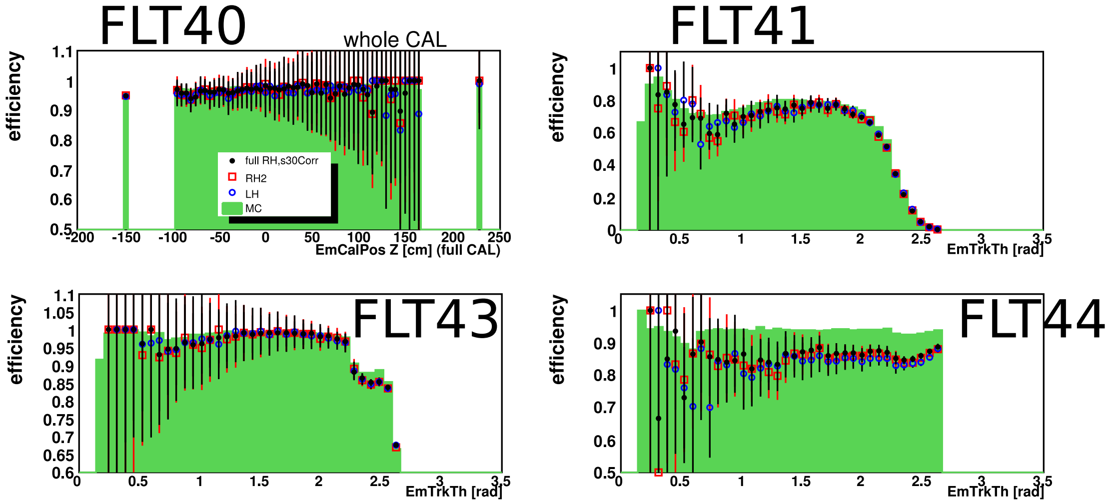

Figure 6.12: Efficiencies of the FLT bits: 40, 41, 43 and 44 in function of z_e for FLT40 and θ_e for the others. Points represent two halves of the RH data (denoted RH1 and RH2), and LH. The shaded histogram represents MC.

Due to inefficiencies in data described in the previous sections, which have been shown to be compensated, in order to check if FLT bits working with isolated EMC clusters as input have their efficiencies described in MC, special samples were required. They were prepared by skipping the RH luminosity corresponding to buggy FLT_REMC cut implementation, and without events with scattered e^+ in the lower-right region of the RCAL. Figure 6.13 depicts the behavior of bits FLT28, FLT30, FLT39, FLT40, FLT46 and FLT47. These plots have been studied

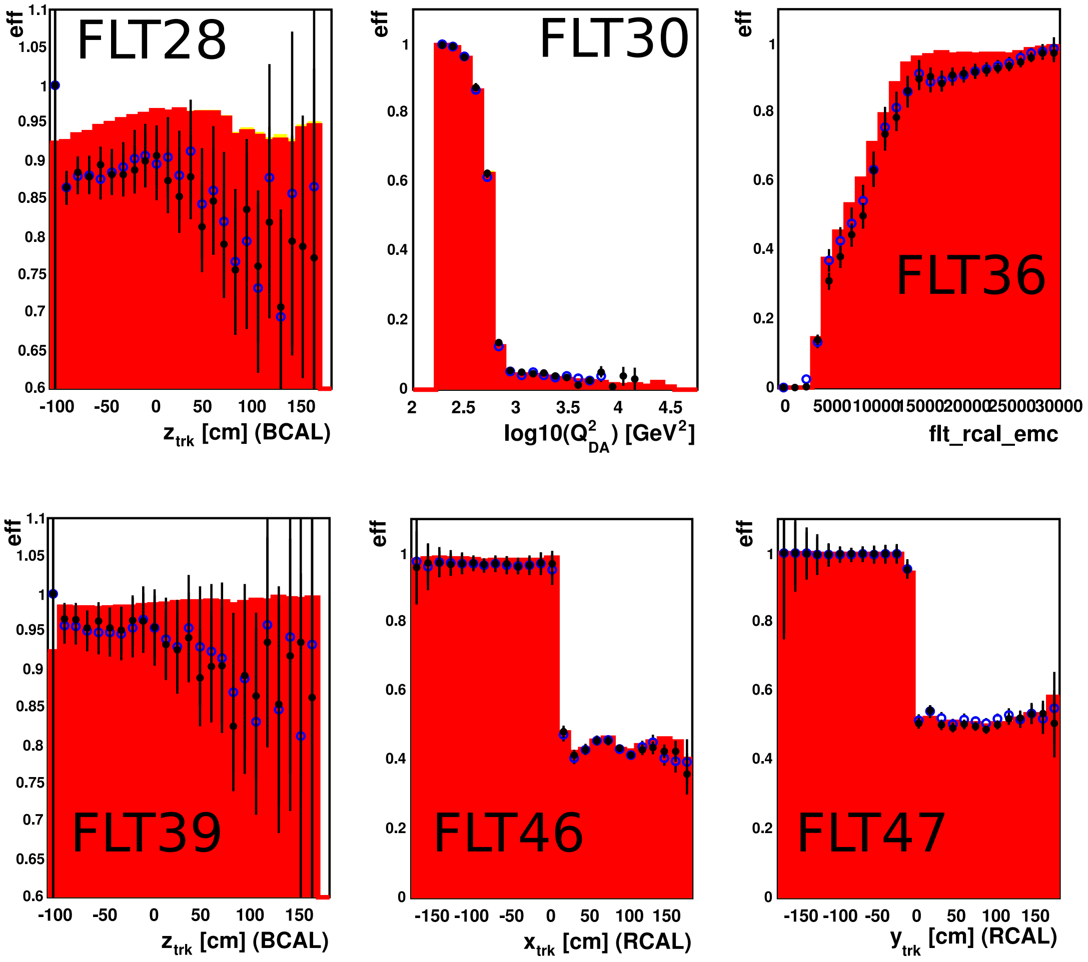

Figure 6.13: Efficiencies of the FLT bits: 28, 30, 36, 39, 46, 47, in function of $z_{e,BCAL}$, $\log(Q^2_{DA})$, FLT_REMC, $z_{e,BCAL}$, $z_{x,RCAL}$ and $z_{y,RCAL}$, respectively. The full points represent RH data, the open ones LH data, and the red histograms represent MC.

in function of many variables, with the ones used here chosen to present various features of the particular FLT bits. FLT28 and FLT39 both disclose a slight inefficiency ascending with $z_{e,BCAL}$ in data, however $\mathcal{E}_{RH}$ equals $\mathcal{E}_{LH}$. FLT36 also shows equal efficiencies in both data samples and lower than the simulated one. All these three cases are then excluded as a possible source of LH data vs. MC discrepancy. FLT30 proves to be very well modelled in the MC, as well as FLT46 and FLT47. The step-shape of the two latter plots is a signature of both trigger slots using just 3 out of 4 RCAL trigger system quadrants. To conclude, all FLT efficiencies are very well simulated, and it has been shown that local flaws of this description do not influence the quality of the final data samples.

6.2.2 SLT and TLT efficiencies

All SLT bits employed in the NC selection have been studied as well. The bits, designed for triggering the middle- and high-Q^2 DIS NC events were checked against an unbiased sample selected by choosing events accepted by SLT slots prepared for triggering exotic processes (requiring e.g. high-E_T). An example of SLT bit DIS02 efficiency is shown in Fig. 6.14 (lower plots), as a function of E'_e and z_e. All SLT bits have equal efficiencies for both RH and LH data samples.

The same method, of creating an unbiased sample by employing other TLT bits, has been used to check the agreement of $\mathcal{E}_{RH}$ against $\mathcal{E}_{LH}$ for TLT bit DIS03, with which the NC sample studied in this thesis has been pre-selected. Fig. 6.14 (upper plots) shows both $\mathcal{E}_{RH}$ and $\mathcal{E}_{LH}$ for this bit as a function of θ_e (left) and ϕ_e (right). In conclusion we see, that all SLT and TLT bits used for this measurement had very stable efficiencies during the 2006/07 e^+p data taking.

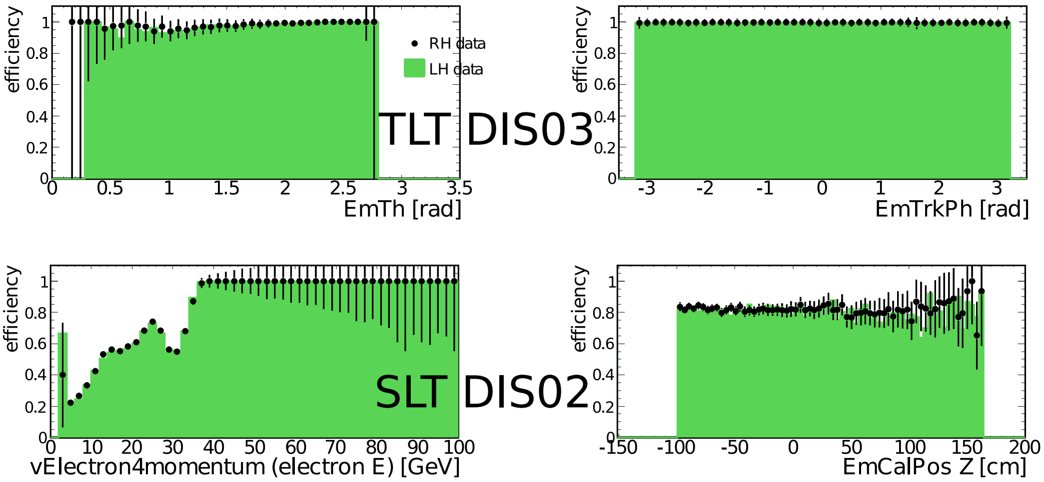

Figure 6.14: Efficiencies of TLT bit DIS03 (upper plots) and SLT bit DIS02 (lower plots). The points represent RH data, while the shaded histograms represent LH data.

6.2.3 Conclusion from the systematic studies

The studies presented in this chapter focused on the issue of imperfect MC description of the LH data sample, particularly pronounced in the Q^2_{DA} distribution. Preceding sections have shown the following:

- no flaw has been recognized when dividing the kinematic plane into slices (geometrically and kinematically);
- the programs used on all levels of the analysis have proven to produce results consistent with previous measurements, when used on older data;

- detector components important to the NC cross section measurement have not disclosed any drawbacks;

- detector simulation of all three levels of the ZEUS trigger system has been found to be very accurate;

- the calorimeter cell-by-cell study of all of its $\sim 12\,000$ channels has confirmed its satisfactory description in the MC;

- the absolute value of the data-vs.-MC normalization of the LH sample has been found to be $\sim 2\%$ different w.r.t. the theory prediction than for the RH one, rendering lower precision of the MC description for the LH case.

None of these thorough checks of each of the measurement elements has shown significant flaws, apart from normalization. As mentioned before, at the time of writing this thesis (Fall 2008), studies concentrated on the ZEUS normalization are still in progress [196, 197] and the final conclusion has not been achieved.

However, two elements allowed for the overall improvement of the data description in the simulation. Due to matters of the ZEUS software development and availability, a significant fraction of the systematic studies was performed on the not re-processed data and the e^+p NC MC parametrized to the former 2004-2006 e^-p sample (e.g. trigger simulation or CAL dead-channels description were then taken from 2004-2006 data).

Let us explain here what is meant by data *re-processing*. When the experiment is running and recording data, its reconstruction software is still being developed and released every few months. Hence, different fragments of a particular sample finish up reconstructed with slightly different software versions. Only after all data of a given sample has been recorded and all algorithms are ready for the full reconstruction process, the data is *re-processed* (i.e. fully reconstructed again from raw files using one consistent software version).

As mentioned in Sec. 5.8, the e^+p data used in this analysis were recorded between June 2006 and March 2007. Then, a few months were needed to complete all the required reconstruction code into a consistent version, so that the re-processing was possible during the winter season 2007/08. By that time, also the MC dedicated particularly for the 2006-2007 e^+p sample was developed and produced. As expected, the agreement of the MC with the data rose significantly, w.r.t. the previously available samples.

A broader description of the quality of the final data-sample understanding has been given in Sec. 5.8. Here, let us compare what the RH vs. LH sample agreement looks like w.r.t. the one observed for the 2004-2006 e^-p case. Fig. 6.15 compares

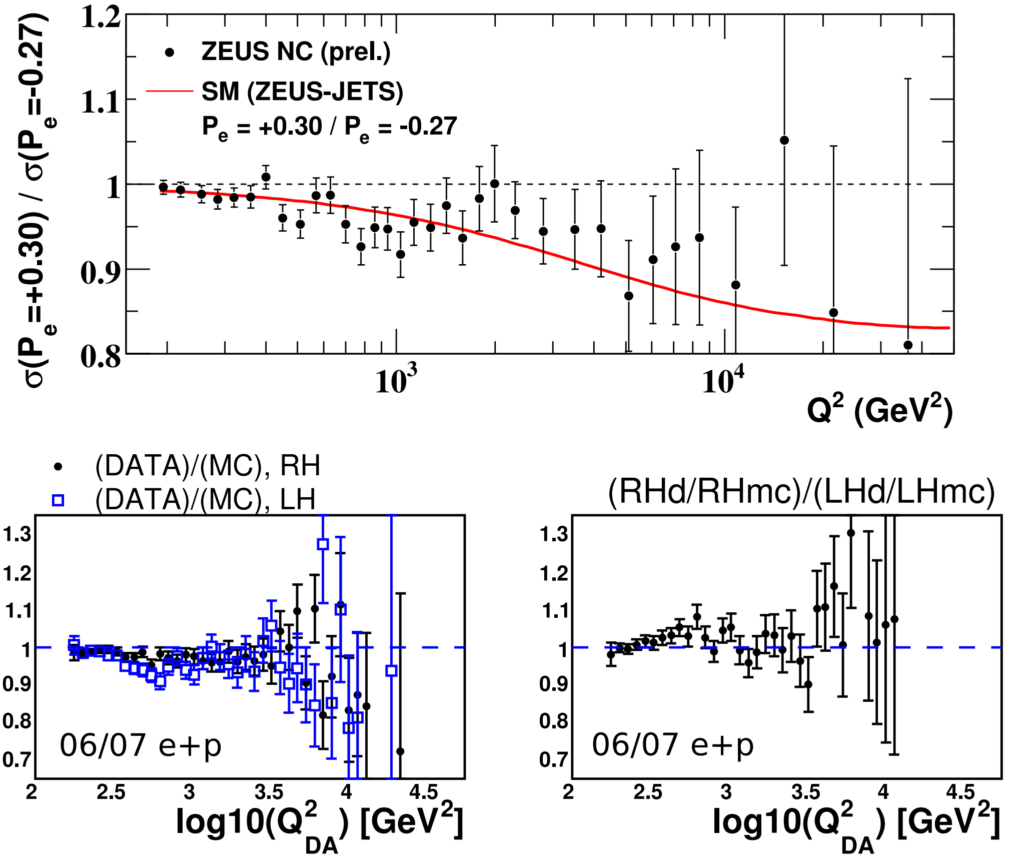

Figure 6.15: Ratio (upper plot) of the RH to LH e^-p NC cross section in function of Q^2 measured by ZEUS in 2004-2006 [203] plotted against a theory curve calculated using ZEUS-JETS PDFs. Single-ratios $(DATA_{RH}/MC_{RH})$, $(DATA_{LH}/MC_{LH})$ (lower left) and the double-ratio $(DATA_{RH}/MC_{RH})/(DATA_{LH}/MC_{LH})$ (lower right) for the 2006/07 e^+p NC signal. In all figures the vertical bars indicate statistical uncertainties.

the RH/LH ratio in function of Q^2 for the e^-p NC measurement (upper plot, cross section ratio) [203] against the one recorded by this analysis (lower right, double-ratio $(DATA_{RH}/MC_{RH})/(DATA_{LH}/MC_{LH})$, where for both cases the MC was re-weighted to the luminosity and polarization of a given sample). One observes, that even though the description of the LH e^+p sample is not perfect, the quality of understanding in both the e^-p and in the e^+p case is similar,[8] especially in the region below 1000 GeV^2, on which the focus of these systematic studies was put.

In conclusion, one notices, that even though the understanding of the data is not perfect, it is certainly good enough for a successful measurement of the NC cross sections and extraction of the PDFs. Saying that, it is also worth mention-

---

[8] It is worth mentioning here, that the total luminosity of the 2004-2006 e^-p NC sample amounts to 169.9 pb^{-1}, in comparison to 113.3 pb^{-1} for the 2006/07 e^+p case.

ing, that a particular difficulty of simulating the middle-Q^2 NC signal was not exclusive to the RH sample. To illustrate this, Fig. 6.16 presents the data/MC ratio in function of Q^2, for six sub-samples of the full 2006/07 e^+p set (and therefore the evolution in time of understanding both the RH and LH data). As this chapter proves, many possible scenarios for such unstable data behavior have been investigated and excluded. However, the origin still remains open, and should be identified and simulated before this measurement is published (which is expected for spring 2009).

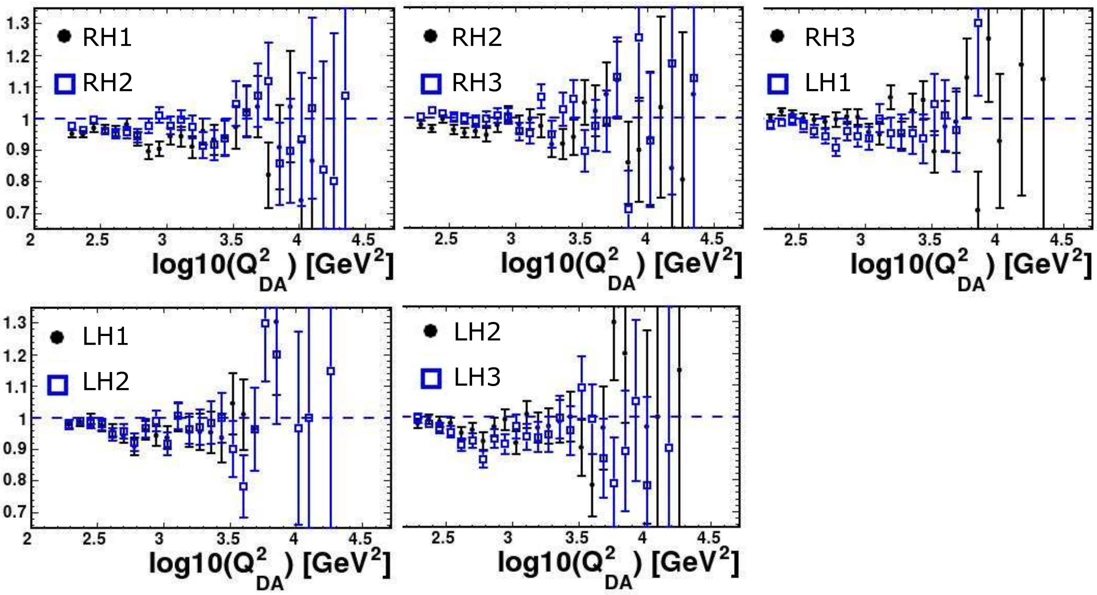

Figure 6.16: Evolution in time of the Q^2_{DA} distribution shown for 6 sub-samples of the total (RH+LH) sample. Each plot shows a comparison of two subsequent sub-samples. In the legends of these plots, RH1 means the first third of the RH sample, RH2 means the second, and so on.

Chapter 7

Results

7.1 Unfolding of the cross sections

In an ideal world, having a detector and trigger system that would record and reconstruct 100% of the interesting physics events, the cross section σ would be given by:

$$\sigma = \frac{N}{\mathcal{L}}, \tag{7.1}$$

where N is the number of recorded events and $\mathcal{L}$ is the integrated luminosity. In case of the real experiment a cross section *unfolding method* needs to be used and Eq. 7.1 modified. Effects that need to be taken into account include: finite detector and trigger acceptances limiting the number of events analyzed, finite detector resolutions leading to smeared measured kinematic variables, and systematic effects that can lead to migration of events between different regions of phase space. Moreover, background events need to be subtracted from the ones recognized as signal in order not to measure too high a cross section. Due to the complexity of the experimental environment, the most common methods of unfolding in the modern high energy physics are based on Monte Carlo simulations.

All the differential cross sections in this analysis have been measured using a one-step bin-by-bin unfolding method [148, 204]. In its framework, the formula for e.g. the Born-level double-differential cross section (Eq. 2.14) at point (x_0, Q_0^2) reads:

$$\left(\frac{d^2\sigma^{NC}}{dxdQ^2}\right)^{Born}_{meas}(x_0, Q_0^2) = \frac{N_{obs} - N_{bg}}{N_{MC}} \cdot \left(\frac{d^2\sigma^{NC}}{dxdQ^2}\right)^{Born}_{theo}(x_0, Q_0^2), \tag{7.2}$$

where N_{obs} is the number of events in the data, N_{MC} is the number of the signal events in the MC, N_{bg} is the number of the simulated background events and

$(d^2\sigma^{NC}/dxdQ^2)^{Born}_{theo}$ is the theoretical cross section. All counted events are binned (in this case in bins of x and Q^2) and had passed the cuts on all levels of the analysis. The bin-centering correction is automatically incorporated in this unfolding method, and the measured cross section can be quoted at any position (x_0, Q_0^2) within a given bin.

The one-step bin-by-bin unfolding method gives reasonable results when the experimental distributions are relatively well simulated and the resolutions are compatible with the bin widths [204]. The control plots (Fig. 5.21-5.24) presented in Section 5.8 secure fulfillment of the former condition, while the previous NC analyses [137, 138] performed on samples of comparable statistics secure the latter one.

7.1.1 Bin selection

When dividing the phase space into a set of bins in which the cross section can be measured, several conditions must be taken into account. Migrations between neighboring bins should be minimized, and therefore bin widths are chosen to be sufficiently large compared to the resolution of the variable being measured. Bins should also not be too wide, in order not to lose information on the shape of the measured cross sections. In addition, the statistical errors should be minimized, and therefore a reasonable number of events should be recorded in each of the chosen bins. As the *ep* cross section (Eq. 2.14) falls with $1/Q^4$ and $1/x$, the binning for the reduced cross section $d\sigma/dxdQ^2$ and single-differential cross sections $d\sigma/dQ^2$ and $d\sigma/dx$ was chosen to be logarithmic, while the binning for $d\sigma/dy$ was chosen to be linear.

The binning in this analysis was adapted from the earlier analyses of e^-p NC DIS with ZEUS [43, 138], where it was optimized for samples of comparable statistics. It is beneficial in view of the comparison of analyses, especially in the case of calculating xF_3 from two sets of e^+p and e^-p reduced cross sections.

Bin-dependent variables: efficiency, purity and acceptance were employed to verify whether the chosen binning sets were suitable to use in the measurements. These variables rely on the true values of kinematic variables, and therefore could only be calculated using MC events. Efficiency and purity are defined by:

$$eff = \frac{N^{rec}_{gen}}{N_{gen}}, \qquad pur = \frac{N^{rec}_{gen}}{N^{rec}}, \tag{7.3}$$

where N_{gen} is the total number of events generated in a given bin, N^{rec} is the number of events generated anywhere and reconstructed in a given bin, and N^{rec}_{gen} is the number of events generated and reconstructed in the same bin. MC events

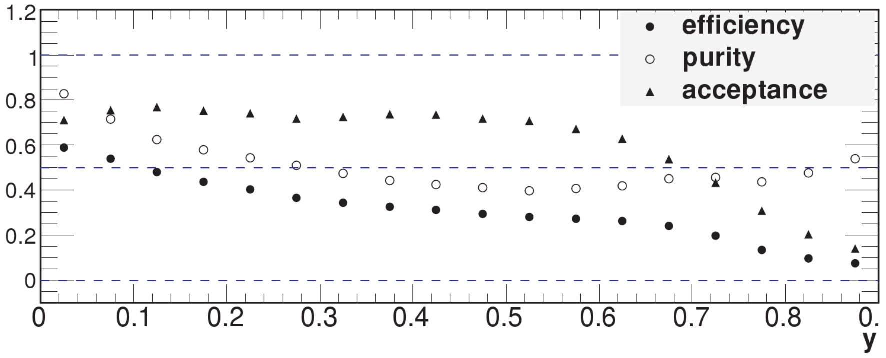

Figure 7.1: Efficiency, purity and acceptance in $d\sigma/dy$ binning, with no distinction between lower- and higher-Q^2 region. At high y efficiency drops below 0.1.

used to accumulate these three numbers (N_{gen}, N^{rec}, N^{rec}_{gen}) passed cuts on the true kinematic values of Q^2 ($Q^2 > 185\,\text{GeV}^2$ or $Q^2 > 3000\,\text{GeV}^2$), and of y ($y < 0.95$). Additionally, the events incrementing the counters of reconstructed events also passed all the analysis cuts. The acceptance is defined as the ratio between efficiency and purity, and therefore $acc = N^{rec}/N_{gen}$.

For bins, in which the efficiency drops below 50%, more than half of the events generated in a bin either do not pass the analysis cuts or migrate to other bins. As long as the MC contains a correct description of the ep scattering, together with accurate detector and trigger acceptances, this effect is corrected for by the unfolding method [148]. If purity on the other hand falls below 50%, the bin is dominated by events generated elsewhere.

It has been found previously [43], that a high fraction of the high-x and high-y MC events migrate to higher Q^2 (they are reconstructed in higher Q^2 bins than they are generated in). Figure 7.1 illustrates this observation, by depicting efficiency, purity and acceptance as a function of y, in the whole spectrum of Q^2 covered by this analysis ($Q^2 > 185\,\text{GeV}^2$), with efficiency dropping to almost zero in high-y bins. This situation has been solved by raising the lower-Q^2 requirement to $Q^2 > 3000\,\text{GeV}^2$ for the highest-x and y bins in the procedure of extraction of $d\sigma/dx$ and $d\sigma/dy$. Therefore, two separate binning sets were used for the measurement of each of these single-differential cross sections: $d\sigma/dx$ and $d\sigma/dy$.

Efficiency, purity and acceptance for the binning chosen for extraction of $d\sigma/dQ^2$ are shown in Fig. 7.2. Purity is typically above 0.6, while efficiency above 0.4. The drop-off of the efficiency in the neighborhood of Q^2 of $600\,\text{GeV}^2$ and its jump in the neighborhood of Q^2 of $2500\,\text{GeV}^2$ correspond to the super-cracks between the BCAL and the R/FCAL (events with positrons heading towards these regions are generated, but excluded using dedicated geometric cuts).

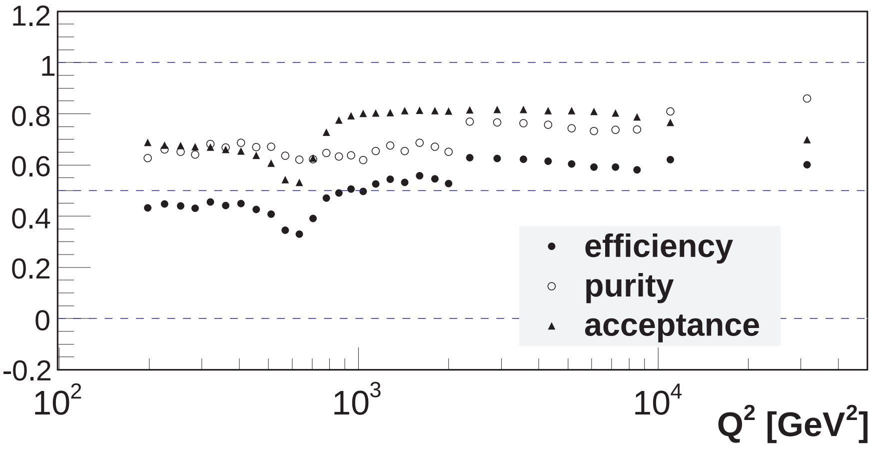

Figure 7.2: Efficiency, purity and acceptance in the chosen $d\sigma/dQ^2$ binning.

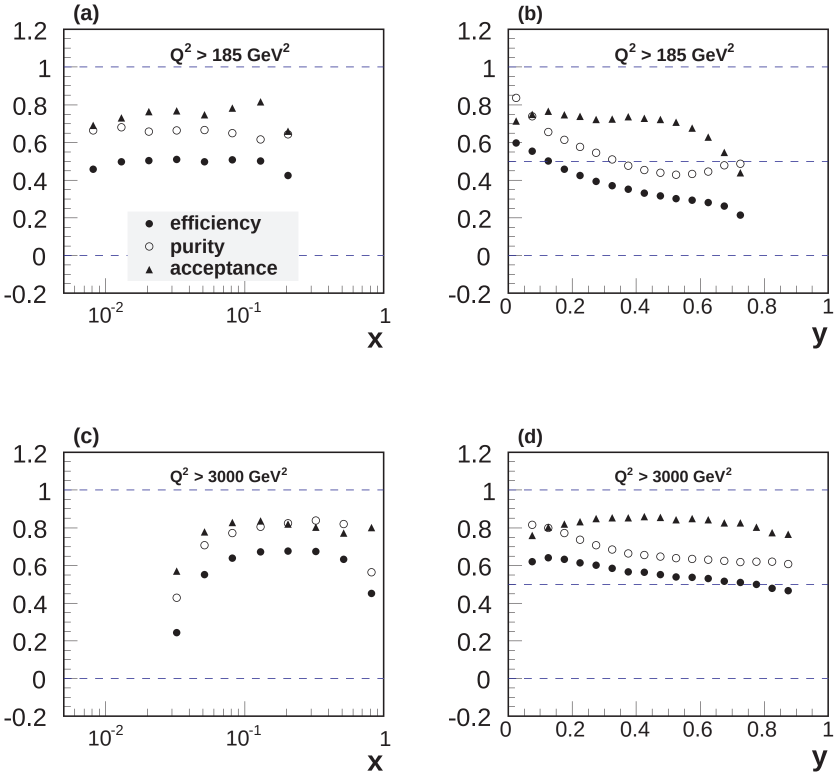

Figure 7.3: Efficiency, purity and acceptance in the chosen $d\sigma/dx$ (a,c) and $d\sigma/dy$ (b,d) binning, in the lower-Q^2 (a,b) and higher-Q^2 (c,d) ranges.

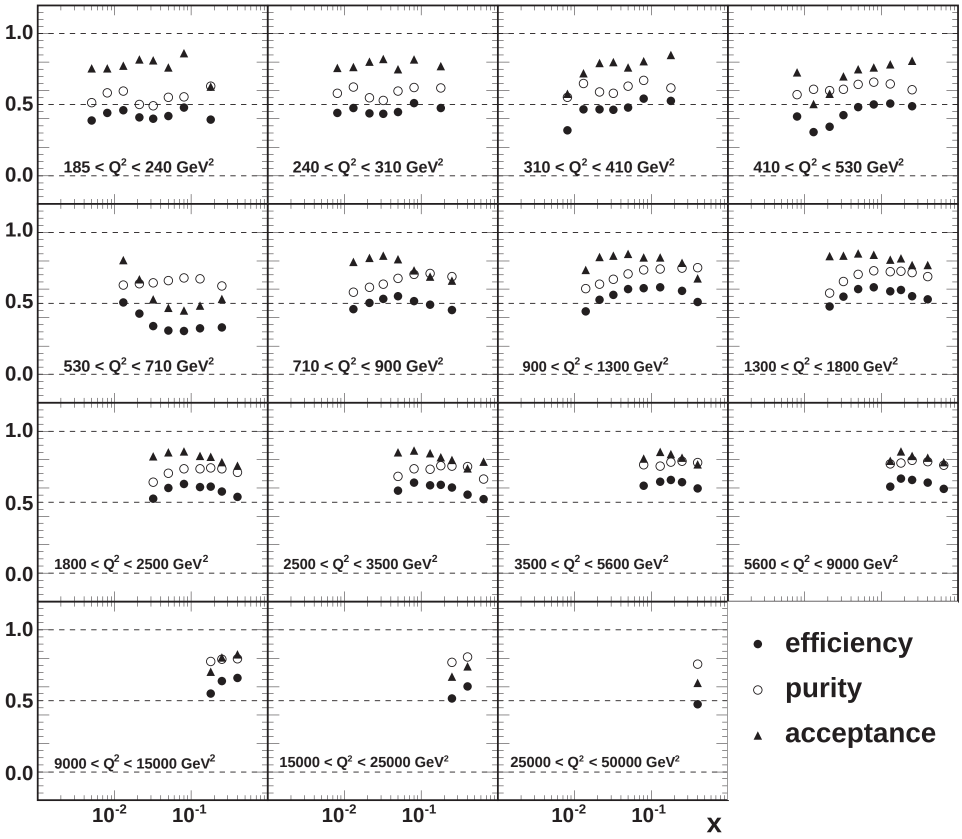

Figure 7.4: Efficiency, purity and acceptance for the (x, Q^2) binning chosen for the double-differential reduced cross section $\tilde{\sigma}$ measurement.

Figure 7.3 presents the efficiency, purity and acceptance in the bins chosen for $d\sigma/dx$ and $d\sigma/dy$ measurements, for the $Q^2 > 185\,\text{GeV}^2$ case (a, b) and the $Q^2 > 3000\,\text{GeV}^2$ one (c, d). The efficiencies for $d\sigma/dx$ are typically higher than 0.4, with one bin for which the efficiency drops to 0.2. The local drop-offs are partially caused by the super-crack cut and the lower efficiency in the higher-x region is also partially caused by the cut on the projection of γ_{had} onto the face of the FCAL (rejecting events of very low γ_{had}). The efficiency for $d\sigma/dy$ for the lower-Q^2 case drops continuously with y from 0.6 to 0.2 (an effect partially caused by the cut on the energy of the reconstructed positron $E'_e > 10\,\text{GeV}$ and partially by the super-crack cut), while for the higher-Q^2 case, it lies above 0.5.

Values of efficiency and purity for all bins of the single-differential cross sections are included in tables listing the results in Appendix A (Tab. A.1-A.5). Finally, efficiency, purity and acceptance for the (x, Q^2) bins chosen for the measurement of the double-differential reduced cross section $\tilde{\sigma}$ are plotted in Fig. 7.4, and listed in Tab. A.7 of Appendix A. All bins presented in Fig. 7.2-7.4 are accepted in this analysis.

7.1.2 Statistical and systematic uncertainties

Statistical uncertainties

The statistical uncertainty on the number of events entering the numerator ($N_{obs} - N_{bg}$) of the cross section formula given in Eq. 7.2 was calculated using Poisson statistics if the number of events was below 100, and Gaussian statistics otherwise. The total number of MC events was high enough (see Sec. 5.3), such that statistical errors induced by the MC could be neglected. The statistical uncertainty for $d\sigma/dQ^2$, $d\sigma/dx$ and $d\sigma/dy$ cross sections is depicted in Fig. 7.5 - 7.7 and confronted with the partial and the total systematic uncertainty. The statistical uncertainty varies between < 0.01 for the low-Q^2 bins and 0.3 for the highest-x bin.

Systematic uncertainties

A realistic description of the systematic uncertainties is one of the central elements of a successful measurement, as the notion of their sources and magnitude defines the limit to which a measurement can be performed using the tools at hand. It is, at the same time, one of the more challenging tasks, as some sources introducing the bias might be persistent and difficult to identify (for example, see Chapter 6). Their sources may vary from detector inefficiencies, through problems in MC generators and detector parameterization to contributions from backgrounds not described by the simulation. Additionally, once they are identified, calculating their total contribution might be difficult due to correlations.

The identified sources of systematic uncertainties are described below. Their influence on the measured cross sections was found by varying the analysis cut (or a reconstruction parameter) corresponding to a given source and recalculating the cross section. The cuts were varied for both the data and the MC signal. Then, the relative difference between the new result σ_i and the nominal value σ is taken as the relative systematic uncertainty δ_i from a given source.

Most of the systematic checks discussed here have been identified and employed for the cross section measurements in the process of previous NC analyses [43, 57, 138, 148, 160]. To a large extent they constitute a common body of a NC DIS analysis at ZEUS. The following list presents the systematic checks performed within the analysis described in this thesis.

- **The electron energy scale** ($\pm 2\%$) - the relative uncertainty on the measured electron energy was found to be 2% [205], and therefore the final simulated electron energy was varied by this amount. Its typical contribution to the systematic uncertainty is smaller than 1%, but dominates in the high-y

region (populated by events with an electron energy close to the 10 GeV cut threshold), where it reaches 5%.

- **The hadronic energy scale** (±2%) - the uncertainty on the hadronic energy scale has been studied within the study dedicated to the backsplash correction [43], and was found to be 2% for the RCAL and 1% for the B/FCAL, and therefore the final simulated hadronic energy was varied by ±2%. Its typical contribution to the total uncertainty lies within 1%.

- **Variation of the P_e' cut** (±1 GeV) - the momentum of the track matched to the electron candidate was varied by ±1 GeV in order to test the MC description of the data and the background contamination in the neighborhood of the nominal cut. Its maximum contribution amounted to 5% and was typically smaller than 1%.

- **Variation of the $|Z_{VTX}|$ cut** (±5 cm) - the cut on the absolute value of the reconstructed longitudinal vertex position was varied by ±5 cm, such that once events for which $-25 < Z_{VTX} < 25$ cm were accepted and the other time, for which $-35 < Z_{VTX} < 35$ cm. Its typical contribution to the total error was smaller than 1%.

- **Variation of the $E - P_Z$ cut** (±2 GeV) - the variation of the cut on the total $E - P_Z$ by ±2 GeV tests the sensitivity of the selection to the contamination by overlaid events. In one configuration events with $40 < E - P_Z < 63$ GeV were accepted, and in the other with $36 < E - P_Z < 67$ GeV. The contribution to the total error was smaller than 3%.

- **Variation of the PHP cross section** ±50% - due to the uncertainty on the normalization of the background coming from photoproduction, its normalization was varied by ±50% (as the factor applied to the MC signal was determined in a study of the PHP enriched sample to be 1.56, see Sec. 5.3.3). The contribution to the total error coming from this variation was typically smaller than 1%.

- **Variation of the cut on the projection of γ_{had} onto FCAL** (±2 cm) - this variation of the cut on the hadronic activity around the forward beampipe was mainly relevant in the highest-x region, and contributed there by 8%.

- **Variation of the electron cluster isolation cut** (±2 GeV) - this check contributes to at most 4% to the total uncertainty at high-Q^2, where the probability for the energetic HFS particle to be found close to the electron cluster is higher.

- **Variation of the $P_T/\sqrt{E_T}$ cut** ($\pm 1\,\mathrm{GeV}^{1/2}$) - this check verifies how sensitive the selection is to the contributions from the cosmic and halo muon background. Its contribution is typically smaller than 1%.
- **Tightening the cut on y_{EL}** (to 0.9) - as the region above $y_{EL} = 0.95$ is not described by the MC, this variation was performed in one direction only. Its contribution is significant only at high-Q^2, where it rises up to 3%.
- **Tightening the cut on DCA** (to 8 cm) - this variation was also performed in one direction only. The systematic uncertainty corresponding to this check lies typically within 1%.
- **Variation of the E'_e resolution in MC** - the resolution of the electron energy in MC was smeared additionally by 3%. The contribution of this check to the total relative uncertainty is smaller than 1% over the whole kinematic space considered.
- **Switch of the BCAL non-uniformity correction** - the correction coming from the BCAL non-uniformity to the reconstructed electron energy was switched from the default version to the one developed at the time of writing of this thesis [172]. It shifts the high-y cross section by maximum of 6%.

The total positive systematic uncertainty δ^+_{syst} is calculated in a given bin by summing in quadrature all the contributions which result in an increase of the cross section. Similarly, the total negative systematic uncertainty δ^-_{syst} is a sum in quadrature of all the contributions decreasing the cross section. Hence, the total systematic uncertainty is given by:

$$\frac{\delta^+_{syst}}{\sigma} = \sqrt{\sum_i \delta_i^2} = \sqrt{\sum_i \left(\frac{\sigma_i - \sigma}{\sigma}\right)^2}, \qquad \sigma_i - \sigma > 0, \tag{7.4}$$

$$\frac{\delta^-_{syst}}{\sigma} = \sqrt{\sum_i \delta_i^2} = \sqrt{\sum_i \left(\frac{\sigma_i - \sigma}{\sigma}\right)^2}, \qquad \sigma_i - \sigma < 0. \tag{7.5}$$

The relative systematic and statistical uncertainties for the single-differential cross sections are depicted in Figures 7.5-7.7. In general, the current measurement of $d\sigma/dQ^2$ is limited by systematic uncertainties up to Q^2 of $\sim 500\,\mathrm{GeV}^2$, where statistical uncertainties become dominant (Fig. 7.5). This observation holds also for the measurement of $d\sigma/dx$, for which, in the $Q^2 > 3000\,\mathrm{GeV}^2$ case, the total uncertainty could still be minimized considerably by increasing the luminosity of the samples, while in the $Q^2 > 185\,\mathrm{GeV}^2$ case the relevance of the statistical and systematic uncertainty is similar (Fig. 7.6). The measurement of $d\sigma/dy$ for $Q^2 > 185\,\mathrm{GeV}^2$ is dominated by systematics only at the highest y, while being dominated by the statistical uncertainty in the $Q^2 > 3000\,\mathrm{GeV}^2$ range (Fig. 7.7).

One should notice that the fractional uncertainty of 2.6% coming from the integrated luminosity measurement was not included in the total uncertainty[1]. Also, systematic uncertainties on the polarization measurement were not included in the total uncertainty shown in the final results.

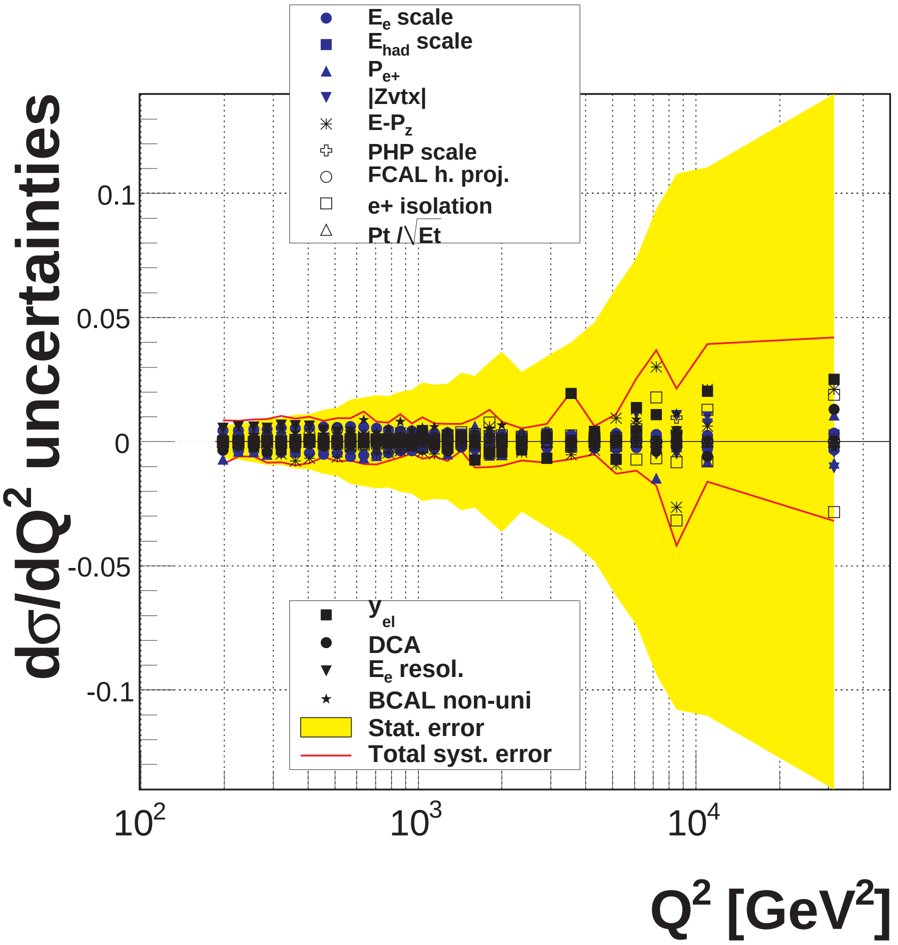

Figure 7.5: Relative systematic and statistical uncertainties for $d\sigma/dQ^2$ as functions of Q^2. The statistical uncertainty is plotted with a filled colored area, the total systematic uncertainty with the solid line. Particular contributions from different sources are indicated using different symbols.

---

[1] It is a standard ZEUS collaboration policy, not to include the fractional uncertainty on the integrated luminosity measurement in plots or tables of cross sections.

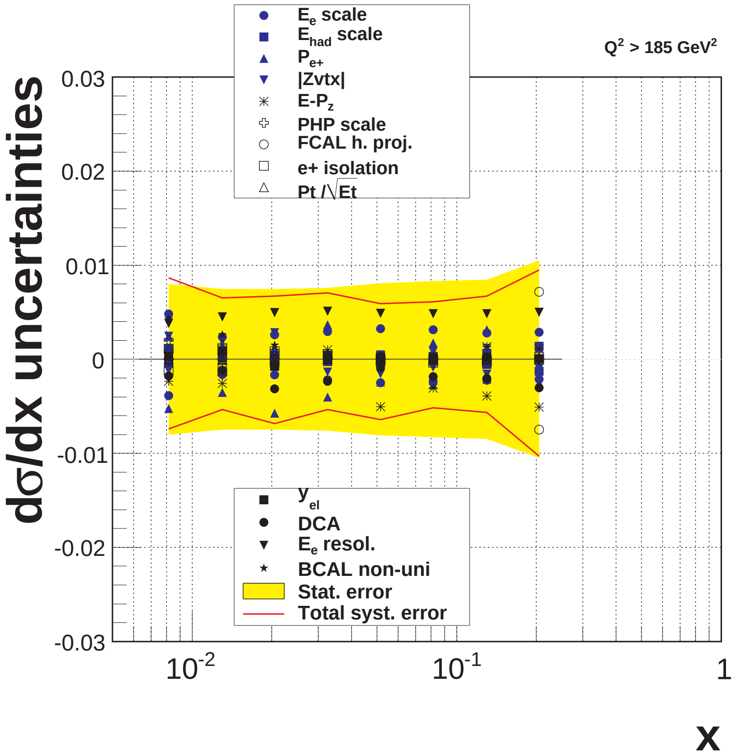

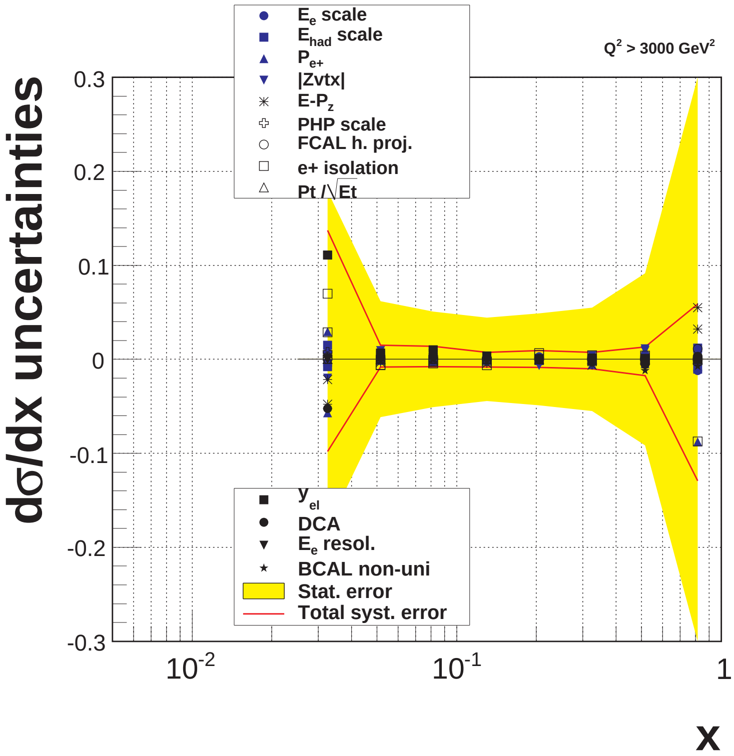

Figure 7.6: Relative systematic and statistical uncertainties for $d\sigma/dx$ as functions of x, for the $Q^2 > 185\,\mathrm{GeV}^2$ case (upper plot) and for the $Q^2 > 3000\,\mathrm{GeV}^2$ case (lower plot).

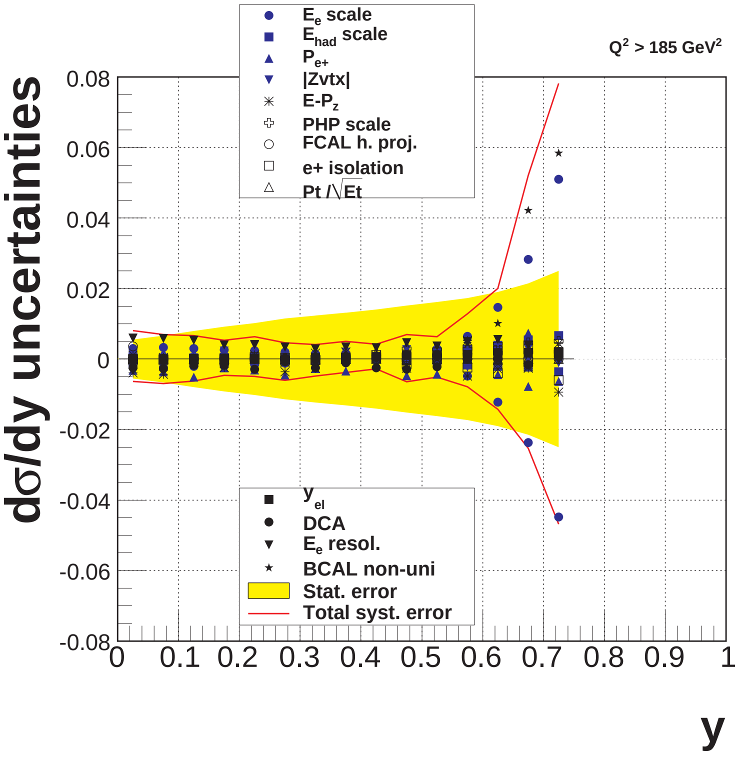

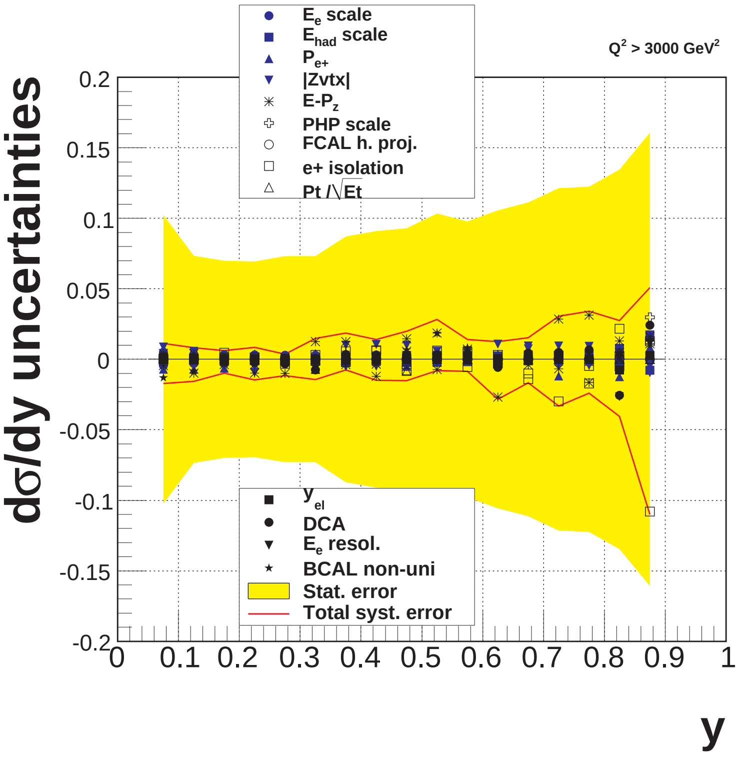

Figure 7.7: Relative systematic and statistical uncertainties for $d\sigma/dy$ as functions of y, for the $Q^2 > 185\,\mathrm{GeV}^2$ case (upper plot) and for the $Q^2 > 3000\,\mathrm{GeV}^2$ case (lower plot).

7.2 Cross sections results

7.2.1 Single differential cross sections $d\sigma/dQ^2$, $d\sigma/dx$ and $d\sigma/dy$

This section presents the results of the measurement of the $d\sigma/dQ^2$, $d\sigma/dx$ and $d\sigma/dy$ single differential cross sections, for the full analyzed sample (of $\mathcal{L} = 113.3\,\mathrm{pb}^{-1}$, $P = 0.07$) as well as for the positively-polarized (of $\mathcal{L} = 70.9\,\mathrm{pb}^{-1}$, $P = 0.32$, RH) and negatively-polarized ($\mathcal{L} = 42.4\,\mathrm{pb}^{-1}$, $P = -0.36$, LH) ones.

Figures 7.8(a), 7.8(c) show the measured absolute values of the $d\sigma/dx$ cross section corresponding to the full analyzed sample (of total integrated luminosity of $113.3\,\mathrm{pb}^{-1}$ and the average lepton-beam polarization $P = 0.07$) for $Q^2 > 185\,\mathrm{GeV}^2$ ($0.0063 < x < 0.25$) and $Q^2 > 3000\,\mathrm{GeV}^2$ ($0.025 < x < 1.0$), respectively. The ratios of these cross sections to the Standard Model theoretical predictions, calculated using the ZEUS-JETS PDF parameterization [206], are presented in Fig. 7.9(a), 7.9(c). Considering the experimental uncertainties, the measured cross sections are in good agreement with the SM. The quality of the $d\sigma/dx$ cross section measured (for the first time for e^+p NC DIS with longitudinally-polarized lepton beams) separately for the RH and LH samples is presented in the corresponding Figures: 7.10(a), 7.10(c), 7.11(a), 7.11(c). Within the limits of the precision of this measurement, all $d\sigma/dx$ cross sections agree well with the predictions.

The measured absolute values of the $d\sigma/dy$ cross section corresponding to the full analyzed sample ($113.3\,\mathrm{pb}^{-1}$) for $Q^2 > 185\,\mathrm{GeV}^2$ ($0.0 < y < 0.75$) and $Q^2 > 3000\,\mathrm{GeV}^2$ ($0.05 < y < 0.9$) are presented in Figures 7.8(b), 7.8(d). Their quality can be evaluated by inspecting the plots of their ratios to the SM predictions, Fig. 7.9(b,d). The shape of the ratio reveals a small step-like behavior for the $Q^2 > 185\,\mathrm{GeV}^2$ case, with the ratio gradually decreasing with increasing y. Hints of this tendency can be observed in both the RH as well as the LH samples (Fig. 7.10(b), 7.11(b), this is also the first measurement of $d\sigma/dy$ e^+p NC DIS with longitudinally-polarized lepton beams). However, having in mind the additional not-displayed luminosity-measurement uncertainty, it is concluded, that within the experimental precision, the measurement agrees with theory. Also, the measured $d\sigma/dy$ cross section for the $Q^2 > 3000\,\mathrm{GeV}^2$ case, presented in Fig. 7.8(d), 7.9(d), 7.10(d), 7.11(d) displays a satisfactory agreement with the theoretical prediction.

The measured single-differential $d\sigma/dQ^2$ cross section corresponding to the full analyzed luminosity $\mathcal{L} = 113.3\,\mathrm{pb}^{-1}$ and average lepton-beam polarization $P = 0.07$ is depicted in Figure 7.8(e). The ratio of the measured cross section to the theoretical prediction is presented in Figure 7.9(e), again for the full analyzed sample.

Similar plots presenting the ratios of the positively-polarized ($\mathcal{L} = 70.9\,\mathrm{pb}^{-1}$, $P = 0.32$) and negatively-polarized ($\mathcal{L} = 42.4\,\mathrm{pb}^{-1}$, $P = -0.36$) samples to the theoretical predictions are depicted in Fig. 7.10(e), 7.11(e), while the absolute measured $d\sigma/dQ^2$ cross sections for these samples are given in Fig. 7.12(a), 7.12(b). All $d\sigma/dQ^2$ cross sections were measured in the kinematic region of $185 < Q^2 < 50\,000\,\mathrm{GeV}^2$ and $y < 0.95$.

The presented $d\sigma/dQ^2$ cross section corresponding to the full analyzed luminosity is in a reasonable agreement with the SM prediction, however a slight decline of the measurement w.r.t. the prediction is observed as a function of Q^2. Figures 7.10(e), 7.11(e) showing the ratio of the two $d\sigma/dQ^2$ measurements (of positively- and negatively-polarized samples, respectively) support the observation discussed in detail in Chapter 6 that the RH sample was better described by the MC than the LH one. While the MC description of the RH sample seems sound and therefore the measured cross section agrees well with the SM prediction, the shape of the ratio of the measured $d\sigma/dQ^2$ signal to the prediction contains a "valley" in the neighborhood of Q^2 of $600\,\mathrm{GeV}^2$, in which the ratio locally declines down to the level of 0.9.

All of the single-differential cross section results are also tabulated in the Appendix A, Tab. A.1-A.5.

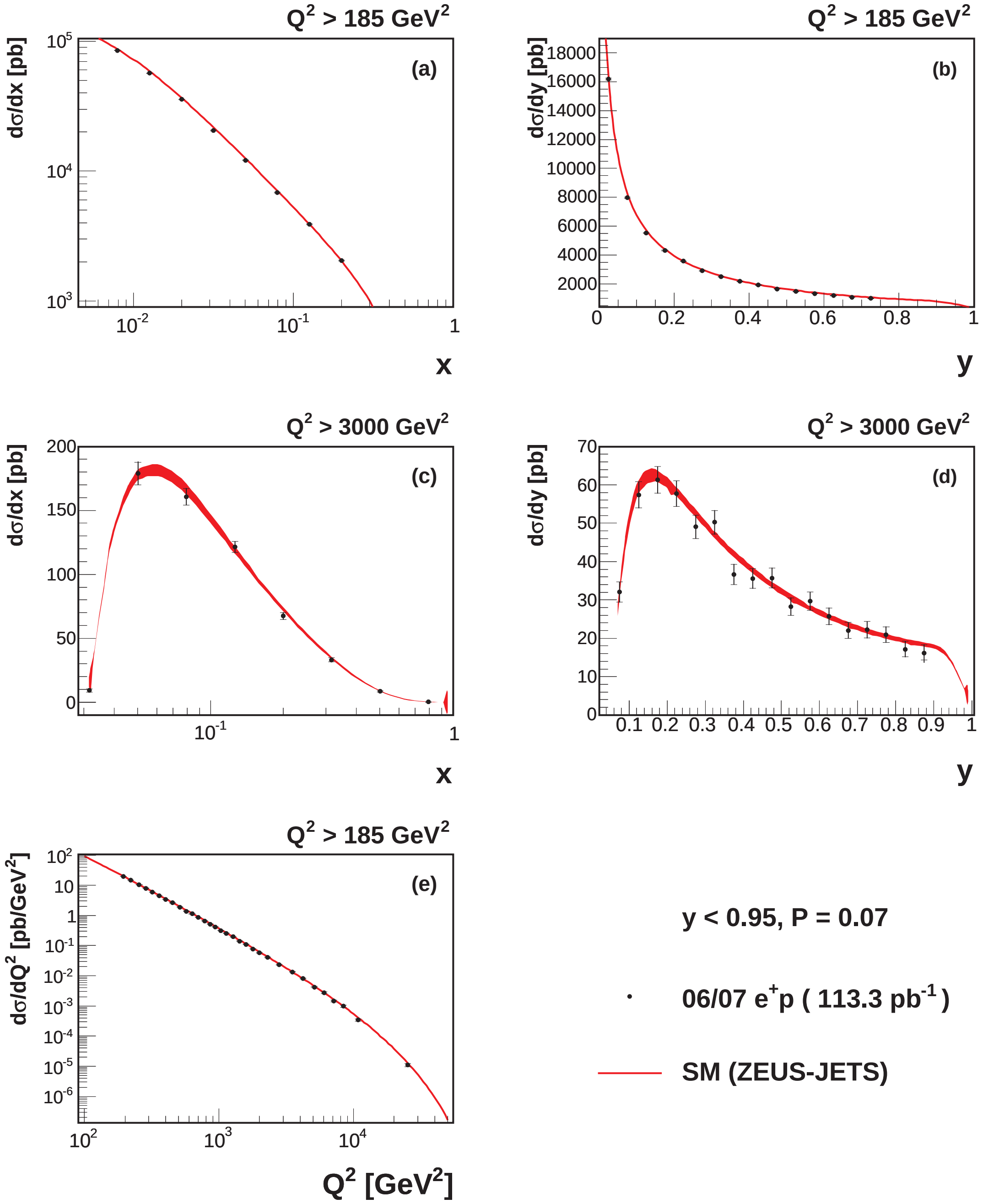

Figure 7.8: The e^+p NC DIS cross sections: (a) $d\sigma/dx$ for $Q^2 > 185\,\text{GeV}^2$, (b) $d\sigma/dy$ for $Q^2 > 185\,\text{GeV}^2$, (c) $d\sigma/dx$ for $Q^2 > 3000\,\text{GeV}^2$, (d) $d\sigma/dy$ for $Q^2 > 3000\,\text{GeV}^2$ and (e) $d\sigma/dQ^2$, all corresponding to the full measured sample of $\mathcal{L} = 113.3\,\text{pb}^{-1}$ and $P = 0.07$. The closed circles represent the data points, with the inner error bar showing the statistical uncertainty, while the full error bar shows the total uncertainty (statistical and systematic uncertainty added in quadrature). The shaded bands depict the SM prediction evaluated using the ZEUS-JETS PDF parameterization, along with the uncertainties from the PDFs. All cross sections measured in a kinematic region of $y < 0.95$.

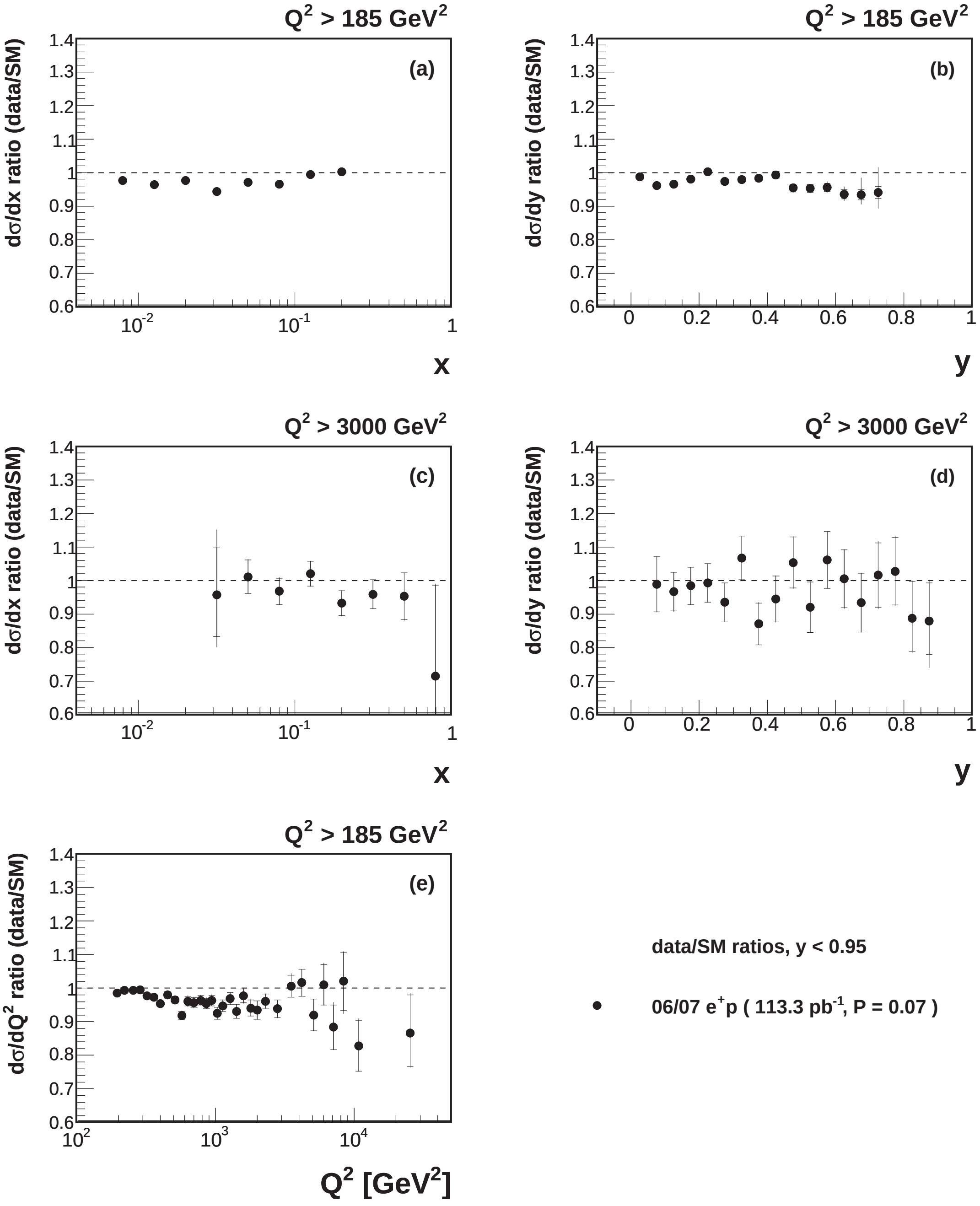

Figure 7.9: The ratios of the following measured e^+p NC DIS cross sections to the theoretical predictions evaluated using the ZEUS-JETS PDFs: (a) $d\sigma/dx$ for $Q^2 > 185\,\mathrm{GeV}^2$, (b) $d\sigma/dy$ for $Q^2 > 185\,\mathrm{GeV}^2$, (c) $d\sigma/dx$ for $Q^2 > 3000\,\mathrm{GeV}^2$, (d) $d\sigma/dy$ for $Q^2 > 3000\,\mathrm{GeV}^2$ and (e) $d\sigma/dQ^2$, all corresponding to the RH measured sample of $\mathcal{L} = 113.3\,\mathrm{pb}^{-1}$ and $P = 0.07$. The inner error bars show the statistical uncertainty, while the full error bars show the total uncertainty. The theoretical uncertainty is not included in the presented ratios.

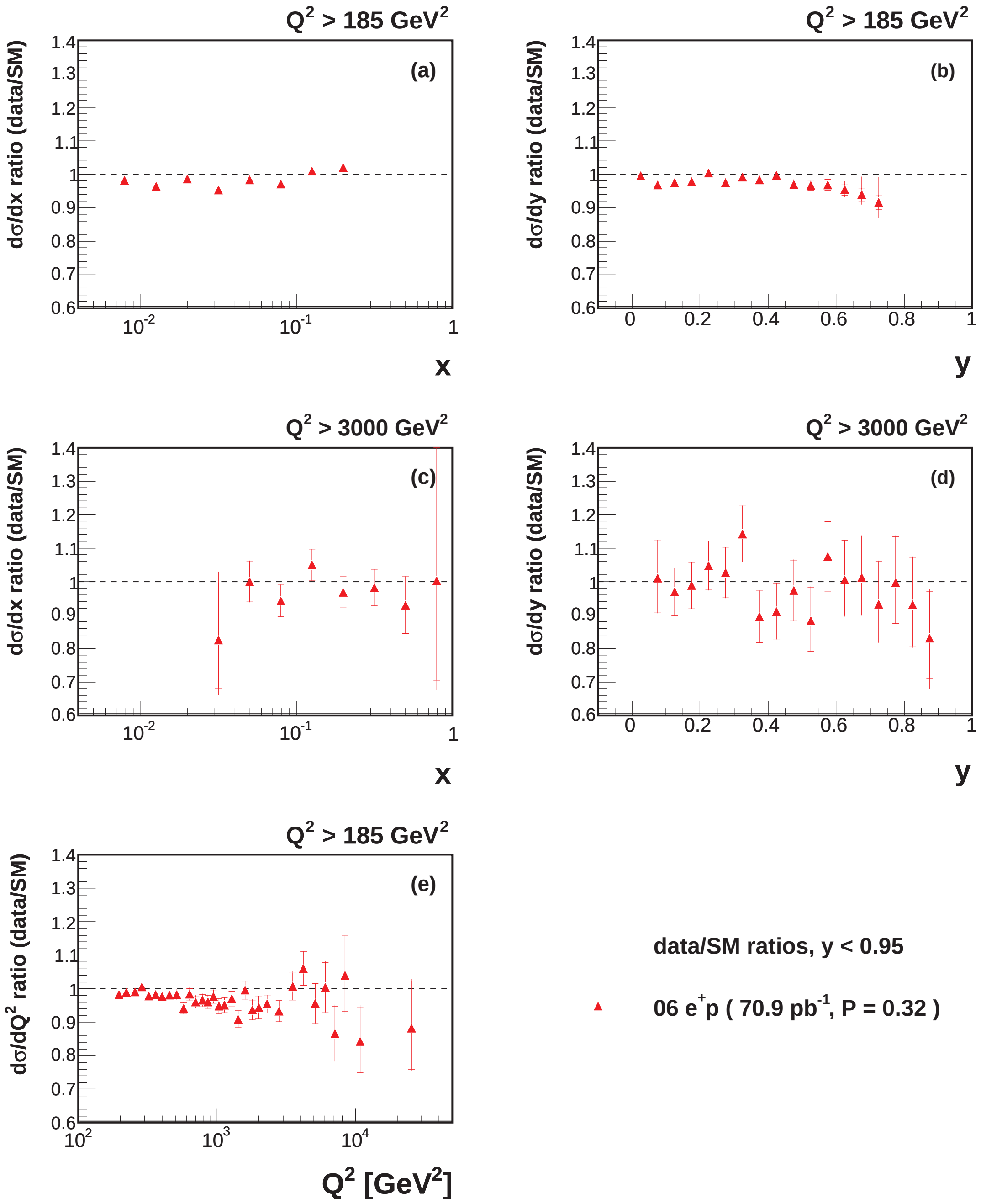

Figure 7.10: The ratios of the following measured e^+p NC DIS cross sections to the theoretical predictions evaluated using the ZEUS-JETS PDFs: (a) $d\sigma/dx$ for $Q^2 > 185\,\mathrm{GeV}^2$, (b) $d\sigma/dy$ for $Q^2 > 185\,\mathrm{GeV}^2$, (c) $d\sigma/dx$ for $Q^2 > 3000\,\mathrm{GeV}^2$, (d) $d\sigma/dy$ for $Q^2 > 3000\,\mathrm{GeV}^2$ and (e) $d\sigma/dQ^2$, all corresponding to the full measured sample of $\mathcal{L} = 70.9\,\mathrm{pb}^{-1}$ and $P = 0.32$. The inner error bars show the statistical uncertainty, while the full error bars show the total uncertainty. The theoretical uncertainty is not included in the presented ratios.

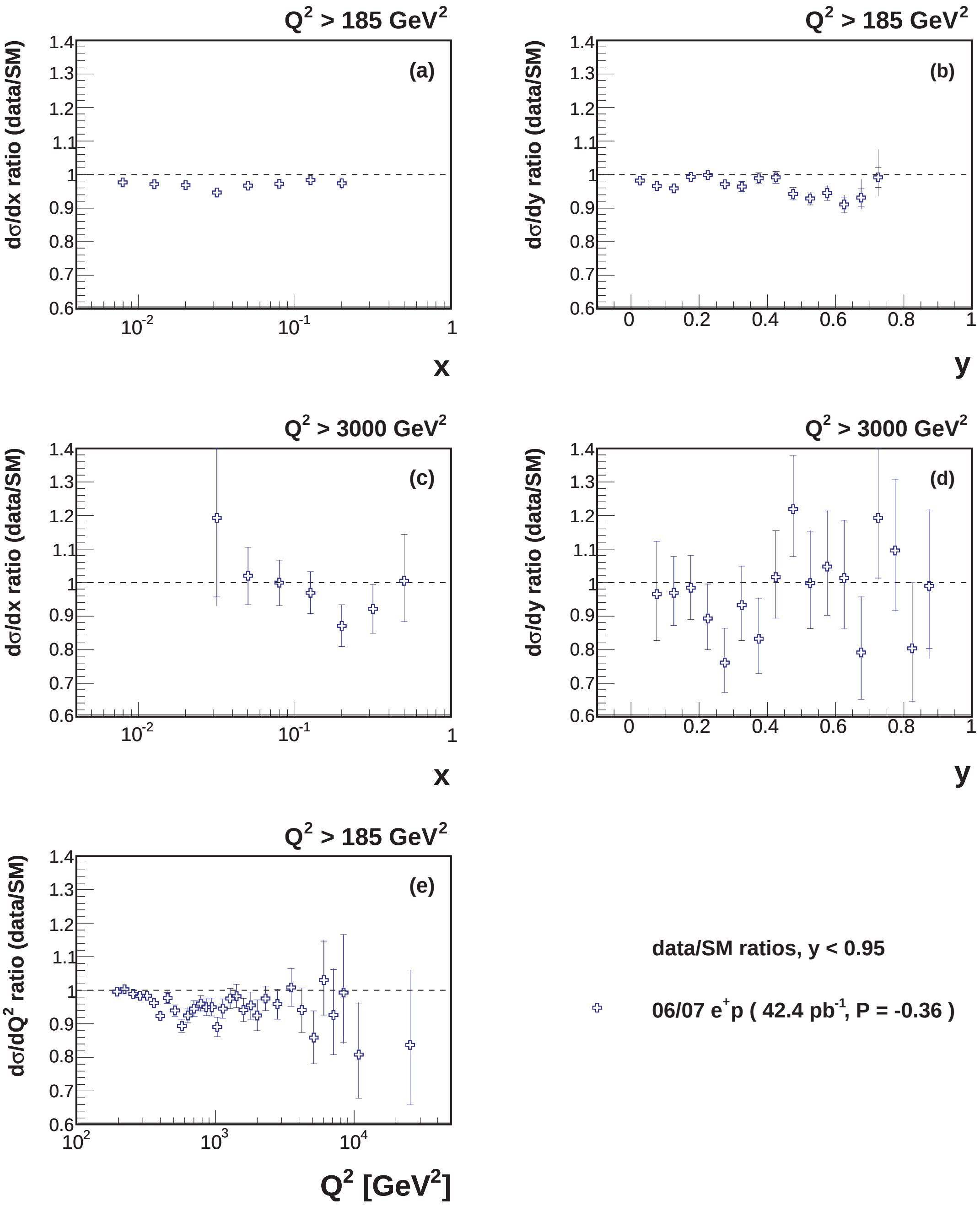

Figure 7.11: The ratios of the following measured e^+p NC DIS cross sections to the theoretical predictions evaluated using the ZEUS-JETS PDFs: (a) $d\sigma/dx$ for $Q^2 > 185\,\text{GeV}^2$, (b) $d\sigma/dy$ for $Q^2 > 185\,\text{GeV}^2$, (c) $d\sigma/dx$ for $Q^2 > 3000\,\text{GeV}^2$, (d) $d\sigma/dy$ for $Q^2 > 3000\,\text{GeV}^2$ and (e) $d\sigma/dQ^2$, all corresponding to the full measured sample of $\mathcal{L} = 42.4\,\text{pb}^{-1}$ and $P = -0.36$. The inner error bars show the statistical uncertainty, while the full error bars show the total uncertainty. The theoretical uncertainty is not included in the presented ratios.

7.2.2 The ratio of $d\sigma/dQ^2$ cross sections and polarization asymmetry A^+

The difference in the interaction of positively- and negatively-polarized positrons with the proton is demonstrated as a ratio of the $d\sigma/dQ^2$ cross sections measured for the RH and the LH samples separately, as well as through a measurement of the polarization asymmetry A^+. These measurements are compared to the SM predictions evaluated using the ZEUS-JETS PDF fits, including the uncertainties on the PDFs.

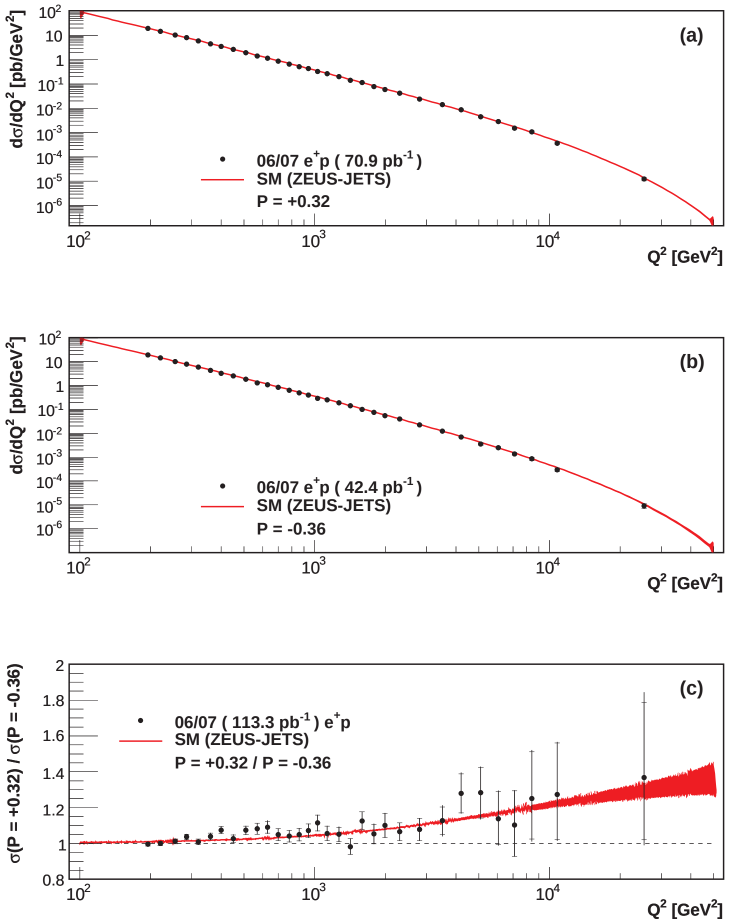

Figure 7.12: The measured e^+p $d\sigma/dQ^2$ NC DIS cross sections corresponding to the positively-polarized sample (a), the negatively-polarized one (b), and the ratio of these cross sections (c). The inner error bars show the statistical uncertainty, and the full error bars show the total uncertainty. The theoretical predictions are evaluated using the ZEUS-JETS PDF fits.

The ratio of $d\sigma/dQ^2$ cross sections measured separately for the samples with positively- and negatively-polarized positron beams is depicted in Figure 7.12(c).

The presented result demonstrates parity violation at the electroweak scale ($Q^2 \gg 1000\,\mathrm{GeV}^2$), as the ratio clearly deviates from unity as Q^2 rises.

The ratio of $d\sigma/dQ^2$ cross sections measured recently by ZEUS [59], separately for the sample with negatively- and positively-polarized electron beams is presented for comparison in Fig. 7.13(a). The ratio considered here was measured first by ZEUS (for e^+p NC DIS, on 2003-2004 data) with a dataset of the total integrated luminosity of $23.8\,\mathrm{pb}^{-1}$ and polarizations of the lepton beams of 0.32 and -0.41 [207]. Hence, the measurement presented in this thesis improves the statistical precision by a factor of 2.2.

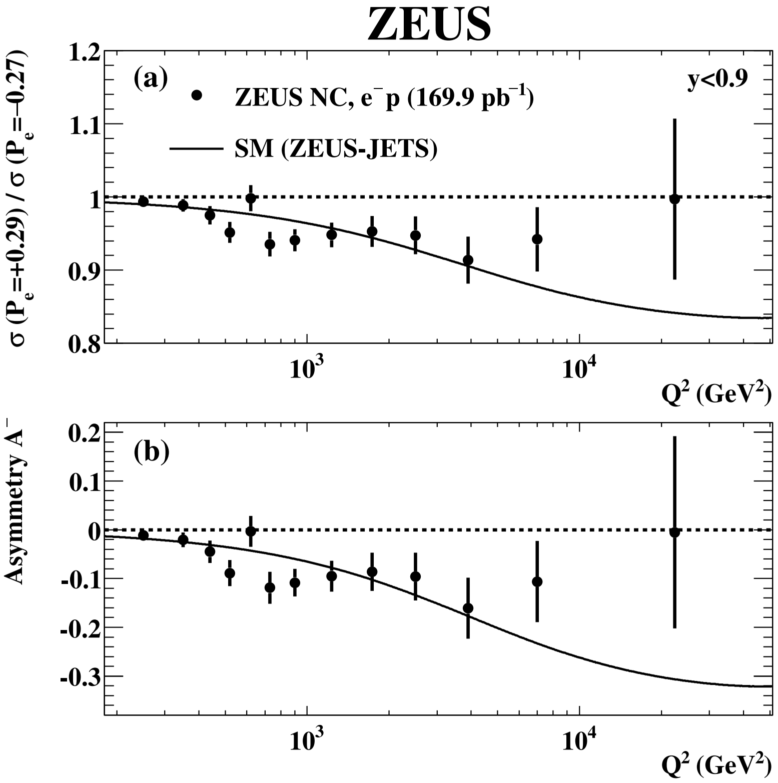

Figure 7.13: The ratio of $d\sigma/dQ^2$ e^+p using positive and negative polarization in (a), and the polarization asymmetry A^- as a function of Q^2 in (b) [59]. Only statistical uncertainties are considered. The curves show the predictions of the SM evaluated using the ZEUS-JETS PDFs.

The A^+ polarization asymmetry, extracted from both of the measured $d\sigma/dQ^2$ e^+p cross sections mentioned above, according to Equation 2.27 is depicted in Fig. 7.14 and also listed in Tab. A.6 (in Appendix A). One may compare the result presented here to a similar one measured for e^-p NC DIS by also examining Fig. 7.13(b). The rise of the precision of the measurement of the polarization asymmetry A^+ can be appreciated also by comparing Fig. 7.14 to the first result obtained from a combination of ZEUS and H1 data, presented in Fig. 2.14. The dataset of this last combination corresponds to the integrated luminosity of $\sim\ 71.4\,\mathrm{pb}^{-1}$ ($P_+ \sim 0.33, P_- \sim -0.40$) for A^+, yielding an increase of the statistical precision by 26% [70].

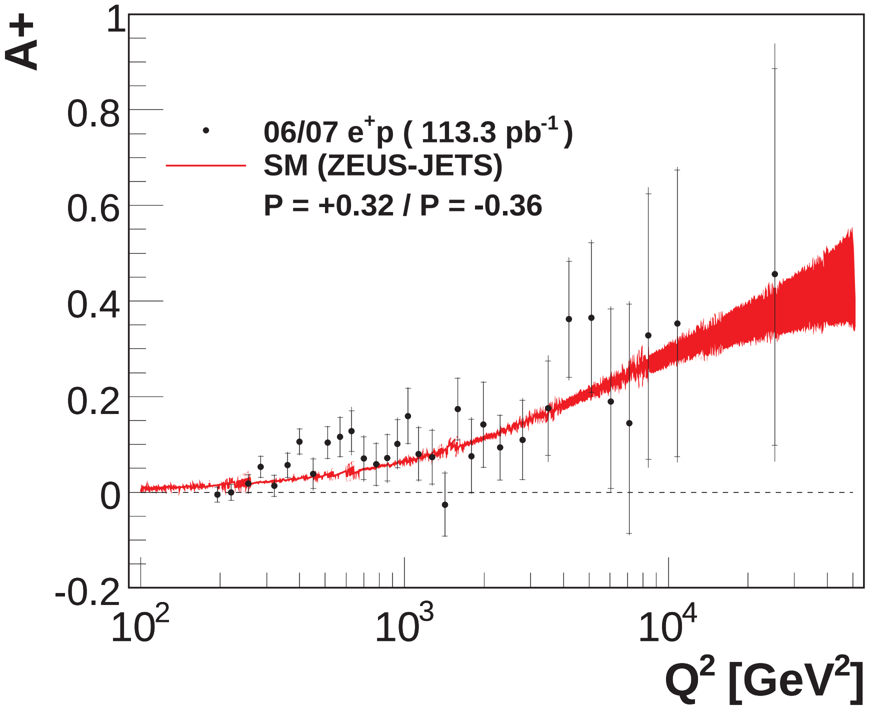

Figure 7.14: The A^+ polarization asymmetry, extracted from the $d\sigma/dQ^2$ e^+p cross sections measured using samples with positively- and negatively-polarized positrons. The inner error bars show the statistical uncertainty, and the full error bar show the total uncertainty. The theoretical predictions are evaluated using the ZEUS-JETS PDF fits.

7.2.3 Reduced cross section $\tilde{\sigma}$

The double-differential reduced e^+p NC DIS cross section $\tilde{\sigma}$, as defined in Eq. 2.15, was measured for the first time ever using the polarized positron beams, for the entire e^+p NC DIS data sample considered here, as well as for the separate samples with positively- and negatively-polarized lepton beams. All these measurements were performed in the following kinematic region: $185 < Q^2 < 50\,000\,\mathrm{GeV}^2$ and $y < 0.95$. The measured $\tilde{\sigma}$ corresponding to the full sample of $\mathcal{L} = 113.3\,\mathrm{pb}^{-1}$ and $P = 0.07$ is presented in Fig. 7.15 and listed in Tab. A.8 of Appendix A, while

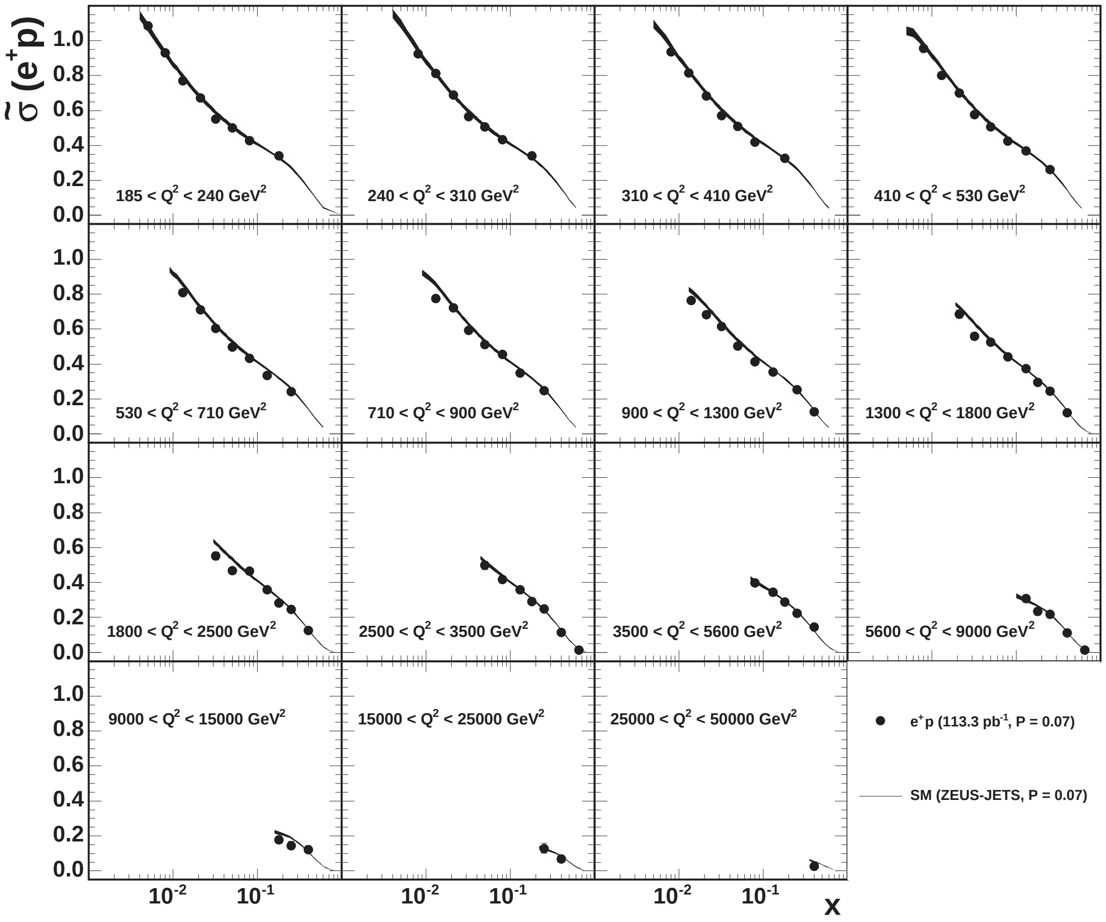

Figure 7.15: The e^+p NC DIS reduced cross section $\tilde{\sigma}$ corresponding to the full measured sample of $\mathcal{L} = 113.3\,\mathrm{pb}^{-1}$ and $P = 0.07$ in the kinematic region of $Q^2 > 185\,\mathrm{GeV}^2$ and $y < 0.95$. The closed circles represent the data points, with the inner error bar showing the statistical uncertainty, the full error bar shows the total uncertainty. The shaded bands depict the SM prediction evaluated using the ZEUS-JETS PDF parameterization, along with the uncertainties from the PDFs.

the ratio of the measured cross section to the SM prediction (evaluated with the ZEUS-JETS PDFs) is depicted in Fig. 7.16. Within the limits of the experimental uncertainties and those of the theory, the measurement is well described by the SM and of similar precision to the e^-p results published recently by ZEUS [59] (corresponding to the total integrated luminosity of $169.9\,\mathrm{pb}^{-1}$). The reduced cross sections measured separately for the samples of $\mathcal{L} = 70.9\,\mathrm{pb}^{-1}$, $P = 0.32$, and $\mathcal{L} = 42.4\,\mathrm{pb}^{-1}$, $P = -0.36$ are presented in Fig. 7.17 and listed in Tab. A.9 and Tab. A.10, while their ratios to the SM predictions appear in Fig. 7.18. They are, as well as the entire sample, well described by the SM prediction evaluated with the ZEUS-JETS PDFs.

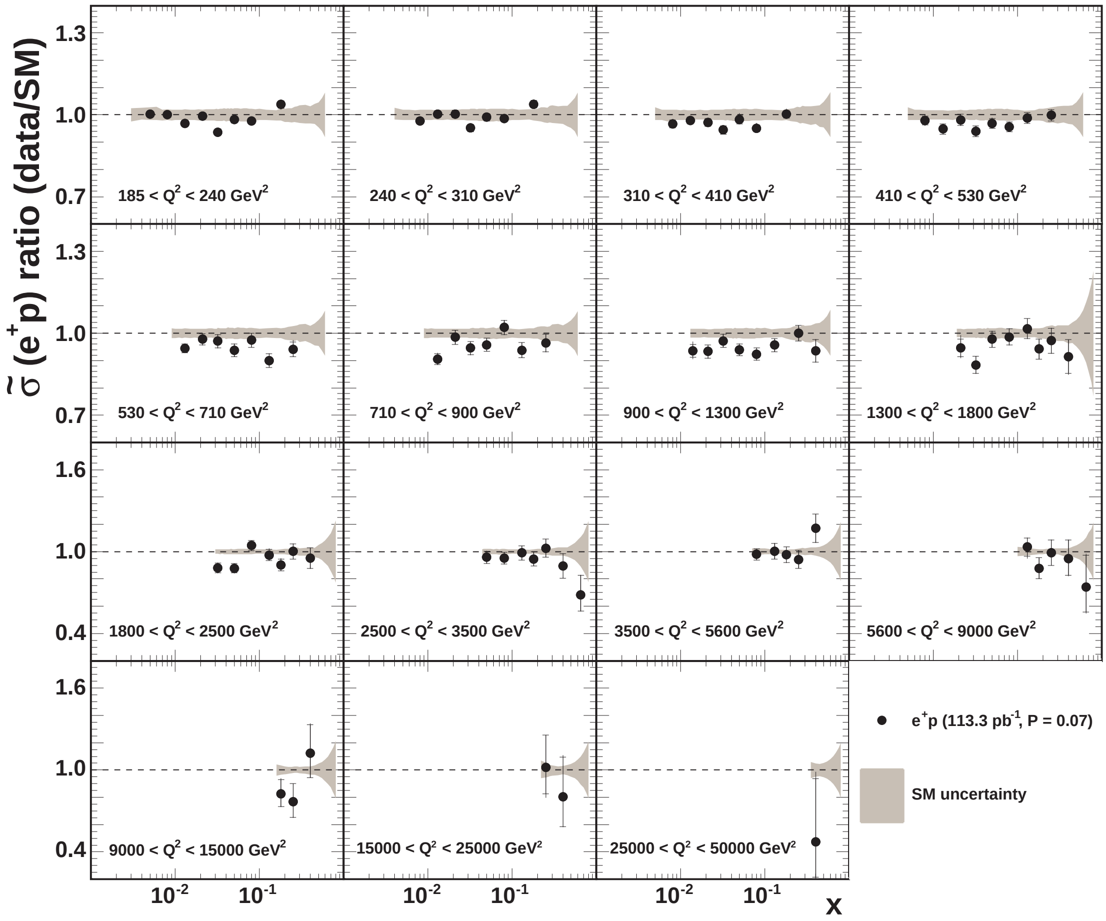

Figure 7.16: The ratio of the e^+p NC DIS reduced cross section $\tilde{\sigma}$ corresponding to the full measured sample ($\mathcal{L} = 113.3\,\text{pb}^{-1}$ and $P = 0.07$) to the theoretical prediction evaluated with the ZEUS-JETS PDFs. The shaded bands depict uncertainties of the PDF fit.

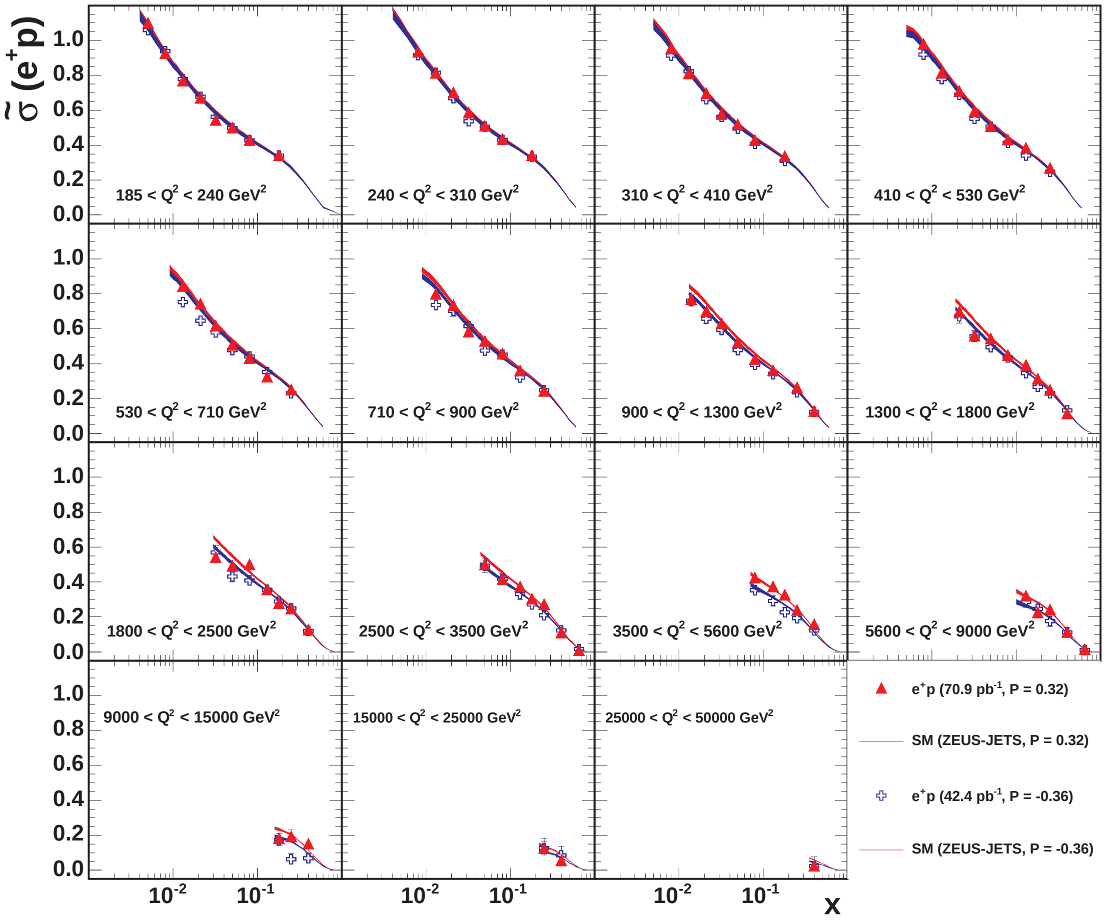

Figure 7.17: The e^+p NC DIS reduced cross section $\tilde{\sigma}$ corresponding to the samples with positively- and negatively-polarized positrons, together with the bands of the SM predictions.

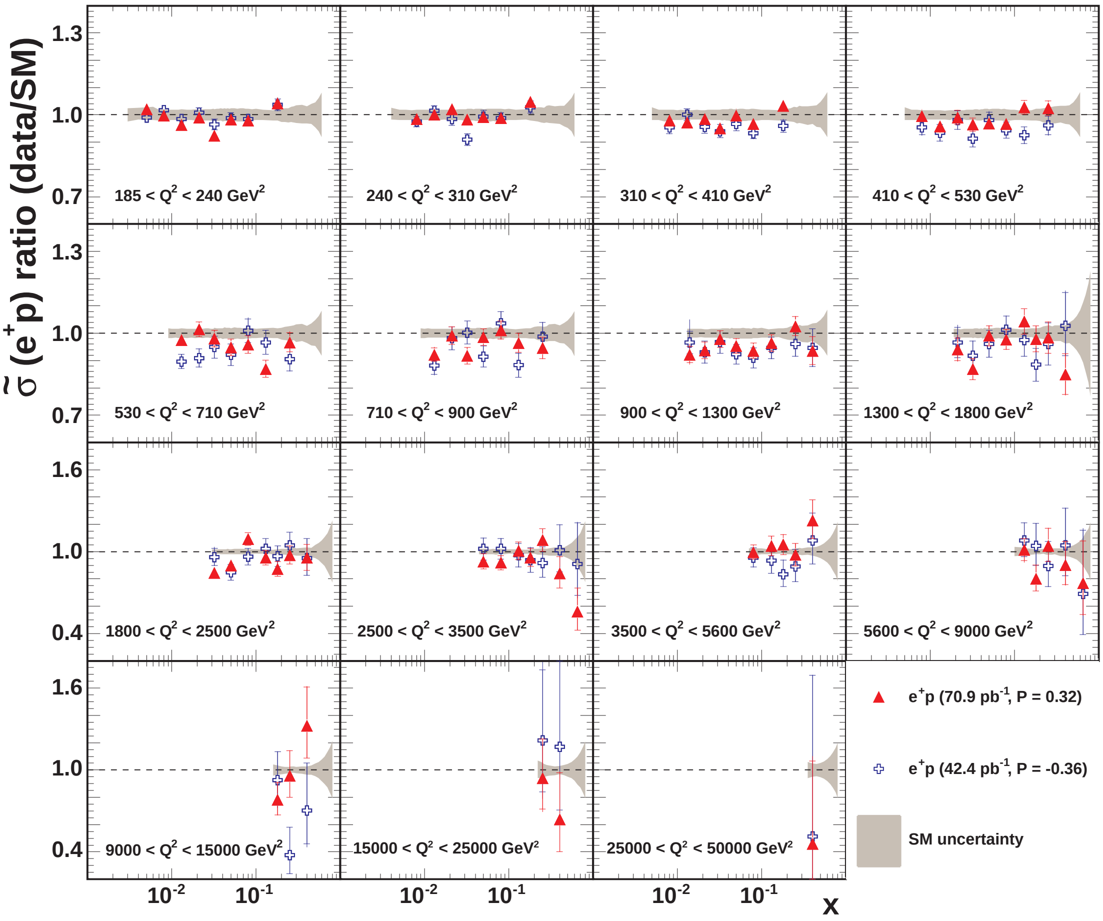

Figure 7.18: The ratio of the e^+p NC DIS reduced cross section $\tilde{\sigma}$ corresponding to the samples of positive and negative lepton-beam polarizations, to the theoretical predictions evaluated with the ZEUS-JETS PDFs. The shaded bands depict uncertainties of the PDF fit.

7.3 Extraction of $x\tilde{F}_3$ structure function

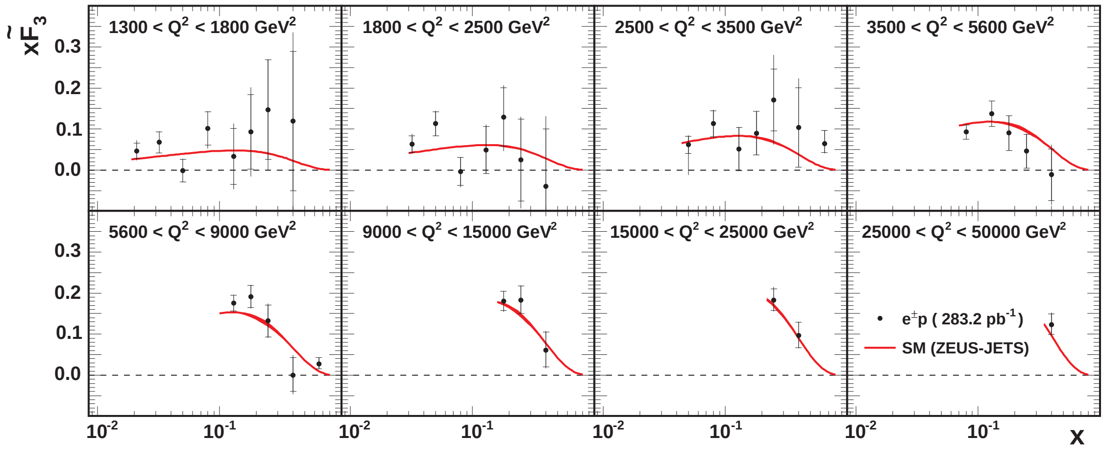

Figure 7.19: The structure function $x\tilde{F}_3$ as a function of x, in 8 bins of Q^2 corresponding to the total luminosity of $283\,\text{pb}^{-1}$. The inner error bars indicate the statistical uncertainty, the full error bars show the total uncertainty. The solid line depicts the SM prediction evaluated with the ZEUS-JETS PDFs.

The parity-violating part of the NC DIS $e^{\pm}p$ cross section with longitudinally unpolarized leptons scattering off protons is contained within the generalized $x\tilde{F}_3$ structure function. This structure function is also proportional to the valence quark content of the proton and is expected to peak at $x \sim 0.2$. In order to extract $x\tilde{F}_3$, the e^+p reduced cross section presented in Sec. 7.2.3 was re-weighted to obtain a measurement corresponding to zero polarization of the positron beam, and combined with the already mentioned recent result on the e^-p NC DIS $\tilde{\sigma}$ [59], according to Eq. 2.22, as a function of x in 8 highest-Q^2 bins. The effect of this combination is shown in Fig. 7.19 (and listed in Tab. A.11 of Appendix A). It corresponds to the total integrated luminosity of $283\,\text{pb}^{-1}$ rendering this result the most precise measurement of $x\tilde{F}_3$ to date (the previous extraction of $x\tilde{F}_3$ corresponds to the total integrated luminosity of $233\,\text{pb}^{-1}$ [59]). Compared to the previous work, two bins of lowest Q^2 were added, and therefore the kinematic region covered by this measurement is restricted by $1300 < Q^2 < 50\,000\,\text{GeV}^2$. The shape of the $x\tilde{F}_3$ structure function extracted here is very well described by the SM prediction obtained using ZEUS-JETS PDF fits.

7.4 Summary of results

Let us summarize the results of measurements of e^+p NC DIS, with longitudinally polarized positrons, presented in this chapter. The single-differential $d\sigma/dQ^2$ cross section was measured for the total analyzed sample, as well as for the partial samples of positive and negative polarization of the incoming positron beam. These partial results were used to calculate the ratio of $d\sigma/dQ^2$ corresponding to samples of positive and negative polarization, as well as the polarization asymmetry A^+, verifying the observation of parity violation in e^+p NC DIS. All results of $d\sigma/dQ^2$ measurements are in a reasonable agreement with the SM predictions. Compared to the previous ZEUS measurements (which are also the first and only published results on $d\sigma/dQ^2$ e^+p NC DIS with longitudinally polarized positrons) [207], the results presented here correspond to 4.75 times the data taken and analyzed before, yielding an increase of the statistical precision by a factor of 2.2. The violation of parity conservation and, more generally, our understanding of the structure of the standard model in e^+p NC DIS is demonstrated down to the spatial scale of $\mathcal{O}[10^{-18}\,\mathrm{m}]$.

The single-differential $d\sigma/dx$ and $d\sigma/dy$ e^+p NC DIS cross sections were measured for the first time using beams of polarized positrons. They also agree well with the SM predictions, as well as with the previously measured $d\sigma/dx$ and $d\sigma/dy$ e^+p NC DIS cross sections measured using positron beams of no longitudinal polarization, e.g. [68, 205, 208, 209]. The integrated luminosity corresponding to data used in the analysis presented here is almost twice as large as in any of the cited previous measurements.

The double-differential reduced e^+p NC DIS cross sections, in function of x and Q^2, were measured for the total analyzed sample, as well as for the samples corresponding to the positive and negative polarizations of the incoming positron beams. It is the first double-differential measurement of e^+p NC DIS at high Q^2, performed using longitudinally polarized positrons. All results confirm the SM predictions, and are in agreement with the previous measurements performed using longitudinally unpolarized positron beams [68, 205, 208, 209].

Combining $\tilde{\sigma}$ results of the e^+p NC DIS analysis presented in this thesis, with the ones of the e^-p NC DIS paper [59], the generalized $x\tilde{F}_3$ NC structure function was calculated in function of x, in 8 bins of Q^2. The total integrated luminosity of the e^+p and e^-p exploited data corresponds to $283\,\mathrm{pb}^{-1}$, making it the most precise measurement of the $x\tilde{F}_3$ structure function to date. The results are consistent with the SM predictions, as well as with the previous measurements from ZEUS and H1, as well from previous DIS experiments, e.g. NC muon-carbon scattering measured by the BCDMS collaboration [59, 68, 210].

Expected influence of the results of this analysis

Apart from the parallel NLO QCD analyses performed on ZEUS and H1 data separately, leading to releasing independent libraries of PDF fits by both collaborations (e.g. [67, 68]), a joint effort has begun, aimed at combining data from both collaborations and releasing a common HERAPDF library [28, 29], obtained with the integrated luminosity of $1\,\mathrm{fb}^{-1}$. So far, the combined data set, of NC and CC inclusive e^+p and e^-p cross sections measured using HERA I samples (corresponding to the integrated luminosity of roughly $0.25\,\mathrm{fb}^{-1}$), has been used. With the consistent treatment of systematic uncertainties, the HERAPDFs have much reduced experimental uncertainties compared to the separate analyses of the ZEUS and H1 experiments [211]. The comparison of the preliminary HERAPDF fits of the valence quarks, sea quarks and gluons, to the recent global PDF fits released by CTEQ and MSTW groups in shown in Fig. 7.20.

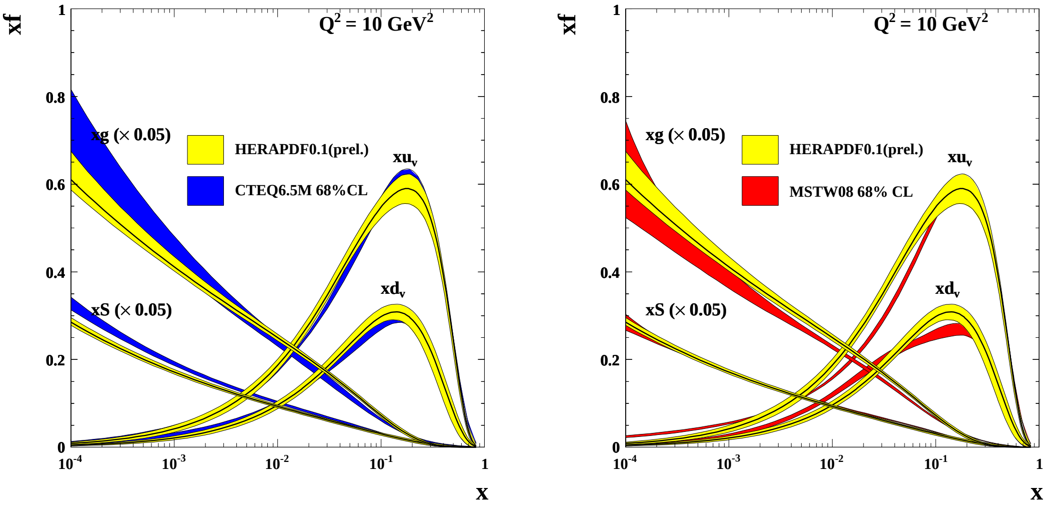

Figure 7.20: Comparison of the PDFs obtained by combining results of DIS measurements from H1 and ZEUS (HERAPDFs, so far obtained using HERA I data only) to the PDFs from CTEQ6.5 (left) and MSTW08 (right) [211].

At the same time, efforts are being invested in combining the full ZEUS DIS data (from various analyses of HERA I and HERA II periods), into a final ZEUS PDF fit. The high-Q^2 DIS data analyzed in this thesis, roughly equals to a quarter of the total integrated luminosity ever recorded by ZEUS. The reduced cross sections presented in the previous sections will therefore have a significant impact on the reduced uncertainties of the parton distributions, especially of the u-valence quark, of both the exclusive ZEUS PDF fits, as well as of the final HERAPDF fit.

In the extended version of the NLO QCD fitting procedure, electroweak NC parameters, as well as PDF parameters, are treated as free and therefore the vector and axial-vector couplings of the u and d quarks to the Z^0 boson, can be obtained from the fit (see Fig. 2.13). It is expected that adding the high-Q^2 e^+p NC DIS data of high statistics, presented in this analysis, will allow to further significantly reduce the contours of uncertainties of v_u, a_u, v_d, a_d electroweak coupling parameters.

Chapter 8

Summary

This thesis presents the measurements of the e^+p neutral current deep inelastic scattering cross sections in the kinematic region of $Q^2 > 185\,\mathrm{GeV}^2$ and $y < 0.95$, with the ZEUS data corresponding to the integrated luminosity of $\mathcal{L} = 113.3\,\mathrm{pb}^{-1}$, recorded in years 2006/07. The upgrade of the HERA collider undertaken in years 2000 - 2003 has given us the possibility to measure DIS $e^\pm p$ for the first time using longitudinally polarized lepton beams. The measurement of the polarized $d\sigma/dQ^2$ e^+p neutral current DIS presented here, is based on 4.75 times higher integrated luminosity than the first one [207]. Moreover, the measurements of $d\sigma/dx$, $d\sigma/dy$ and $\tilde{\sigma}$, presented here, are the first ever performed, of the e^+p neutral current DIS with longitudinally polarized e^+ beams. Results on the reduced double-differential cross section $\tilde{\sigma}$ are particularly interesting in context of fitting the next to leading order QCD parton density functions.

The results presented above are in agreement with the predictions of the Standard Model. The extraction of the $x\tilde{F}_3$ structure function achieved by combining the e^+p and e^-p neutral current DIS data introduces the most precise measurement of this structure function to date, further constraining our knowledge on the valence quarks in the proton. Furthermore, the measurement of the A^+ polarization asymmetry (also of unprecedented precision) confirms our understanding of the phenomenon of parity violation in e^+p neutral current DIS, down to the spatial scale of $10^{-3}\,\mathrm{fb}^{-1}$, about 1/1000 of the proton size.

The e^+p cross section and $x\tilde{F}_3$ structure function results are complementary to the (just published) e^-p neutral current DIS measurements performed with the data of integrated luminosity of $169.9\,\mathrm{pb}^{-1}$.

The measurements presented here will improve (after being formally published, which is expected for Summer of 2009) the precision of the extraction of the parton density functions via the next to leading order QCD fits (in all editions: ZEUS stand-alone, H1/ZEUS combined and the global QCD fits). Moreover they will allow further improvement in the precision of fits of the axial-vector and vector couplings of the u and d quarks to the Z^0 weak boson. Therefore, results obtained in the process of preparation of this thesis are expected to have a direct influence on the precision of parton density functions, which are currently expected to be employed e.g. in the Monte Carlo generators prepared for the measurements at the Large Hadron Collider [211].

These results will also enter as input to the effort of combination of the HERA DIS data from the H1 and ZEUS experiments recorded over 15 years of running of this unique machine. The analysis aimed at obtaining reduced DIS cross sections corresponding to the integrated luminosity of $1\,\text{fb}^{-1}$ (about half from each experiment) has begun [28], and will result in releasing combined H1/ZEUS next to leading order QCD parton density functions [29], based exclusively on full HERA inclusive data.

Appendix A

Tables of cross sections

$Q^2 >$ [GeV^2]	x range	x_c	$d\sigma/dx$ [pb]		N_{DATA}	N_{MC}	N_{MC}^{bg}	eff	pur
			measured ($P = 0.07$)	SM ($P = 0$)					
185	$0.006 - 0.010$	0.008	$(8.50\ ^{+0.05}_{-0.05}\ ^{+0.07}_{-0.06}) \cdot 10^4$	$8.82 \cdot 10^4$	26737	27605	140	0.46	0.66
	$0.010 - 0.016$	0.013	$(5.67\ ^{+0.03}_{-0.03}\ ^{+0.04}_{-0.03}) \cdot 10^4$	$5.87 \cdot 10^4$	30283	31268	112	0.50	0.68
	$0.016 - 0.025$	0.020	$(3.56\ ^{+0.02}_{-0.02}\ ^{+0.02}_{-0.02}) \cdot 10^4$	$3.65 \cdot 10^4$	29808	30454	66	0.50	0.66
	$0.025 - 0.040$	0.032	$(2.06\ ^{+0.01}_{-0.01}\ ^{+0.01}_{-0.01}) \cdot 10^4$	$2.18 \cdot 10^4$	28854	30547	26	0.51	0.66
	$0.040 - 0.063$	0.050	$(1.21\ ^{+0.01}_{-0.01}\ ^{+0.01}_{-0.01}) \cdot 10^4$	$1.26 \cdot 10^4$	25329	26245	13	0.50	0.67
	$0.063 - 0.100$	0.079	$(6.83\ ^{+0.04}_{-0.04}\ ^{+0.04}_{-0.04}) \cdot 10^3$	$7.11 \cdot 10^3$	24143	25113	10	0.51	0.65
	$0.10 - 0.16$	0.13	$(3.89\ ^{+0.03}_{-0.03}\ ^{+0.03}_{-0.02}) \cdot 10^3$	$3.91 \cdot 10^3$	22993	23111	1	0.50	0.62
	$0.16 - 0.25$	0.20	$(2.05\ ^{+0.02}_{-0.02}\ ^{+0.02}_{-0.02}) \cdot 10^3$	$2.02 \cdot 10^3$	14754	14589	1	0.42	0.64
3000	$0.025 - 0.040$	0.032	$(9.16\ ^{+1.36}_{-1.19}\ ^{+1.26}_{-0.90}) \cdot 10^0$	$10.99 \cdot 10^0$	58	69	1	0.24	0.43
	$0.040 - 0.063$	0.050	$(1.79\ ^{+0.09}_{-0.09}\ ^{+0.03}_{-0.01}) \cdot 10^2$	$1.78 \cdot 10^2$	411	409	3	0.55	0.71
	$0.063 - 0.100$	0.079	$(1.61\ ^{+0.06}_{-0.06}\ ^{+0.02}_{-0.01}) \cdot 10^2$	$1.67 \cdot 10^2$	616	638	4	0.64	0.77
	$0.10 - 0.16$	0.13	$(1.21\ ^{+0.04}_{-0.04}\ ^{+0.01}_{-0.01}) \cdot 10^2$	$1.19 \cdot 10^2$	748	735	0	0.67	0.80
	$0.16 - 0.25$	0.20	$(6.75\ ^{+0.27}_{-0.27}\ ^{+0.06}_{-0.06}) \cdot 10^1$	$7.16 \cdot 10^1$	617	654	1	0.68	0.82
	$0.25 - 0.40$	0.32	$(3.32\ ^{+0.15}_{-0.15}\ ^{+0.02}_{-0.03}) \cdot 10^1$	$3.37 \cdot 10^1$	491	499	0	0.67	0.84
	$0.40 - 0.63$	0.50	$(8.47\ ^{+0.62}_{-0.62}\ ^{+0.11}_{-0.15}) \cdot 10^0$	$8.50 \cdot 10^0$	187	188	0	0.63	0.82
	$0.63 - 1.00$	0.79	$(1.71\ ^{+0.65}_{-0.49}\ ^{+0.10}_{-0.22}) \cdot 10^{-1}$	$2.15 \cdot 10^{-1}$	12	15	0	0.45	0.56

Table A.1: The single-differential e^+p NC DIS cross section $d\sigma/dx$ (for $y < 0.95$), for $Q^2 > 185\,\mathrm{GeV}^2$ and $Q^2 > 3000\,\mathrm{GeV}^2$, corresponding to $\mathcal{L} = 113.3\,\mathrm{pb}^{-1}, P = 0.07$. The columns contain: the lower Q^2 limit, x-bin range, x-bin center, the cross section measured at the Born level (the first error on the cross section corresponds to the statistical, while the second to the systematic uncertainty), the theoretical cross section at $P = 0.0$ used for the unfolding procedure (SM, calculated with CTEQ5D PDFs), the number of observed data (N_{DATA}), signal MC (N_{MC}) and background MC (N_{MC}^{bg}) events, efficiency and purity, for a given x bin.

$Q^2 >$	y range	y_c	$d\sigma/dy$ [pb]		N_{DATA}	N_{MC}	N^{bg}_{MC}	eff	pur
[GeV^2]			measured ($P = 0.07$)	SM ($P = 0$)					
185	$0.00 - 0.05$	0.03	$(1.62\ ^{+0.01}_{-0.01}\ ^{+0.01}_{-0.01}) \cdot 10^4$	$1.64 \cdot 10^4$	55425	56122	4	0.60	0.84
	$0.05 - 0.10$	0.08	$(7.97\ ^{+0.04}_{-0.04}\ ^{+0.06}_{-0.06}) \cdot 10^3$	$8.30 \cdot 10^3$	37437	39001	3	0.55	0.74
	$0.10 - 0.15$	0.13	$(5.53\ ^{+0.03}_{-0.03}\ ^{+0.04}_{-0.03}) \cdot 10^3$	$5.74 \cdot 10^3$	26045	27010	3	0.50	0.66
	$0.15 - 0.20$	0.18	$(4.30\ ^{+0.03}_{-0.03}\ ^{+0.02}_{-0.02}) \cdot 10^3$	$4.41 \cdot 10^3$	19747	20240	8	0.46	0.61
	$0.20 - 0.25$	0.23	$(3.57\ ^{+0.03}_{-0.03}\ ^{+0.02}_{-0.02}) \cdot 10^3$	$3.59 \cdot 10^3$	16060	16139	4	0.43	0.58
	$0.25 - 0.30$	0.28	$(2.90\ ^{+0.03}_{-0.03}\ ^{+0.01}_{-0.02}) \cdot 10^3$	$3.01 \cdot 10^3$	12719	13170	7	0.39	0.55
	$0.30 - 0.35$	0.33	$(2.50\ ^{+0.02}_{-0.02}\ ^{+0.01}_{-0.01}) \cdot 10^3$	$2.57 \cdot 10^3$	11007	11330	14	0.37	0.51
	$0.35 - 0.40$	0.38	$(2.17\ ^{+0.02}_{-0.02}\ ^{+0.01}_{-0.01}) \cdot 10^3$	$2.24 \cdot 10^3$	9746	10024	17	0.35	0.48
	$0.40 - 0.45$	0.43	$(1.93\ ^{+0.02}_{-0.02}\ ^{+0.01}_{-0.01}) \cdot 10^3$	$1.97 \cdot 10^3$	8573	8739	29	0.33	0.45
	$0.45 - 0.50$	0.48	$(1.65\ ^{+0.02}_{-0.02}\ ^{+0.01}_{-0.01}) \cdot 10^3$	$1.76 \cdot 10^3$	7345	7752	55	0.32	0.44
	$0.50 - 0.55$	0.53	$(1.47\ ^{+0.02}_{-0.02}\ ^{+0.01}_{-0.01}) \cdot 10^3$	$1.58 \cdot 10^3$	6384	6815	46	0.30	0.43
	$0.55 - 0.60$	0.58	$(1.33\ ^{+0.02}_{-0.02}\ ^{+0.02}_{-0.01}) \cdot 10^3$	$1.42 \cdot 10^3$	5611	5971	39	0.29	0.43
	$0.60 - 0.65$	0.63	$(1.18\ ^{+0.02}_{-0.02}\ ^{+0.02}_{-0.02}) \cdot 10^3$	$1.29 \cdot 10^3$	4635	5029	51	0.28	0.45
	$0.65 - 0.70$	0.68	$(1.07\ ^{+0.02}_{-0.02}\ ^{+0.06}_{-0.03}) \cdot 10^3$	$1.18 \cdot 10^3$	3711	4036	44	0.26	0.48
	$0.70 - 0.75$	0.73	$(9.97\ ^{+0.19}_{-0.19}\ ^{+0.78}_{-0.47}) \cdot 10^2$	$10.85 \cdot 10^2$	2791	2998	34	0.21	0.49
3000	$0.05 - 0.10$	0.08	$(3.20\ ^{+0.27}_{-0.27}\ ^{+0.04}_{-0.05}) \cdot 10^1$	$3.08 \cdot 10^1$	145	140	0	0.62	0.82
	$0.10 - 0.15$	0.13	$(5.74\ ^{+0.34}_{-0.34}\ ^{+0.05}_{-0.09}) \cdot 10^1$	$5.76 \cdot 10^1$	284	285	0	0.64	0.80
	$0.15 - 0.20$	0.18	$(6.13\ ^{+0.35}_{-0.35}\ ^{+0.04}_{-0.06}) \cdot 10^1$	$6.12 \cdot 10^1$	315	313	1	0.63	0.77
	$0.20 - 0.25$	0.23	$(5.77\ ^{+0.33}_{-0.33}\ ^{+0.05}_{-0.08}) \cdot 10^1$	$5.73 \cdot 10^1$	300	298	0	0.61	0.74
	$0.25 - 0.30$	0.28	$(4.91\ ^{+0.30}_{-0.30}\ ^{+0.02}_{-0.06}) \cdot 10^1$	$5.22 \cdot 10^1$	260	276	0	0.60	0.71
	$0.30 - 0.35$	0.33	$(5.02\ ^{+0.31}_{-0.31}\ ^{+0.07}_{-0.07}) \cdot 10^1$	$4.68 \cdot 10^1$	267	249	0	0.58	0.68
	$0.35 - 0.40$	0.38	$(3.66\ ^{+0.26}_{-0.26}\ ^{+0.07}_{-0.03}) \cdot 10^1$	$4.19 \cdot 10^1$	195	223	0	0.57	0.66
	$0.40 - 0.45$	0.43	$(3.56\ ^{+0.26}_{-0.26}\ ^{+0.05}_{-0.05}) \cdot 10^1$	$3.77 \cdot 10^1$	190	201	0	0.56	0.66
	$0.45 - 0.50$	0.48	$(3.57\ ^{+0.26}_{-0.26}\ ^{+0.07}_{-0.05}) \cdot 10^1$	$3.40 \cdot 10^1$	190	181	0	0.55	0.65
	$0.50 - 0.55$	0.53	$(2.82\ ^{+0.23}_{-0.23}\ ^{+0.08}_{-0.02}) \cdot 10^1$	$3.09 \cdot 10^1$	148	162	0	0.54	0.64
	$0.55 - 0.60$	0.58	$(2.97\ ^{+0.24}_{-0.24}\ ^{+0.04}_{-0.03}) \cdot 10^1$	$2.82 \cdot 10^1$	157	149	0	0.54	0.63
	$0.60 - 0.65$	0.63	$(2.57\ ^{+0.22}_{-0.22}\ ^{+0.03}_{-0.07}) \cdot 10^1$	$2.57 \cdot 10^1$	136	136	0	0.53	0.63
	$0.65 - 0.70$	0.68	$(2.20\ ^{+0.21}_{-0.21}\ ^{+0.03}_{-0.04}) \cdot 10^1$	$2.38 \cdot 10^1$	113	122	0	0.52	0.62
	$0.70 - 0.75$	0.73	$(2.22\ ^{+0.21}_{-0.21}\ ^{+0.07}_{-0.07}) \cdot 10^1$	$2.21 \cdot 10^1$	112	111	0	0.51	0.62
	$0.75 - 0.80$	0.78	$(2.10\ ^{+0.21}_{-0.21}\ ^{+0.07}_{-0.05}) \cdot 10^1$	$2.07 \cdot 10^1$	104	103	0	0.50	0.62
	$0.80 - 0.85$	0.83	$(1.71\ ^{+0.21}_{-0.19}\ ^{+0.05}_{-0.07}) \cdot 10^1$	$1.95 \cdot 10^1$	82	92	1	0.48	0.62
	$0.85 - 0.90$	0.88	$(1.62\ ^{+0.21}_{-0.19}\ ^{+0.08}_{-0.18}) \cdot 10^1$	$1.95 \cdot 10^1$	80	86	5	0.47	0.61

Table A.2: The single-differential e^+p NC DIS cross section $d\sigma/dy$, for $Q^2 > 185\,\mathrm{GeV}^2$ and $Q^2 > 3000\,\mathrm{GeV}^2$, corresponding to $\mathcal{L} = 113.3\,\mathrm{pb}^{-1}, P = 0.07$. The columns contain: the lower Q^2 limit, y-bin range, y-bin center, the cross section measured at the Born level (the first error on the cross section corresponds to the statistical, while the second to the systematic uncertainty), the theoretical cross section at $P = 0.0$ used for the unfolding procedure (SM, calculated with CTEQ5D PDFs), the number of observed data (N_{DATA}), signal MC (N_{MC}) and background MC (N^{bg}_{MC}) events, efficiency and purity, for a given y bin.

Q^2 range [GeV^2]	Q^2_c [GeV^2]	$d\sigma/dQ^2$ [pb/ GeV^2] measured ($P = 0.07$)	SM ($P = 0$)	N_{DATA}	N_{MC}	N^{bg}_{MC}	eff	pur
$185 - 210$	195	$(1.94\,^{+0.01}_{-0.01}\,^{+0.02}_{-0.02}) \cdot 10^{1}$	$2.00 \cdot 10^{1}$	38087	39097	38	0.43	0.63
$210 - 240$	220	$(1.47\,^{+0.01}_{-0.01}\,^{+0.01}_{-0.01}) \cdot 10^{1}$	$1.50 \cdot 10^{1}$	33709	34348	35	0.45	0.66
$240 - 270$	255	$(1.03\,^{+0.01}_{-0.01}\,^{+0.01}_{-0.01}) \cdot 10^{1}$	$1.06 \cdot 10^{1}$	25022	25532	20	0.44	0.65
$270 - 300$	285	$(7.96\,^{+0.06}_{-0.06}\,^{+0.07}_{-0.07}) \cdot 10^{0}$	$8.10 \cdot 10^{0}$	19248	19563	20	0.43	0.64
$300 - 340$	320	$(5.95\,^{+0.04}_{-0.04}\,^{+0.06}_{-0.05}) \cdot 10^{0}$	$6.13 \cdot 10^{0}$	19317	19877	22	0.46	0.68
$340 - 380$	360	$(4.46\,^{+0.04}_{-0.04}\,^{+0.04}_{-0.04}) \cdot 10^{0}$	$4.62 \cdot 10^{0}$	14357	14876	21	0.44	0.67
$380 - 430$	400	$(3.39\,^{+0.03}_{-0.03}\,^{+0.03}_{-0.03}) \cdot 10^{0}$	$3.56 \cdot 10^{0}$	13270	13914	24	0.45	0.69
$430 - 480$	450	$(2.61\,^{+0.03}_{-0.03}\,^{+0.02}_{-0.02}) \cdot 10^{0}$	$2.69 \cdot 10^{0}$	9947	10236	25	0.43	0.67
$480 - 540$	510	$(1.89\,^{+0.02}_{-0.02}\,^{+0.02}_{-0.02}) \cdot 10^{0}$	$1.98 \cdot 10^{0}$	8486	8845	26	0.41	0.67
$540 - 600$	570	$(1.38\,^{+0.02}_{-0.02}\,^{+0.01}_{-0.01}) \cdot 10^{0}$	$1.50 \cdot 10^{0}$	5599	6066	34	0.34	0.64
$600 - 670$	630	$(1.12\,^{+0.02}_{-0.02}\,^{+0.01}_{-0.01}) \cdot 10^{0}$	$1.17 \cdot 10^{0}$	5104	5302	31	0.33	0.62
$670 - 740$	700	$(8.63\,^{+0.13}_{-0.13}\,^{+0.07}_{-0.08}) \cdot 10^{-1}$	$9.06 \cdot 10^{-1}$	4633	4849	18	0.39	0.62
$740 - 820$	780	$(6.62\,^{+0.10}_{-0.10}\,^{+0.05}_{-0.05}) \cdot 10^{-1}$	$6.90 \cdot 10^{-1}$	4821	5002	23	0.47	0.65
$820 - 900$	860	$(5.12\,^{+0.08}_{-0.08}\,^{+0.06}_{-0.03}) \cdot 10^{-1}$	$5.40 \cdot 10^{-1}$	3976	4171	14	0.49	0.63
$900 - 990$	940	$(4.16\,^{+0.07}_{-0.07}\,^{+0.03}_{-0.02}) \cdot 10^{-1}$	$4.31 \cdot 10^{-1}$	3689	3808	13	0.51	0.64
$990 - 1080$	1030	$(3.16\,^{+0.06}_{-0.06}\,^{+0.03}_{-0.02}) \cdot 10^{-1}$	$3.42 \cdot 10^{-1}$	2824	3033	21	0.50	0.62
$1080 - 1200$	1130	$(2.57\,^{+0.05}_{-0.05}\,^{+0.02}_{-0.02}) \cdot 10^{-1}$	$2.71 \cdot 10^{-1}$	3059	3213	14	0.53	0.65
$1200 - 1350$	1270	$(1.95\,^{+0.04}_{-0.04}\,^{+0.01}_{-0.02}) \cdot 10^{-1}$	$2.00 \cdot 10^{-1}$	2956	3020	16	0.54	0.68
$1350 - 1500$	1420	$(1.41\,^{+0.03}_{-0.03}\,^{+0.01}_{-0.01}) \cdot 10^{-1}$	$1.50 \cdot 10^{-1}$	2143	2281	10	0.53	0.65
$1500 - 1700$	1590	$(1.09\,^{+0.02}_{-0.02}\,^{+0.01}_{-0.01}) \cdot 10^{-1}$	$1.12 \cdot 10^{-1}$	2221	2261	13	0.56	0.69
$1700 - 1900$	1790	$(7.74\,^{+0.20}_{-0.20}\,^{+0.10}_{-0.08}) \cdot 10^{-2}$	$8.22 \cdot 10^{-2}$	1583	1665	15	0.55	0.67
$1900 - 2100$	1990	$(5.82\,^{+0.17}_{-0.17}\,^{+0.05}_{-0.06}) \cdot 10^{-2}$	$6.21 \cdot 10^{-2}$	1183	1257	5	0.53	0.65
$2100 - 2600$	2300	$(4.08\,^{+0.09}_{-0.09}\,^{+0.02}_{-0.03}) \cdot 10^{-2}$	$4.22 \cdot 10^{-2}$	2031	2086	15	0.63	0.77
$2600 - 3200$	2800	$(2.34\,^{+0.06}_{-0.06}\,^{+0.02}_{-0.02}) \cdot 10^{-2}$	$2.47 \cdot 10^{-2}$	1355	1418	13	0.63	0.77
$3200 - 3900$	3500	$(1.35\,^{+0.04}_{-0.04}\,^{+0.03}_{-0.01}) \cdot 10^{-2}$	$1.33 \cdot 10^{-2}$	954	944	1	0.62	0.76
$3900 - 4700$	4200	$(8.15\,^{+0.32}_{-0.32}\,^{+0.05}_{-0.04}) \cdot 10^{-3}$	$7.97 \cdot 10^{-3}$	640	625	1	0.61	0.76
$4700 - 5600$	5100	$(4.19\,^{+0.21}_{-0.21}\,^{+0.05}_{-0.05}) \cdot 10^{-3}$	$4.53 \cdot 10^{-3}$	384	413	2	0.60	0.74
$5600 - 6600$	6050	$(2.74\,^{+0.16}_{-0.16}\,^{+0.07}_{-0.03}) \cdot 10^{-3}$	$2.71 \cdot 10^{-3}$	281	277	1	0.59	0.73
$6600 - 7800$	7100	$(1.47\,^{+0.11}_{-0.11}\,^{+0.05}_{-0.03}) \cdot 10^{-3}$	$1.66 \cdot 10^{-3}$	175	198	0	0.59	0.74
$7800 - 9200$	8400	$(9.88\,^{+0.84}_{-0.84}\,^{+0.21}_{-0.41}) \cdot 10^{-4}$	$9.64 \cdot 10^{-4}$	140	133	3	0.58	0.74
$9200 - 12800$	10800	$(3.40\,^{+0.31}_{-0.31}\,^{+0.13}_{-0.05}) \cdot 10^{-4}$	$4.13 \cdot 10^{-4}$	120	146	0	0.62	0.81
$12800 - 50000$	25300	$(1.10\,^{+0.14}_{-0.13}\,^{+0.05}_{-0.04}) \cdot 10^{-5}$	$1.25 \cdot 10^{-5}$	73	83	0	0.60	0.86

Table A.3: The single-differential e^+p NC DIS cross section $d\sigma/dQ^2$, for $Q^2 > 185\,\mathrm{GeV}^2$ and $y < 0.95$, corresponding to $\mathcal{L} = 113.3\,\mathrm{pb}^{-1}, P = 0.07$. The columns contain: the Q^2-bin range, Q^2-bin center, the cross section measured at the Born level (the first error on the cross section corresponds to the statistical, while the second to the systematic uncertainty), the theoretical cross section at $P = 0.0$ used for the unfolding procedure (SM, calculated with CTEQ5D PDFs), the number of observed data (N_{DATA}), signal MC (N_{MC}) and background MC (N^{bg}_{MC}) events, efficiency and purity, for a given (Q^2) bin.

Q^2 range	Q^2_c	$d\sigma/dQ^2$ [pb/ GeV^2]		N_{DATA}	N_{MC}	N^{bg}_{MC}	eff	pur
[GeV^2]	[GeV^2]	measured ($P = 0.32$)	SM ($P = 0$)					
$185 - 210$	195	$(1.95\,^{+0.01}_{-0.01}\,^{+0.02}_{-0.02}) \cdot 10^{1}$	$2.00 \cdot 10^{1}$	23920	24522	24	0.43	0.63
$210 - 240$	220	$(1.47\,^{+0.01}_{-0.01}\,^{+0.01}_{-0.01}) \cdot 10^{1}$	$1.50 \cdot 10^{1}$	21195	21542	23	0.45	0.66
$240 - 270$	255	$(1.04\,^{+0.01}_{-0.01}\,^{+0.01}_{-0.01}) \cdot 10^{1}$	$1.06 \cdot 10^{1}$	15805	16013	13	0.44	0.65
$270 - 300$	285	$(8.09\,^{+0.07}_{-0.07}\,^{+0.07}_{-0.07}) \cdot 10^{0}$	$8.10 \cdot 10^{0}$	12265	12269	13	0.43	0.64
$300 - 340$	320	$(5.99\,^{+0.05}_{-0.05}\,^{+0.06}_{-0.05}) \cdot 10^{0}$	$6.13 \cdot 10^{0}$	12189	12465	13	0.46	0.68
$340 - 380$	360	$(4.53\,^{+0.05}_{-0.05}\,^{+0.04}_{-0.04}) \cdot 10^{0}$	$4.62 \cdot 10^{0}$	9156	9328	13	0.44	0.67
$380 - 430$	400	$(3.49\,^{+0.04}_{-0.04}\,^{+0.03}_{-0.03}) \cdot 10^{0}$	$3.56 \cdot 10^{0}$	8567	8726	15	0.45	0.69
$430 - 480$	450	$(2.64\,^{+0.03}_{-0.03}\,^{+0.02}_{-0.02}) \cdot 10^{0}$	$2.69 \cdot 10^{0}$	6318	6422	16	0.43	0.67
$480 - 540$	510	$(1.95\,^{+0.03}_{-0.03}\,^{+0.02}_{-0.02}) \cdot 10^{0}$	$1.98 \cdot 10^{0}$	5478	5550	16	0.41	0.67
$540 - 600$	570	$(1.42\,^{+0.02}_{-0.02}\,^{+0.01}_{-0.01}) \cdot 10^{0}$	$1.50 \cdot 10^{0}$	3625	3806	21	0.34	0.64
$600 - 670$	630	$(1.16\,^{+0.02}_{-0.02}\,^{+0.01}_{-0.01}) \cdot 10^{0}$	$1.17 \cdot 10^{0}$	3305	3326	20	0.33	0.62
$670 - 740$	700	$(8.77\,^{+0.16}_{-0.16}\,^{+0.07}_{-0.08}) \cdot 10^{-1}$	$9.06 \cdot 10^{-1}$	2954	3042	11	0.39	0.62
$740 - 820$	780	$(6.72\,^{+0.12}_{-0.12}\,^{+0.05}_{-0.05}) \cdot 10^{-1}$	$6.90 \cdot 10^{-1}$	3069	3138	14	0.47	0.65
$820 - 900$	860	$(5.23\,^{+0.10}_{-0.10}\,^{+0.06}_{-0.03}) \cdot 10^{-1}$	$5.40 \cdot 10^{-1}$	2543	2616	9	0.49	0.63
$900 - 990$	940	$(4.28\,^{+0.09}_{-0.09}\,^{+0.03}_{-0.02}) \cdot 10^{-1}$	$4.31 \cdot 10^{-1}$	2378	2388	9	0.51	0.64
$990 - 1080$	1030	$(3.30\,^{+0.08}_{-0.08}\,^{+0.03}_{-0.02}) \cdot 10^{-1}$	$3.42 \cdot 10^{-1}$	1846	1902	14	0.50	0.62
$1080 - 1200$	1130	$(2.63\,^{+0.06}_{-0.06}\,^{+0.02}_{-0.02}) \cdot 10^{-1}$	$2.71 \cdot 10^{-1}$	1962	2015	9	0.53	0.65
$1200 - 1350$	1270	$(1.99\,^{+0.05}_{-0.05}\,^{+0.01}_{-0.02}) \cdot 10^{-1}$	$2.00 \cdot 10^{-1}$	1893	1895	10	0.54	0.68
$1350 - 1500$	1420	$(1.40\,^{+0.04}_{-0.04}\,^{+0.01}_{-0.01}) \cdot 10^{-1}$	$1.50 \cdot 10^{-1}$	1339	1431	6	0.53	0.65
$1500 - 1700$	1590	$(1.15\,^{+0.03}_{-0.03}\,^{+0.01}_{-0.01}) \cdot 10^{-1}$	$1.12 \cdot 10^{-1}$	1457	1418	8	0.56	0.69
$1700 - 1900$	1790	$(7.91\,^{+0.25}_{-0.25}\,^{+0.10}_{-0.08}) \cdot 10^{-2}$	$8.22 \cdot 10^{-2}$	1014	1044	9	0.55	0.67
$1900 - 2100$	1990	$(6.04\,^{+0.22}_{-0.22}\,^{+0.05}_{-0.06}) \cdot 10^{-2}$	$6.21 \cdot 10^{-2}$	770	789	3	0.53	0.65
$2100 - 2600$	2300	$(4.18\,^{+0.12}_{-0.12}\,^{+0.02}_{-0.03}) \cdot 10^{-2}$	$4.22 \cdot 10^{-2}$	1307	1308	9	0.63	0.77
$2600 - 3200$	2800	$(2.41\,^{+0.08}_{-0.08}\,^{+0.02}_{-0.02}) \cdot 10^{-2}$	$2.47 \cdot 10^{-2}$	875	890	8	0.63	0.77
$3200 - 3900$	3500	$(1.41\,^{+0.06}_{-0.06}\,^{+0.03}_{-0.01}) \cdot 10^{-2}$	$1.33 \cdot 10^{-2}$	626	592	1	0.62	0.76
$3900 - 4700$	4200	$(8.90\,^{+0.43}_{-0.43}\,^{+0.06}_{-0.05}) \cdot 10^{-3}$	$7.97 \cdot 10^{-3}$	438	392	1	0.61	0.76
$4700 - 5600$	5100	$(4.57\,^{+0.28}_{-0.28}\,^{+0.05}_{-0.06}) \cdot 10^{-3}$	$4.53 \cdot 10^{-3}$	263	259	1	0.60	0.74
$5600 - 6600$	6050	$(2.87\,^{+0.21}_{-0.21}\,^{+0.07}_{-0.03}) \cdot 10^{-3}$	$2.71 \cdot 10^{-3}$	185	174	1	0.59	0.73
$6600 - 7800$	7100	$(1.52\,^{+0.14}_{-0.14}\,^{+0.06}_{-0.03}) \cdot 10^{-3}$	$1.66 \cdot 10^{-3}$	114	124	0	0.59	0.74
$7800 - 9200$	8400	$(1.07\,^{+0.12}_{-0.11}\,^{+0.02}_{-0.04}) \cdot 10^{-3}$	$0.96 \cdot 10^{-3}$	95	84	2	0.58	0.74
$9200 - 12800$	10800	$(3.71\,^{+0.46}_{-0.41}\,^{+0.15}_{-0.06}) \cdot 10^{-4}$	$4.13 \cdot 10^{-4}$	82	91	0	0.62	0.81
$12800 - 50000$	25300	$(1.23\,^{+0.20}_{-0.17}\,^{+0.05}_{-0.04}) \cdot 10^{-5}$	$1.25 \cdot 10^{-5}$	51	52	0	0.60	0.86

Table A.4: The single-differential e^+p NC DIS cross section $d\sigma/dQ^2$, for $Q^2 > 185\,\text{GeV}^2$ and $y < 0.95$, corresponding to $\mathcal{L} = 70.9\,\text{pb}^{-1}, P = 0.32$. The columns contain: the Q^2-bin range, Q^2-bin center, the cross section measured at the Born level (the first error on the cross section corresponds to the statistical, while the second to the systematic uncertainty), the theoretical cross section at $P = 0.0$ used for the unfolding procedure (SM, calculated with CTEQ5D PDFs), the number of observed data (N_{DATA}), signal MC (N_{MC}) and background MC (N^{bg}_{MC}) events, efficiency and purity, for a given (Q^2) bin.

Q^2 range [GeV^2]	Q^2_c [GeV^2]	$d\sigma/dQ^2$ [pb/ GeV^2]		N_{DATA}	N_{MC}	N^{bg}_{MC}	eff	pur
		measured ($P = -0.36$)	SM ($P = 0$)					
$185 - 210$	195	$(1.95\ ^{+0.02}_{-0.02}\ ^{+0.02}_{-0.01}) \cdot 10^{1}$	$2.00 \cdot 10^{1}$	14167	14474	14	0.43	0.63
$210 - 240$	220	$(1.47\ ^{+0.01}_{-0.01}\ ^{+0.01}_{-0.01}) \cdot 10^{1}$	$1.50 \cdot 10^{1}$	12514	12713	13	0.45	0.66
$240 - 270$	255	$(1.03\ ^{+0.01}_{-0.01}\ ^{+0.01}_{-0.01}) \cdot 10^{1}$	$1.06 \cdot 10^{1}$	9217	9450	8	0.44	0.65
$270 - 300$	285	$(7.80\ ^{+0.09}_{-0.09}\ ^{+0.07}_{-0.06}) \cdot 10^{0}$	$8.10 \cdot 10^{0}$	6983	7240	8	0.43	0.64
$300 - 340$	320	$(5.93\ ^{+0.07}_{-0.07}\ ^{+0.05}_{-0.05}) \cdot 10^{0}$	$6.13 \cdot 10^{0}$	7128	7355	8	0.46	0.68
$340 - 380$	360	$(4.36\ ^{+0.06}_{-0.06}\ ^{+0.04}_{-0.04}) \cdot 10^{0}$	$4.62 \cdot 10^{0}$	5201	5506	8	0.44	0.67
$380 - 430$	400	$(3.24\ ^{+0.05}_{-0.05}\ ^{+0.03}_{-0.02}) \cdot 10^{0}$	$3.56 \cdot 10^{0}$	4703	5147	9	0.45	0.69
$430 - 480$	450	$(2.57\ ^{+0.04}_{-0.04}\ ^{+0.03}_{-0.03}) \cdot 10^{0}$	$2.69 \cdot 10^{0}$	3629	3787	10	0.43	0.67
$480 - 540$	510	$(1.81\ ^{+0.03}_{-0.03}\ ^{+0.02}_{-0.01}) \cdot 10^{0}$	$1.98 \cdot 10^{0}$	3008	3270	10	0.41	0.67
$540 - 600$	570	$(1.31\ ^{+0.03}_{-0.03}\ ^{+0.01}_{-0.01}) \cdot 10^{0}$	$1.50 \cdot 10^{0}$	1974	2241	13	0.34	0.64
$600 - 670$	630	$(1.06\ ^{+0.03}_{-0.03}\ ^{+0.01}_{-0.01}) \cdot 10^{0}$	$1.17 \cdot 10^{0}$	1799	1973	12	0.33	0.62
$670 - 740$	700	$(8.36\ ^{+0.20}_{-0.20}\ ^{+0.07}_{-0.11}) \cdot 10^{-1}$	$9.06 \cdot 10^{-1}$	1679	1814	7	0.39	0.62
$740 - 820$	780	$(6.46\ ^{+0.15}_{-0.15}\ ^{+0.04}_{-0.05}) \cdot 10^{-1}$	$6.90 \cdot 10^{-1}$	1752	1863	8	0.47	0.65
$820 - 900$	860	$(4.98\ ^{+0.13}_{-0.13}\ ^{+0.05}_{-0.03}) \cdot 10^{-1}$	$5.40 \cdot 10^{-1}$	1433	1548	5	0.49	0.63
$900 - 990$	940	$(3.99\ ^{+0.11}_{-0.11}\ ^{+0.04}_{-0.06}) \cdot 10^{-1}$	$4.31 \cdot 10^{-1}$	1311	1410	5	0.51	0.64
$990 - 1080$	1030	$(2.96\ ^{+0.09}_{-0.09}\ ^{+0.02}_{-0.03}) \cdot 10^{-1}$	$3.42 \cdot 10^{-1}$	978	1123	8	0.50	0.62
$1080 - 1200$	1130	$(2.49\ ^{+0.08}_{-0.08}\ ^{+0.01}_{-0.03}) \cdot 10^{-1}$	$2.71 \cdot 10^{-1}$	1097	1190	5	0.53	0.65
$1200 - 1350$	1270	$(1.89\ ^{+0.06}_{-0.06}\ ^{+0.02}_{-0.03}) \cdot 10^{-1}$	$2.00 \cdot 10^{-1}$	1063	1118	6	0.54	0.68
$1350 - 1500$	1420	$(1.43\ ^{+0.05}_{-0.05}\ ^{+0.01}_{-0.02}) \cdot 10^{-1}$	$1.50 \cdot 10^{-1}$	804	844	4	0.53	0.65
$1500 - 1700$	1590	$(1.02\ ^{+0.04}_{-0.04}\ ^{+0.01}_{-0.02}) \cdot 10^{-1}$	$1.12 \cdot 10^{-1}$	764	836	5	0.56	0.69
$1700 - 1900$	1790	$(7.51\ ^{+0.32}_{-0.32}\ ^{+0.07}_{-0.12}) \cdot 10^{-2}$	$8.22 \cdot 10^{-2}$	569	616	6	0.55	0.67
$1900 - 2100$	1990	$(5.49\ ^{+0.27}_{-0.27}\ ^{+0.04}_{-0.06}) \cdot 10^{-2}$	$6.21 \cdot 10^{-2}$	413	465	2	0.53	0.65
$2100 - 2600$	2300	$(3.93\ ^{+0.15}_{-0.15}\ ^{+0.03}_{-0.02}) \cdot 10^{-2}$	$4.22 \cdot 10^{-2}$	724	772	6	0.63	0.77
$2600 - 3200$	2800	$(2.23\ ^{+0.10}_{-0.10}\ ^{+0.02}_{-0.04}) \cdot 10^{-2}$	$2.47 \cdot 10^{-2}$	480	525	5	0.63	0.77
$3200 - 3900$	3500	$(1.25\ ^{+0.07}_{-0.07}\ ^{+0.01}_{-0.02}) \cdot 10^{-2}$	$1.33 \cdot 10^{-2}$	328	350	0	0.62	0.76
$3900 - 4700$	4200	$(6.95\ ^{+0.49}_{-0.49}\ ^{+0.13}_{-0.16}) \cdot 10^{-3}$	$7.97 \cdot 10^{-3}$	202	231	0	0.61	0.76
$4700 - 5600$	5100	$(3.56\ ^{+0.32}_{-0.32}\ ^{+0.09}_{-0.06}) \cdot 10^{-3}$	$4.53 \cdot 10^{-3}$	121	153	1	0.60	0.74
$5600 - 6600$	6050	$(2.53\ ^{+0.28}_{-0.26}\ ^{+0.06}_{-0.04}) \cdot 10^{-3}$	$2.71 \cdot 10^{-3}$	96	103	0	0.59	0.73
$6600 - 7800$	7100	$(1.38\ ^{+0.20}_{-0.18}\ ^{+0.03}_{-0.05}) \cdot 10^{-3}$	$1.66 \cdot 10^{-3}$	61	73	0	0.59	0.74
$7800 - 9200$	8400	$(8.55\ ^{+1.49}_{-1.28}\ ^{+0.44}_{-0.20}) \cdot 10^{-4}$	$9.64 \cdot 10^{-4}$	45	49	1	0.58	0.74
$9200 - 12800$	10800	$(2.91\ ^{+0.55}_{-0.47}\ ^{+0.15}_{-0.05}) \cdot 10^{-4}$	$4.13 \cdot 10^{-4}$	38	54	0	0.62	0.81
$12800 - 50000$	25300	$(8.97\ ^{+2.35}_{-1.90}\ ^{+0.83}_{-1.21}) \cdot 10^{-6}$	$12.45 \cdot 10^{-6}$	22	31	0	0.60	0.86

Table A.5: The single-differential e^+p NC DIS cross section $d\sigma/dQ^2$, for $Q^2 > 185\,\text{GeV}^2$ and $y < 0.95$, corresponding to $\mathcal{L} = 42.4\,\text{pb}^{-1}, P = -0.36$. The columns contain: the Q^2-bin range, Q^2-bin center, the cross section measured at the Born level (the first error on the cross section corresponds to the statistical, while the second to the systematic uncertainty), the theoretical cross section at $P = 0.0$ used for the unfolding procedure (SM, calculated with CTEQ5D PDFs), the number of observed data (N_{DATA}), signal MC (N_{MC}) and background MC (N^{bg}_{MC}) events, efficiency and purity, for a given (Q^2) bin.

Q^2 range $[\mathrm{GeV}^2]$	Q^2_c $[\mathrm{GeV}^2]$	Asymmetry A^+
$185 - 210$	195	$-0.005\,^{+0.016}_{-0.016}\,^{+0.006}_{-0.005}$
$210 - 240$	220	$-0.001\,^{+0.017}_{-0.017}\,^{+0.004}_{-0.004}$
$240 - 270$	255	$0.018\,^{+0.019}_{-0.019}\,^{+0.007}_{-0.008}$
$270 - 300$	285	$0.053\,^{+0.022}_{-0.022}\,^{+0.010}_{-0.010}$
$300 - 340$	320	$0.013\,^{+0.022}_{-0.022}\,^{+0.010}_{-0.010}$
$340 - 380$	360	$0.057\,^{+0.025}_{-0.025}\,^{+0.012}_{-0.012}$
$380 - 430$	400	$0.106\,^{+0.026}_{-0.026}\,^{+0.011}_{-0.011}$
$430 - 480$	450	$0.039\,^{+0.031}_{-0.031}\,^{+0.016}_{-0.018}$
$480 - 540$	510	$0.104\,^{+0.033}_{-0.033}\,^{+0.010}_{-0.011}$
$540 - 600$	570	$0.116\,^{+0.041}_{-0.041}\,^{+0.015}_{-0.013}$
$600 - 670$	630	$0.128\,^{+0.043}_{-0.043}\,^{+0.027}_{-0.026}$
$670 - 740$	700	$0.071\,^{+0.045}_{-0.045}\,^{+0.019}_{-0.020}$
$740 - 820$	780	$0.058\,^{+0.044}_{-0.044}\,^{+0.016}_{-0.015}$
$820 - 900$	860	$0.072\,^{+0.048}_{-0.048}\,^{+0.019}_{-0.021}$
$900 - 990$	940	$0.101\,^{+0.050}_{-0.050}\,^{+0.023}_{-0.020}$
$990 - 1080$	1030	$0.160\,^{+0.058}_{-0.058}\,^{+0.020}_{-0.018}$
$1080 - 1200$	1130	$0.080\,^{+0.055}_{-0.055}\,^{+0.020}_{-0.019}$
$1200 - 1350$	1270	$0.073\,^{+0.056}_{-0.056}\,^{+0.021}_{-0.021}$
$1350 - 1500$	1420	$-0.026\,^{+0.066}_{-0.066}\,^{+0.025}_{-0.013}$
$1500 - 1700$	1590	$0.174\,^{+0.065}_{-0.065}\,^{+0.013}_{-0.019}$
$1700 - 1900$	1790	$0.075\,^{+0.077}_{-0.077}\,^{+0.028}_{-0.015}$
$1900 - 2100$	1990	$0.141\,^{+0.089}_{-0.089}\,^{+0.020}_{-0.019}$
$2100 - 2600$	2300	$0.093\,^{+0.068}_{-0.068}\,^{+0.014}_{-0.011}$
$2600 - 3200$	2800	$0.110\,^{+0.083}_{-0.083}\,^{+0.026}_{-0.011}$
$3200 - 3900$	3500	$0.175\,^{+0.099}_{-0.099}\,^{+0.051}_{-0.053}$
$3900 - 4700$	4200	$0.362\,^{+0.121}_{-0.121}\,^{+0.046}_{-0.040}$
$4700 - 5600$	5100	$0.365\,^{+0.157}_{-0.157}\,^{+0.044}_{-0.056}$
$5600 - 6600$	6050	$0.189\,^{+0.194}_{-0.182}\,^{+0.050}_{-0.055}$
$6600 - 7800$	7100	$0.144\,^{+0.249}_{-0.230}\,^{+0.056}_{-0.043}$
$7800 - 9200$	8400	$0.328\,^{+0.296}_{-0.260}\,^{+0.090}_{-0.098}$
$9200 - 12800$	10800	$0.353\,^{+0.321}_{-0.279}\,^{+0.064}_{-0.080}$
$12800 - 50000$	25300	$0.456\,^{+0.430}_{-0.358}\,^{+0.220}_{-0.160}$

Table A.6: The polarization asymmetry A^+, corresponding to the integrated luminosity of $\mathcal{L} = 113.3\,\mathrm{pb}^{-1}$, and positron beam polarizations of $P_+ = +0.32, P_- = -0.36$. The columns contain: the Q^2-bin range, Q^2-bin center, the A^+ asymmetry (the first error on the cross section corresponds to the statistical, while the second to the systematic uncertainty), for a given (Q^2) bin.

Q^2 range [GeV^2]	Q^2_c [GeV^2]	x range	x_c	eff	pur	acc
185 – 240	200	0.004 – 0.006	0.005	0.39	0.51	0.76
185 – 240	200	0.006 – 0.010	0.008	0.44	0.58	0.75
185 – 240	200	0.010 – 0.017	0.013	0.46	0.60	0.78
185 – 240	200	0.017 – 0.025	0.021	0.41	0.50	0.82
185 – 240	200	0.025 – 0.037	0.032	0.40	0.49	0.81
185 – 240	200	0.037 – 0.060	0.050	0.42	0.55	0.76
185 – 240	200	0.060 – 0.120	0.080	0.48	0.56	0.86
185 – 240	200	0.120 – 0.250	0.180	0.39	0.63	0.63
240 – 310	250	0.006 – 0.010	0.008	0.44	0.58	0.76
240 – 310	250	0.010 – 0.017	0.013	0.48	0.62	0.77
240 – 310	250	0.017 – 0.025	0.021	0.44	0.55	0.80
240 – 310	250	0.025 – 0.037	0.032	0.44	0.53	0.82
240 – 310	250	0.037 – 0.060	0.050	0.45	0.60	0.75
240 – 310	250	0.060 – 0.120	0.080	0.51	0.62	0.82
240 – 310	250	0.120 – 0.250	0.180	0.48	0.62	0.77
310 – 410	350	0.006 – 0.010	0.008	0.32	0.55	0.58
310 – 410	350	0.010 – 0.017	0.013	0.47	0.65	0.72
310 – 410	350	0.017 – 0.025	0.021	0.47	0.59	0.79
310 – 410	350	0.025 – 0.037	0.032	0.46	0.58	0.80
310 – 410	350	0.037 – 0.060	0.050	0.48	0.63	0.76
310 – 410	350	0.060 – 0.120	0.080	0.54	0.67	0.81
310 – 410	350	0.120 – 0.250	0.180	0.53	0.62	0.85
410 – 530	450	0.006 – 0.010	0.008	0.42	0.57	0.73
410 – 530	450	0.010 – 0.017	0.013	0.31	0.61	0.51
410 – 530	450	0.017 – 0.025	0.021	0.34	0.60	0.58
410 – 530	450	0.025 – 0.037	0.032	0.43	0.61	0.70
410 – 530	450	0.037 – 0.060	0.050	0.48	0.64	0.75
410 – 530	450	0.060 – 0.100	0.080	0.50	0.66	0.76
410 – 530	450	0.100 – 0.170	0.130	0.51	0.64	0.79
410 – 530	450	0.170 – 0.300	0.250	0.49	0.61	0.81
530 – 710	650	0.010 – 0.017	0.013	0.51	0.63	0.80
530 – 710	650	0.017 – 0.025	0.021	0.43	0.64	0.67
530 – 710	650	0.025 – 0.037	0.032	0.34	0.64	0.53
530 – 710	650	0.037 – 0.060	0.050	0.31	0.66	0.47
530 – 710	650	0.060 – 0.100	0.080	0.31	0.68	0.45
530 – 710	650	0.100 – 0.170	0.130	0.33	0.67	0.48
530 – 710	650	0.170 – 0.300	0.250	0.33	0.62	0.53
710 – 900	800	0.009 – 0.017	0.013	0.46	0.58	0.79
710 – 900	800	0.017 – 0.025	0.021	0.50	0.61	0.82
710 – 900	800	0.025 – 0.037	0.032	0.53	0.63	0.84
710 – 900	800	0.037 – 0.060	0.050	0.55	0.68	0.81
710 – 900	800	0.060 – 0.100	0.080	0.52	0.70	0.73
710 – 900	800	0.100 – 0.170	0.130	0.49	0.71	0.69
710 – 900	800	0.170 – 0.300	0.250	0.45	0.69	0.66

Table A.7: Characteristics of the binning for the double-differential e^+p NC DIS reduced cross section $\tilde{\sigma}$ measurement, in bins of Q^2 and Bjorken x. The columns contain: the Q^2-bin range, Q^2-bin center, x-bin range, x-bin center, efficiency (eff), purity (pur) and acceptance (acc), for a given (x, Q^2) bin.

Q^2 range [GeV^2]	Q^2_c [GeV^2]	x range	x_c	eff	pur	acc
$900 - 1300$	1200	$0.010 - 0.017$	0.014	0.44	0.60	0.73
$900 - 1300$	1200	$0.017 - 0.025$	0.021	0.53	0.64	0.83
$900 - 1300$	1200	$0.025 - 0.037$	0.032	0.56	0.67	0.84
$900 - 1300$	1200	$0.037 - 0.060$	0.050	0.60	0.71	0.85
$900 - 1300$	1200	$0.060 - 0.100$	0.080	0.61	0.73	0.82
$900 - 1300$	1200	$0.100 - 0.170$	0.130	0.61	0.74	0.82
$900 - 1300$	1200	$0.170 - 0.300$	0.250	0.59	0.75	0.79
$900 - 1300$	1200	$0.300 - 0.530$	0.400	0.51	0.75	0.68
$1300 - 1800$	1500	$0.017 - 0.025$	0.021	0.48	0.57	0.83
$1300 - 1800$	1500	$0.025 - 0.037$	0.032	0.55	0.65	0.84
$1300 - 1800$	1500	$0.037 - 0.060$	0.050	0.60	0.71	0.85
$1300 - 1800$	1500	$0.060 - 0.100$	0.080	0.61	0.73	0.84
$1300 - 1800$	1500	$0.100 - 0.150$	0.130	0.58	0.72	0.81
$1300 - 1800$	1500	$0.150 - 0.230$	0.180	0.60	0.73	0.82
$1300 - 1800$	1500	$0.230 - 0.350$	0.250	0.55	0.72	0.77
$1300 - 1800$	1500	$0.350 - 0.530$	0.400	0.53	0.69	0.77
$1800 - 2500$	2000	$0.023 - 0.037$	0.032	0.53	0.64	0.82
$1800 - 2500$	2000	$0.037 - 0.060$	0.050	0.60	0.70	0.85
$1800 - 2500$	2000	$0.060 - 0.100$	0.080	0.63	0.73	0.86
$1800 - 2500$	2000	$0.100 - 0.150$	0.130	0.61	0.73	0.82
$1800 - 2500$	2000	$0.150 - 0.230$	0.180	0.61	0.74	0.82
$1800 - 2500$	2000	$0.230 - 0.350$	0.250	0.57	0.74	0.78
$1800 - 2500$	2000	$0.350 - 0.530$	0.400	0.54	0.71	0.76
$2500 - 3500$	3000	$0.037 - 0.060$	0.050	0.58	0.68	0.85
$2500 - 3500$	3000	$0.060 - 0.100$	0.080	0.64	0.74	0.87
$2500 - 3500$	3000	$0.100 - 0.150$	0.130	0.62	0.73	0.85
$2500 - 3500$	3000	$0.150 - 0.230$	0.180	0.62	0.76	0.82
$2500 - 3500$	3000	$0.230 - 0.350$	0.250	0.60	0.75	0.80
$2500 - 3500$	3000	$0.350 - 0.530$	0.400	0.55	0.75	0.74
$2500 - 5600$	3000	$0.530 - 1.000$	0.650	0.52	0.66	0.79
$3500 - 5600$	5000	$0.040 - 0.100$	0.080	0.62	0.76	0.81
$3500 - 5600$	5000	$0.100 - 0.150$	0.130	0.64	0.75	0.85
$3500 - 5600$	5000	$0.150 - 0.230$	0.180	0.66	0.78	0.84
$3500 - 5600$	5000	$0.230 - 0.350$	0.250	0.64	0.79	0.81
$3500 - 5600$	5000	$0.350 - 0.530$	0.400	0.60	0.78	0.77
$5600 - 9000$	8000	$0.070 - 0.150$	0.130	0.61	0.77	0.79
$5600 - 9000$	8000	$0.150 - 0.230$	0.180	0.66	0.78	0.86
$5600 - 9000$	8000	$0.230 - 0.350$	0.250	0.65	0.79	0.82
$5600 - 9000$	8000	$0.350 - 0.530$	0.400	0.64	0.78	0.81
$5600 - 15000$	8000	$0.530 - 1.000$	0.650	0.59	0.76	0.78
$9000 - 15000$	12000	$0.090 - 0.230$	0.180	0.55	0.78	0.71
$9000 - 15000$	12000	$0.230 - 0.350$	0.250	0.64	0.79	0.81
$9000 - 15000$	12000	$0.350 - 0.530$	0.400	0.66	0.80	0.83
$15000 - 25000$	20000	$0.150 - 0.350$	0.250	0.52	0.77	0.67
$15000 - 25000$	20000	$0.350 - 1.000$	0.400	0.60	0.81	0.74
$25000 - 50000$	30000	$0.250 - 1.000$	0.400	0.48	0.76	0.63

Continuation of Table A.7.

Q^2 range $[\mathrm{GeV}^2]$	Q^2_c $[\mathrm{GeV}^2]$	x range	x_c	$\tilde{\sigma}$		N_{DATA}	N_{MC}	N^{bg}_{MC}
				measured $(P = 0.07)$	SM $(P = 0)$			
$185 - 240$	200	$0.004 - 0.006$	0.005	$1.083\,^{+0.011}_{-0.011}\,^{+0.008}_{-0.005}$	1.104	10359	10514	43
$185 - 240$	200	$0.006 - 0.010$	0.008	$0.929\,^{+0.009}_{-0.009}\,^{+0.007}_{-0.004}$	0.942	10801	10941	7
$185 - 240$	200	$0.010 - 0.017$	0.013	$0.770\,^{+0.007}_{-0.007}\,^{+0.005}_{-0.004}$	0.798	10568	10945	6
$185 - 240$	200	$0.017 - 0.025$	0.021	$0.672\,^{+0.008}_{-0.008}\,^{+0.009}_{-0.003}$	0.677	7512	7569	0
$185 - 240$	200	$0.025 - 0.037$	0.032	$0.550\,^{+0.007}_{-0.007}\,^{+0.004}_{-0.005}$	0.589	6537	7003	1
$185 - 240$	200	$0.037 - 0.060$	0.050	$0.499\,^{+0.006}_{-0.006}\,^{+0.004}_{-0.002}$	0.512	7022	7200	0
$185 - 240$	200	$0.060 - 0.120$	0.080	$0.428\,^{+0.004}_{-0.004}\,^{+0.002}_{-0.002}$	0.442	9580	9881	0
$185 - 240$	200	$0.120 - 0.250$	0.180	$0.342\,^{+0.004}_{-0.004}\,^{+0.003}_{-0.004}$	0.328	6179	5933	0
$240 - 310$	250	$0.006 - 0.010$	0.008	$0.925\,^{+0.011}_{-0.011}\,^{+0.005}_{-0.005}$	0.962	7713	8002	12
$240 - 310$	250	$0.010 - 0.017$	0.013	$0.813\,^{+0.009}_{-0.009}\,^{+0.006}_{-0.003}$	0.814	8011	8020	1
$240 - 310$	250	$0.017 - 0.025$	0.021	$0.689\,^{+0.009}_{-0.009}\,^{+0.006}_{-0.004}$	0.688	5606	5597	0
$240 - 310$	250	$0.025 - 0.037$	0.032	$0.566\,^{+0.008}_{-0.008}\,^{+0.006}_{-0.002}$	0.596	5092	5359	0
$240 - 310$	250	$0.037 - 0.060$	0.050	$0.507\,^{+0.007}_{-0.007}\,^{+0.003}_{-0.002}$	0.516	5288	5375	0
$240 - 310$	250	$0.060 - 0.120$	0.080	$0.433\,^{+0.005}_{-0.005}\,^{+0.003}_{-0.003}$	0.443	7031	7188	4
$240 - 310$	250	$0.120 - 0.250$	0.180	$0.340\,^{+0.005}_{-0.005}\,^{+0.004}_{-0.003}$	0.326	5674	5440	0
$310 - 410$	350	$0.006 - 0.010$	0.008	$0.936\,^{+0.014}_{-0.014}\,^{+0.009}_{-0.006}$	0.986	4600	4811	31
$310 - 410$	350	$0.010 - 0.017$	0.013	$0.814\,^{+0.011}_{-0.011}\,^{+0.005}_{-0.002}$	0.835	5937	6088	5
$310 - 410$	350	$0.017 - 0.025$	0.021	$0.682\,^{+0.010}_{-0.010}\,^{+0.004}_{-0.003}$	0.703	4392	4529	0
$310 - 410$	350	$0.025 - 0.037$	0.032	$0.572\,^{+0.009}_{-0.009}\,^{+0.004}_{-0.003}$	0.606	4059	4305	1
$310 - 410$	350	$0.037 - 0.060$	0.050	$0.510\,^{+0.008}_{-0.008}\,^{+0.010}_{-0.002}$	0.521	4456	4556	1
$310 - 410$	350	$0.060 - 0.120$	0.080	$0.420\,^{+0.006}_{-0.006}\,^{+0.006}_{-0.001}$	0.445	5561	5885	0
$310 - 410$	350	$0.120 - 0.250$	0.180	$0.326\,^{+0.005}_{-0.005}\,^{+0.005}_{-0.001}$	0.323	5117	5070	0
$410 - 530$	450	$0.006 - 0.010$	0.008	$0.956\,^{+0.016}_{-0.016}\,^{+0.013}_{-0.012}$	0.996	3767	3891	33
$410 - 530$	450	$0.010 - 0.017$	0.013	$0.800\,^{+0.016}_{-0.016}\,^{+0.003}_{-0.005}$	0.849	2661	2811	11
$410 - 530$	450	$0.017 - 0.025$	0.021	$0.699\,^{+0.015}_{-0.015}\,^{+0.003}_{-0.005}$	0.714	2199	2245	0
$410 - 530$	450	$0.025 - 0.037$	0.032	$0.576\,^{+0.012}_{-0.012}\,^{+0.004}_{-0.003}$	0.613	2438	2595	0
$410 - 530$	450	$0.037 - 0.060$	0.050	$0.507\,^{+0.009}_{-0.009}\,^{+0.006}_{-0.002}$	0.525	3014	3123	0
$410 - 530$	450	$0.060 - 0.100$	0.080	$0.424\,^{+0.008}_{-0.008}\,^{+0.002}_{-0.002}$	0.446	2793	2940	0
$410 - 530$	450	$0.100 - 0.170$	0.130	$0.368\,^{+0.007}_{-0.007}\,^{+0.001}_{-0.002}$	0.372	2616	2647	0
$410 - 530$	450	$0.170 - 0.300$	0.250	$0.262\,^{+0.006}_{-0.006}\,^{+0.002}_{-0.001}$	0.258	2238	2209	0
$530 - 710$	650	$0.010 - 0.017$	0.013	$0.808\,^{+0.014}_{-0.014}\,^{+0.005}_{-0.004}$	0.862	3406	3604	27
$530 - 710$	650	$0.017 - 0.025$	0.021	$0.709\,^{+0.015}_{-0.015}\,^{+0.004}_{-0.003}$	0.727	2102	2150	6
$530 - 710$	650	$0.025 - 0.037$	0.032	$0.604\,^{+0.015}_{-0.015}\,^{+0.004}_{-0.005}$	0.623	1602	1652	0
$530 - 710$	650	$0.037 - 0.060$	0.050	$0.496\,^{+0.013}_{-0.013}\,^{+0.003}_{-0.002}$	0.530	1543	1651	0
$530 - 710$	650	$0.060 - 0.100$	0.080	$0.434\,^{+0.011}_{-0.011}\,^{+0.002}_{-0.002}$	0.447	1426	1471	1
$530 - 710$	650	$0.100 - 0.170$	0.130	$0.334\,^{+0.009}_{-0.009}\,^{+0.002}_{-0.002}$	0.371	1266	1405	0
$530 - 710$	650	$0.170 - 0.300$	0.250	$0.243\,^{+0.007}_{-0.007}\,^{+0.005}_{-0.001}$	0.254	1188	1242	0
$710 - 900$	800	$0.009 - 0.017$	0.013	$0.774\,^{+0.017}_{-0.017}\,^{+0.013}_{-0.008}$	0.863	2180	2396	32
$710 - 900$	800	$0.017 - 0.025$	0.021	$0.720\,^{+0.019}_{-0.019}\,^{+0.006}_{-0.004}$	0.733	1505	1527	3
$710 - 900$	800	$0.025 - 0.037$	0.032	$0.593\,^{+0.015}_{-0.015}\,^{+0.003}_{-0.003}$	0.627	1465	1549	0
$710 - 900$	800	$0.037 - 0.060$	0.050	$0.510\,^{+0.013}_{-0.013}\,^{+0.003}_{-0.002}$	0.533	1649	1724	0
$710 - 900$	800	$0.060 - 0.100$	0.080	$0.455\,^{+0.012}_{-0.012}\,^{+0.004}_{-0.003}$	0.448	1490	1466	0
$710 - 900$	800	$0.100 - 0.170$	0.130	$0.347\,^{+0.010}_{-0.010}\,^{+0.002}_{-0.002}$	0.370	1144	1218	0
$710 - 900$	800	$0.170 - 0.300$	0.250	$0.247\,^{+0.008}_{-0.008}\,^{+0.002}_{-0.003}$	0.252	924	942	0

Table A.8: The e^+p NC DIS reduced cross section $\tilde{\sigma}$ (for $Q^2 > 185\,\mathrm{GeV}^2$ and $y < 0.95$), corresponding to $\mathcal{L} = 113.3\,\mathrm{pb}^{-1}, P = 0.07$. The columns contain: the Q^2-bin range, Q^2-bin center, x-bin range, x-bin center, the measured cross section (the first error on the cross section corresponds to the statistical, the second to the systematic uncertainty), the theoretical cross section at $P = 0.0$, the number of observed data (N_{DATA}), signal MC (N_{MC}) and background MC (N^{bg}_{MC}) events, for a given (x, Q^2) bin.

Q^2 range	Q^2_c	x range	x_c	$\tilde{\sigma}$		N_{DATA}	N_{MC}	N^{bg}_{MC}
$[\mathrm{GeV}^2]$	$[\mathrm{GeV}^2]$			measured ($P = 0.07$)	SM ($P = 0$)			
$900 - 1300$	1200	$0.010 - 0.017$	0.014	$0.763^{+0.020\ +0.021}_{-0.020\ -0.016}$	0.827	1550	1636	40
$900 - 1300$	1200	$0.017 - 0.025$	0.021	$0.683^{+0.018\ +0.005}_{-0.018\ -0.006}$	0.734	1519	1619	13
$900 - 1300$	1200	$0.025 - 0.037$	0.032	$0.615^{+0.015\ +0.006}_{-0.015\ -0.003}$	0.632	1597	1642	0
$900 - 1300$	1200	$0.037 - 0.060$	0.050	$0.504^{+0.012\ +0.002}_{-0.012\ -0.003}$	0.536	1866	1983	3
$900 - 1300$	1200	$0.060 - 0.100$	0.080	$0.414^{+0.010\ +0.003}_{-0.010\ -0.002}$	0.449	1705	1849	0
$900 - 1300$	1200	$0.100 - 0.170$	0.130	$0.353^{+0.009\ +0.002}_{-0.009\ -0.003}$	0.368	1570	1635	1
$900 - 1300$	1200	$0.170 - 0.300$	0.250	$0.252^{+0.007\ +0.002}_{-0.007\ -0.001}$	0.248	1276	1253	0
$900 - 1300$	1200	$0.300 - 0.530$	0.400	$0.126^{+0.006\ +0.001}_{-0.006\ -0.001}$	0.130	523	538	0
$1300 - 1800$	1500	$0.017 - 0.025$	0.021	$0.686^{+0.024\ +0.023}_{-0.024\ -0.014}$	0.728	840	876	14
$1300 - 1800$	1500	$0.025 - 0.037$	0.032	$0.559^{+0.020\ +0.006}_{-0.020\ -0.007}$	0.632	808	911	2
$1300 - 1800$	1500	$0.037 - 0.060$	0.050	$0.524^{+0.016\ +0.004}_{-0.016\ -0.005}$	0.537	1110	1132	4
$1300 - 1800$	1500	$0.060 - 0.100$	0.080	$0.442^{+0.013\ +0.004}_{-0.013\ -0.004}$	0.448	1092	1108	0
$1300 - 1800$	1500	$0.100 - 0.150$	0.130	$0.374^{+0.014\ +0.002}_{-0.014\ -0.003}$	0.367	768	752	0
$1300 - 1800$	1500	$0.150 - 0.230$	0.180	$0.296^{+0.012\ +0.002}_{-0.012\ -0.002}$	0.311	650	683	0
$1300 - 1800$	1500	$0.230 - 0.350$	0.250	$0.243^{+0.011\ +0.002}_{-0.011\ -0.003}$	0.245	448	452	0
$1300 - 1800$	1500	$0.350 - 0.530$	0.400	$0.122^{+0.008\ +0.002}_{-0.008\ -0.003}$	0.128	218	230	0
$1800 - 2500$	2000	$0.023 - 0.037$	0.032	$0.551^{+0.022\ +0.011}_{-0.022\ -0.011}$	0.625	615	681	15
$1800 - 2500$	2000	$0.037 - 0.060$	0.050	$0.469^{+0.018\ +0.003}_{-0.018\ -0.005}$	0.534	650	736	4
$1800 - 2500$	2000	$0.060 - 0.100$	0.080	$0.466^{+0.017\ +0.003}_{-0.017\ -0.003}$	0.447	789	757	0
$1800 - 2500$	2000	$0.100 - 0.150$	0.130	$0.357^{+0.016\ +0.008}_{-0.016\ -0.002}$	0.365	520	531	0
$1800 - 2500$	2000	$0.150 - 0.230$	0.180	$0.282^{+0.014\ +0.007}_{-0.014\ -0.002}$	0.308	436	477	0
$1800 - 2500$	2000	$0.230 - 0.350$	0.250	$0.247^{+0.014\ +0.006}_{-0.014\ -0.002}$	0.243	331	325	0
$1800 - 2500$	2000	$0.350 - 0.530$	0.400	$0.125^{+0.010\ +0.001}_{-0.010\ -0.002}$	0.126	158	159	0
$2500 - 3500$	3000	$0.037 - 0.060$	0.050	$0.497^{+0.024\ +0.007}_{-0.024\ -0.005}$	0.521	441	461	1
$2500 - 3500$	3000	$0.060 - 0.100$	0.080	$0.417^{+0.019\ +0.004}_{-0.019\ -0.004}$	0.439	480	504	2
$2500 - 3500$	3000	$0.100 - 0.150$	0.130	$0.357^{+0.019\ +0.002}_{-0.019\ -0.003}$	0.360	370	372	0
$2500 - 3500$	3000	$0.150 - 0.230$	0.180	$0.291^{+0.016\ +0.002}_{-0.016\ -0.002}$	0.304	317	331	1
$2500 - 3500$	3000	$0.230 - 0.350$	0.250	$0.249^{+0.016\ +0.002}_{-0.016\ -0.002}$	0.239	247	237	0
$2500 - 3500$	3000	$0.350 - 0.530$	0.400	$0.115^{+0.011\ +0.004}_{-0.011\ -0.001}$	0.123	102	109	0
$2500 - 5600$	3000	$0.530 - 1.000$	0.650	$0.014^{+0.003\ +0.000}_{-0.002\ -0.001}$	0.019	32	44	0
$3500 - 5600$	5000	$0.040 - 0.100$	0.080	$0.398^{+0.017\ +0.003}_{-0.017\ -0.005}$	0.409	567	580	3
$3500 - 5600$	5000	$0.100 - 0.150$	0.130	$0.343^{+0.020\ +0.004}_{-0.020\ -0.002}$	0.342	305	304	0
$3500 - 5600$	5000	$0.150 - 0.230$	0.180	$0.288^{+0.017\ +0.003}_{-0.017\ -0.002}$	0.293	283	288	0
$3500 - 5600$	5000	$0.230 - 0.350$	0.250	$0.223^{+0.016\ +0.004}_{-0.016\ -0.001}$	0.231	203	211	0
$3500 - 5600$	5000	$0.350 - 0.530$	0.400	$0.145^{+0.013\ +0.001}_{-0.013\ -0.002}$	0.119	124	102	0
$5600 - 9000$	8000	$0.070 - 0.150$	0.130	$0.308^{+0.020\ +0.006}_{-0.020\ -0.015}$	0.302	245	237	3
$5600 - 9000$	8000	$0.150 - 0.230$	0.180	$0.234^{+0.020\ +0.002}_{-0.020\ -0.003}$	0.266	133	151	0
$5600 - 9000$	8000	$0.230 - 0.350$	0.250	$0.217^{+0.020\ +0.007}_{-0.020\ -0.003}$	0.216	117	116	0
$5600 - 9000$	8000	$0.350 - 0.530$	0.400	$0.112^{+0.016\ +0.002}_{-0.014\ -0.005}$	0.114	60	61	0
$5600 - 15000$	8000	$0.530 - 1.000$	0.650	$0.014^{+0.004\ +0.001}_{-0.003\ -0.001}$	0.017	16	20	0
$9000 - 15000$	12000	$0.090 - 0.230$	0.180	$0.178^{+0.023\ +0.009}_{-0.020\ -0.007}$	0.219	78	96	0
$9000 - 15000$	12000	$0.230 - 0.350$	0.250	$0.145^{+0.025\ +0.003}_{-0.022\ -0.003}$	0.188	44	57	0
$9000 - 15000$	12000	$0.350 - 0.530$	0.400	$0.121^{+0.023\ +0.007}_{-0.019\ -0.002}$	0.105	39	34	0
$15000 - 25000$	20000	$0.150 - 0.350$	0.250	$0.127^{+0.030\ +0.004}_{-0.024\ -0.014}$	0.126	27	27	0
$15000 - 25000$	20000	$0.350 - 1.000$	0.400	$0.068^{+0.024\ +0.008}_{-0.019\ -0.002}$	0.082	13	16	0
$25000 - 50000$	30000	$0.250 - 1.000$	0.400	$0.026^{+0.025\ +0.012}_{-0.014\ -0.003}$	0.053	3	6	0

Continuation of Table A.8.

Q^2 range [GeV^2]	Q^2_c [GeV^2]	x range	x_c	$\tilde{\sigma}$		N_{DATA}	N_{MC}	N^{bg}_{MC}
				measured ($P = 0.32$)	SM ($P = 0$)			
$185 - 240$	200	$0.004 - 0.006$	0.005	$1.102^{+0.014}_{-0.014}{}^{+0.008}_{-0.005}$	1.104	6609	6593	27
$185 - 240$	200	$0.006 - 0.010$	0.008	$0.928^{+0.011}_{-0.011}{}^{+0.007}_{-0.004}$	0.942	6768	6861	5
$185 - 240$	200	$0.010 - 0.017$	0.013	$0.769^{+0.009}_{-0.009}{}^{+0.005}_{-0.004}$	0.798	6614	6863	4
$185 - 240$	200	$0.017 - 0.025$	0.021	$0.673^{+0.010}_{-0.010}{}^{+0.009}_{-0.003}$	0.677	4712	4746	0
$185 - 240$	200	$0.025 - 0.037$	0.032	$0.545^{+0.009}_{-0.009}{}^{+0.004}_{-0.005}$	0.589	4060	4392	1
$185 - 240$	200	$0.037 - 0.060$	0.050	$0.501^{+0.008}_{-0.008}{}^{+0.004}_{-0.002}$	0.512	4422	4515	0
$185 - 240$	200	$0.060 - 0.120$	0.080	$0.430^{+0.006}_{-0.006}{}^{+0.002}_{-0.002}$	0.442	6028	6196	0
$185 - 240$	200	$0.120 - 0.250$	0.180	$0.344^{+0.006}_{-0.006}{}^{+0.003}_{-0.004}$	0.328	3905	3720	0
$240 - 310$	250	$0.006 - 0.010$	0.008	$0.936^{+0.013}_{-0.013}{}^{+0.005}_{-0.005}$	0.962	4894	5018	8
$240 - 310$	250	$0.010 - 0.017$	0.013	$0.815^{+0.011}_{-0.011}{}^{+0.006}_{-0.003}$	0.814	5036	5029	1
$240 - 310$	250	$0.017 - 0.025$	0.021	$0.704^{+0.012}_{-0.012}{}^{+0.006}_{-0.004}$	0.688	3589	3510	0
$240 - 310$	250	$0.025 - 0.037$	0.032	$0.587^{+0.010}_{-0.010}{}^{+0.006}_{-0.003}$	0.596	3307	3361	0
$240 - 310$	250	$0.037 - 0.060$	0.050	$0.511^{+0.009}_{-0.009}{}^{+0.003}_{-0.002}$	0.516	3340	3371	0
$240 - 310$	250	$0.060 - 0.120$	0.080	$0.436^{+0.007}_{-0.007}{}^{+0.003}_{-0.003}$	0.443	4438	4507	2
$240 - 310$	250	$0.120 - 0.250$	0.180	$0.345^{+0.006}_{-0.006}{}^{+0.004}_{-0.003}$	0.326	3609	3411	0
$310 - 410$	350	$0.006 - 0.010$	0.008	$0.954^{+0.018}_{-0.018}{}^{+0.009}_{-0.006}$	0.986	2939	3017	19
$310 - 410$	350	$0.010 - 0.017$	0.013	$0.813^{+0.013}_{-0.013}{}^{+0.005}_{-0.002}$	0.835	3719	3818	3
$310 - 410$	350	$0.017 - 0.025$	0.021	$0.696^{+0.013}_{-0.013}{}^{+0.004}_{-0.003}$	0.703	2810	2841	0
$310 - 410$	350	$0.025 - 0.037$	0.032	$0.579^{+0.011}_{-0.011}{}^{+0.004}_{-0.003}$	0.606	2578	2700	1
$310 - 410$	350	$0.037 - 0.060$	0.050	$0.520^{+0.010}_{-0.010}{}^{+0.010}_{-0.002}$	0.521	2853	2858	1
$310 - 410$	350	$0.060 - 0.120$	0.080	$0.429^{+0.007}_{-0.007}{}^{+0.006}_{-0.002}$	0.445	3562	3691	0
$310 - 410$	350	$0.120 - 0.250$	0.180	$0.337^{+0.006}_{-0.006}{}^{+0.005}_{-0.001}$	0.323	3320	3180	0
$410 - 530$	450	$0.006 - 0.010$	0.008	$0.980^{+0.020}_{-0.020}{}^{+0.014}_{-0.012}$	0.996	2423	2440	21
$410 - 530$	450	$0.010 - 0.017$	0.013	$0.814^{+0.020}_{-0.020}{}^{+0.004}_{-0.005}$	0.849	1698	1763	7
$410 - 530$	450	$0.017 - 0.025$	0.021	$0.711^{+0.019}_{-0.019}{}^{+0.003}_{-0.005}$	0.714	1403	1408	0
$410 - 530$	450	$0.025 - 0.037$	0.032	$0.595^{+0.015}_{-0.015}{}^{+0.004}_{-0.003}$	0.613	1579	1628	0
$410 - 530$	450	$0.037 - 0.060$	0.050	$0.510^{+0.012}_{-0.012}{}^{+0.006}_{-0.002}$	0.525	1903	1959	0
$410 - 530$	450	$0.060 - 0.100$	0.080	$0.432^{+0.010}_{-0.010}{}^{+0.002}_{-0.002}$	0.446	1786	1844	0
$410 - 530$	450	$0.100 - 0.170$	0.130	$0.386^{+0.009}_{-0.009}{}^{+0.001}_{-0.002}$	0.372	1721	1660	0
$410 - 530$	450	$0.170 - 0.300$	0.250	$0.270^{+0.007}_{-0.007}{}^{+0.002}_{-0.001}$	0.258	1450	1385	0
$530 - 710$	650	$0.010 - 0.017$	0.013	$0.844^{+0.018}_{-0.018}{}^{+0.005}_{-0.005}$	0.862	2231	2261	17
$530 - 710$	650	$0.017 - 0.025$	0.021	$0.744^{+0.020}_{-0.020}{}^{+0.005}_{-0.003}$	0.727	1384	1348	4
$530 - 710$	650	$0.025 - 0.037$	0.032	$0.617^{+0.019}_{-0.019}{}^{+0.004}_{-0.005}$	0.623	1026	1036	0
$530 - 710$	650	$0.037 - 0.060$	0.050	$0.507^{+0.016}_{-0.016}{}^{+0.003}_{-0.002}$	0.530	990	1035	0
$530 - 710$	650	$0.060 - 0.100$	0.080	$0.432^{+0.014}_{-0.014}{}^{+0.002}_{-0.002}$	0.447	890	922	1
$530 - 710$	650	$0.100 - 0.170$	0.130	$0.326^{+0.012}_{-0.012}{}^{+0.002}_{-0.002}$	0.371	775	881	0
$530 - 710$	650	$0.170 - 0.300$	0.250	$0.252^{+0.009}_{-0.009}{}^{+0.005}_{-0.002}$	0.254	774	779	0
$710 - 900$	800	$0.009 - 0.017$	0.013	$0.799^{+0.021}_{-0.021}{}^{+0.013}_{-0.009}$	0.863	1412	1503	21
$710 - 900$	800	$0.017 - 0.025$	0.021	$0.735^{+0.024}_{-0.024}{}^{+0.006}_{-0.004}$	0.733	963	958	2
$710 - 900$	800	$0.025 - 0.037$	0.032	$0.583^{+0.019}_{-0.019}{}^{+0.002}_{-0.003}$	0.627	903	972	0
$710 - 900$	800	$0.037 - 0.060$	0.050	$0.531^{+0.016}_{-0.016}{}^{+0.003}_{-0.002}$	0.533	1078	1081	0
$710 - 900$	800	$0.060 - 0.100$	0.080	$0.457^{+0.015}_{-0.015}{}^{+0.004}_{-0.003}$	0.448	938	919	0
$710 - 900$	800	$0.100 - 0.170$	0.130	$0.362^{+0.013}_{-0.013}{}^{+0.002}_{-0.002}$	0.370	748	764	0
$710 - 900$	800	$0.170 - 0.300$	0.250	$0.245^{+0.010}_{-0.010}{}^{+0.002}_{-0.003}$	0.252	575	591	0

Table A.9: The e^+p NC DIS reduced cross section $\tilde{\sigma}$ (for $Q^2 > 185\,\text{GeV}^2$ and $y < 0.95$), corresponding to $\mathcal{L} = 70.9\,\text{pb}^{-1}, P = 0.32$. The columns contain: the Q^2-bin range, Q^2-bin center, x-bin range, x-bin center, the measured cross section (the first error on the cross section corresponds to the statistical, the second to the systematic uncertainty), the theoretical cross section at $P = 0.0$, the number of observed data (N_{DATA}), signal MC (N_{MC}) and background MC (N^{bg}_{MC}) events, for a given (x, Q^2) bin.

Q^2 range	Q^2_c	x range	x_c	$\tilde{\sigma}$		N_{DATA}	N_{MC}	N^{bg}_{MC}
$[\mathrm{GeV}^2]$	$[\mathrm{GeV}^2]$			measured $(P = 0.32)$	SM $(P = 0)$			
$900 - 1300$	1200	$0.010 - 0.017$	0.014	$0.768\,^{+0.025}_{-0.025}\,^{+0.021}_{-0.016}$	0.827	978	1026	26
$900 - 1300$	1200	$0.017 - 0.025$	0.021	$0.700\,^{+0.023}_{-0.023}\,^{+0.005}_{-0.006}$	0.734	977	1015	9
$900 - 1300$	1200	$0.025 - 0.037$	0.032	$0.631\,^{+0.020}_{-0.020}\,^{+0.007}_{-0.003}$	0.632	1028	1030	0
$900 - 1300$	1200	$0.037 - 0.060$	0.050	$0.521\,^{+0.015}_{-0.015}\,^{+0.003}_{-0.003}$	0.536	1210	1244	2
$900 - 1300$	1200	$0.060 - 0.100$	0.080	$0.427\,^{+0.013}_{-0.013}\,^{+0.003}_{-0.002}$	0.449	1104	1160	0
$900 - 1300$	1200	$0.100 - 0.170$	0.130	$0.363\,^{+0.011}_{-0.011}\,^{+0.002}_{-0.003}$	0.368	1012	1025	1
$900 - 1300$	1200	$0.170 - 0.300$	0.250	$0.263\,^{+0.009}_{-0.009}\,^{+0.002}_{-0.002}$	0.248	834	786	0
$900 - 1300$	1200	$0.300 - 0.530$	0.400	$0.128\,^{+0.007}_{-0.007}\,^{+0.001}_{-0.001}$	0.130	333	337	0
$1300 - 1800$	1500	$0.017 - 0.025$	0.021	$0.698\,^{+0.030}_{-0.030}\,^{+0.024}_{-0.014}$	0.728	536	549	9
$1300 - 1800$	1500	$0.025 - 0.037$	0.032	$0.562\,^{+0.025}_{-0.025}\,^{+0.006}_{-0.007}$	0.632	510	572	1
$1300 - 1800$	1500	$0.037 - 0.060$	0.050	$0.544\,^{+0.020}_{-0.020}\,^{+0.004}_{-0.005}$	0.537	722	710	2
$1300 - 1800$	1500	$0.060 - 0.100$	0.080	$0.448\,^{+0.017}_{-0.017}\,^{+0.004}_{-0.004}$	0.448	694	695	0
$1300 - 1800$	1500	$0.100 - 0.150$	0.130	$0.392\,^{+0.017}_{-0.017}\,^{+0.002}_{-0.003}$	0.367	505	472	0
$1300 - 1800$	1500	$0.150 - 0.230$	0.180	$0.313\,^{+0.015}_{-0.015}\,^{+0.002}_{-0.002}$	0.311	432	428	0
$1300 - 1800$	1500	$0.230 - 0.350$	0.250	$0.251\,^{+0.015}_{-0.015}\,^{+0.002}_{-0.004}$	0.245	290	284	0
$1300 - 1800$	1500	$0.350 - 0.530$	0.400	$0.116\,^{+0.010}_{-0.010}\,^{+0.002}_{-0.003}$	0.128	130	144	0
$1800 - 2500$	2000	$0.023 - 0.037$	0.032	$0.543\,^{+0.028}_{-0.028}\,^{+0.011}_{-0.011}$	0.625	380	427	9
$1800 - 2500$	2000	$0.037 - 0.060$	0.050	$0.494\,^{+0.024}_{-0.024}\,^{+0.003}_{-0.005}$	0.534	429	462	2
$1800 - 2500$	2000	$0.060 - 0.100$	0.080	$0.502\,^{+0.022}_{-0.022}\,^{+0.003}_{-0.003}$	0.447	533	475	0
$1800 - 2500$	2000	$0.100 - 0.150$	0.130	$0.359\,^{+0.020}_{-0.020}\,^{+0.008}_{-0.002}$	0.365	328	333	0
$1800 - 2500$	2000	$0.150 - 0.230$	0.180	$0.279\,^{+0.017}_{-0.017}\,^{+0.007}_{-0.002}$	0.308	271	299	0
$1800 - 2500$	2000	$0.230 - 0.350$	0.250	$0.248\,^{+0.017}_{-0.017}\,^{+0.006}_{-0.002}$	0.243	208	204	0
$1800 - 2500$	2000	$0.350 - 0.530$	0.400	$0.128\,^{+0.013}_{-0.013}\,^{+0.001}_{-0.002}$	0.126	102	100	0
$2500 - 3500$	3000	$0.037 - 0.060$	0.050	$0.502\,^{+0.030}_{-0.030}\,^{+0.007}_{-0.005}$	0.521	279	289	1
$2500 - 3500$	3000	$0.060 - 0.100$	0.080	$0.418\,^{+0.024}_{-0.024}\,^{+0.004}_{-0.004}$	0.439	302	316	1
$2500 - 3500$	3000	$0.100 - 0.150$	0.130	$0.376\,^{+0.024}_{-0.024}\,^{+0.002}_{-0.003}$	0.360	244	233	0
$2500 - 3500$	3000	$0.150 - 0.230$	0.180	$0.304\,^{+0.021}_{-0.021}\,^{+0.002}_{-0.002}$	0.304	208	207	1
$2500 - 3500$	3000	$0.230 - 0.350$	0.250	$0.274\,^{+0.021}_{-0.021}\,^{+0.003}_{-0.002}$	0.239	170	148	0
$2500 - 3500$	3000	$0.350 - 0.530$	0.400	$0.111\,^{+0.016}_{-0.014}\,^{+0.004}_{-0.001}$	0.123	62	69	0
$2500 - 5600$	3000	$0.530 - 1.000$	0.650	$0.012\,^{+0.004}_{-0.003}\,^{+0.000}_{-0.000}$	0.019	17	27	0
$3500 - 5600$	5000	$0.040 - 0.100$	0.080	$0.427\,^{+0.022}_{-0.022}\,^{+0.003}_{-0.005}$	0.409	381	364	2
$3500 - 5600$	5000	$0.100 - 0.150$	0.130	$0.375\,^{+0.026}_{-0.026}\,^{+0.004}_{-0.002}$	0.342	209	191	0
$3500 - 5600$	5000	$0.150 - 0.230$	0.180	$0.326\,^{+0.023}_{-0.023}\,^{+0.004}_{-0.003}$	0.293	201	180	0
$3500 - 5600$	5000	$0.230 - 0.350$	0.250	$0.241\,^{+0.021}_{-0.021}\,^{+0.005}_{-0.001}$	0.231	138	132	0
$3500 - 5600$	5000	$0.350 - 0.530$	0.400	$0.159\,^{+0.019}_{-0.017}\,^{+0.001}_{-0.002}$	0.119	85	64	0
$5600 - 9000$	8000	$0.070 - 0.150$	0.130	$0.323\,^{+0.026}_{-0.026}\,^{+0.007}_{-0.016}$	0.302	161	148	2
$5600 - 9000$	8000	$0.150 - 0.230$	0.180	$0.227\,^{+0.028}_{-0.025}\,^{+0.002}_{-0.003}$	0.266	81	95	0
$5600 - 9000$	8000	$0.230 - 0.350$	0.250	$0.243\,^{+0.030}_{-0.027}\,^{+0.008}_{-0.004}$	0.216	82	73	0
$5600 - 9000$	8000	$0.350 - 0.530$	0.400	$0.113\,^{+0.021}_{-0.018}\,^{+0.002}_{-0.005}$	0.114	38	38	0
$5600 - 15000$	8000	$0.530 - 1.000$	0.650	$0.015\,^{+0.006}_{-0.004}\,^{+0.001}_{-0.001}$	0.017	11	13	0
$9000 - 15000$	12000	$0.090 - 0.230$	0.180	$0.182\,^{+0.030}_{-0.026}\,^{+0.010}_{-0.007}$	0.219	50	60	0
$9000 - 15000$	12000	$0.230 - 0.350$	0.250	$0.194\,^{+0.038}_{-0.032}\,^{+0.004}_{-0.004}$	0.188	37	36	0
$9000 - 15000$	12000	$0.350 - 0.530$	0.400	$0.154\,^{+0.033}_{-0.027}\,^{+0.008}_{-0.003}$	0.105	31	21	0
$15000 - 25000$	20000	$0.150 - 0.350$	0.250	$0.128\,^{+0.039}_{-0.031}\,^{+0.004}_{-0.014}$	0.126	17	17	0
$15000 - 25000$	20000	$0.350 - 1.000$	0.400	$0.058\,^{+0.031}_{-0.021}\,^{+0.007}_{-0.002}$	0.082	7	10	0
$25000 - 50000$	30000	$0.250 - 1.000$	0.400	$0.027\,^{+0.036}_{-0.018}\,^{+0.013}_{-0.004}$	0.053	2	4	0

Continuation of Table A.9.

Q^2 range $[\mathrm{GeV}^2]$	Q^2_c $[\mathrm{GeV}^2]$	x range	x_c	$\tilde{\sigma}$		N_{DATA}	N_{MC}	N^{bg}_{MC}
				measured $(P = -0.36)$	SM $(P = 0)$			
$185 - 240$	200	$0.004 - 0.006$	0.005	$1.060\,^{+0.017}_{-0.017}\,^{+0.008}_{-0.006}$	1.104	3750	3889	16
$185 - 240$	200	$0.006 - 0.010$	0.008	$0.937\,^{+0.015}_{-0.015}\,^{+0.004}_{-0.006}$	0.942	4033	4049	3
$185 - 240$	200	$0.010 - 0.017$	0.013	$0.779\,^{+0.012}_{-0.012}\,^{+0.003}_{-0.003}$	0.798	3954	4052	2
$185 - 240$	200	$0.017 - 0.025$	0.021	$0.677\,^{+0.013}_{-0.013}\,^{+0.003}_{-0.005}$	0.677	2800	2802	0
$185 - 240$	200	$0.025 - 0.037$	0.032	$0.563\,^{+0.011}_{-0.011}\,^{+0.004}_{-0.003}$	0.589	2477	2590	0
$185 - 240$	200	$0.037 - 0.060$	0.050	$0.499\,^{+0.010}_{-0.010}\,^{+0.002}_{-0.003}$	0.512	2600	2667	0
$185 - 240$	200	$0.060 - 0.120$	0.080	$0.429\,^{+0.007}_{-0.007}\,^{+0.004}_{-0.001}$	0.442	3552	3662	0
$185 - 240$	200	$0.120 - 0.250$	0.180	$0.340\,^{+0.007}_{-0.007}\,^{+0.005}_{-0.002}$	0.328	2274	2193	0
$240 - 310$	250	$0.006 - 0.010$	0.008	$0.915\,^{+0.017}_{-0.017}\,^{+0.004}_{-0.008}$	0.962	2819	2959	5
$240 - 310$	250	$0.010 - 0.017$	0.013	$0.816\,^{+0.015}_{-0.015}\,^{+0.006}_{-0.004}$	0.814	2975	2967	0
$240 - 310$	250	$0.017 - 0.025$	0.021	$0.670\,^{+0.015}_{-0.015}\,^{+0.004}_{-0.002}$	0.688	2017	2071	0
$240 - 310$	250	$0.025 - 0.037$	0.032	$0.537\,^{+0.013}_{-0.013}\,^{+0.004}_{-0.005}$	0.596	1785	1983	0
$240 - 310$	250	$0.037 - 0.060$	0.050	$0.505\,^{+0.011}_{-0.011}\,^{+0.005}_{-0.003}$	0.516	1948	1990	0
$240 - 310$	250	$0.060 - 0.120$	0.080	$0.431\,^{+0.008}_{-0.008}\,^{+0.005}_{-0.004}$	0.443	2593	2664	1
$240 - 310$	250	$0.120 - 0.250$	0.180	$0.334\,^{+0.007}_{-0.007}\,^{+0.002}_{-0.004}$	0.326	2065	2013	0
$310 - 410$	350	$0.006 - 0.010$	0.008	$0.913\,^{+0.022}_{-0.022}\,^{+0.007}_{-0.006}$	0.986	1661	1781	11
$310 - 410$	350	$0.010 - 0.017$	0.013	$0.823\,^{+0.017}_{-0.017}\,^{+0.004}_{-0.002}$	0.835	2218	2249	2
$310 - 410$	350	$0.017 - 0.025$	0.021	$0.664\,^{+0.017}_{-0.017}\,^{+0.004}_{-0.002}$	0.703	1582	1677	0
$310 - 410$	350	$0.025 - 0.037$	0.032	$0.563\,^{+0.015}_{-0.015}\,^{+0.007}_{-0.002}$	0.606	1481	1593	0
$310 - 410$	350	$0.037 - 0.060$	0.050	$0.496\,^{+0.012}_{-0.012}\,^{+0.005}_{-0.003}$	0.521	1603	1686	0
$310 - 410$	350	$0.060 - 0.120$	0.080	$0.408\,^{+0.009}_{-0.009}\,^{+0.002}_{-0.003}$	0.445	1999	2181	0
$310 - 410$	350	$0.120 - 0.250$	0.180	$0.309\,^{+0.007}_{-0.007}\,^{+0.003}_{-0.002}$	0.323	1797	1878	0
$410 - 530$	450	$0.006 - 0.010$	0.008	$0.917\,^{+0.025}_{-0.025}\,^{+0.018}_{-0.013}$	0.996	1344	1445	12
$410 - 530$	450	$0.010 - 0.017$	0.013	$0.778\,^{+0.025}_{-0.025}\,^{+0.007}_{-0.008}$	0.849	963	1047	4
$410 - 530$	450	$0.017 - 0.025$	0.021	$0.689\,^{+0.024}_{-0.024}\,^{+0.007}_{-0.003}$	0.714	796	825	0
$410 - 530$	450	$0.025 - 0.037$	0.032	$0.552\,^{+0.019}_{-0.019}\,^{+0.008}_{-0.002}$	0.613	859	955	0
$410 - 530$	450	$0.037 - 0.060$	0.050	$0.506\,^{+0.015}_{-0.015}\,^{+0.007}_{-0.003}$	0.525	1111	1153	0
$410 - 530$	450	$0.060 - 0.100$	0.080	$0.413\,^{+0.013}_{-0.013}\,^{+0.004}_{-0.002}$	0.446	1007	1088	0
$410 - 530$	450	$0.100 - 0.170$	0.130	$0.340\,^{+0.011}_{-0.011}\,^{+0.002}_{-0.003}$	0.372	895	980	0
$410 - 530$	450	$0.170 - 0.300$	0.250	$0.249\,^{+0.009}_{-0.009}\,^{+0.003}_{-0.004}$	0.258	788	817	0
$530 - 710$	650	$0.010 - 0.017$	0.013	$0.751\,^{+0.022}_{-0.022}\,^{+0.004}_{-0.005}$	0.862	1175	1337	10
$530 - 710$	650	$0.017 - 0.025$	0.021	$0.647\,^{+0.024}_{-0.024}\,^{+0.005}_{-0.004}$	0.727	718	805	2
$530 - 710$	650	$0.025 - 0.037$	0.032	$0.579\,^{+0.024}_{-0.024}\,^{+0.003}_{-0.003}$	0.623	576	619	0
$530 - 710$	650	$0.037 - 0.060$	0.050	$0.477\,^{+0.020}_{-0.020}\,^{+0.005}_{-0.003}$	0.530	553	614	0
$530 - 710$	650	$0.060 - 0.100$	0.080	$0.441\,^{+0.019}_{-0.019}\,^{+0.008}_{-0.003}$	0.447	536	543	0
$530 - 710$	650	$0.100 - 0.170$	0.130	$0.352\,^{+0.016}_{-0.016}\,^{+0.004}_{-0.003}$	0.371	491	517	0
$530 - 710$	650	$0.170 - 0.300$	0.250	$0.230\,^{+0.011}_{-0.011}\,^{+0.003}_{-0.001}$	0.254	414	457	0
$710 - 900$	800	$0.009 - 0.017$	0.013	$0.735\,^{+0.027}_{-0.027}\,^{+0.011}_{-0.012}$	0.863	768	887	12
$710 - 900$	800	$0.017 - 0.025$	0.021	$0.700\,^{+0.030}_{-0.030}\,^{+0.005}_{-0.005}$	0.733	542	566	1
$710 - 900$	800	$0.025 - 0.037$	0.032	$0.614\,^{+0.026}_{-0.026}\,^{+0.003}_{-0.004}$	0.627	562	574	0
$710 - 900$	800	$0.037 - 0.060$	0.050	$0.475\,^{+0.020}_{-0.020}\,^{+0.004}_{-0.003}$	0.533	571	641	0
$710 - 900$	800	$0.060 - 0.100$	0.080	$0.452\,^{+0.019}_{-0.019}\,^{+0.003}_{-0.003}$	0.448	552	548	0
$710 - 900$	800	$0.100 - 0.170$	0.130	$0.321\,^{+0.016}_{-0.016}\,^{+0.004}_{-0.002}$	0.370	396	457	0
$710 - 900$	800	$0.170 - 0.300$	0.250	$0.248\,^{+0.013}_{-0.013}\,^{+0.002}_{-0.002}$	0.252	349	354	0

Table A.10: The e^+p NC DIS reduced cross section $\tilde{\sigma}$ (for $Q^2 > 185\,\mathrm{GeV}^2$ and $y < 0.95$), corresponding to $\mathcal{L} = 42.4\,\mathrm{pb}^{-1}, P = -0.36$. The columns contain: the Q^2-bin range, Q^2-bin center, x-bin range, x-bin center, the measured cross section (the first error on the cross section corresponds to the statistical, the second to the systematic uncertainty), the theoretical cross section at $P = 0.0$, the number of observed data (N_{DATA}), signal MC (N_{MC}) and background MC (N^{bg}_{MC}) events, for a given (x, Q^2) bin.

Q^2 range	Q^2_c	x range	x_c	$\tilde{\sigma}$		N_{DATA}	N_{MC}	N^{bg}_{MC}
[GeV^2]	[GeV^2]			measured ($P=-0.36$)	SM ($P=0$)			
$900-1300$	1200	$0.010-0.017$	0.014	$0.761\,^{+0.032}_{-0.032}\,^{+0.058}_{-0.018}$	0.827	572	605	15
$900-1300$	1200	$0.017-0.025$	0.021	$0.658\,^{+0.028}_{-0.028}\,^{+0.005}_{-0.007}$	0.734	542	599	5
$900-1300$	1200	$0.025-0.037$	0.032	$0.591\,^{+0.025}_{-0.025}\,^{+0.007}_{-0.005}$	0.632	569	608	0
$900-1300$	1200	$0.037-0.060$	0.050	$0.478\,^{+0.019}_{-0.019}\,^{+0.005}_{-0.003}$	0.536	656	734	1
$900-1300$	1200	$0.060-0.100$	0.080	$0.394\,^{+0.016}_{-0.016}\,^{+0.002}_{-0.002}$	0.449	601	684	0
$900-1300$	1200	$0.100-0.170$	0.130	$0.339\,^{+0.014}_{-0.014}\,^{+0.001}_{-0.003}$	0.368	558	605	0
$900-1300$	1200	$0.170-0.300$	0.250	$0.235\,^{+0.011}_{-0.011}\,^{+0.003}_{-0.002}$	0.248	442	465	0
$900-1300$	1200	$0.300-0.530$	0.400	$0.124\,^{+0.009}_{-0.009}\,^{+0.002}_{-0.002}$	0.130	190	199	0
$1300-1800$	1500	$0.017-0.025$	0.021	$0.670\,^{+0.039}_{-0.039}\,^{+0.023}_{-0.007}$	0.728	304	324	5
$1300-1800$	1500	$0.025-0.037$	0.032	$0.556\,^{+0.032}_{-0.032}\,^{+0.010}_{-0.006}$	0.632	298	337	1
$1300-1800$	1500	$0.037-0.060$	0.050	$0.495\,^{+0.025}_{-0.025}\,^{+0.005}_{-0.004}$	0.537	388	419	1
$1300-1800$	1500	$0.060-0.100$	0.080	$0.435\,^{+0.022}_{-0.022}\,^{+0.005}_{-0.003}$	0.448	398	410	0
$1300-1800$	1500	$0.100-0.150$	0.130	$0.346\,^{+0.021}_{-0.021}\,^{+0.003}_{-0.004}$	0.367	263	278	0
$1300-1800$	1500	$0.150-0.230$	0.180	$0.268\,^{+0.018}_{-0.018}\,^{+0.001}_{-0.003}$	0.311	218	253	0
$1300-1800$	1500	$0.230-0.350$	0.250	$0.232\,^{+0.018}_{-0.018}\,^{+0.002}_{-0.003}$	0.245	158	167	0
$1300-1800$	1500	$0.350-0.530$	0.400	$0.133\,^{+0.016}_{-0.014}\,^{+0.005}_{-0.002}$	0.128	88	85	0
$1800-2500$	2000	$0.023-0.037$	0.032	$0.569\,^{+0.038}_{-0.038}\,^{+0.021}_{-0.010}$	0.625	235	252	6
$1800-2500$	2000	$0.037-0.060$	0.050	$0.431\,^{+0.029}_{-0.029}\,^{+0.004}_{-0.005}$	0.534	221	272	1
$1800-2500$	2000	$0.060-0.100$	0.080	$0.408\,^{+0.026}_{-0.026}\,^{+0.004}_{-0.004}$	0.447	256	280	0
$1800-2500$	2000	$0.100-0.150$	0.130	$0.357\,^{+0.026}_{-0.026}\,^{+0.002}_{-0.002}$	0.365	192	196	0
$1800-2500$	2000	$0.150-0.230$	0.180	$0.288\,^{+0.022}_{-0.022}\,^{+0.003}_{-0.003}$	0.308	165	177	0
$1800-2500$	2000	$0.230-0.350$	0.250	$0.248\,^{+0.022}_{-0.022}\,^{+0.003}_{-0.002}$	0.243	123	120	0
$1800-2500$	2000	$0.350-0.530$	0.400	$0.119\,^{+0.018}_{-0.016}\,^{+0.001}_{-0.002}$	0.126	56	59	0
$2500-3500$	3000	$0.037-0.060$	0.050	$0.494\,^{+0.039}_{-0.039}\,^{+0.013}_{-0.004}$	0.521	162	171	0
$2500-3500$	3000	$0.060-0.100$	0.080	$0.418\,^{+0.031}_{-0.031}\,^{+0.004}_{-0.008}$	0.439	178	186	1
$2500-3500$	3000	$0.100-0.150$	0.130	$0.329\,^{+0.029}_{-0.029}\,^{+0.003}_{-0.004}$	0.360	126	138	0
$2500-3500$	3000	$0.150-0.230$	0.180	$0.270\,^{+0.026}_{-0.026}\,^{+0.011}_{-0.003}$	0.304	109	122	0
$2500-3500$	3000	$0.230-0.350$	0.250	$0.210\,^{+0.027}_{-0.024}\,^{+0.005}_{-0.001}$	0.239	77	88	0
$2500-3500$	3000	$0.350-0.530$	0.400	$0.121\,^{+0.022}_{-0.019}\,^{+0.002}_{-0.002}$	0.123	40	40	0
$2500-5600$	3000	$0.530-1.000$	0.650	$0.017\,^{+0.006}_{-0.004}\,^{+0.001}_{-0.002}$	0.019	15	16	0
$3500-5600$	5000	$0.040-0.100$	0.080	$0.352\,^{+0.026}_{-0.026}\,^{+0.006}_{-0.009}$	0.409	186	215	1
$3500-5600$	5000	$0.100-0.150$	0.130	$0.292\,^{+0.033}_{-0.030}\,^{+0.004}_{-0.004}$	0.342	96	113	0
$3500-5600$	5000	$0.150-0.230$	0.180	$0.226\,^{+0.028}_{-0.025}\,^{+0.007}_{-0.004}$	0.293	82	106	0
$3500-5600$	5000	$0.230-0.350$	0.250	$0.192\,^{+0.027}_{-0.024}\,^{+0.004}_{-0.003}$	0.231	65	78	0
$3500-5600$	5000	$0.350-0.530$	0.400	$0.123\,^{+0.023}_{-0.020}\,^{+0.002}_{-0.002}$	0.119	39	38	0
$5600-9000$	8000	$0.070-0.150$	0.130	$0.285\,^{+0.035}_{-0.031}\,^{+0.009}_{-0.008}$	0.302	84	88	1
$5600-9000$	8000	$0.150-0.230$	0.180	$0.247\,^{+0.039}_{-0.034}\,^{+0.003}_{-0.006}$	0.266	52	56	0
$5600-9000$	8000	$0.230-0.350$	0.250	$0.176\,^{+0.035}_{-0.030}\,^{+0.002}_{-0.007}$	0.216	35	43	0
$5600-9000$	8000	$0.350-0.530$	0.400	$0.111\,^{+0.029}_{-0.023}\,^{+0.003}_{-0.004}$	0.114	22	23	0
$5600-15000$	8000	$0.530-1.000$	0.650	$0.011\,^{+0.008}_{-0.005}\,^{+0.002}_{-0.000}$	0.017	5	8	0
$9000-15000$	12000	$0.090-0.230$	0.180	$0.173\,^{+0.039}_{-0.033}\,^{+0.005}_{-0.021}$	0.219	28	35	0
$9000-15000$	12000	$0.230-0.350$	0.250	$0.062\,^{+0.034}_{-0.023}\,^{+0.001}_{-0.001}$	0.188	7	21	0
$9000-15000$	12000	$0.350-0.530$	0.400	$0.067\,^{+0.033}_{-0.023}\,^{+0.001}_{-0.011}$	0.105	8	12	0
$15000-25000$	20000	$0.150-0.350$	0.250	$0.128\,^{+0.054}_{-0.040}\,^{+0.026}_{-0.020}$	0.126	10	10	0
$15000-25000$	20000	$0.350-1.000$	0.400	$0.084\,^{+0.050}_{-0.033}\,^{+0.019}_{-0.013}$	0.082	6	6	0
$25000-50000$	30000	$0.250-1.000$	0.400	$0.023\,^{+0.053}_{-0.019}\,^{+0.001}_{-0.004}$	0.053	1	2	0

Continuation of Table A.10.

Q^2 range [GeV^2]	Q^2_c [GeV^2]	x range	x_c	$x\tilde{F}_3$
1300 – 1800	1500	0.017 – 0.025	0.021	$0.047\,^{+0.019}_{-0.019}\,^{+0.018}_{-0.015}$
	1500	0.025 – 0.037	0.032	$0.068\,^{+0.026}_{-0.026}\,^{+0.005}_{-0.006}$
	1500	0.037 – 0.060	0.050	$-0.001\,^{+0.028}_{-0.028}\,^{+0.006}_{-0.007}$
	1500	0.060 – 0.100	0.080	$0.101\,^{+0.041}_{-0.041}\,^{+0.010}_{-0.027}$
	1500	0.100 – 0.150	0.130	$0.033\,^{+0.068}_{-0.068}\,^{+0.042}_{-0.043}$
	1500	0.150 – 0.230	0.180	$0.093\,^{+0.091}_{-0.091}\,^{+0.059}_{-0.059}$
	1500	0.230 – 0.350	0.250	$0.147\,^{+0.122}_{-0.122}\,^{+0.016}_{-0.085}$
	1500	0.350 – 0.530	0.400	$0.119\,^{+0.170}_{-0.170}\,^{+0.135}_{-0.138}$
1800 – 2500	2000	0.023 – 0.037	0.032	$0.063\,^{+0.020}_{-0.020}\,^{+0.015}_{-0.010}$
	2000	0.037 – 0.060	0.050	$0.113\,^{+0.029}_{-0.029}\,^{+0.011}_{-0.005}$
	2000	0.060 – 0.100	0.080	$-0.004\,^{+0.034}_{-0.034}\,^{+0.004}_{-0.019}$
	2000	0.100 – 0.150	0.130	$0.049\,^{+0.058}_{-0.058}\,^{+0.024}_{-0.006}$
	2000	0.150 – 0.230	0.180	$0.129\,^{+0.071}_{-0.071}\,^{+0.030}_{-0.044}$
	2000	0.230 – 0.350	0.250	$0.024\,^{+0.100}_{-0.100}\,^{+0.036}_{-0.062}$
	2000	0.350 – 0.530	0.400	$-0.039\,^{+0.140}_{-0.140}\,^{+0.099}_{-0.101}$
2500 – 3500	3000	0.037 – 0.060	0.050	$0.061\,^{+0.021}_{-0.021}\,^{+0.009}_{-0.070}$
	3000	0.060 – 0.100	0.080	$0.113\,^{+0.032}_{-0.032}\,^{+0.012}_{-0.012}$
	3000	0.100 – 0.150	0.130	$0.051\,^{+0.053}_{-0.053}\,^{+0.004}_{-0.006}$
	3000	0.150 – 0.230	0.180	$0.090\,^{+0.053}_{-0.053}\,^{+0.006}_{-0.006}$
	3000	0.230 – 0.350	0.250	$0.171\,^{+0.075}_{-0.075}\,^{+0.080}_{-0.080}$
	3000	0.350 – 0.530	0.400	$0.104\,^{+0.097}_{-0.097}\,^{+0.070}_{-0.007}$
	3000	0.530 – 1.000	0.650	$0.064\,^{+0.032}_{-0.032}\,^{+0.000}_{-0.011}$
3500 – 5600	5000	0.040 – 0.100	0.080	$0.093\,^{+0.018}_{-0.018}\,^{+0.007}_{-0.003}$
	5000	0.100 – 0.150	0.130	$0.137\,^{+0.031}_{-0.031}\,^{+0.004}_{-0.002}$
	5000	0.150 – 0.230	0.180	$0.090\,^{+0.042}_{-0.042}\,^{+0.005}_{-0.003}$
	5000	0.230 – 0.350	0.250	$0.046\,^{+0.042}_{-0.042}\,^{+0.009}_{-0.002}$
	5000	0.350 – 0.530	0.400	$-0.011\,^{+0.063}_{-0.063}\,^{+0.038}_{-0.039}$
5600 – 9000	8000	0.070 – 0.150	0.130	$0.176\,^{+0.019}_{-0.019}\,^{+0.008}_{-0.012}$
	8000	0.150 – 0.230	0.180	$0.192\,^{+0.027}_{-0.027}\,^{+0.010}_{-0.010}$
	8000	0.230 – 0.350	0.250	$0.132\,^{+0.039}_{-0.039}\,^{+0.017}_{-0.014}$
	8000	0.350 – 0.530	0.400	$0.000\,^{+0.044}_{-0.044}\,^{+0.024}_{-0.026}$
	8000	0.530 – 1.000	0.650	$0.027\,^{+0.015}_{-0.015}\,^{+0.004}_{-0.004}$
9000 – 15000	12000	0.090 – 0.230	0.180	$0.181\,^{+0.023}_{-0.023}\,^{+0.008}_{-0.013}$
	12000	0.230 – 0.350	0.250	$0.183\,^{+0.034}_{-0.034}\,^{+0.009}_{-0.009}$
	12000	0.350 – 0.530	0.400	$0.061\,^{+0.044}_{-0.044}\,^{+0.017}_{-0.015}$
15000 – 25000	20000	0.150 – 0.350	0.250	$0.183\,^{+0.027}_{-0.027}\,^{+0.016}_{-0.013}$
	20000	0.350 – 1.000	0.400	$0.096\,^{+0.032}_{-0.032}\,^{+0.011}_{-0.009}$
25000 – 50000	30000	0.250 – 1.000	0.400	$0.123\,^{+0.027}_{-0.027}\,^{+0.013}_{-0.006}$

Table A.11: The generalized structure function $x\tilde{F}_3$ extracted using the e^+p and e^-p NC DIS data sets corresponding to the integrated luminosity of $283\,\mathrm{pb}^{-1}$. The columns contain: the Q^2-bin range, Q^2-bin center, x-bin range, x-bin center, the extracted $x\tilde{F}_3$, with the first error on the cross section corresponds to the statistical, the second to the systematic uncertainty, for a given (x, Q^2) bin.

References

[1] H.W. Kendall, Rev. Mod. Phys. **63**, 597 (1991).

[2] F. Wilczek, Proc. Nat. Acad. Sci. **102**, 8403 (2005).

[3] A.D. Martin, Contemp. Phys. **36**, 335 (1995).

[4] A.D. Martin, *Proton structure, Partons, QCD, DGLAP and beyond*, 2007. In the proceedings of Summer School on QCD, Low X Physics, Saturation and Diffraction, Calabria, Italy.

[5] F. Halzen and A.D. Martin, *Quarks and Leptons: An Introductory Course in Modern Particle Physics*. John Wiley & Sons, Inc, 1984.

[6] S.L. Glashow, Rev. Mod. Phys. **52**, 539 (1980).

[7] A. Salam, Rev. Mod. Phys. **52**, 525 (1980).

[8] S. Weinberg, Rev. Mod. Phys. **52**, 515 (1980).

[9] L. Lederman, D. Teresi, *The God particle: If the universe is the answer, what is the question?* Houghton Mifflin, Boston, USA, 1993.

[10] E. Rutherford, Phil. Mag. **21**, 669 (1911).

[11] H. Geiger and E. Marsden, Proc. Roy. Soc. (London) **82**, 495 (1909).

[12] R. Hofstadter, R.W. McAllister, Phys. Rev. **98**, 217 (1955).

[13] G. Zweig, *An SU(3) model for strong interaction symmetry and its breaking.* CERN-TH-401.

[14] M. Gell-Mann, Phys. Lett. **8**, 214 (1964).

[15] M.Y. Han, Y. Nambu, Phys. Rev. **139**, B1006 (1965).

[16] E.D. Bloom et al., Phys. Rev. Lett. **23**, 930 (1969).

[17] M. Breidenbach et al., Phys. Rev. Lett. **23**, 935 (1969).

[18] J.D. Bjorken, Phys. Rev. **179**, 1547 (1969).

[19] J.I. Friedman, H.W. Kendall, R.E. Taylor, *Nobel lectures in physics 1990.* SLAC-REPRINT-1991-019.

[20] R.P. Feynman, Phys. Rev. Lett. **23**, 1415 (1969).

[21] C.G. Callan and D.J. Gross, Phys. Rev. Lett. **22**, 156 (1969).

[22] R.P. Feynman, *Photon-hadron interactions.* W. A. Benjamin, 1972.

[23] J.J. Aubert et al., Phys. Lett. **B105**, 315 (1981).

[24] A.C. Benvenuti et al., Phys. Lett. **B223**, 490 (1989).

[25] D. Allasia et al., Phys. Lett. **B249**, 366 (1990).

[26] M. Derrick et al., Phys. Lett. **B316**, 412 (1993).

[27] I. Abt et al., Nucl. Phys. **B407**, 515 (1993).

[28] H1 and ZEUS Collab., *Combination of H1 and ZEUS Deep Inelastic* $e^{\pm}p$ *Scattering Cross Sections.* H1prelim-07-007, ZEUS-prel-07-026, preliminary results.

[29] H1 and ZEUS Collab., *QCD Fits using combined H1 and ZEUS inclusive data.* H1prelim-08-045, ZEUS-prel-08-003, preliminary results.

[30] D.J. Gross, F. Wilczek, Phys. Rev. **D8**, 3633 (1973).

[31] D.J. Gross, F. Wilczek, Phys. Rev. Lett. **30**, 1343 (1973).

[32] D.J. Gross, F. Wilczek, Phys. Rev. **D9**, 980 (1974).

[33] H. Fritzsch, M. Gell-Mann, P. Minkowski, Physics Letters B **59**, 256 (1975).

[34] D. Gross, F. Wilczek, P.J. Steinhardt, M. Gell-Mann, S.L. Glashow, E. Weinberg, S. Weinberg, G't Hooft, E. Witten, *QFT & QCD Past, Present, and Future: March 18-19, 2005.* Harvard University, 2005.

[35] S. Bethke, Prog. Part. Nucl. Phys. **58**, 351 (2007).

[36] P. Soding, B. Wiik, G. Wolf, S.L. Wu, *The first evidence for three-jet events in e+e- collisions at PETRA: First direct observation of the gluon.* Prepared for International Europhysics Conference on High-Energy Physics (HEP 95), Brussels, Belgium, 1995.

[37] S. Albino, Preprint 0810.4255, 2008.

[38] I. Montvay, Rev. Mod. Phys. **59**, 263 (1987).

[39] S. Durr at al., Science **322**, 1224 (2008).

[40] R. Brandelik et al., Phys. Lett. **B86**, 243 (1979).

[41] G. Altarelli, Ann. Rev. Nucl. Part. Sci. **39**, 357 (1989).

[42] C. Glasman, *Precision tests of QCD with jets and vector bosons at HERA and TevaTron.* Plenary talk at 34th International Conference on High Energy Physics (ICHEP 2008).

[43] S.U. Noor, *Measurement of neutral current electron-proton cross sections with longitudinally polarised electrons using the ZEUS detector.* Ph.D. Thesis, York University, 2007.

[44] G. Altarelli, Phys. Rept. **81**, 1 (1982).

[45] R. Devenish and A. Cooper-Sarkar, *Deep Inelastic Scattering.* Oxford University Press, 2003.

[46] E. Fermi, Z. Phys. **88**, 161 (1934).

[47] T.D. Lee, C-N. Yang,, Phys. Rev. **104**, 254 (1956).

[48] C.S. Wu et al., Phys. Rev. **105**, 1413 (1957).

[49] R.P. Feynman, M. Gell-Mann, Phys. Rev. **109**, 193 (1958).

[50] S.L. Glashow, Nucl. Phys. **22**, 579 (1961).

[51] S. Weinberg, Phys. Rev. Lett. **19**, 1264 (1967).

[52] A. Salam, J.C. Ward, Phys. Lett. **13**, 168 (1964).

[53] F.J. Hasert et al., Phys. Lett. **B46**, 138 (1973).

[54] UA1 Coll., G. Arnison et al., Phys. Lett. **B 122**, 103 (1983).

[55] G. Arnisonand et al., Phys. Lett. **B126**, 398 (1983).

[56] U.F. Katz, *Deep-Inelastic Positron–Proton Scattering in the High-Momentum-Transfer Regime of HERA*, Springer Tracts in Modern Physics, Vol. 168. Springer, Berlin, Heidelberg, 2000.

[57] A. Kappes, *Measurement of* $e^-p \rightarrow e^-X$ *differential cross sections at high* Q^2 *and of the structure function* xF_3 *with ZEUS at HERA.* Ph.D. Thesis, Universität Bonn, Bonn, Germany, Report BONN-IR-01-16, 2001.

[58] M. Klein and T. Riemann, Z. Phys. **C 24**, 151 (1984).

[59] ZEUS Collab., *Measurement of high-*Q^2 *neutral current deep inelastic* e^-p *scattering cross sections with a longitudinally polarised electron beam at HERA*, 2009. DESY-08-202, to be published in Eur.Phys.J C.

[60] C. Diaconu, AIP Conf. Proc. **972**, 203 (2008).

[61] K. Long, *A pedagogical introduction to DIS* (unpublished), available on `http://www-zeus.desy.de/lectures`. ZEUS Lecture Series, DESY, October 2000.

[62] M. Klein, *First Measurements of FL at Low Bjorken x*, 2008. Prepared for the 34th International Conference on High Energy Physics (ICHEP 2008).

[63] A.M. Cooper-Sarkar et al., Z. Phys. **C39**, 281 (1988).

[64] F.D. Aaron et al., Phys. Lett. **B665**, 139 (2008).

[65] H.L. Lai et al., Phys. Rev. **D 51**, 4763 (1995).

[66] A.D. Martin et al., Eur. Phys. J. **C 23**, 73 (2002).

[67] S. Chekanov et al., Eur. Phys. J. **C42**, 1 (2005).

[68] C. Adloff et al., Eur. Phys. J. **C30**, 1 (2003).

[69] A.D. Tapper, *Inclusive high Q2 cross sections and QCD and EW fits at HERA*, 2008. To be published in proceedings of the ICHEP08 conference, Philadelphia.

[70] H1 and ZEUS Collab., *Electroweak Neutral Currents at HERA.* H1prelim-06-142, ZEUS-prel-06-022, preliminary results.

[71] B.H. Wiik et al., *HERA. A proposal for a Large Electron-Proton Colliding Beam Facility at DESY.* DESY HERA-81-10, 1981.

[72] F.R. Elder, A.M. Gurewitsch, R.V. Langmuir and H.C. Pollock, Phys. Rev. **71**, 829 (1947).

[73] A.A. Sokolov, D.V. Gel'tsov, M.M.Kolesnikova, Russian Physics Journal **14**, 436 (1970).

[74] M.G. Minty, *HERA Performance Upgrade: Achievements and Plans for the Future.* Presented at the 9th European Particle Accelerator Conference (EPAC 2004).

[75] B. Foster, *ZEUS at HERA II*, 2001. Contributed to 9th International Workshop on Deep Inelastic Scattering (DIS 2001), Bologna, Italy.

[76] ZEUS collaboration, *ZEUS luminosity calculation*, available on `http://www-zeus.desy.de/physics/lumi/`.

[77] G. Ingelman, A. De Roeck, R. Klanner (editors), *Future Physics at HERA*, 1995-1996, available on `http://www.desy.de/~heraws96/`.

[78] A.A. Sokolov and I.M. Ternov, Sov. Phys. Dokl. **8**, 1203 (1964).

[79] V.N. Baier, V.A. Khoze, Sov. J. Nucl. Phys. **9**, 238 (1969).

[80] D.P. Barber, Phys. Lett. **B 343**, 436 (1995).

[81] W. Lorenzon, *Proposal to DESY for a longitudinal electron polarimeter at HERA east section* (unpublished). DESY-HERMES-95-23.

[82] M. Beckmann et al., Nucl. Instrum. Meth. **A479**, 334 (2002).

[83] DESY POL2000 group, *Using the HERA Polarization Measurements - Recommendations for the Summer 2007 Conferences* (unpublished). June 2007.

[84] P.J. Bryant, *A brief history and review of accelerators.* In Jyvaeskylae 1992, Proceedings, General accelerator physics, CERN Geneva - CERN-94-01.

[85] HERMES collaboration, *Physics highlights*, available on `http://www-hermes.desy.de/physics/spinphysics.html`.

[86] A. J. Schwartz, NUCL. INSTRUM. METH. A **446**, 199 (2000).

[87] C.H. Llewellyn-Smith and B.H. Wiik, *Physics with Large electron-Proton Colliding Rings.* DESY 77/38.

[88] D. Harris, *The end of the HERA era*, September 2007. Symmetry Magazine.

[89] M. Klein and R. Yoshida, *Collider Physics at HERA*, 2008. To be published in *Progress in Particle and Nuclear Physics.*

[90] H. Abramowicz and A. Caldwell, Rev. Mod. Phys. **71**, 1275 (1999).

[91] A.M. Cooper-Sarkar, R.C.E. Devenish and A. De Roeck, Int. J. Mod. Phys. **A 13**, 3385 (1998).

[92] ZEUS Coll., U. Holm (ed.), *The ZEUS Detector.* Status Report (unpublished), DESY (1993), available on `http://www-zeus.desy.de/bluebook/bluebook.html`.

[93] M. Derrick et al., Nucl. Inst. Meth. **A 309**, 77 (1991);
A. Andresen et al., Nucl. Inst. Meth. **A 309**, 101 (1991);
A. Caldwell et al., Nucl. Inst. Meth. **A 321**, 356 (1992);
A. Bernstein et al., Nucl. Inst. Meth. **A 336**, 23 (1993).

[94] M. Barbi, *Calibration and monitoring of the ZEUS uranium scintillator calorimeter at HERA.* Prepared for 10th International Conference on Calorimetry in High Energy Physics (CALOR 2002), Pasadena, California.

[95] I. Bohnet, *Investigations on uniformity, radiation resistance and calibration of ZEUS calorimeter components at HERA*. DESY-THESIS-1999-041.

[96] R. Yoshida, *Introduction to Calorimetry and the ZEUS Calorimeter* (unpublished), available on `http://www-zeus.desy.de/lectures`. ZEUS Lecture Series, DESY, November 2000.

[97] R.K. Bock and A. Vasilescu, *The particle detector briefbook.* Berlin, Germany: Springer (1998) 131 p.

[98] A. Bamberger et al., Nucl. Inst. Meth. **A 382**, 419 (1996).

[99] N. Harnew et al., Nucl. Inst. Meth. **A 279**, 290 (1989);
B. Foster et al., Nucl. Phys. Proc. Suppl. **B 32**, 181 (1993);
B. Foster et al., Nucl. Inst. Meth. **A 338**, 254 (1994).

[100] B. Foster, *Introduction to Drift Chambers and the ZEUS CTD* (unpublished), available on `http://www-zeus.desy.de/lectures`. ZEUS Lecture Series, DESY, March 2001.

[101] I.C. Brock et al., Nucl. Instrum. Meth. **A581**, 656 (2007).

[102] C. Coldewey, Nucl. Inst. Meth. **A 447**, 44 (2000).

[103] V. Chiochia, Nucl. Instrum. Meth. **A501**, 60 (2003).

[104] B. Bock et al., Nucl. Inst. Meth. **A 344**, 335 (1994).

[105] S. Fourletov, Nucl. Instrum. Meth. **A535**, 191 (2004).

[106] ZEUS collaboration, *A Straw-Tube Tracker for ZEUS* (unpublished). ZEUS Note 98-046.

[107] R. Mankel, *ZEUS Tracking Tutorial* (unpublished), available on `http://www-zeus.desy.de/lectures`. ZEUS Lecture Series, DESY, November 2006.

[108] J. Andruszków et al., Acta Phys. Pol. **B 32**, 2025 (2001).

[109] M. Helbich et al., Nucl. Instrum. Meth. **A565**, 572 (2006).

[110] H. Bethe and W. Heitler, Proc. Roy. Soc. Lond. **A 146**, 83 (1934).

[111] S.D. Paganis, Int. J. Mod. Phys. **A16S1C**, 1147 (2001).

[112] ZEUS Collab., *Measurement of charged current deep inelastic scattering cross sections with a longitudinally polarised electron beam at HERA*, 2008. DESY-08-177, to be published in Eur.Phys.J C.

[113] R. Carlin, W.H. Smith, K. Tokushuku and L.W. Wiggers, Nucl. Instrum. Meth. **A379**, 542 (1996).

[114] P. Pluciński, *Setup and Optimisation of the Muon Trigger System for the ZEUS Backing Calorimeter*. Ph.D. Thesis, The Andrzej Soltan Institute for Nuclear Studies, 2007.

[115] O.M. Kind, *Production of heavy flavours with associated jets at HERA*. Ph.D. Thesis, Universität Bonn, Report BONN-IR-2006-01, 2006.

[116] H. J. van der Lugt, *The Data acquisition and second level trigger system for the ZEUS calorimeter*. PhD thesis, RX-1426 (AMSTERDAM).

[117] W.H. Smith et al., Nucl. Inst. Meth. **A 355**, 278 (1995).

[118] M. Własenko, *Simulation of the muon trigger for the backing calorimeter (ZEUS experiment).* M.Sc. Thesis, Łódź University, 2004.

[119] T. Schlichting, *Control and analysis of data flow in the ZEUS event builder. (In German).* Hamburg DESY - Internal Rep. F35D-92-01 (92/04,rec.May) 72 p.

[120] S. Bhadra, M. Crombie, D. Kirkby and R.S. Orr, Comput. Phys. Commun. **57**, 321 (1989).

[121] L. Koepke, *The ZEUS Primer.* ZEUS, 1993.

[122] J.C. Hart, *Experience with ADAMO in ZEUS.* In *Erice 1990, Proceedings, Data structures for particle physics experiments* 51-57.

[123] B. Straub, *Introduction to ORANGE* (unpublished), available on `http://www-zeus.desy.de/lectures`. ZEUS Lecture Series, DESY, November 2002.

[124] L.A.T. Bauerdick, O. Derugin, D. Gilkinson, M. Kasemann, O. Manczak, *The physics analysis environment of the ZEUS experiment.* Prepared for International Conference on Computing in High- energy Physics (CHEP 95), Rio de Janeiro, Brazil, 1995.

[125] M. Kowal, K. Wrona, T.M. Haas, I. Martens, R. Mankel, *A Linux PC farm for physics batch analysis in the ZEUS experiment.* Prepared for International Conference on Computing in High-Energy Physics and Nuclear Physics (CHEP 2000), Padova, Italy.

[126] R. Brun, O. Couet,C.E. Vandoni, P. Zanarini, Comput. Phys. Commun. **57**, 432 (1989).

[127] R. Brun and F. Rademakers, Nucl. Instrum. Meth. **A389**, 81 (1997).

[128] P. Cloth, V. Drueke, D. Filges, R.D. Neef, H. Schaal, *Full Monte Carlo systems for ZEUS calorimeter simulations.* In Amsterdam 1991, Proceedings, MC 91: Detector and event simulation in high energy physics, 342-360.

[129] R. Brun, R. Hagelberg, M. Hansroul, and J.C. Lassalle, *GEANT: simulation program for particle physics experiments. User guide and reference manual.* CERN-DD-78-2-REV.

[130] H. Stadie, M. Ernst, J. Ferrando, R. Mankel, K. Wrona, Nucl. Instrum. Meth. **A559**, 43 (2006).

[131] M. Wing, *Calorimeter Clustering* (unpublished), available on `http://www-zeus.desy.de/lectures`. ZEUS Lecture Series, DESY, September 2002.

[132] D. Szuba, *Calorimeter Data Quality Monitoring Report* (unpublished). Talk at the ZEUS Collaboration Week, DESY, March 2007.

[133] A. Caldwell, W. Liu, B. Mellado, B. Straub, *BCAL Electron Studies Part II: Energy Scale Calibration* (unpublished). ZEUS Note 98-018.

[134] B. Reisert, *CAL Energy Scale Calibration* (unpublished). Talk at the ZEUS F_L Monthly Meeting, DESY, January 2008.

[135] J. Ferrando, *Energy Scale and EM showers in 06-07* e^+p *data* (unpublished). Talk at the ZEUS Physics Coordinator Meeting, DESY, 10.07.2008.

[136] K. Nagano, *Hadronic Energy Scale checked with NC events* (unpublished). Talk at the ZEUS Collaboration Week, Amsterdam, October 2005.

[137] S.U. Noor, *High Q^2 NC DIS in e^-p at HERAII (status report)* (unpublished). Talk at the ZEUS Collaboration Week, DESY, March 2007.

[138] Y. Ri, *Measurement of e^-p Neutral-Current Deep Inelastic Scattering Cross Sections with Longitudinally Polarised Electron Beams at $\sqrt{s}$ =* 318 GeV. Ph.D. Thesis, Tokyo Metropolitan University, 2008. In preparation.

[139] G. Hartner, *VCTRAK - ZEUS Track and Vertex Reconstruction* (unpublished), available on `http://www-zeus.desy.de/lectures`. ZEUS Lecture Series, DESY, July 2002.

[140] R. Mankel, *ZEUS Tracking Tutorial* (unpublished), available on `http://www-zeus.desy.de/lectures`. ZEUS Lecture Series, DESY, November 2006.

[141] D. Shaw, *Pattern Recognition in the ZEUS Central Tracking Detector*, 1990. Ph.D. Thesis, University Coll. London, 1990, RALT-102.

[142] G.F. Hartner, *VCTRAK Briefing: Program and Math* (unpublished). ZEUS-98-058, internal ZEUS Note, 1998.

[143] D. Bartsch, *Energy-loss measurement with the ZEUS central tracking detector.* Ph.D. Thesis, Universität Bonn, Report BONN-IR-2007-05, 2007.

[144] M. Bell, *Measurement of Heavy Quark Production in Deep Inelastic Scattering at HERA-II.* Ph.D. Thesis, University of Oxford, 2007.

[145] P. Billoir and S. Qian, Nucl. Inst. Meth. **A 311** (1992).

[146] B. Straub, *The `em` Electron Finder* (unpublished), 1998, available on `http://www-zeus.desy.de/~straub/ZEUS_ONLY/doc/em.ps` .

[147] G.M. Briskin, *Diffractive Dissociation in ep Deep Inelastic Scattering.* Ph.D. Thesis, Tel Aviv University, Report DESY-THESIS 1998-036, 1998.

[148] J.R. Gonçalo, *Measurement of the High-Q^2 Neutral Current Deep Inelastic Scattering Cross Sections with the ZEUS Detector at HERA*. Ph.D. Thesis, University of London, Report DESY-THESIS-03-022, 2003.

[149] R. Sinkus and T. Voss, Nucl. Inst. Meth. **A 391**, 360 (1997).

[150] A. López-Durán Viani and S. Schlenstedt, *Electron Finder Efficiencies and Impurities. A Comparison Between SINISTRA95, EM and EMNET* (unpublished). ZEUS-99-077, internal ZEUS Note, 1999.

[151] J. Grosse-Knetter, *Corrections for the Hadronic Final State* (unpublished). ZEUS-98-031, internal ZEUS Note, 1998.

[152] N. Tuning, *Proton Structure Functions at HERA*. Ph.D. Thesis, Amsterdam University, 2001.

[153] G. Brandt, *HERA Physics Feynman Diagram Gallery* (unpublished), available on `http://www.desy.de/~gbrandt/feyn/`.

[154] S. Bentvelsen, J. Engelen and P. Kooijman, *Proc. Workshop on Physics at HERA*, W. Buchmüller and G. Ingelman (eds.), Vol. 1, p. 23. Hamburg, Germany, DESY (1992).

[155] D. Kollar, *Prospects for a measurement of F(L) at HERA with the ZEUS detector.* Prepared for 14th International Workshop on Deep Inelastic Scattering (DIS 2006), Tsukuba, Japan.

[156] O. Kind et al., *A ROOT-based client-server event display for the ZEUS experiment*, 2003. In the Proceedings of 2003 Conference for Computing in High-Energy and Nuclear Physics (CHEP 03), La Jolla, California.

[157] F. Willeke, *Summary of the HERA Proton-Positron Luminosity Run 2004*. HERA Note, HERA-04-01, 2004.

[158] *ZEUS Feynman Diagram Gallery* (unpublished), available on `http://www-zeus.desy.de/ZEUS_ONLY/feyn/`.

[159] J. Rautenberg, *Measurement of high-Q^2 charged current cross sections in e^+p deep inelastic scattering at HERA.* Ph.D. Thesis, Universität Bonn, Bonn, Germany, Report BONN-IR-2004-08, 2004.

[160] M. Moritz, *Measurement of the High Q^2 Neutral Current DIS Cross Section at HERA.* Ph.D. Thesis, Universität Hamburg, Report DESY-THESIS-02-009, 2001.

[161] T. Sjostrand, Comput. Phys. Commun. **82**, 74 (1994).

[162] G.A. Schuler, H. Spiesberger, *DJANGO: The Interface for the event generators HERACLES and LEPTO.* In *Hamburg 1991, Proceedings, Physics at HERA, vol. 3* 1419-1432.

[163] CTEQ Coll., H.L. Lai et al., Eur. Phys. J. **C 12**, 375 (2000).

[164] A. Kwiatkowski, H. Spiesberger, H.J. Mohring, Comp. Phys. Commun. **69**, 155 (1992).

[165] L. Lonnblad, Comput. Phys. Commun. **71**, 15 (1992).

[166] U. Pettersson, *ARIADNE: A MONTE CARLO FOR QCD CASCADES IN THE COLOR DIPOLE FORMULATION.* LU-TP-88-5.

[167] T. Sjostrand, M. Bengtsson, Comput. Phys. Commun. **43**, 367 (1987).

[168] M. Derrick et al. (ZEUS Collab.), Phys. Lett. **B315**, 481 (1993).

[169] H. Jung, Comp. Phys. Commun. **86**, 147 (1995).

[170] G. Marchesini et al., Comput. Phys. Commun. **67**, 465 (1992).

[171] B. Reisert, *Updates on the CAL energy scale calibration* (unpublished). Talk at the ZEUS F_L Meeting, DESY, March 2008.

[172] K. Horton, *Non-Uniformity Corrections for BCAL Electron Energy* (unpublished). ZEUS Note 08-004.

[173] K. Oliver, J. Ferrando, R. Devenish, *A Minimum Bias Z Vertex Distribution for 2005-2007 ep Interactions at ZEUS* (unpublished). ZEUS-07-008, internal ZEUS note, 2007.

[174] ZEUS Offline Team, *zesLite manual*, available on `http://www-zeus.desy.de/zes` .

[175] P.D. Allfrey et al., Nucl. Instrum. Meth. **A580**, 1257 (2007).

[176] A. Bornheim, *Messung der Protonstrukturfunktionen F_2 und F_L in radiativer ep-Streuung mit dem ZEUS-Detektor.* Ph.D. Thesis, Universität Bonn, Bonn, Germany, Report BONN-IR-99-17, 1999.

[177] A. Quadt, *Measurement and QCD Analysis of the Proton Structure Function F_2 from the 1994 HERA Data Using the ZEUS Detector.* Ph.D. Thesis, University of Oxford, Report RAL-TH-97-004, 1997.

[178] R. Deffner, *Measurement of the Proton Structure Function F_2 at HERA using the 1996 and 1997 ZEUS Data.* Ph.D. Thesis, Universität Bonn, Bonn, Germany, Report BONN-IR-99-20, 1999.

[179] A. Lopez-Duran-Viani, *Measurement of the proton structure function xF3 in high Q2 DIS Events using ZEUS data.* Ph.D. Thesis, Humboldt-Universität zu Berlin, 2001. DESY-THESIS-2001-056.

[180] J.T. Breitweg, *Neutral current deep inelastic scattering at large momentum transfer with ZEUS at HERA*. Ph.D. Thesis, Wisconsin University, 2001. UMI-30-20652.

[181] G.A. Schuler and H. Spiesberger, *Proc. Workshop on Physics at HERA*, W. Buchmüller and G. Ingelman (eds.), Vol. 3, p. 1419. Hamburg, Germany, DESY (1991).

[182] C. Gwenlan, AIP Conf. Proc. **792**, 396 (2005).

[183] S.U. Noor, *Neutral current cross sections with polarised lepton beam at ZEUS.* Prepared for 14th International Workshop on Deep Inelastic Scattering (DIS 2006), Tsukuba, Japan.

[184] M. Własenko, J. Ferrando, *06/07 e^+p NC status report* (unpublished). Talk at the ZEUS Collaboration Week, DESY, June 2007.

[185] A. Arbuzov et al., Comp. Phys. Comm. **94**, 128 (1996).

[186] M. Własenko, J. Ferrando, *06/07 e^+p NC status report* (unpublished). Talk at the ZEUS Collaboration Week, Chios, September 2007.

[187] J. Ferrando. Private communication.

[188] M. Własenko, J. Ferrando, K. Korcsak-Gorzo, *NC in e^+p* (unpublished). Talk at the ZEUS Collaboration Week, DESY, February 2008.

[189] J. Ferrando, M. Własenko, *NC DIS in e^+p - Update* (unpublished). Talk at the monthly ZEUS Collaboration Meeting, DESY, February 2008.

[190] M. Własenko, *NC in e^+p: update* (unpublished). Talk at the monthly ZEUS Meeting, high-Q^2 session, DESY, May 2008.

[191] S. Chekanov et al., Nucl. Phys. **B765**, 1 (2007).

[192] S. Chekanov et al., Phys. Rev. **D76**, 072011 (2007).

[193] ZEUS Coll., S. Chekanov et al., Phys. Rev. **D 69**, 012004 (2004).

[194] V. Drugakov, J. Ferrando, C. Glasman, M. Własenko, *Data rates for different processes in HERA II* (unpublished). Talk at the ZEUS Analysis Forum, DESY, March 2008.

[195] C. Glasman, *Rates with HERA II data* (unpublished). Talk at the ZEUS QCD-group meeting, DESY, April 3, 2008.

[196] K. Olkiewicz, *Status of luminosity measurements* (unpublished). Talk at the ZEUS Collaboration Week, Madrid, July 2008.

[197] A. Caldwell, *Status of luminosity measurements* (unpublished). Talk at the ZEUS Analysis Forum, DESY, March 2008.

[198] M. Własenko, *NC* e^+p*: Zvtx vs time* (unpublished). Talk at the ZEUS high-Q^2 meeting, DESY, November 2008.

[199] Y. Yamazaki. Private communication.

[200] M. Własenko, J. Ferrando, *06/07* e^+p *NC status report* (unpublished). Talk at the ZEUS Collaboration Week, Madrid, July 2008.

[201] M. Własenko, *NC* e^+p*: trigger studies* (unpublished). Talk at the monthly ZEUS Meeting, high-Q^2 session, DESY, April 2008.

[202] E. Brownson, *Investigation and Simulation of a Localized Electron Finding Inefficiency in the ZEUS CFLT for Data Taken Since the Start of the 04* e^+ *Running Period until Present* (unpublished), 2007, available on `http://www-zeus.desy.de/~brownson/data/physics/flt30` . Internal ZEUS note.

[203] S.U. Noor, *Proton Structure Functions at High* Q^2 *and High* x *at HERA*, 2007. In proceedings of the 42nd Rencontres de Moriond on QCD and Hadronic Interactions, La Thuile.

[204] G. Zech, *Comparing statistical data to Monte Carlo simulation: Parameter fitting and unfolding.* DESY-95-113.

[205] S. Chekanov, et al., Eur. Phys. J. **C21**, 443 (2001).

[206] ZEUS Collab., *ZEUS-JETS QCD fit.* ZEUS-prel-04-014, preliminary results.

[207] S. Chekanov et al., Phys. Lett. **B637**, 210 (2006).

[208] ZEUS Collab., J. Breitweg et al., Eur. Phys. J. **C11**, 427 (1999).

[209] H1 Collab., C. Adloff et al., Eur. Phys. J. **C13**, 609 (2000).

[210] A. Argento et al., Phys. Lett. **B140**, 142 (1984).

[211] M. Dittmar et al., Preprint 0901.2504, 2009. Summary report of Working Group I for the HERA-LHC workshop.

Acknowledgments

It has been quite a special time - these four and a half years, working on my PhD at the University of Bonn and at DESY in Hamburg. Intellectually challenging, socially enriching, sometimes tough, sometimes delightful - a good time altogether. And all this would have not been possible without help, guidance or friendship of a bunch of people, all deserving more credit than coming in these lines below.

Meeting professor Erwin Hilger, my thesis advisor, was a discovery on its own. His good spirit, energy, friendliness and attention shared with his students and collaborators are truly contagious. I owe professor Hilger my deep gratitude for inviting me to work in his group and for being a genuine mentor. Additionally, I am truly indebted to him for his wise and flexible attitude, which allowed for my private life to flourish.

When I arrived in Bonn in 2004, I became a member of the CAL subgroup of the ZEUS Bonn crowd. All of its members welcomed me kindly, and helped in various ways to start a life in a new place. Let my thanks go to Detlef, Felix, Julian, Meng and both Stefans.

After about a year in Bonn, I went to Hamburg for two and a half years, to work on-site in DESY within the ZEUS collaboration. It is quite a unique place, full of smart and energetic people from different parts of the planet. Making friends there was easy and natural, as young physicists happen to be quite an open-minded and outgoing flock. Therefore, my thanks go to all these with whom I worked (in particular Umer and Yongdok, who patiently answered all of my numerous questions concerning the Neutral Currents analysis), and especially to all friends who made this time interesting and unforgettable, like Agnieszka, Daniela, Dano, Dorota, Florian, James, Janusz, Jarek, Jerome, John, Klaus, Łukasz, both Pawełs and others.

After coming back from Hamburg in 2008, I became a member of the the Atlas/ZEUS Bonn group, led by professor Ian Brock. I owe thanks to all of its members, and especially to Markus and Oliver, who were always eager to discuss physics, culture and life in various circumstances. I was also lucky to meet (in Bonn) such friends as Gui, Michael, Robert and Stefan, who - all quite different -

really know how to make use of their time and vigor.

Almost every PhD student in a big particle physics collaboration needs not only the guidance from his thesis advisor, but also help, discussion and support of young but already experienced researchers. At different stages of my PhD I was lucky to work closely with Robert Ciesielski, James Ferrando (who was also my NC analysis partner) and Julian Rautenberg - talented, enthusiastic, hard-working and just fun to be around postdocs.

Robert Ciesielski, professor Klaus Desch, James Ferrando, professor Erwin Hilger and Markus Jüngst kindly agreed to read different iterations of the manuscript of this thesis and are responsible for numerous valuable corrections. The old phrase saying that everything that is good about this text comes from them, and all the imperfections are my fault alone, seems very appropriate with respect to this particular writing process.

The list of people I would like to thank would also not be complete without my previous teachers: Alicja Stelmach and professor Jacek Ciborowski. Mrs. Stelmach encouraged me to study physics and professor Ciborowski gave me the first chance to experience DESY, supervised my MSc thesis and introduced me to my future ZEUS Bonn colleagues and employers.

Last but certainly not least, my deep gratitude goes to my loved ones: my family in Poland, friends in Łódź and other places of the world, and my wise and beautiful partner Aleksandra. All of them I need to apologize for (by far too often) not being around when I should have. And all of them I thank - for the love, support, friendship and understanding.